Mechanisms of Nanoparticle Synthesis for the Production of Well-Defined Models of Heterogeneous Catalysts

MAJED YAHEA A ALMASHNOWI

Mechanisms of Nanoparticle Synthesis for the Production of Well-Defined Models of Heterogeneous Catalysts

By

Majed Yahea Almashnowi

Thesis submitted for the degree of Doctor of Philosophy

Department of Chemistry

Durham University

2018-2022

Statement of Copyright

The work on this thesis is conducted by the author in the Department of Chemistry at Durham University starting from October, 2018 to October, 2022. All the work in this thesis is original unless otherwise acknowledged in the text and listed in the references. The work on this thesis has not been submitted for any degree in this or any other university.

Abstract

The synthesis of metal nanoparticles (NPs) by hot-injection/heating-up chemical reduction methods is a widely used method for generating size-controlled nanoparticles with narrow dispersity. These are important in a number of fields, for instance, their use in studies to understand structure-activity relationships in catalysis (the focus of our research group). These methods generate capping agent-controlled metal NPs. This thesis focuses mainly on methods using an organic solvent with long-chain amines and acids, along with a reducing agent, to carry out nanoparticle synthesis by chemical reduction.

Chapter 4 starts to build on a procedure reported (but not thoroughly investigated) in the literature that has shown it was possible to synthesize 3.2 nm Ni NPs by using oleic acid (OA), oleylamine (Oly) and borane tributylamine (BTB). This chapter studies the changes in the colour of the solution over time before the reducing agent is added (including with UV-vis-NIR spectroscopy) and develops the method further to produce smaller 1.3 nm Ni NPs.

Chapter 5 continues the work done by previous group members to develop a method to synthesise size-controlled Cu NPs. This chapter shows the ability to manipulate the reaction temperature to yield a uniform size of 4.3 nm Cu NPs. Then, the study of the solvent system over time before the reduction reaction shows the ability to produce monodispersed 1.8 nm Cu NPs.

Chapter 6 reports studies to investigate the amine-borane type reducing agent used in the previous chapters. Amine-borane (AB) compounds are used without understanding how the reduction process is happening. This chapter uses several approaches to suggest that the amine-borane is releasing H_2 that supersaturates the solution, and then the H_2 reduces the $M(acac)_2$ directly.

Finally, Chapter 7 presents a way to couple two metals NPs of different metals (i.e. unsymmetrical pairs) with covalent tethers. Cu, Pd, and Ni NPs were used with a series of more complex amide linkage coupling systems more commonly used in biological applications. While early attempts were unsuccessful when more complex combinations of coupling reagents were used, it was shown that it was possible to get around 60% of nanoparticles in pairs.

In summary, the thesis examines the synthesis of metal nanoparticles in detail, both the formation of *in situ* precursors and the impact of this on the resultant nanoparticles and the behaviour of the now widely used amine-borane class of reducing agents. It then goes on to demonstrate their use in developing nanostructures with the long-term goal of exploring mechanisms in catalysis using materials that cannot be prepared without recourse to nanoparticle synthesis.

List of Abbreviations

Abbreviation	*Definition*
ASAP	Atmospheric solids Analysis probe
BMNPs	Bimetallic nanoparticles
BTM	borane trimethylamine
DPE	Diphenyl ether
EDC	N-(3-Dimethylaminopropyl)-N’-ethylcarbodiimide hydrochloride
EDTA	ethylenediaminetetraacetic acid
EM	Electron microscopy
GC-MS	Gas chromatography – Mass spectroscopy
HOMO	Highest occupied molecular orbital
ICP-OES	Inductive coupled plasma optical emission spectrometry
LB Trough	Langmuir Blodgett Trough
LUMO	lowest unoccupied molecular orbital
MB	Morpholine borane complex
MMNPs	Monometallic nanoparticles
NC	Nanoclusters
NMR	Nuclear magnetic resonance
NPs	Nanoparticles
OA	Oleic acid
OCA	Octadecylamine
Oly	Oleylamine
PEG	Poly ethylene glycol
PVA	polyvinyl alcohol
PVP	polyvinylpyrrolidone
PXRD	Powder X-ray diffraction
RT	Room temperature
STEM	Scanning transmission electron microscopy
TD-DFT	Time-dependent density functional theory
TEM	Transmission electron microscopy

Acknowledgements

I would like to thank Jazan University for giving me such a good opportunity to complete my Ph.D. degree in the United Kingdom. Also, I would like to thank Durham University for accepting me in the first place and allowing me to be one of its own students. My sincere thanks go to the Department of Chemistry for having me for the last four years and providing me with all the technical support that I need.

There are not enough words to express my gratitude to Dr. Simon Beaumont for helping me to improve my knowledge of chemistry and how I can become a scientist. Therefore, I would like to thank Dr. Simon Beaumont for helping me and providing me with all the materials and instruments that I need to do my Ph.D. work.

I would like to thank my family in Saudi Arabia, my wife and my daughter. Truly, I would not be able to reach this point without your support from the beginning.

I would also like to thank my research group, past and present. Also, I want to let my research group know that I made four goodbye presents to them: 1- a video of me showing you how to make NPs from A to Z, 2- a PDF file about preparing TEM samples and using TEM, EDX and double tilt holder, 3- a PDF file about using temperature controller, 4- a PDF file about using/ handling Schlenk line and testing Schlenk line.

To my reviewer members, I would like to thank you for accepting to be in the reviewer team for my viva, and it is my honour to have you.

Table of Contents

Chapter 1 Introduction

The work contained in this thesis is concerned with the synthesis of nanoparticles and their assembly for use in studying catalysis. As such a brief background of catalysis is given before looking at nanoparticles in general and then specifically at the background of processes that occur in the colloidal synthesis approaches in this study.

1.1 Catalysis

1.1.1 Introduction to Catalysts

Catalysis is a phenomenon that has been used in a wide range of technology applications because most industrial synthesis processes (*e.g*. the production of most energy carriers from gas, oil, and coal)[1,2] and nearly all biological reactions use catalysts in the form of enzymes (*e.g*. the fixation of nitrogen by enzyme nitrogenase to form ammonia that is happened in prokaryotic organisms).[3,4] Prevention of emissions for protecting the environment is another vital technology application that uses catalysis. For example, catalysts that are used on automobiles protect the environment (and humans) from carbon monoxide and nitrogen oxide emissions; the typical location of a catalyst in the exhaust can be seen in Figure 1.[5]

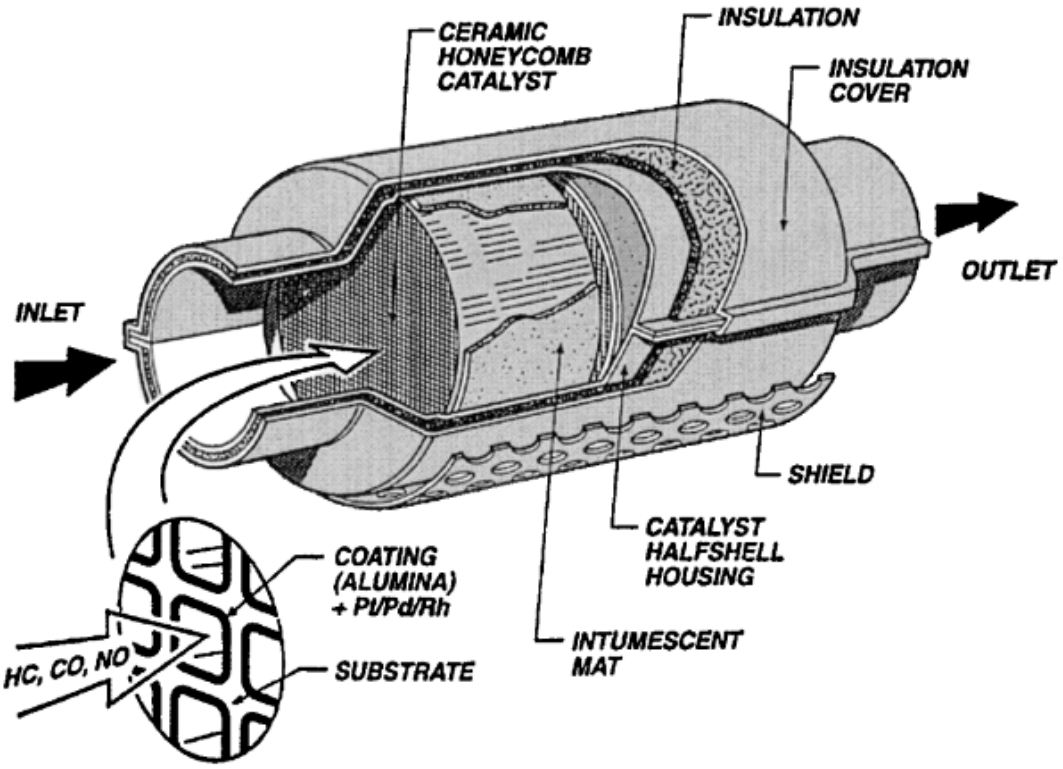

Figure 1: Automotive catalyst carton. Reproduced with permission from ref [5] (Copyright 2001 Applied Catalysis A: General)

A catalyst is a substance that can accelerate a reaction without itself being chemically changed. Today, the phrase "being chemically unchanged" can be described in more chemical detail. For example, in the oxidation of SO_2 to SO_3 it has been shown that vanadium oxide (V_2O_5) is reduced (to V_2O_4) during the catalysis process and then converted back to vanadium oxide again (V_2O_5).[4] A catalyst cannot change thermodynamic equilibrium but can enhance the rate of a feasible thermodynamic reaction, as shown by the reaction profile diagram in Figure 2. The catalysts can be solid, liquid, or even gas. Over the last 200 years, scientists have been developing ways to synthesize and use catalysts effectively.[6-9]

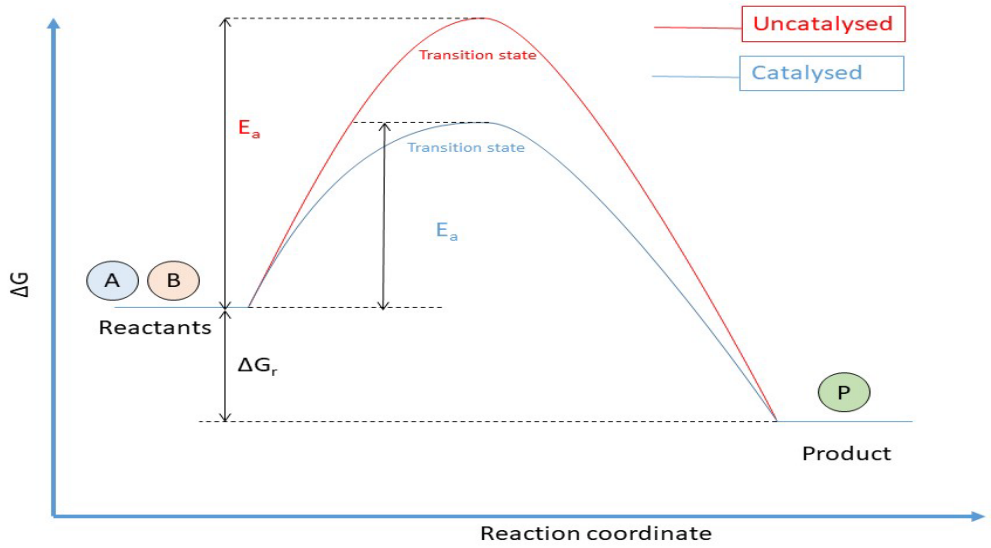

Figure 2: Energy profile diagram for catalysed and un-catalysed reactions.

Catalytic processes offer an alternative path for reactions that are energetically favourable. The activation energy for the catalytic reaction is smaller than the uncatalysed reaction. The catalyst can form intermediate products, which later leave the catalyst to form the final product, and the catalyst is regenerated again. For example, the hydrogenation of ethene to ethane over a Pd catalyst, Figure 3.[10]

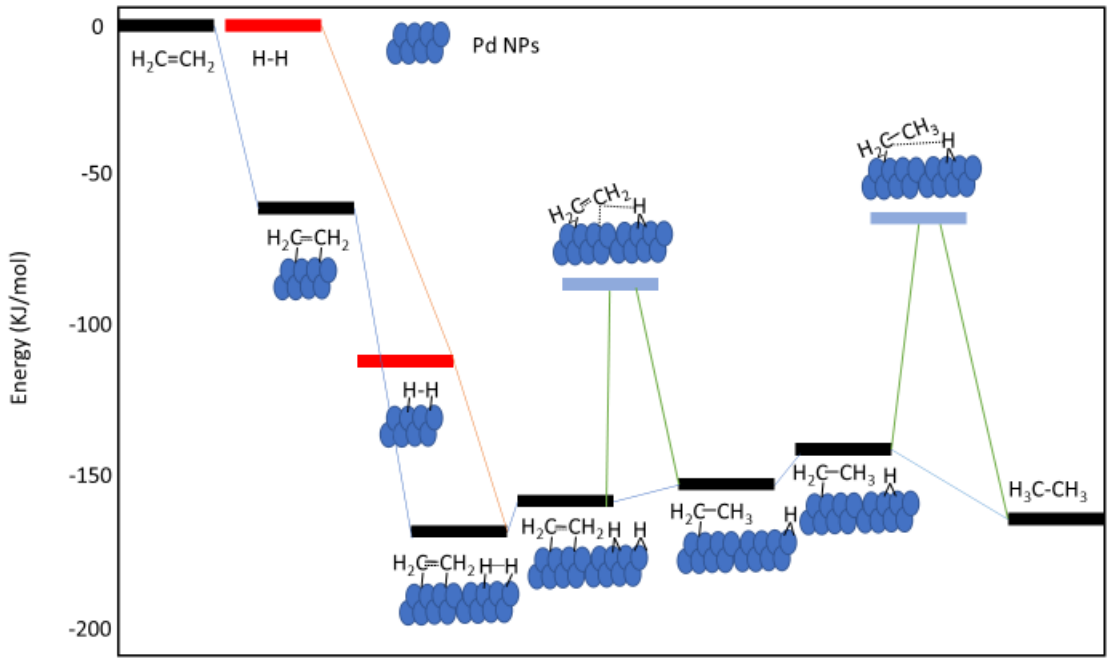

Figure 3: Enthalpy profile of the catalytic hydrogenation of ethene to ethane over Pd catalyst. Reproduced from literature.[11]

1.1.2 History of Catalysis

In 1835, a Swedish chemist J.J. Berzelius (Figure 4), reported an 'action of several simples' by naming this 'action' by a new 'force'. This force decomposed the other bodies and remained indifferent "It is, then, proved that several simple or compound bodies, soluble and insoluble, have the property of exercising on other bodies an action very different from chemical affinity. By means of this action, they produce, in these bodies, decompositions of their elements and different re-combinations of these same elements to which they remain indifferent". Therefore, Berzelius was the first one to use the term catalysis, and he published this in 1836.[7,12]

Figure 4: J.J. Berzelius (1779-1848). Reproduced with permission from ref [12] (Copyright 1948 American Chemical Society)

In 1909, Wilhelm Ostwald (Figure 5) won the Noble Prize for chemistry in recognition of his work in catalysis. His definition of the catalyst was "a catalyst accelerates a chemical reaction without affecting the position of the equilibrium".[13] This means the catalyst changes the rate of the reaction but not the equilibrium of the reaction.[4]

Figure 5: Wilhelm Ostwald in about 1897. Reproduced with permission from ref [13] (Copyright 2009 Angewante Chemie International Edition)

Before 1800, Joseph Priestley and Martinus van Marum noticed that the dehydrogenation of alcohol could occur on metal surfaces. Another discovery was by Louis Jacques, who noticed that ammonia could be decomposed to hydrogen and nitrogen when he passed the ammonia over various red-hot metals. From that point, a scientist called Pierre Dulong measured the activity of ammonia's decomposition, which increased from platinum to gold, silver, copper, and then iron.[7] Since these times, catalysis has had a major impact on everything from the production of necessary chemicals for society to function to maintaining the environment, such as the automotive catalysts mentioned in the previous section. It has also become a developed science in its own right, with many tools (including nanoparticle mimics of catalysts) being used to characterise and understand catalytic reactions.

1.1.3 Types of Catalysts

Typically, there are three types of catalysts, and this classification is based on the mode of action. The first type is homogenous catalysts. This type is called homogenous because the catalyst and the reactants are in a single phase (usually solution). The second type is heterogeneous catalysts, in which the reactants and the catalyst are in separate phases (usually catalyst is in a solid phase, and the reactant is a gas or liquid). The third type is the enzymatic catalysts or biocatalysts.[14]

Homogeneous or soluble catalysts, as referred to in some literature, are described in terms of chemical composition and structure.[15] Most homogeneous catalysts are well characterized, which makes homogenous catalysts more likely to be used with reactions that are complex, difficult, or need highly selective transformations. For example, methanol and carbon monoxide are used to synthesize acetic acid in a homogeneous catalytic process.[4]

For heterogeneous catalysis, the catalyst is in a different state (mostly solid) from the reactants (liquid or gas); as mentioned earlier, the vanadium oxide (V_2O_5) catalyst is a

solid catalyst that is used to convert gaseous SO_2 to SO_3. The reaction happens only on the surface. Therefore, in order to increase the catalyst surface area, the diameter of the particles needs to be small. The small (nano) particles can cause problems such as sintering (becoming larger particles) or are restrictive to gas flow (there can be difficulty in flowing gaseous or liquid reactants around small catalyst particles). The way to solve these problems is to deposit the catalyst NPs on other materials called support materials (usually, support particles are larger than catalyst particles), such as SiO_2 that, in this case, is used to support vanadium oxide (V_2O_5).[4]

Biochemical reactions can be catalyzed by enzymes or microorganisms. These catalysts can also be immobilized by various carriers, such as silicon dioxide, porous glass, and organic polymers. [9] Isomerization of glucose to fructose is a prominent example of a biochemical reaction. Also, the production of some soft drinks uses glucoamylase immobilized on silicon dioxide. Another example is cells of corynebacteria, which convert acrylonitrile to acrylamide while entrapped in a polyacrylamide gel.[9]

The different types of catalysts both have some strengths and some weaknesses. Heterogeneous catalysts have strengths such as being cheap, long-lived, can be regenerated, and being in a solid state, they can be separated easily. Homogeneous catalysts have strengths such as being able to be used in mild conditions, being highly selective, being robust to poisons, and being more easily tuned. Each strength point of a heterogeneous catalyst is a weak point of homogenous catalysts and vice versa.[16,6]

1.1.4 Properties of Catalysts

The key figures of merit that need to be known for any catalyst are activity, selectivity, and stability. These properties are important to know in order to establish which catalyst is suitable for a reaction. Activity is the measurement of the reaction rate per catalyst amount to know how fast the reaction is in the presence of the catalyst. Selectivity is the specific fraction of the reactants that are converted to the desired product. Stability

is the lifetime of the catalyst in the reaction, and this parameter can be affected by many factors, *e.g*. poisoning, coking, and decomposition.[8]

1.2 Nanoparticles

Nano is a measurement prefix used to denote 10^{-9}, so for sizes, typically, this refers to length scales of nanometers. Nanoparticles are particles that have a size between 1-100 $x10^{-9}$ nm.[6] The National Science Foundation defines 'Nanotechnology' as the ability to understand individual atoms at that level (nanometer lengthscales).[17] The understanding of atoms in this context can include the synthesis, control, and manipulation of structures at the nanoscale. Understanding atomic assembly can give insight into how atoms are organized and how this could be changed to give new materials. The synthesis of nanoparticles is a hotspot for research into nanotechnology.[6]

1.2.1 Synthesis of Nanoparticles

The synthesis of nanoparticles is typically divided into 'top-down' approaches, in which bulk materials are broken up, and 'bottom-up' approaches, where nanoparticles are assembled from atomic or molecular precursors.

1.2.1.1 Top-down approaches to nanoparticle synthesis

This method must have an external force to pressure bulk materials to end up as smaller materials. Top-down techniques are generally physical methods that use physical force to get the product. Top-down routes can be divided into four common methods. Firstly, mechanical energy includes ball milling,[18] grinding,[19] and mechanochemical methods[20]. Secondly, thermal methods, including electrospinning,[21] thermolysis,[22] annealing,[23] and (thermal[24] or emulsion[25]) evaporation. Thirdly, chemical methods, such as etching,[26] electropolishing,[26] and anodizing.[27] Lastly, high-energy approaches such as laser

ablation,[28] electron beam(lithography) ,[29] sonication,[30] and arc discharge.[31,6,32] Figure 6 shows a summary of top-down methods.

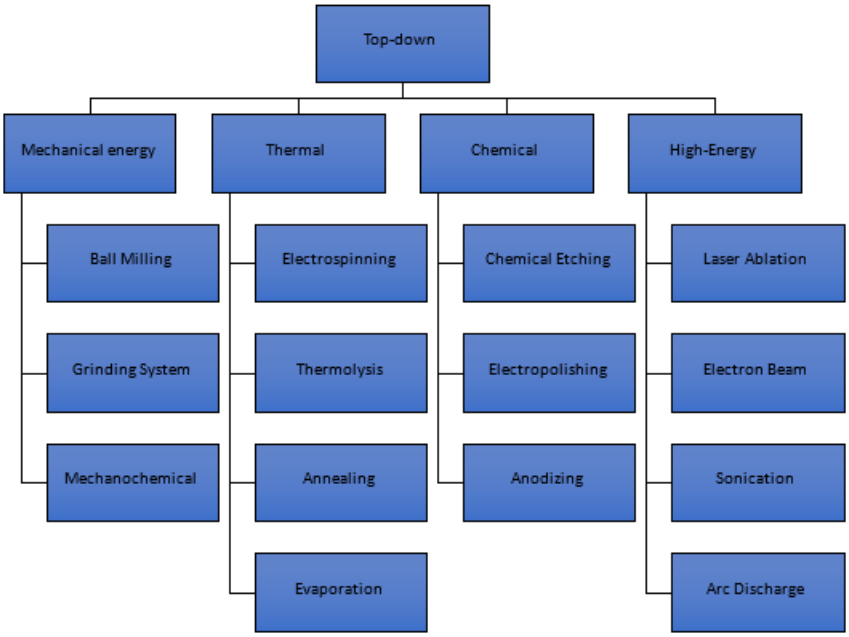

Figure 6: Summary of 'top-down' methods for nanoparticle synthesis

1.2.1.2 Bottom-up approaches to nanoparticle synthesis

These approaches are usually made by using a chemical reaction to combine molecular or atomic species in order to grow particles. Bottom-up methods are more widely used than top-down methods for controlled synthesis of small < 20 nm nanoparticles because of the greater ability to control the shape and size of the resultant nanoparticles.[32] The bottom-up method can be divided into three classes. Firstly, gas-phase methods included chemical vapour deposition,[33] atomic layer deposition,[33] epitaxy,[34] and combustion processes.[35] Secondly, liquid phase methods which include molecular self-assembly,[36] sol-gel / gel-sol,[37] electrodeposition,[38] and supramolecular chemistry.[39] Lastly, solid-phase methods such as thermal decomposition[40], solution plasma,[41] and electric furnace techniques (ceramic heater).[42],[6,32] Figure 7 summarises bottom-up methods.

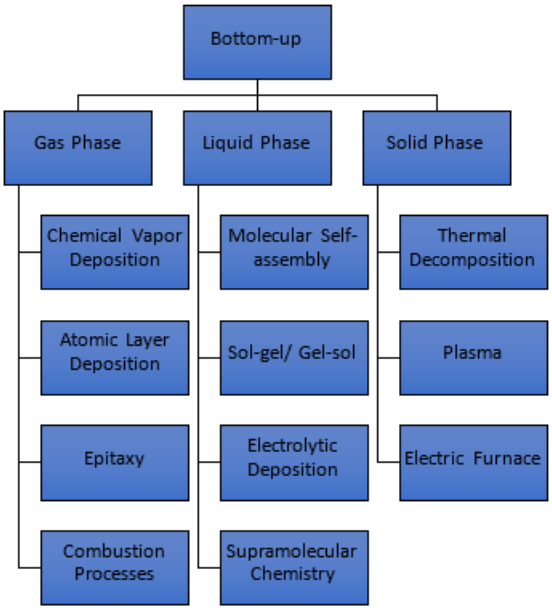

Figure 7: Summary of 'bottom-up' methods for nanoparticle synthesis.

In summary, the final desired nanoparticles play into the choice between the two methods. For example, metal nanoparticles are often synthesized by the chemical reduction method. Chemical reduction methods are often used to synthesize metal nanoparticles because of their reliability. In this method, a metallic ion is reduced by the transfer of an electron from the reducing agent to get zero-valent metal atoms in solution, which then aggregate due to the driving force of metal bond formation. By this chemical reduction method, monometallic, bimetallic, and multi-metal nanoparticles can be generated.

1.3 Colloidal nanoparticle synthesis routes.

In this section, the current state of knowledge of colloidal nanoparticle synthesis routes, the type studied in this thesis, will be reviewed in more detail.

1.3.1 Understanding the theories behind the synthesis of nanoparticles

The synthesis of nanoparticles (NPs) has received considerable interest because of their chemical and physical properties, such as catalytic activity[43] and magnetic and optical properties.[44,45] This attention was to understand the size-dependent properties, which are what make the synthesis of size-controlled small NPs important. Also, the attainment of narrow size distributions of the resultant NPs gives uniform properties, which are essential for many uses, such as optical applications.[46]

1.3.1.1 Classical nucleation theory and LaMer model

NP syntheses are often described using Classical Nucleation Theory (CNT) and the LaMer model for growth. At the beginning of the twentieth century, researchers took the first-order Gibbs phase transition and used it to describe the phase transition from supersaturated vapours to liquid (increasing the entropy of the system will lead to minimizing the Gibbs free energy). They then applied these theories to the formation of crystals, now known as the classical nucleation theory.[47-49] CNT considers a spherical nucleus forming (*e.g.* condensation of a droplet from the vapour phase).[50,51] The nuclei could be formed homogeneously, which, in the context of nanoparticle synthesis, happens when there is no help from a foreign surface, such as the synthesis of Ni NPs by using oleylamine and oleic acid.[43] In contrast, heterogeneous nucleation occurs at the foreign surface, such as the synthesis of Ni NPs by using a seed-assistance method.[44] It was identified in CNT that homogeneous nucleation could be considered thermodynamically. Therefore, the total free energy (ΔG) of a particle (a spherical nucleus with a radius, *r*, Figure 8) can be defined as the sum of the surface free energy ($4\pi r^2\gamma$; where γ is the surface energy of the spherical particle) and bulk-free energy ($\frac{4}{3}\pi r^3\Delta G_v$; where ΔG_v is volume free energy of the particle), as can be seen in Equation1.

$$\Delta G = 4\pi r^2\gamma + \frac{4}{3}\pi r^3 \Delta G_v \quad (1)$$

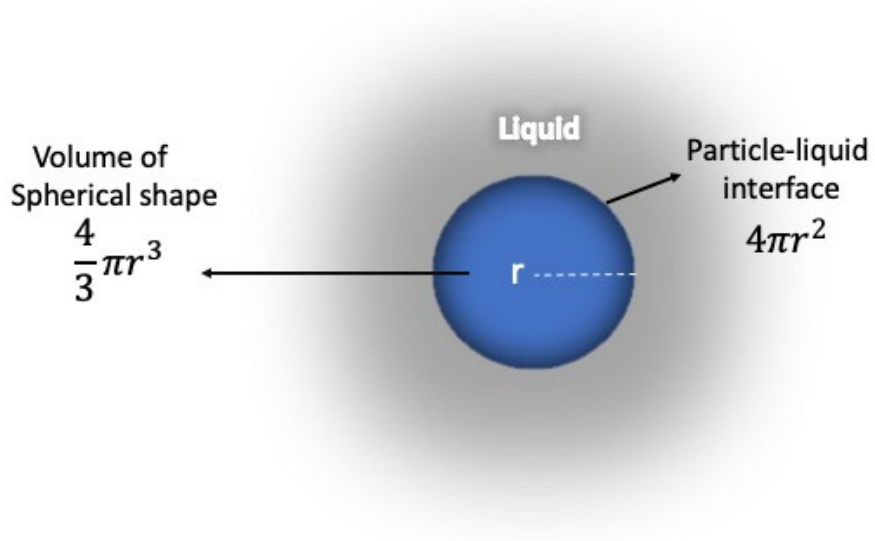

Figure 8: Spherical shape solid particle in liquid phase surroundings. Once the total free energy is negative, the transformation from phase to phase should happen spontaneously, but the particle-liquid interface is why there is a resistance that requires energy to complete that transformation.

In order to make the total energy negative such that the process happens energetically favourably, the surface free energy (always positive) must be overcome by the bulk-free energy term (favourable or negative), and the variation between them with respect to *r* makes the bulk free energy dominant in larger particles. A nucleus at the beginning of particle growth needs the energy to pass the critical radius, r^*. For nuclei with a radius greater than r^*, the energy will start to decrease, which means further increasing the size of the nuclei will decrease the total energy, and the growth will happen spontaneously. At r^*, if the nuclei do not have enough energy to pass r^*, they will redissolve by lowering the total energy and shrinking the particle back into the solution, as can be seen in Figure 9

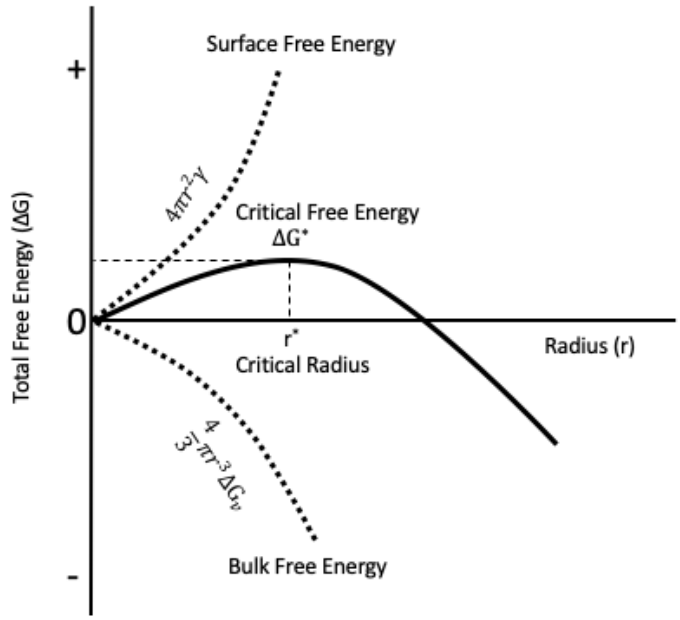

Figure 9: The total free energy of a spherical particle. [52]

One of the early studies of NPs was by LaMer in 1950.[52] His theory explains the three stages of synthesizing NPs, based on CNT. These three stages are pre-nucleation (I), nucleation (II), and growth (III), as can be seen in Figure 10. In the first stage, he suggested that the pre-nucleation stage is the forming of a high enough number of monomers. These monomers are individual; once they start to gather, the number of monomers will start to decrease. In this stage (stage II), where the number of monomers decreases again, nucleation occurs. Once most of the monomers have made nuclei, the growth stage (stage III) will start, which means no more nucleation at that stage (as the monomer concentration is too low, and the remaining monomer can only become attached to existing nuclei). This theory leads to the idea of burst nucleation.[53] The idea that a narrow size distribution is achieved when the monomer concentration is rapidly increased in (I), section (II) is short, and so nucleation occurs for all particles more or less independently to grow. The growth is controlled only by the diffusion of the monomer to the surface. The rate of the growth of the smaller (r_1) particles is faster than the rate of growth of larger particles (r_2) in a

relationship inverse to particle size ($\frac{dr}{dt} \propto \frac{1}{r}$) where; $\frac{dr}{dt}$ is the rate of the growth, and r is the radii size of the particle,[54-57,] as can be seen in Figure 11. This means that growth in a regime where diffusion of monomer to the surface is the dominant factor will also lead to more uniform-sized nanoparticles.

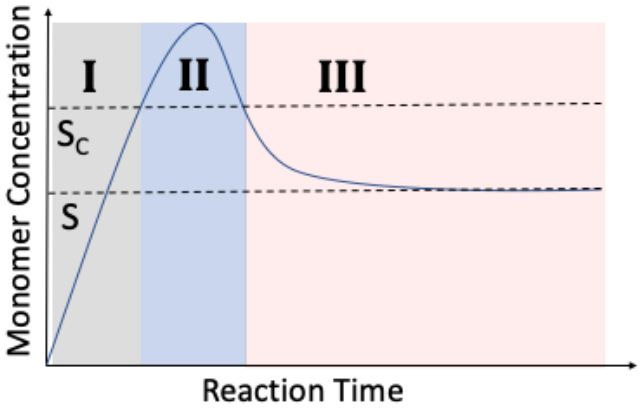

Figure 10: LaMer's theory of nucleation. I) the number of monomers starts to increase until the point that no more monomers can be formed is reached, I I) the number of monomers decreases due to the formation of nuclei and no more nuclei can be formed after the monomer concentration drops below the critical supersaturation S_C, I I I) these nuclei start to grow.

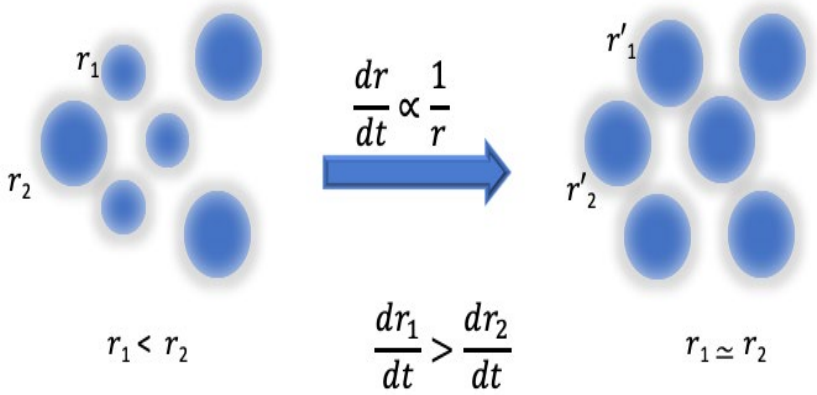

Figure 11: Focussing mechanism during growth. The smaller particles (labelled r_1) are growing faster than the larger particles (labelled r_2).

1.3.1.2 Ripening mechanisms

After the initial NP synthesis (*i.e.* once all initial monomer has been consumed), ripening can occur (which implies some particles or atoms dissolving again, possibly involving the capping agent to affect the final size and size distribution). There are two ripening mechanisms that have been studied by many groups, which are Ostwald and digestive ripening. Ostwald ripening has been used to describe particle growth since 1900 for two-phase systems[58] and can be used to explain changes in particle size.[59] Ostwald ripening is the growth of large particles at the expense of smaller particles.[60, 61] The smaller particles have higher surface energy; therefore, they redissolve again to form small nuclei and then, larger particles use the metal monomer in the solution to become even larger.[62] This is thermodynamically driven because large particles are more energetically stable (as seen earlier in Figure 11). However, for it to occur (kinetics), the metal must be able to redissolve to become a metal monomer again and then re-adsorb on the particles reversibly (eventually favouring the more thermodynamically stable particles).

Another ripening mechanism is called digestive ripening. It is the opposite of Ostwald ripening which means the smaller NPs (or particles of a specific size) grow faster than the larger particles, such that they all become a similar size.[62] Some literature refers to Ostwald ripening as "size un-focusing" due to the growth of the large particles and redissolving of the smaller particles resulting in broad size distribution.[63] Correspondingly, digestive ripening is often called "size-focusing" as particles become more similar in size, which can be achieved by stabilising the NPs (thermodynamically) by using a digestive ripening agent (often the capping agent). The digestive ripening agent may play the role of promoting the redissolution of the monomers (or small NPs) or selectively stabilising particles of a certain size to achieve a uniform size and smaller size distribution.[64]

1.3.2 Understanding the stages of metal nanoparticle synthesis via a chemical reduction of a metal precursor

The synthesis of metal nanoparticles can be described following the following steps.

1. The reducing agent provides electrons that can be used to reduce the metal precursor and generate metal atoms that are supersaturated in solution (pre-nucleation).
2. These metal atoms will be gathered into nuclei because the total energy, ΔG, is negative above the critical radius, favouring the formation of particles happening spontaneously (nucleation).
3. Above the critical size, r*, the overall energy is lowered by gathering further atoms, which means re-dissolving the nuclei need energy, but to keep growing is energetically favourable (growth).
4. The capping agent will stabilize the surfaces, which stops or slows the access to more atoms being deposited and means the particle will stop growing (particle formed). The capping agent also prevents metal surfaces from coming into contact, which could lead to particle coalescence (the joining of two particles).
5. Finally, suppose metal atoms can be temporarily redissolved in solution reversibly, even in small numbers. Although it is not favourable for them to remain in solution, it can result in the transfer of metal between particles, so digestive or Ostwald ripening may occur.

1.3.2.1 Chemical reaction

Despite nanoparticle synthesis being more than a century old.[65] The role of concomitant chemical reactions has often not been fully understood. Even though the CNT is considered the most common approach for explaining the nucleation processes, there are often several aspects to the chemical reaction steps that need to be considered to understand these processes, rather than only using the phase transition to model the nucleation process. The nucleation process in nanoparticle synthesis typically occurs intimately linked to the result of a chemical reaction, which means the understanding of the effects of the chemical reaction on the nucleation and growth processes (as well as the impact of synthesis products on ripening and capping processes) is essential for a better understanding of the synthesis of uniform size and narrow size distribution NPs.[47]

The wet chemical synthesis of NPs can be divided into the three stages outlined in the Le Mer model: first, the pre-nucleation stage; second, the nucleation stage; and finally, the growth stage. It is instructive to think about the chemistry that occurs in each stage.

1.3.2.2 Pre-nucleation stage

The wet chemical approach includes a large number of experimental parameters. Each parameter can influence produced NPs. These parameters can be divided into two groups. The first group is physical parameters, which include the reaction pressure and temperature. The second group is chemical parameters, which include solvents, pH, reducing agents, and metal precursors.[66] The pre-nucleation stage can be tuned to produce metal or metal oxide, different morphologies, and different particle sizes.

The role of temperature has been shown to enable the formation of different size and shape NPs.[67] This can be due to the fact that the temperature can activate the chemical reaction between the capping agent, reducing agent, metal precursor, and/or solvents, alter diffusion or solution viscosity, and alter the solubility of reagents and the reduced

metal atoms. This can be positive or produce undesired effects during the synthesis of NPs., as illustrated in a number of simulation literature studies.[68-70]

In terms of chemical parameters, solvents show an effect on the synthesis of NPs. For instance, when using pyridine as a solvent, pyridine became bound to the metal precursor as a ligand and, in turn, affected the size of the NPs.[71] Another example is using oleic acid while synthesizing Ni NPs; the resulting NPs showed higher magnetic properties compared (forming fcc phase) to the same method but without using oleic acid (forming hcp phase).[71] Interestingly, the type of solvent aliphatic or aromatic, can influence the size of the NPs. For example, Au NPs capped with oleylamine had a different size depending on the solvent that was used. Smaller Au NPs 5.3 nm were obtained using aliphatic long-chain hydrocarbon (*n*-hexane) as a solvent. In contrast, larger Au NPs, 7.3 nm, were obtained using an aromatic solvent such as toluene or benzene, where the synthetic procedure was otherwise the same.[71]

Changing the pH of the reaction system can influence the size of the NPs. A study showed that for Ag NPs synthesized by a chemical reduction method, the size of the resulting NPs can be controlled by changing the pH of the system (smaller NPs obtained by high pH because the electrostatic effect).[72,73]

The concentration of metal precursor that is used in the synthesis can have an effect on the shape and size of resulting NPs. For example, a study shows iron oxide NPs can be synthesized by the same method to have different sizes just by changing the concentration of metal precursor ($Fe(CO)_5$) that was used.[74] The concentration of ($Fe(CO)_5$) was increased from 0.4-4 mmol with keeping the reducing agent oleylamine at the same concentration 3 mmol. The changing in size is because the changing on the ration between the metal precursor and the reducing agent.

In recent years, many groups have been studying the reduction rate of the metal precursor in order to fully exploit the properties that can be obtained from different sizes and shapes of NPs. One interesting study shows that different metal precursors will have different reduction pathways. The reduction rate of the metal precursor can lead to

different morphology and size.[75] For example, the reduction of $PdCl_4^{2-}$ and $PdBr_4^{2-}$ shows different sizes and morphology in the presence of seeds or without seeds. The $PdCl_4^{2-}$ formed two different shapes (concave cubes and spherical), and the size was around 20 and 3.4 nm, respectively. In contrast, the Pd Br_4^{2-} just showed uniform size and dispersion (concave cubes with size 20 nm). Therefore, the type of ligand in the precursor influences the nanoparticle size, morphology, and dispersity.[75] Another study shows the effect of the reducing agent on the reduction rate and its ability to control the shape of the NPs.[76] This study used Na_2PdCl_4 and reduced it with either ethylene glycol or with diethylene glycol. The resulting NPs were truncated octahedral shape and icosahedra, respectively, and the difference is attributed to the difference in reduction potential of ethylene glycol and diethylene glycol. These two reducing agents were able to convert the Pd (II) to Pd (0) by 98.3% and 29.9% in the first 10 min, respectively.[76]

The reduction rate can affect the size of the particles. Slow reduction gives metal atoms (NP monomers) at different times – the opposite of burst nucleation described earlier. The first atoms to gather together and nucleate will have a longer growth time and so be expected to be bigger in size than the metal atoms that formed at the end of the reaction. This can cause bi-modal or broad-size distributions. The proposed mechanism can be seen in Figure 12.

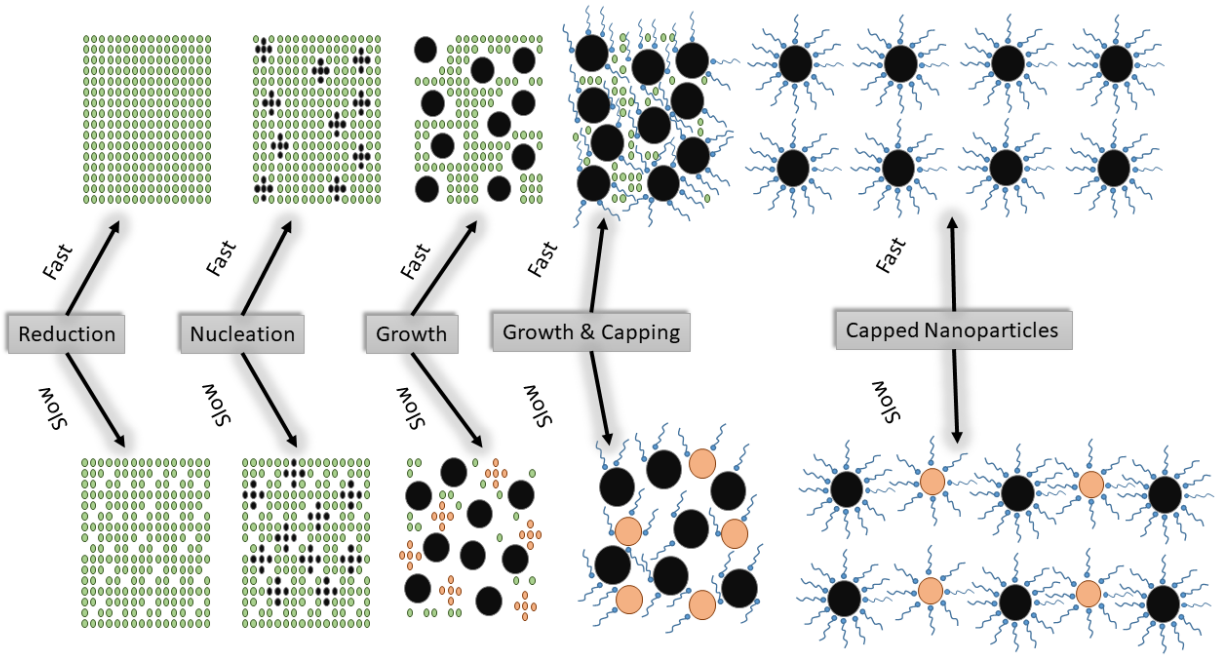

Figure 12: Fast reduction rate provides a high number of metal atoms that can be condensed at different spots before they are capped by a capping agent; the resulting particles have uniform size and shape. The slow reduction provides metal atoms on a slower timescale. The first atoms that are located close to each other will generate nuclei (first-generation – black coloured); Then, the metal atoms that are generated after the first generation is formed will condense together and form a new nucleus (the second-generation orange coloured). The slow reduction can therefore form bimodal or broad-size distributions.

1.3.2.3 Nucleation stage

At the nucleation stage, simulation studies show that the forming of the nuclei starts from a high-density region of metal atoms. A simulation was done with up to 10^6 atoms to account for the homogenous nucleation of bcc Fe crystals.[77] In another example, it was shown that the reduction rate of the metal precursors could be tuned by ligand exchange.[78] In this study, PdPt core-shell octahedral nanocrystals were synthesized; then, they synthesized PdPt alloy nanocubes by adding KBr to the reaction. They explained the change in morphology by the change in the reduction rate. The Br^- exchanged with Cl^- ligand, and because of the strong bonding of Br^- to Pd and Pt, the reduction rate was slower than with

Cl^- bonding to Pd and Pt. The different reduction rate was shown to cause different morphology nanocrystals.[78]

1.3.2.4 Growth stage

The most common technique to stop the NPs from keeping growing excessively is using capping agents. These capping agents have the ability to reduce surface energy, and consequently, the NPs will stop growing due to surface stabilization. These capping agents consist of a long hydrocarbon chain (hydrophobic) and the terminal group, usually phosphines, amines, or thiol (hydrophilic and metal-binding). These capping agents not only stabilize the surface energetically but also prevent the smaller nanoparticles or other nanoparticles in general from agglomerating and attaching to the NPs to make them bigger. Also, a study shows the effect of the capping agents on Ag NPs size was only slight but did cause some change in size for particles prepared under otherwise identical conditions. This study compared polyethylene glycol (PEG), ethylenediaminetetraacetic acid (EDTA), polyvinylpyrrolidone (PVP), and polyvinyl alcohol (PVA) and the average particle sizes were 44, 39, 35, and 31 nm, respectively.[79]

1.3.3 Understanding catalysis by mono and bimetallic catalysts and nanoparticle catalysts

Although a lot of this thesis is focused on the preparation of monometallic nanoparticles, Chapter 7 looks at combining these nanoparticles into pairs for eventual applications in catalysis. Having looked at catalysis and nanoparticle formation as background for the ideas in this chapter, the conventional understanding of bimetallic catalysts is discussed and reviewed in this section.

1.3.3.1 Introduction to monometallic catalysts

Monometallic means NPs or catalysts of only one metal. As discussed in the introduction to catalysts, the surface area of the catalyst is essential for catalytic activity. Monometallic nanocatalysts can provide a large surface area, which makes the catalytic activity of the metal nanocatalysts higher. For example, copper nanoparticles have been used as a catalyst due to better yields, shorter reaction time, inexpensive fabrication and recyclability.[80] Catalysts with one metal have some limitations, which is the reason why scientists have often considered using more than one metal in a single catalyst, known as bimetallic catalysts.

1.3.3.2 Introduction to Bimetallic catalysts

During the previous decade, the synthesis and investigation of bimetallic nanoparticles have received much attention because of the way they show improvements in the catalytic activity, selectivity, and stability over monometallic nanoparticle catalysts.[81-84] The different components of the catalysts affect the overall reaction mechanism, which can achieve new chemical transformations that cannot be achieved via monometallic catalysts.[85-87] Figure 13 shows some general advantages of bimetallic nanoparticles (BMNPs) over monometallic nanoparticles (MMNPs).[82, 84, 88, 89]

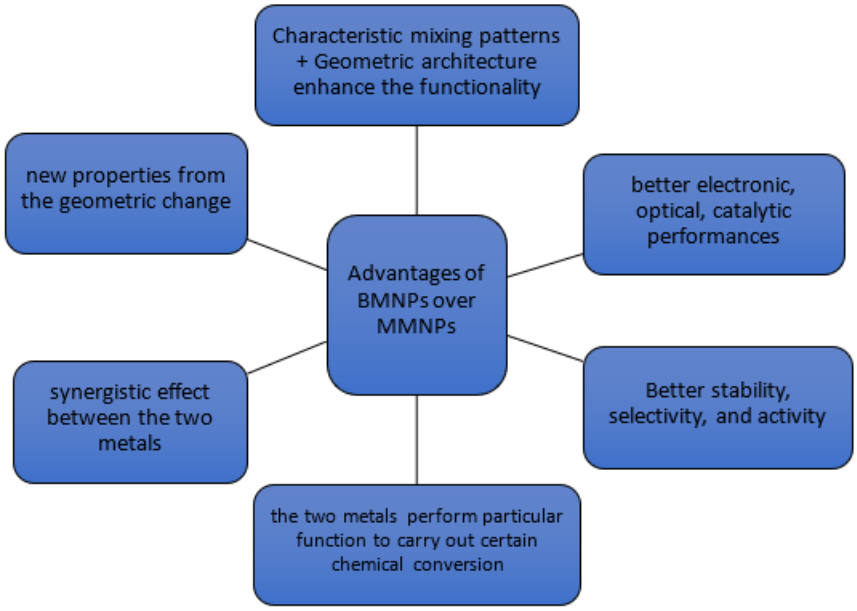

Figure 13: The advantages of the BMNPs over MMNPs.

1.3.3.3 Synthesis of bimetallic nanoparticles with various architectures

As mentioned before, bimetallic particles comprise two metals, but the architecture of bimetallic NPs can be different due to atomic ordering (alloyed or intermetallic, subclusters, and core shells), crystal structure and internal structure. Bimetallic nanoparticles can be classified into two types: mixed structures and segregated structures, as seen in Figure 14.

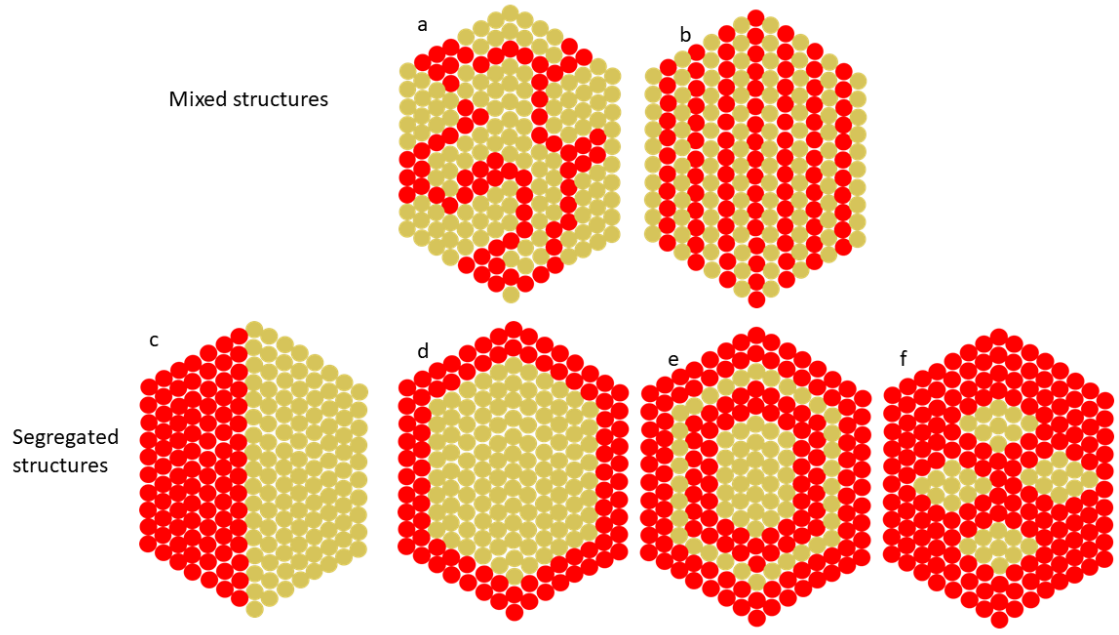

Figure 14: Different bimetallic architectures (a, and b top) are mixed structures, and (c, d, e, and f) are segregated structures. Based on ref.[90]

The atomic ordering of a randomly mixed structure type can be seen in Figure 14a, which is an example of an alloyed structure. Alloyed NPs are composed of nanocrystals in which two metals are mixed randomly. An ordered configuration mixed structure can be seen in Figure 14 b, which is an example of an intermetallic structure. Intermetallic NPs are mixed in an ordered (repeating patterned) way. The segregated structures are comprised of two metals with a shared interface between the two metals. This interface may be across the whole particle, as seen in Figure 14c. When one metal is located in the core of the structure and it has been surrounded by another metal, it is known as a core-shell structure, Figure 14d. When shells are in an alternating arrangement, the multi-shell core-shell structure can be formed, as seen in Figure 14e. Finally, when cores are shelled by one metal shell, the multi-cores core-shell structure can be formed, as seen in Figure 14f. Bimetallic architectures can be tuned to get an effect that can enhance the properties of the bimetallic catalyst.[90]

1.3.3.4 Catalytic properties of BMNPs.

Bimetallic nanoparticles show massive potential in catalytic applications compared to monometallic nanoparticles. The reason for the better performance of the BMNPs as catalysts is the presence of the two metals in one nanoparticle.[91] The close interaction of the two metals can enhance the catalytic properties in different ways, but most commonly, these are classified as structure (geometric),[81, 91, 92] and electronic (ligand) effects.[92]

1.3.3.4.1 Structure effect

The structure effect applies where a local geometric system exists of individual atoms. The two metals can form a specific structure based on activity and selectivity for a particular reaction. Each geometry can enhance specific catalytic properties.[81] For example, Au-Cu BMNPs improve the stability of COOH by having a Cu atom adjacent to an Au atom (alloy structure). In this case, Cu forms a bond towards the O atom (end of the COOH), and Au forms a bond towards the C atom. The other architectures, such as the core-shell structure, cannot have this stability because the Au atoms will be inside the structure, and the Cu atoms will be on the surface.[92]

1.3.3.4.2 Electronic (ligand) effect

Electronic effects are defined as changes in chemical reactivity based on the changes in the electronic structure of the surface metal atoms on the nanoparticle. Yang and co-workers have explained how the binding of the intermediates can be affected by the kind of electronic structure of the surface composition. Figure 15 shows the electronic effect in terms of the binding strength of an Au-Cu bimetallic catalyst. The illustration shows proposed mechanism for CO_2 reduction on the catalyst surface of Au-Cu BMNPs. In the case of the Au_3Cu catalyst the binding between the COOH and the catalyst surface was week but with increasing the ratio of Cu to Au (from Au_3Cu to AuCu to $AuCu_3$) the interaction between the COOH and the catalyst surface increased (more absorbing of COOH and less adsorbing CO) favouring the formation of hydrocarbons.

For transition metals, the way the *d*-band of the metal interacts with the adsorbate determines the binding strength.[92]

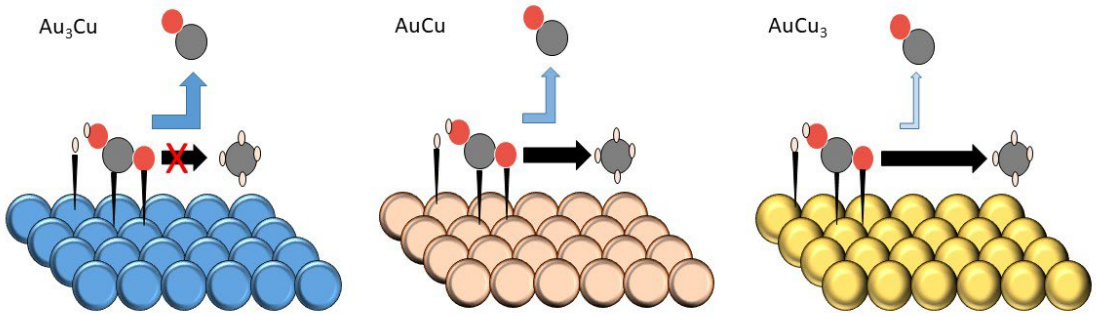

Figure 15: The proposed mechanism for CO_2 reduction on Au-Cu bimetallic catalyst. Grey circles are C, red circles are O, and white circles are H. Based on ref.[92]

1.3.3.5 Two catalytic sites.

The reason for using the catalysts in the first place is to promote some chemical reactions that are intrinsically (thermodynamically) favoured. However, there are situations in which more than one molecular process could be catalytically promoted. For example, in some cases where the chemical reaction involves hydrogen, a catalytic site is needed to dissociate the H_2 before subsequent steps occur. For the hydrogenation process, the hydrogen atom can be dissociated by solid catalysts (*e.g.* Ni catalyst); then, the hydrogen atoms can be involved in hydrogenation processes at other sites via a so-called spillover process. As seen in Figure 16(a), the hydrogen gas absorbs onto a metal surface (first site); then, the catalysis process on the first metal surface will be the dissociation of the hydrogen gas (H_2) into H atoms. In Figure 16(b), the hydrogen atom migrates to the other metal

surface (second site). The catalysis process on the second site involves reacting the hydrogen atom with the other adsorbed atoms or molecules.

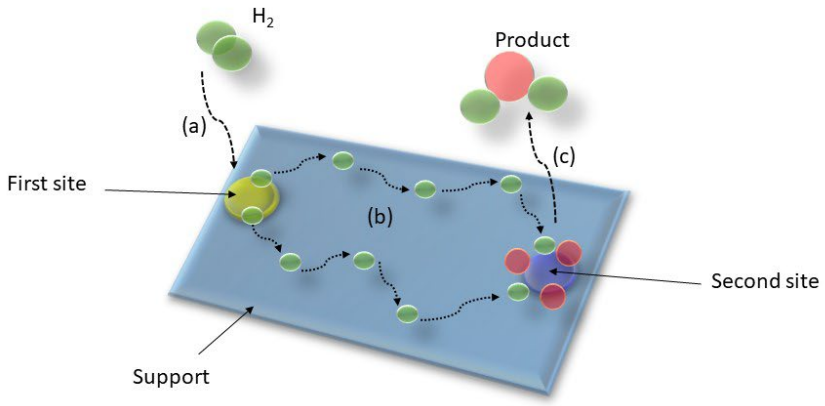

Figure 16: spillover technique for hydrogenation catalysis process. Based on ref.[93]

Many publications show that the use of two active sites results in some improvement in the catalytic activity and selectivity.[94, 95] Not just this, they go further to show that the distance between these two catalytic sites can cause some improvement in the activation process. For example, Zhao *et al.* reported that the closest distance between Ru and Ni, the higher the guaiacol hydrogenolysis activity attained, as presented in Figure 17.[96]

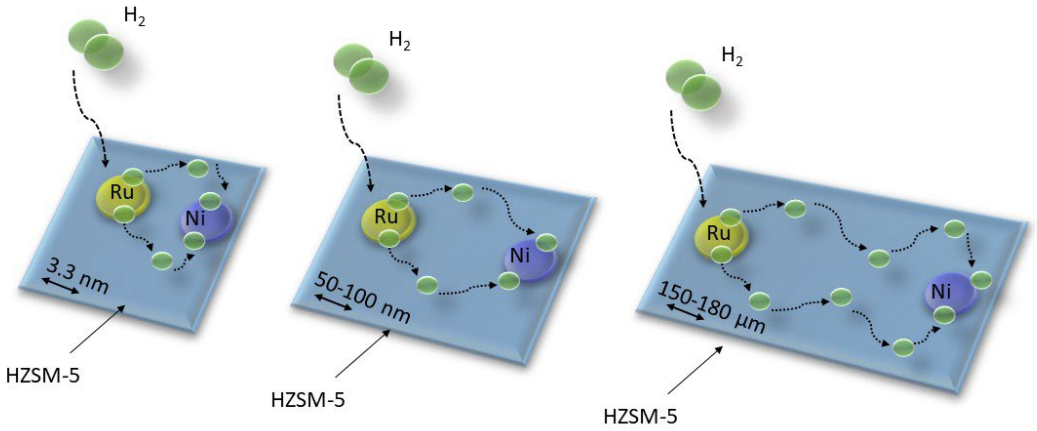

Figure 17: The hydrogenolysis activities on the Ru and Ni catalysts at different distances. Based on ref.[96]

Bokhoven *et al.* reported the supported catalyst effect on hydrogen spillover. He used two different catalytic sites (platinum nanoparticles and iron oxide) on the top of different supports (aluminium oxide and titanium oxide). The H_2 gas flowed over the surface of the supports to be dissociated; then, hydrogen atoms reduced the iron oxide to iron metal. The reason for using two types of support is to see the effect of the support and the distance on the reduction process. Figure 18 shows the model system they used to observe hydrogen spillover.[97]

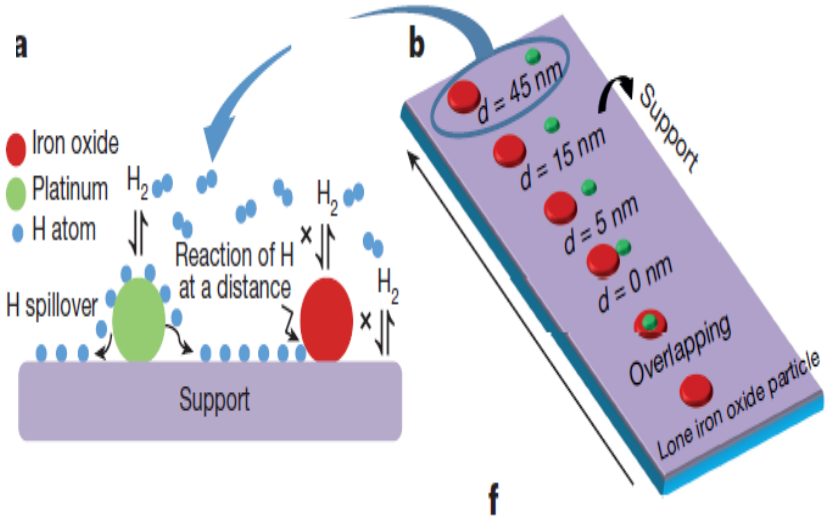

Figure 18: Hydrogen spillover model to analyze the effect of the distance on the catalytic process. Reproduced with permission from ref [97] (Copyright 2017 Springer Nature BV)

1.4 Introduction to Ni NPs

The growing need for more abundant and low-cost metals in industrial catalytic processes has been the target of many research groups. For example, the cost of using Pd is high, and the abundance is low compared to Ni, which can be used to catalyze many of the same reactions.[98] Therefore, the use of Ni NPs catalyst has been developed over the past few years for the hydrogenation of nitroarenes. For instance, Venegas-Yazigi *et al*.[99] reported that the reduction of $Ni(acac)_2$ to form uniform Ni NPs leads to the best performance in the selective hydrogenation of nitroarenes with high selectivity and activity to achieve a 99% yield of aniline.

The synthesis of Ni NPs via the decomposition of Ni complexes has been developed by many groups.[43,100-103] The small size and the narrow diameter distribution of the produced NPs are commonly expected for this route to synthesizing Ni NPs. For example, the synthesis of Ni NPs with 3.2 nm size in the presence of oleylamine and oleic acid showed the best catalytic activity for the hydrolysis of the amino borane complex, as reported by Mazumder.[43] Synthesizing Ni NPs during the reduction reaction between the reducing agent

and Ni precursor in the presence of a capping agent has been studied.[43] Long hydrocarbon chains with a terminal amine group (*e.g*. oleylamine) have been used as reducing agent or/and capping agent for synthesizing Ni NPs.[44]

1.4.1 The effect of using oleylamine and oleic acid with the synthesis of transition metal nanoparticles

The combination of oleylamine with long-chain carboxylic acid (*e.g*. oleic acid) has been shown to vary the result of the synthesis. For example, a combination of oleylamine with oleic acid formed the fcc phase, while oleylamine by itself formed the hcp phase.[71] Some studies were done to understand the rules of the combination of oleylamine with oleic acid on the formation of nanoparticles more generally. For instance, Yan Li *et al*. proposed that the formation of a carboxylate anion that will occur from the reaction between long-chain acid and long-chain amine is significant. The carboxylate anion is more electron-donating and so binds more strongly as a capping agent than the carboxylic acid in the absence of amine and leads to 4.2 nm NPs with small size distribution.[104] This work was further used by Wenbo Bu *et al*. to describe the formation of monodisperse tetragonal bipyramid $NaLa(MoO_4)_2$ nanocrystals by using oleylamine with oleic acid, the same combination of capping agents mentioned above in relation to nickel nanoparticle syntheses.[105]

1.5 Introduction to Cu NPs.

Copper is one of the metals that has been used in many cases for catalysis not just because it is highly natural abundance (69.15%; ^{107}) but also its low price.[106] Copper is one of the transition metals (3d), which gives it its chemical and physical properties. Transition metals are well known for having a wide range of oxidation states. This makes them promote and undergoes a variety of reactions. For example, Cu can have different oxidation states from 0 to III. The most common oxidation states are 0 for Cu metal and Cu^{I} and Cu^{II}.

Because around 90% of the production in industrial and pharmaceutical settings is achieved by using catalysis, the use of Cu as a catalyst has been studied worldwide. Cu NPs and Cu-based (CuO or Cu_2O) NPs have been used as a catalyst by different groups. For example, using transition metals and their complexes, such as Ru (ruthenium), Pd (palladium), Pt (platinum), Au (gold) and Ir (iridium) was catalytically important for organic transformations, but because of the higher cost, the use of Cu has been focused on with comparable efficiency in some cases to the above metals. [108] Ranu *et al*.[109] used Cu NPs to couple aryl iodides with thiophenols and alkanethiols under ligand-free conditions, as can be seen in Figure 19.

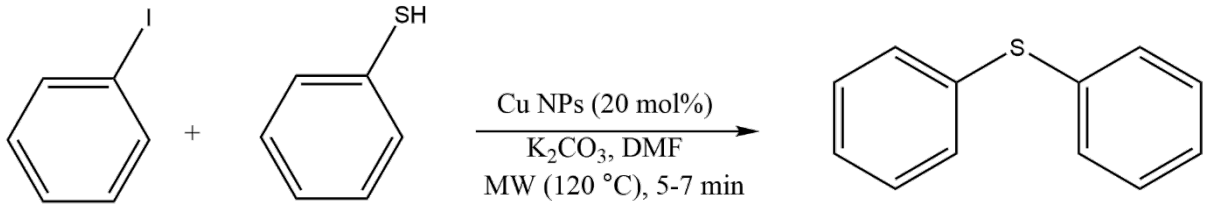

Figure 19: Cu NPs for catalyzing the S-arylation of thiols.

Also, Cu(I) oxide NPs have been used as a catalyst. For example, Kim *et al*.[110] used the copper(I) oxide or Cu_2O for the Ullmann cross-coupling reaction of aryl halides with phenols, as can be seen in Figure 20. This method has been known for performing Ullmann condensation (Ullmann biaryl ether synthesis) since 1906, as reported by Iram Goldberg.[111] In his paper, he claimed the formation of an arylamine could be achieved by reacting an aryl halide with an amide, but this reaction should be done in the presence of K_2CO_3/CuI; at that time, this reaction was known as the Goldberg reaction, or Goldberg modified Ullmann condensation.

Cu_2O NPs are thermal and air-stable (because it has oxygen, which makes them stable, which is the opposite of Cu (0) which is not stable in the air). Kim synthesized Cu_2O nanocubes by using $Cu(acac)_2$ as a metal precursor, PVP as a surfactant and 1,5-pentanediol as a reducing agent and solvent[110]. This method of synthesis is known as one-pot polyol synthesis.

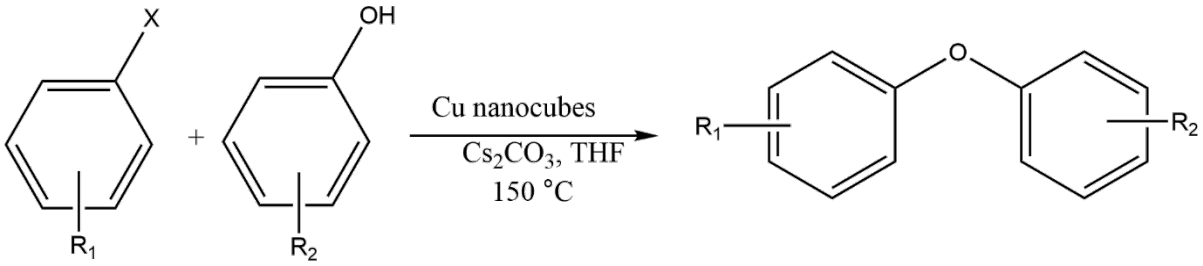

Figure 20: Cu NPs for catalyzing the aryl halides. [110]

Using Cu NPs to decompose dyestuffs has received enormous attention in the last decades. Dyeing industries have been known as a major source of contaminants for water. The United Nations World Water Development Report: Water for People Water for Life estimates 2 million tons per day of waste from dyeing industries are discharged into water.[112] [113] They are harmful, not just because these wastes produce harmful by-products after they react with the water (ether oxidation, hydrolysis or other chemical reactions)[114], but also they stop one of the essential mechanisms for producing oxygen for the biodegradation of micro-organisms by reducing the penetration of light to the water needed for oxygen generation by photosynthesis.[115] Therefore, Cu NPs (because of being inexpensive and copper having a high natural abundance) have been used in this context. Furthermore, Cu NPs can be synthesized by using biosynthetic approaches, which makes the Cu NPs more environmentally friendly (it does not involve any organic solvents, surfactants or reducing agents). Sinha *et al.* reported a method to synthesize Cu NPs by using the egg-shells extract of anas platyrhynchos (the size of these Cu NPs is 5-18 nm with a very broad size distribution).[112] The resulting Cu NPs were used (photocatalysts) to remediate three different types of dyes, which are Rose Bengal, Methylene Blue and Methyl Violet 6**.** The results show a high efficiency for removing dyes from effluents.[112]

The use of Cu NPs has many applications, but because of its instability under atmospheric conditions (forms Cu_2O or CuO), developing a method that can synthesize Cu NPs that are uniform in shape and small in size (high surface-to-volume ratio) is essential and remains challenging. The chemical reduction was one of the methods that can synthesize Cu NPs. This method was reported by Mott *et al.*[116] to produce size-controlled

and shape-controlled capped Cu NPs. The synthesis was done in an organic solvent with an amine and acid capping agent. They reported the effect of changing the reaction temperature (150-190 °C) on the size of the Cu NPs ranging from 5-25 nm. Similarly, Chapter 5 will demonstrate the synthesis of size-controllable capped Cu NPs, which is done in an inert atmosphere (*e.g*. N_2 gas) to give better control of the size (4 nm) and the shape of the Cu NPs. Also, the effect of using solvents such as pyridine and oleic acid for a period of time before the reduction will be discussed because of the ability to produce well-controlled monodisperse 1.8 nm Cu NPs. This method requires the choice of metal precursor (*e.g.* $Cu(acac)_2$), reducing agent (*e.g*. morpholine boron) and capping agent (*e.g*. octadecylamine) but mainly by manipulating reaction temperature (150 – 210 °C).

1.6 Aims and objectives

Controlling the chemical reaction parameters leads to having ways to synthesize NPs controllably. This thesis will aim to carefully investigate these parameters in the synthesis of Cu NPs and Ni NPs, and the findings have allowed the preparation of nanoparticles having a smaller size and narrower size distribution.

The Ni NP synthesis gave monodisperse 1.3 nm average size and narrow size distribution, and Chapter 4 will consider the *in situ* changes that occur to the metal precursor, $Ni(acac)_2$, during the reaction and before the reduction.

The new method for synthesis of Cu NPs presented gives a 1.8 nm average size with narrow size distribution after testing and trying different temperatures and reagents. Chapter 5 will discuss these details and highlights the effect of using pyridine as a solvent on the synthesis of Cu NPs.

The role of the reducing agent is the main factor that will be discussed in more detail in Chapter 6– explicitly understanding how the amino boron complexes (increasingly used for nanoparticle synthesis) are working will have a huge influence on how we can synthesise the NPs.

The motivations for coupling nanoparticles to control catalytic reactions were discussed in the introduction above to form a different class of bimetallic structures in 3D. Chapter 7 will show the initial evidence of work to coupling Pd with Ni NPs with an organic linker to form NP pairs, as evidenced by TEM images and the attempts made to improve the quantity of the NP pairs by changing the coupling reaction with the organic linker.

1. Nejat Veziroglu, T.; Sherif, S. A.; Barbir, F., Hydrogen Energy Solutions. In *Environmental Solutions*, Elsevier: 2005; pp 143-180.
2. Srinivasan, S.; Sherif, S.; Barbir, F.; Veziroglu, T.; Mahishi, M.; Pratt, R., Hydrogen Energy Technologies. In *The CRC Press Series in Mechanical and Aerospace Engineering*, CRC Press: 2015; pp 1669-1701.
3. Hinnemann, B.; Nørskov, J. K., Catalysis by Enzymes: The Biological Ammonia Synthesis. *Topics in Catalysis* **2006,** *37* (1), 55-70
4. Prins, R.; Wang, A.; Li, X., *Introduction to Heterogeneous Catalysis*. IMPERIAL COLLEGE PRESS: 2016
5. Heck, R. M.; Farrauto, R. J., Automobile exhaust catalysts. *Applied Catalysis A: General* **2001,** *221* (1-2), 443-457.
6. Singh, S. B.; Tandon, P. K., Catalysis: a brief review on nano-catalyst. *J. Energy Chem. Eng* **2014,** *2* (3), 106-115.
7. Robertson, A. J. B., The early history of catalysis. *Platinum Metals Review* **1975,** *19* (2), 64-69.
8. Roduner, E., Understanding catalysis. *Chem. Soc. Rev.* **2014,** *43* (24), 8226-8239.
9. Deutschmann, O.; Knözinger, H.; Kochloefl, K.; Turek, T., Heterogeneous Catalysis and Solid Catalysts, 2. Development and Types of Solid Catalysts. In *Ullmann's Encyclopedia of Industrial Chemistry*, Wiley-VCH Verlag GmbH & Co. KGaA: 2011.
10. Twigg, G., The mechanism of the catalytic hydrogenation of ethylene. *Discuss. Faraday Soc.* **1950,** *8*, 152-159.
11. Neurock, M.; Van Santen, R. A., A first principles analysis of C− H bond formation in ethylene hydrogenation. *J. Phys. Chem. B* **2000,** *104* (47), 11127-11145.
12. Winderlich, R., Jons Jakob Berzelius. *Journal of Chemical Education* **1948,** *25* (9), 500
13. Ertl, G., Wilhelm Ostwald: Founder of physical chemistry and Nobel laureate 1909. *Angew. Chem., Int. Ed. Engl.* **2009,** *48* (36), 6600-6606.

14. Barbato, M.; Bruno, C., Heterogeneous Catalysis: Theory, Models and Applications. 1996; pp 139-160.

15. Bhaduri, S.; Mukesh, D., *Homogeneous catalysis: mechanisms and industrial applications*. John Wiley & Sons: 2014.

16. van Santen, R. A.; Averill, B.; Moulijn, J. A.; van Leeuwen, P., *Catalysis: an integrated approach*. Elsevier: 2000; Vol. 123.

17. Roco, M. C., International strategy for nanotechnology research. *J. Nanoparticle Res.* **2001,** *3* (5-6), 353-360.

18. Giri, P. K.; Bhattacharyya, S.; Singh, D. K.; Kesavamoorthy, R.; Panigrahi, B. K.; Nair, K. G. M., Correlation between microstructure and optical properties of ZnO nanoparticles synthesized by ball milling. *J. Appl. Phys.* **2007,** *102* (9), 093515.

19. Naeimi, H.; Foroughi, H., Facile three-component preparation of benzodiazepine derivatives catalyzed by zinc sulfide nanoparticles via grinding method. *Res. Chem. Intermed.* **2016,** *42* (5), 3999-4020.

20. Tsuzuki, T.; McCormick, P. G., Mechanochemical synthesis of nanoparticles. *J. Mater. Sci.* **2004,** *39* (16-17), 5143-5146.

21. Tański, T.; Matysiak, W.; Krzemiński, Ł.; Jarka, P.; Gołombek, K., Optical properties of thin fibrous PVP/SiO2 composite mats prepared via the sol-gel and electrospinning methods. *Appl. Surf. Sci.* **2017,** *424*, 184-189.

22. Trindade, T.; O'Brien, P., Synthesis of CdS and CdSe nanoparticles by thermolysis of diethyldithio-or diethyldiseleno-carbamates of cadmium. *J. Mater. Chem.* **1996,** *6* (3), 343-347.

23. Saita, S.; Maenosono, S., Chemical ordering of FePt nanoparticles by pulsed laser annealing. *J. Condens. Matter Phys.* **2004,** *16* (36), 6385.

24. Shaalan, N. M.; Yamazaki, T.; Kikuta, T., Influence of morphology and structure geometry on NO2 gas-sensing characteristics of SnO2 nanostructures synthesized via a thermal evaporation method. *Sens. Actuators B Chem.: Chemical* **2011,** *153* (1), 11-16.

25. Astete, C. E.; Kumar, C. S. S. R.; Sabliov, C. M., Size control of poly (d, l-lactide-co-glycolide) and poly (d, l-lactide-co-glycolide)-magnetite nanoparticles synthesized by emulsion evaporation technique. *Colloids Surf, A Physicochem Eng Asp* **2007,** *299* (1-3), 209-216.

26. Luo, Z.; Lu, Y.; Singer, D. W.; Berck, M. E.; Somers, L. A.; Goldsmith, B. R.; Johnson, A. T. C., Effect of substrate roughness and feedstock concentration on growth of wafer-scale graphene at atmospheric pressure. *Chem. Mater.* **2011,** *23* (6), 1441-1447. Zhang, Z.-P.; Zhu, W.; Yan, C.-H.; Zhang, Y.-W., Selective synthesis of rhodium-based nanoframe catalysts by chemical etching of 3d metals. *ChemComm* **2015,** *51* (19), 3997-4000.

27. Momeni, M. M.; Ghayeb, Y., Fabrication, characterization and photocatalytic properties of Au/TiO2-WO3 nanotubular composite synthesized by photo-assisted deposition and electrochemical anodizing methods. *J Mol Catal A Chem* **2016,** *417*, 107-115.

28. Gondal, M. A.; Drmosh, Q. A.; Yamani, Z. H.; Saleh, T. A., Synthesis of ZnO2 nanoparticles by laser ablation in liquid and their annealing transformation into ZnO nanoparticles. *Appl. Surf. Sci.* **2009,** *256* (1), 298-304.

29. Hicks, E. M.; Zou, S.; Schatz, G. C.; Spears, K. G.; Van Duyne, R. P.; Gunnarsson, L.; Rindzevicius, T.; Kasemo, B.; Käll, M., Controlling plasmon line shapes through diffractive coupling in linear arrays of cylindrical nanoparticles fabricated by electron beam lithography. *Nano lett.* **2005,** *5* (6), 1065-1070.

30. Fang, R. H.; Aryal, S.; Hu, C.-M. J.; Zhang, L., Quick synthesis of lipid− polymer hybrid nanoparticles with low polydispersity using a single-step sonication method. *Langmuir* **2010,** *26* (22), 16958-16962.

31. Ashkarran, A. A., A novel method for synthesis of colloidal silver nanoparticles by arc discharge in liquid. *Curr Appl Phys* **2010,** *10* (6), 1442-1447.

32. Alshammari, A.; Kalevaru, D. V. N.; Martin, A., *Metal Nanoparticles as Emerging Green Catalysts*. 2016.

33. Knez, M.; Nielsch, K.; Niinistö, L., Synthesis and surface engineering of complex nanostructures by atomic layer deposition. *Adv. Mater.* **2007,** *19* (21), 3425-3438. Colomer, 2000, Large-scale synthesis of single-wall carbon nanotubes by catalytic chemical vapour deposition (CCVD) method.

34. Suteewong, T.; Sai, H.; Hovden, R.; Muller, D.; Bradbury, M. S.; Gruner, S. M.; Wiesner, U., Multicompartment mesoporous silica nanoparticles with branched shapes: An epitaxial growth mechanism. *Science* **2013,** *340* (6130), 337-341.

35. Peng, T.; Yang, H.; Pu, X.; Hu, B.; Jiang, Z.; Yan, C., Combustion synthesis and photoluminescence of SrAl2O4: Eu, Dy phosphor nanoparticles. *Mater. Lett.* **2004,** *58* (3-4), 352-356.

36. Yue-Jian, C.; Juan, T.; Fei, X.; Jia-Bi, Z.; Ning, G.; Yi-Hua, Z.; Ye, D.; Liang, G., Synthesis, self-assembly, and characterization of PEG-coated iron oxide nanoparticles as potential MRI contrast agent. *Drug Dev. Ind. Pharm* **2010,** *36* (10), 1235-1244.

37. Lee, S.; Cho, I.-S.; Lee, J. H.; Kim, D. H.; Kim, D. W.; Kim, J. Y.; Shin, H.; Lee, J.-K.; Jung, H. S.; Park, N.-G., Two-step sol− gel method-based TiO2 nanoparticles with uniform morphology and size for efficient photo-energy conversion devices. *Chem. Mater.* **2010,** *22* (6), 1958-1965. Sugimoto, T.; Zhou, X.; Muramatsu, A., Synthesis of uniform anatase TiO2 nanoparticles by gel–sol method: 3. Formation process and size control. *J. Colloid Interface Sci. J COLLOID INTERF SCI* **2003,** *259* (1), 43-52.

38. Mohanty, U. S., Electrodeposition: a versatile and inexpensive tool for the synthesis of nanoparticles, nanorods, nanowires, and nanoclusters of metals. *J. Appl. Electrochem.* **2011,** *41* (3), 257-270.

39. Daniel, M.-C.; Astruc, D., Gold nanoparticles: assembly, supramolecular chemistry, quantum-size-related properties, and applications toward biology, catalysis, and nanotechnology. *Chem. Rev.* **2004,** *104* (1), 293-346.

40. Salavati-Niasari, M.; Davar, F., Synthesis of copper and copper (I) oxide nanoparticles by thermal decomposition of a new precursor. *Mater. Lett.***2009,** *63* (3-4), 441-443.

41. Kang, J.; Li, O. L.; Saito, N., A simple synthesis method for nano-metal catalyst supported on mesoporous carbon: the solution plasma process. *Nanoscale* **2013,** *5* (15), 6874-6882.

42. Tran, Q. H.; Le, A.-T., Silver nanoparticles: synthesis, properties, toxicology, applications and perspectives. ANSN **2013,** *4* (3), 033001.

43. Metin, Ö.; Mazumder, V.; Özkar, S.; Sun, S., Monodisperse Nickel Nanoparticles and Their Catalysis in Hydrolytic Dehydrogenation of Ammonia Borane. *Journal of the American Chemical Society* **2010,** *132* (5), 1468-1469.

44. Zhang, H. T.; Wu, G.; Chen, X. H.; Qiu, X. G., Synthesis and magnetic properties of nickel nanocrystals. *Mater. Res. Bull.* **2006,** *41* (3), 495-501.

45. Zhu, S.; Wang, L.; Zu, X.; Xiang, X., Optical and magnetic properties of Ni nanoparticles in rutile formed by Ni ion implantation. *Appl. Phys. Lett.* **2006,** *88* (4), 043107.

46. Scaffardi, L.; Tocho, J., Size effects on the optical properties of metal nanoparticles: Applications to sizing by analysis of extinction spectra. 2007; pp 249-276.

47. Wall, M. A.; Cossairt, B. M.; Liu, J. T., Reaction-Driven Nucleation Theory. *Appl. Phys. Lett.J. Phys. Chem. A C* **2018,** *122* (17), 9671-9679.

48. Sosso, G. C.; Chen, J.; Cox, S. J.; Fitzner, M.; Pedevilla, P.; Zen, A.; Michaelides, A., Crystal Nucleation in Liquids: Open Questions and Future Challenges in Molecular Dynamics Simulations. *Chem. Rev.* **2016,** *116* (12), 7078-7116.

49. Polte, J., Fundamental growth principles of colloidal metal nanoparticles–a new perspective. *CrystEngComm* **2015,** *17* (36), 6809-6830.

50. Mullin, J. W., *Crystallization*. Elsevier: 2001.

51. Strey, R.; Wagner, P.; Viisanen, Y., The problem of measuring homogeneous nucleation rates and the molecular contents of nuclei: progress in the form of nucleation pulse measurements. *J. Phys. Chem. A* **1994,** *98* (32), 7748-7758.

52. LaMer, V. K.; Dinegar, R. H., Theory, production and mechanism of formation of monodispersed hydrosols. *J. Am. Chem. Soc.* **1950,** *72* (11), 4847-4854.

53. Baronov, A.; Bufkin, K.; Shaw, D. W.; Johnson, B. L.; Patrick, D. L., A simple model of burst nucleation. *Phys. Chem. Chem. Phys.* **2015,** *17* (32), 20846-20852.

54. Tamang, S.; Lee, S.; Choi, H.; Jeong, S., Tuning size and size distribution of colloidal InAs nanocrystals via continuous supply of prenucleation clusters on nanocrystal seeds. *Chem. Mater.* **2016,** *28* (22), 8119-8122.

55. Reiss, H., The growth of uniform colloidal dispersions. *Chem. Phys.* **1951,** *19* (4), 482-487.

56. Sugimoto, T., Preparation of monodispersed colloidal particles. *Adv. Colloid Interface Sci.* **1987,** *28*, 65-108.

57. Clark, M. D.; Kumar, S. K.; Owen, J. S.; Chan, E. M., Focusing nanocrystal size distributions via production control. *Nano lett.* **2011,** *11* (5), 1976-1980.

58. Ostwald, W., Über die vermeintliche Isomerie des roten und gelben Quecksilberoxyds und die Oberflächenspannung fester Körper. Z. Phys. Chem **1900,** *34* (1), 495-503.

59. Voorhees, P. W., The theory of Ostwald ripening. *J. Stat. Phys.* **1985,** *38* (1-2), 231-252.

60. Weiss, J.; McClements, D., Influence of Ostwald ripening on rheology of oil-in-water emulsions containing electrostatically stabilized droplets. *Langmuir* **2000,** *16* (5), 2145-2150.

61. Niethammer, B., Derivation of the LSW-theory for Ostwald ripening by homogenization methods. *Arch Ration Mech Anal* **1999,** *147* (2), 119-178.

62. Thanh, N. T. K.; Maclean, N.; Mahiddine, S., Mechanisms of Nucleation and Growth of Nanoparticles in Solution. *Chem. Rev.* **2014,** *114* (15), 7610-7630.

63. Lee, D.-K.; Park, S.-I.; Lee, J. K.; Hwang, N.-M., A theoretical model for digestive ripening. *Acta Materialia* **2007,** *55* (15), 5281-5288.

64. Lin, X.; Sorensen, C.; Klabunde, K., Digestive ripening, nanophase segregation and superlattice formation in gold nanocrystal colloids. *J. Nanoparticle Res.* **2000,** *2* (2), 157-164.

65. Bayda, S.; Adeel, M.; Tuccinardi, T.; Cordani, M.; Rizzolio, F., The History of Nanoscience and Nanotechnology: From Chemical–Physical Applications to Nanomedicine. *Molecules* **2020,** *25* (1), 112.

66. Yang, T.-H.; Gilroy, K. D.; Xia, Y., Reduction rate as a quantitative knob for achieving deterministic synthesis of colloidal metal nanocrystals. *Chem. sci.***2017,** *8* (10), 6730-6749.

67. Furuzono, T.; Walsh, D.; Sato, K.; Sonoda, K.; Tanaka, J., Effect of reaction temperature on the morphology and size of hydroxyapatite nanoparticles in an emulsion system. *J. Mater. Sci. Lett.* **2001,** *20* (2), 111-114.

68. Madras, G.; McCoy, B. J., Temperature effects on the transition from nucleation and growth to Ostwald ripening. *Chem. Eng. Sci.* **2004,** *59* (13), 2753-2765.

69. Xue, X.; Penn, R. L.; Leite, E.; Lin, Z., Crystal Growth by Oriented Attachment: Kinetic Models and Control Factors. *CrystEngComm* **2014,** *16*, 1419.

70. Madras, G.; McCoy, B., Temperature effects during Ostwald ripening. *Chem. Phys.* **2003,** *119*.

71. Chen, Y.; Peng, D.-L.; Lin, D.; Luo, X., Preparation and magnetic properties of nickel nanoparticles via the thermal decomposition of nickel organometallic precursor in alkylamines. *Nanotechnology* **2007,** *18* (50), 505703. Mozaffari, S.; Li, W.; Thompson, C.; Ivanov, S.; Seifert, S.; Lee, B.; Kovarik, L.; Karim, A. M., Colloidal nanoparticle size control: experimental and kinetic modeling investigation of the ligand–metal binding role in controlling the nucleation and growth kinetics. *Nanoscale* **2017,** *9* (36), 13772-13785.

72. Alqadi, M. K.; Noqtah, O. A. A.; Alzoubi, F. Y.; Alzouby, J.; Aljarrah, K., pH effect on the aggregation of silver nanoparticles synthesized by chemical reduction. *Mater. Sci.- Poland* **2014,** *32* (1), 107-111.

73. Huang, L.; Luo, F.; Chen, Z.; Megharaj, M.; Naidu, R., Green synthesized conditions impacting on the reactivity of Fe NPs for the degradation of malachite green. *Spectrochimica Acta Part A: Spectrochim. Acta A Mol. Biomol. Spectrosc.* **2015,** *137*, 154-159.

74. Cozzoli, P. D.; Snoeck, E.; Garcia, M. A.; Giannini, C.; Guagliardi, A.; Cervellino, A.; Gozzo, F.; Hernando, A.; Achterhold, K.; Ciobanu, N., Colloidal synthesis and characterization of tetrapod-shaped magnetic nanocrystals. *Nano lett.* **2006,** *6* (9), 1966-1972.

75. Yang, T.-H.; Peng, H.-C.; Zhou, S.; Lee, C.-T.; Bao, S.; Lee, Y.-H.; Wu, J.-M.; Xia, Y., Toward a quantitative understanding of the reduction pathways of a salt precursor in the synthesis of metal nanocrystals. *Nano lett.* **2017,** *17* (1), 334-340.

76. Wang, Y.; Peng, H.-C.; Liu, J.; Huang, C. Z.; Xia, Y., Use of Reduction Rate as a Quantitative Knob for Controlling the Twin Structure and Shape of Palladium Nanocrystals. *Nano Lett.* **2015,** *15* (2), 1445-1450.

77. Shibuta, Y.; Oguchi, K.; Takaki, T.; Ohno, M., Homogeneous nucleation and microstructure evolution in million-atom molecular dynamics simulation. *Sci. Rep.* **2015,** *5*, 13534.

78. Zhou, M.; Wang, H.; Vara, M.; Hood, Z. D.; Luo, M.; Yang, T.-H.; Bao, S.; Chi, M.; Xiao, P.; Zhang, Y., Quantitative analysis of the reduction kinetics responsible for the one-pot synthesis of Pd–Pt bimetallic nanocrystals with different structures. *J. Am. Chem. Soc.* **2016,** *138* (37), 12263-12270.

79. Ajitha, B.; Reddy, Y. A. K.; Reddy, P. S.; Jeon, H.-J.; Ahn, C. W., Role of capping agents in controlling silver nanoparticles size, antibacterial activity and potential application as optical hydrogen peroxide sensor. *RSC advances* **2016,** *6* (42), 36171-36179.

80. Ojha, N. K.; Zyryanov, G. V.; Majee, A.; Charushin, V. N.; Chupakhin, O. N.; Santra, S., Copper nanoparticles as inexpensive and efficient catalyst: A valuable contribution in organic synthesis. *Coord. Chem. Rev.* **2017,** *353*, 1-57.

81. Liu, X.; Wang, D.; Li, Y., Synthesis and catalytic properties of bimetallic nanomaterials with various architectures. *Nano Today* **2012,** *7* (5), 448-466.

82. Stamenkovic, V. R.; Fowler, B.; Mun, B. S.; Wang, G.; Ross, P. N.; Lucas, C. A.; Marković, N. M., Improved oxygen reduction activity on Pt3Ni (111) via increased surface site availability. *science* **2007,** *315* (5811), 493-497.

83. Tao, F.; Grass, M. E.; Zhang, Y.; Butcher, D. R.; Renzas, J. R.; Liu, Z.; Chung, J. Y.; Mun, B. S.; Salmeron, M.; Somorjai, G. A., Reaction-driven restructuring of Rh-Pd and Pt-Pd core-shell nanoparticles. *Science* **2008,** *322* (5903), 932-934.

84. Lim, B.; Jiang, M.; Camargo, P. H. C.; Cho, E. C.; Tao, J.; Lu, X.; Zhu, Y.; Xia, Y., Pd-Pt bimetallic nanodendrites with high activity for oxygen reduction. *science* **2009,** *324* (5932), 1302-1305.

85. Chen, M.; Kumar, D.; Yi, C.-W.; Goodman, D. W., The promotional effect of gold in catalysis by palladium-gold. *Science* **2005,** *310* (5746), 291-293.

86. Kesavan, L.; Tiruvalam, R.; Ab Rahim, M. H.; bin Saiman, M. I.; Enache, D. I.; Jenkins, R. L.; Dimitratos, N.; Lopez-Sanchez, J. A.; Taylor, S. H.; Knight, D. W., Solvent-free oxidation of primary carbon-hydrogen bonds in toluene using Au-Pd alloy nanoparticles. *Science* **2011,** *331* (6014), 195-199.

87. Kyriakou, G.; Boucher, M. B.; Jewell, A. D.; Lewis, E. A.; Lawton, T. J.; Baber, A. E.; Tierney, H. L.; Flytzani-Stephanopoulos, M.; Sykes, E. C. H., Isolated metal atom

geometries as a strategy for selective heterogeneous hydrogenations. *Science* **2012,** *335* (6073), 1209-1212.

88. Rodriguez, J. A.; Goodman, D. W., The nature of the metal-metal bond in bimetallic surfaces. *Science* **1992,** *257* (5072), 897-903.

89. Tanori, J.; Duxin, N.; Petit, C.; Lisiecki, I.; Veillet, P.; Pileni, M. P., Synthesis of nanosize metallic and alloyed particles in ordered phases. *Colloid and Polymer Science* **1995,** *273* (9), 886-892.

90. Srinoi, P.; Chen, Y.-T.; Vittur, V.; Marquez, M.; Lee, T., Bimetallic nanoparticles: Enhanced magnetic and optical properties for emerging biological applications. *Applied Sciences* **2018,** *8* (7), 1106.

91. bin Saiman, M. I.; Brett, G. L.; Tiruvalam, R.; Forde, M. M.; Sharples, K.; Thetford, A.; Jenkins, R. L.; Dimitratos, N.; Lopez-Sanchez, J. A.; Murphy, D. M., Involvement of surface-bound radicals in the oxidation of toluene using supported Au-Pd nanoparticles. *Angew. Chem.* **2012,** *124* (24), 6083-6087.

92. Kim, D.; Resasco, J.; Yu, Y.; Asiri, A. M.; Yang, P., Synergistic geometric and electronic effects for electrochemical reduction of carbon dioxide using gold–copper bimetallic nanoparticles. *Nat. commun.* **2014,** *5*, 4948.

93. Zaera, F., Chemistry: The long and winding road to catalysis. *Nature* **2017,** *541* (7635), 37.

94. Zou, H.; Dai, J.; Suo, J.; Ettelaie, R.; Li, Y.; Xue, N.; Wang, R.; Yang, H., Dual metal nanoparticles within multicompartmentalized mesoporous organosilicas for efficient sequential hydrogenation. *Nat. Commun.* **2021,** *12* (1), 4968.

95. Choi, M.; Yook, S.; Kim, H., Hydrogen Spillover in Encapsulated Metal Catalysts: New Opportunities for Designing Advanced Hydroprocessing Catalysts. *ChemCatChem* **2015,** *7* (7), 1048-1057.

96. Luo, Z.; Zheng, Z.; Li, L.; Cui, Y.-T.; Zhao, C., Bimetallic Ru–Ni Catalyzed Aqueous-Phase Guaiacol Hydrogenolysis at Low H2 Pressures. *ACS Catalysis* **2017,** *7* (12), 8304-8313.

97. Karim, W.; Spreafico, C.; Kleibert, A.; Gobrecht, J.; VandeVondele, J.; Ekinci, Y.; van Bokhoven, J. A., Catalyst support effects on hydrogen spillover. *Nature* **2017,** *541* (7635), 68.

98. Mala, B. Utilising a novel Ni/Zn catalytic system in small molecule synthesis. Lancaster University, 2022.

99. Negrete-Vergara, C.; Álvarez-Alcalde, D.; Moya, S. A.; Paredes-García, V.; Fuentes, S.; Venegas-Yazigi, D., Selective Hydrogenation of Aromatic Nitro Compounds Using Unsupported Nickel Catalysts. *ChemistrySelect* **2022,** *7* (20), e202200220.

100. Carenco, S.; Labouille, S.; Bouchonnet, S.; Boissière, C.; Le Goff, X.-F.; Sanchez, C.; Mézailles, N., Revisiting the Molecular Roots of a Ubiquitously Successful Synthesis: Nickel(0) Nanoparticles by Reduction of [Ni(acetylacetonate)2]. *Eur. J. Chem.* **2012,** *18* (44), 14165-14173.

101. Carenco, S.; Boissiere, C.; Nicole, L.; Sanchez, C.; Le Floch, P.; Mézailles, N., Controlled design of size-tunable monodisperse nickel nanoparticles. *Chem. Mater.* **2010,** *22* (4), 1340-1349.

102. Choi, S.-I.; Xie, S.; Shao, M.; Odell, J. H.; Lu, N.; Peng, H.-C.; Protsailo, L.; Guerrero, S.; Park, J.; Xia, X.; Wang, J.; Kim, M. J.; Xia, Y., Synthesis and Characterization of 9 nm Pt–Ni Octahedra with a Record High Activity of 3.3 A/mgPt for the Oxygen Reduction Reaction. *Nano Lette.* **2013,** *13* (7), 3420-3425.

103. Liu, Q.; Diaz, A.; Prosvirin, A.; Luo, Z.; Batteas, J. D., Shape-controlled synthesis of nanopyramids and nanoprisms of nickel sulfide (Ni3S4). *Nanoscale* **2014,** *6* (15), 8935-42.

104. Li, Y.; Liu, J.; Wang, Y.; Wang, Z. L., Preparation of Monodispersed Fe−Mo Nanoparticles as the Catalyst for CVD Synthesis of Carbon Nanotubes. *Chemi. Mater.***2001,** *13* (3), 1008-1014.

105. Bu, W.; Chen, Z.; Chen, F.; Shi, J., Oleic acid/oleylamine cooperative-controlled crystallization mechanism for monodisperse tetragonal bipyramid NaLa (MoO4) 2 nanocrystals. *J. Phys. Chem. A C* **2009,** *113* (28), 12176-12185.

106. Gawande, M. B.; Goswami, A.; Felpin, F.-X.; Asefa, T.; Huang, X.; Silva, R.; Zou, X.; Zboril, R.; Varma, R. S., Cu and Cu-based nanoparticles: synthesis and applications in catalysis. *Chem. Rev.* **2016,** *116* (6), 3722-3811.

107. Li, J.; Tang, S. H.; Zhu, X. K.; Li, Z. H.; Li, S. Z.; Yan, B.; Wang, Y.; Sun, J.; Shi, Y.; Dong, A.; Belshaw, N. S.; Zhang, X.; Liu, S. A.; Liu, J. H.; Wang, D.; Jiang, S. Y.; Hou, K.; Cohen, A. S., Basaltic and Solution Reference Materials for Iron, Copper and Zinc Isotope Measurements. *Geostand Geoanal Res* **2019,** *43* (1), 163-175.

108. Babu, S. G.; Karvembu, R., Copper based nanoparticles-catalyzed organic transformations. *Catal. Surv.* **2013,** *17* (3), 156-176.

109. Ranu, B. C.; Saha, A.; Jana, R., Microwave-assisted simple and efficient ligand free copper nanoparticle catalyzed aryl-sulfur bond formation. *Adv. Synth. Catal.* **2007,** *349* (17-18), 2690-2696.

110. Kim, J. Y.; Park, J. C.; Kim, A.; Kim, A. Y.; Lee, H. J.; Song, H.; Park, K. H., Cu2O Nanocube-Catalyzed Cross-Coupling of Aryl Halides with Phenols via Ullmann Coupling. *Eur. J. Inorg. Chem.* **2009,** *2009* (28), 4219-4223.

111. Goldberg, I., Ueber phenylirungen bei gegenwart von kupfer als katalysator. *Ber. Dtsch. Chem. Ges.* **1906,** *39* (2), 1691-1692.

112. Sinha, T.; Ahmaruzzaman, M., Photocatalytic decomposition behavior and reaction pathways of organic compounds using Cu nanoparticles synthesized via a green route. *Photochem. Photobiol. Sci.* **2016,** *15* (10), 1272-1281.

113. Nations, U., The United Nations World Water Development Report: Water for People Water for Life. UNESCO Publishing & Berghahn books Paris: 2003.

114. Safavi, A.; Momeni, S., Highly efficient degradation of azo dyes by palladium/hydroxyapatite/Fe3O4 nanocatalyst. *J. Hazard. Mater.* **2012,** *201*, 125-131.

115. Prado, A. G.; Bolzon, L. B.; Pedroso, C. P.; Moura, A. O.; Costa, L. L., Nb2O5 as efficient and recyclable photocatalyst for indigo carmine degradation. *Appl. Catal. B* **2008,** *82* (3-4), 219-224.

116. Mott, D.; Galkowski, J.; Wang, L.; Luo, J.; Zhong, C.-J., Synthesis of size-controlled and shaped copper nanoparticles. *Langmuir* **2007,** *23* (10), 5740-5745.

Chapter 2 Methodology

2.1 X-Ray Diffraction (XRD)

XRD is a technique that has been used since 1913 after W.L Bragg formulated Bragg's Law (Equation 1, Figure 21) and his father, W.H. Bragg, designed the first XRD equipment (Nobel Prize 1915). XRD is capable of determining the structure of crystalline materials. XRD uses radiation diffracting off the sample and goes to the detector, which picks up the radiation at a certain angle and measures the intensity. Different atomic planes (hkl = Miller indices of the plane, black lines, Figure 21) within a crystal can reflect the X-rays (blue lines, Figure 21), which have a defined wavelength (λ) due to the X-ray source. The number of planes indicates the order of reflection (N) and the distance between hkl planes, indicated by *d*, as seen in Figure 21**.** The X-rays scattered from different planes can constructively interfere or destructively interfere depending on how the wavelength compares to the spacing in the direction of the reflection, giving different intensities at different values of theta. [1]

$$n\lambda = 2d \sin\theta \quad (1)$$

Where:

n= order of reflection

λ= wavelength of the X-ray source

d= inter-planar spacing

θ= Bragg's angle

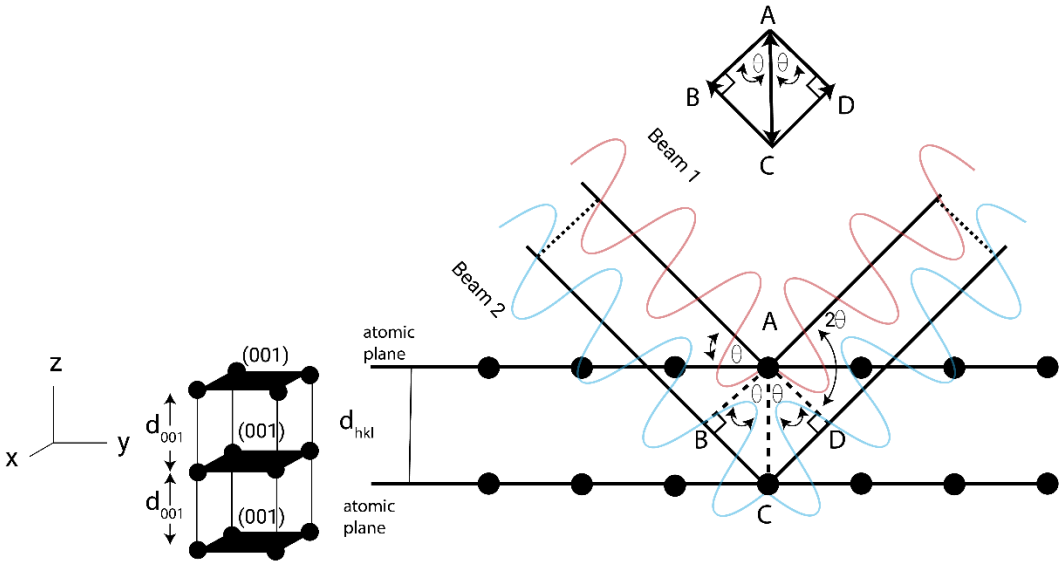

Figure 21: Bragg's Law description of X-ray (wavelength λ) that reflects by atoms in lattice plane which incidents at an angle. The atomic plane is a repeating of the 001) simple cubic unite cell demonstrated on the left side.

The principle used in this technique is that the X-ray can be scattered by electrons in molecules and atoms when they are organized to form planes of the same dimension as their wavelength.

XRD instruments contain three key parts, as seen in Figure 22. The first part is the X-ray source, typically an X-ray tube. In an evacuated tube, an applied current heats up the electron gun (*e.g.* tungsten filament) to generate electrons. These electrons are accelerated in a high voltage field and hit the X-ray target (*e.g.* a copper tube), where the source generates monochromatic X-rays (*e.g.* K α_1 and K α_2 at a wavelength of 1.5406, and 1.5444 Å for copper, respectively). The second part is the sample holder. When the X-rays exit the tube, they hit the sample that is located on the sample holder (*e.g.* Si low background sample holder); then, they are diffracted into the third part, which is the detector. In the detector, the beam passes through a slit (determines the angular width of the beam) and a nickel filter (removes the k-β energy). For our purposes, the resulting reflections can be compared (position and intensity) against a crystal database (*e.g.* ICSD database) to identify the crystalline phases present in the sample. [1]

The incident beam hits the sample at an angle, θ, which is half of the detector angle, 2θ, as seen in Figure 22. At a precise direction relative to a large crystallite, the incident beam causes coherent scattering (*i.e.* natural diffraction peaks) and incoherent scattering (this cancels out with another incoherent scattering). On the other hand, small crystallites do not have sufficient lattice planes to cancel all incoherent scattering, which results in a broadening of the reflections around the Bragg angle. This phenomenon is called particle size broadening. In this case, the crystallite size (and therefore particle size if single crystals) can be estimated by using the Scherrer equation.[1]

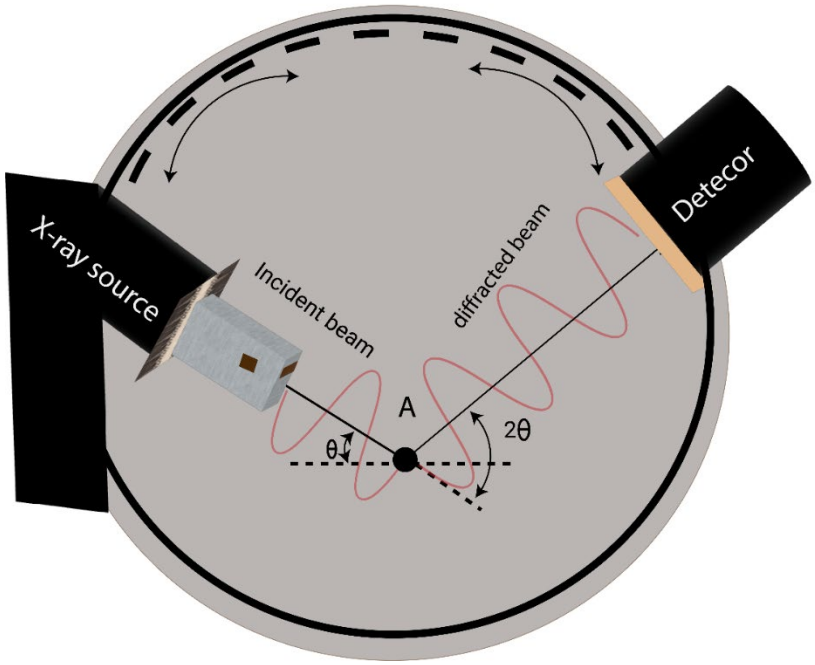

Figure 22: XRD diagram. On the X-ray .source, electrons got generated and hit the x-ray source to generate an x-ray beam. The X-ray beam hits the sample at an angle θ and another x-ray beam gets generated and reflected to the detector at 2θ angle.

The Scherrer equation enables the estimation of the average size of the crystallites of the material from the XRD pattern (Equation 2).[1]

$$D_{hkl} = \frac{K\lambda}{B\ Cos\ \theta_{hkl}} \quad (2)$$

Where;

hkl= Miller indices of the plane

D= diameter of the particles (perpendicular to the crystal plane; hkl)

K= shape factor (most of the time is 0.9)

θ= (half of the 2θ), which is the reflection position (perpendicular to the crystal plane; hkl)

B= broadening constant (full width at the height of the reflection position)

Advanced methods exist, such as Reitvald refinement, but for the purpose of this thesis, XRD is used to give a size approximation only and as a fingerprinting tool for phase identification.

2.2 Electron Microscopy

The electron was discovered by J.J. Thompson in the late part of the nineteenth century. At that time, scientists were using the optical microscope to magnify objects in order to investigate their properties visually. The optical microscope was limited by the wavelength of the light source, as can be seen in the ray diagram below in Figure 23.

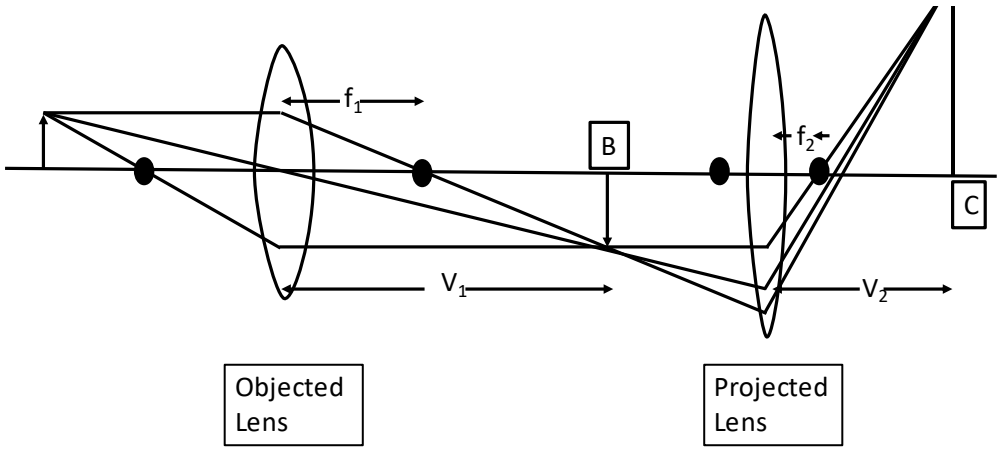

Figure 23: Ray diagram of the optical microscope. The maximum resolution that one can obtain with a light microscope has been limited by the wavelength λ and the numerical aperture of the system, NA. NA= numerical aperture, and is a function of the lens NA = n sin α. Where n is the refractive index of the medium (air =1, oil = 1.5), and α is the acceptance angle of the lens. Reproduced from Williams. [2]

Thirty years later (1925), L. De Broglie suggested the ability of electrons to behave as both a wave and as particles (negative particles - as he explained) once they got accelerated inside a chamber, which means they will have a wavelength (he was awarded the 1929 Nobel Prize on his particle wave theory). The wavelength of the electron can be varied by changing the velocity (determined by the voltage of the acceleration), Equations 3, 4, 5 and 6. Table 1 summarizes different acceleration voltages and the corresponding wavelengths.[3]

$$\lambda = \frac{h}{p} \tag{3}$$

Where λ is the wavelength, h is Plank's constant (6.6x10^{-34} kg m^2/s), and p is momentum.

$$p = mv \tag{4}$$

Where m is the mass of an electron (9.109x10^{-31}Kg), and v is velocity.

Equation 5 results from combining Equations 3 and 4.

$$\lambda = \frac{h}{mv} \tag{5}$$

De Broglie explained that in order for electrons to move at the same velocity, they would lose potential (acceleration voltage) P, and that gives Equation 6.

$$\frac{1}{2}mv^2 = eP \tag{6}$$

Where e is electron charge (1.60x10^{-19} C)

Rearrangement of Equation 6 gives Equation 7.

$$v = \sqrt{2meP} \tag{7}$$

Substituting in numbers, Equations 5 and 7 can be rewritten as Equation 8:

$$\lambda = \frac{1.224}{\sqrt{P}}\ 10^{-9} \tag{8}$$

Where P is in volts and λ in nm.

Table 1: The table shows different acceleration voltages and the corresponding wavelength of electrons generated.

Voltage in kV	Wavelength in nm
10	0.0122
50	0.0055
200	0.0027

One year after De Broglie came up with particle wave theory, Hans Busch published a paper about the ability of a magnetic field to make accelerated electrons behave like photons passing through a glass lens.[4] This paper inspired Ernst Ruska in 1931 to invent the first transmission electron microscope (TEM).[5] Ruska received the Nobel prize in 1986.[6] TEM

was commercially available in 1939 by Siemens and Halske in Germany.[2] Scanning electron microscopy (SEM) was developed by Zworykin *et al*. in 1942, and 23 years later, Cambridge Instrument Company in the United Kingdom started to sell the first commercially available SEM with the name Stereoscan 1.[7] The main difference between TEM and SEM is the acceleration of the electrons. SEM uses low acceleration, around 30 kV, so the electron will not have high energy to pass through the sample and will give an image of the surface as a result of backscattered electrons. In contrast, TEM uses high acceleration voltages around 60-300 kV. The electrons have high energy, so they pass through thin samples and give an image of the sample.

The high-energy electron beam can generate a variety of signals once the beam hits the sample, as can be seen in Figure 24. SEM uses the signals that return from the surface of the sample, such as backscattered electrons and secondary electrons. TEM uses the transmitted beam to create an image of the sample with the elastically scattered electrons missing when compared to the illumination beam, just as in conventional optical microscopy. Other, more advanced techniques can also make use of these signals that have been generated from the samples, such as Scanning Transition Electron Microscopy STEM and Electron Energy Loss Spectroscopy EELS.

TEM machines consist of four main parts, as can be seen in Figure 25. The electron beam is generated on the top of the TEM machine, which is called an electron gun system, then the electron beam passes through some magnetic lenses (condenser lens system) to hit the sample (objective lens system), and then beyond the sample, an image will be generated. The image will be magnified on the objective lens system before it can be seen on the CCD camera (charge-coupled device camera) or on the phosphor screen.

Because of the presence of samples in the way of the electron beam, the points where the sample is dense to electron transmission will appear as dark spots on the phosphor or camera. The bright area shows that there is no (or less electron scattering) sample in the beam's way. The phosphor screen shows the image because the electrons

that hit the phosphor screen excite photons - here green (as can be seen on the left-bottom of Figure 25.[2]

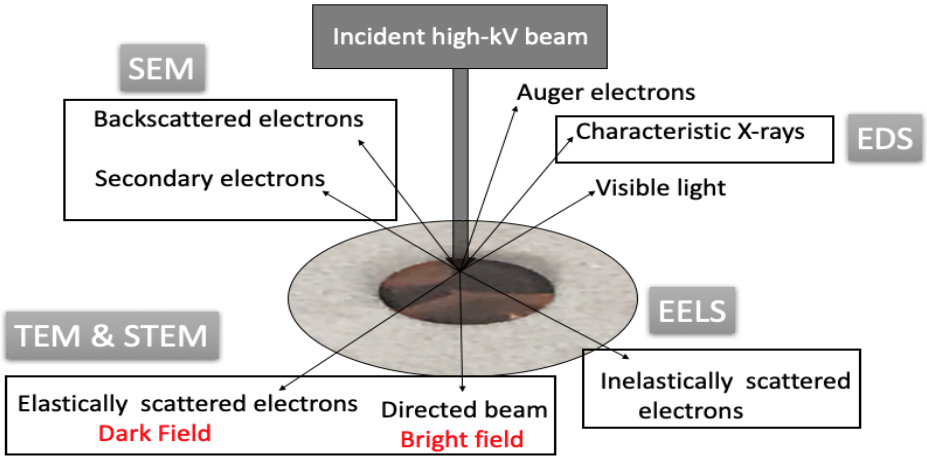

Figure 24: Schematic of signals generated when an electron beam interacts with a sample. The original beam hits the sample on the carbon film grid (known by specimen). Different signals can be generated, and these signals will be used to characterize the sample.

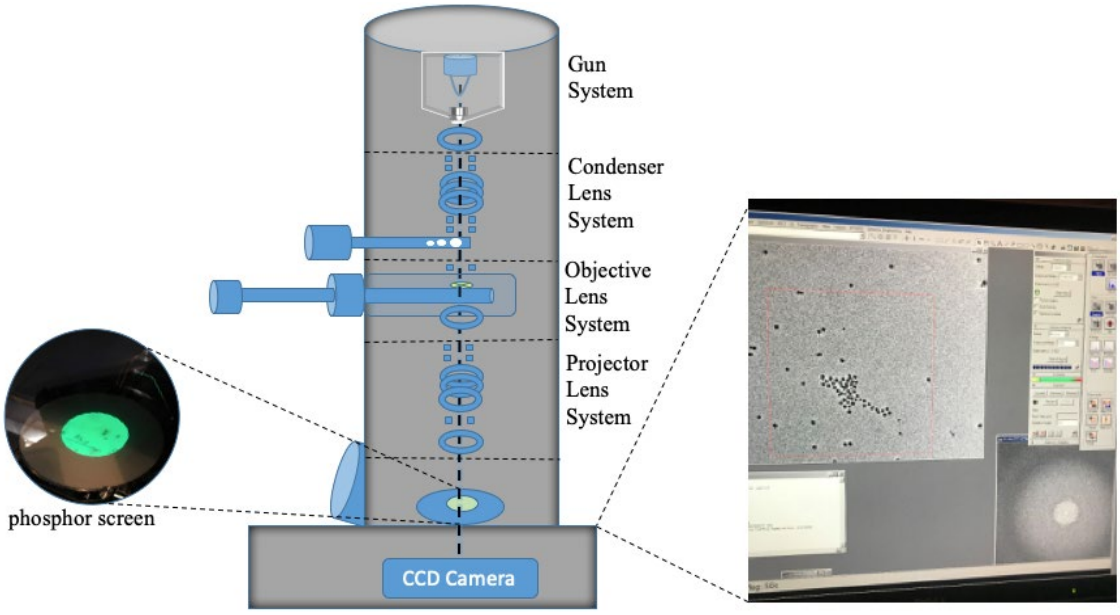

Figure 25: Schematic of a TEM instrument. From top to bottom, the gun system- where the electron beam is generated, the condenser lens system - where the beam is aligned with the optical axis (shown as a dashed vertical line from top to bottom), the objective lens system- where the beam meets the sample and generates the image, projective lens system- where the image is magnified. On the right-bottom, an image of an actual sample is recorded by the CCD camera. On the left-bottom, the beam passes through to the phosphor screen.

The gun system consists of parts, as can be seen in Figure 26. The first part is the filament, which is a metal wire that can be heated by passing a current through it and generating electrons (this method is known as thermionic emission). The filament is the cathode [-ve]. The second part is the Wehnelt which has a cone-shaped cap. This part has a negative bias which is important to focus the beam within the optical axis. The third part is the anode [+ve]. The accelerating zone is between the Wehnelt and the anode, which is the part that is responsible for accelerating the electrons.[2]

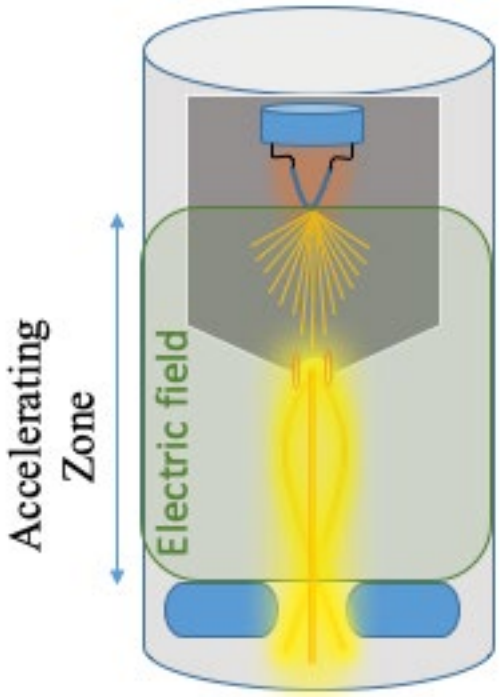

Figure 26: Electron gun. On the top, the metal wire has been heated by a passing current. This generates a cloud of electrons inside the Wehnelt (the grey cone-shaped cap). Because of the negative bias, the hole in the bottom of the Wehnelt will focus on the electrons within the optical axis. In the accelerating zone, the electron will be accelerated to generate an electron beam passing through the hole in the anode.

The second part is the condenser lens system. This part consists of gun deflectors, condenser lenses, condenser lens stigmater, and spot alignment. Each part has a job to do to align the beam in the right position. Gun deflectors bend the beam and align it with the condenser lenses. The condenser lenses are magnetic lenses that use Lorentz force to condense the beam on a focal point within the optical axis. The equation of the Lorentz force can be seen in Equation 9.[2]

$$F = q\overrightarrow{V} \times \vec{B} \tag{9}$$

Where; F is the Lorentz force, q is the charge, $\vec{V}$ is velocity, and $\vec{B}$ is the magnetic field.

This equation can be illustrated as the right-hand rule, in which the fingers are the velocity of the beam perpendicular to the velocity of the magnetic field, and the thumb will point in the direction of the Lorentz force. The positive charge makes the Lorentz force up (thumb is up) the negative charge makes the Lorentz force down (thumb is down). Because the magnetic field surrounds the magnetic lens, the beam will travel in a spiral trajectory shape. Increasing or decreasing the current on the magnetic lenses will change the focal point and the spot size of the beam[2], as can be seen in Figure 27.

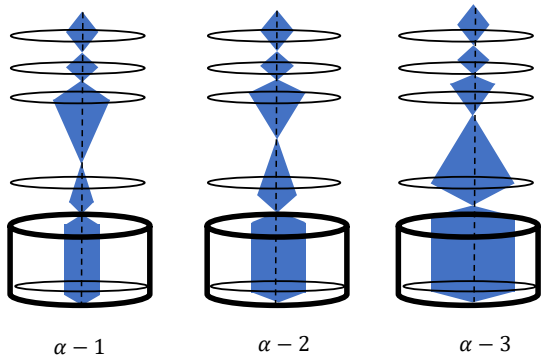

Figure 27: The focal point and the spot size can be changed by changing the alpha from 1 to 3. This change is the change of the current on the magnetic lenses. The small spot α 1 has a high number of electrons on a small spot area, whereas the bigger spot α 3 will have lower number of electrons.[2]

Also, the condenser lens system has a condenser aperture, which is basically an aperture with different diameter sizes that can be used to focus the beam on a small spot.[2] The condenser lens system can be seen in Figure 28.

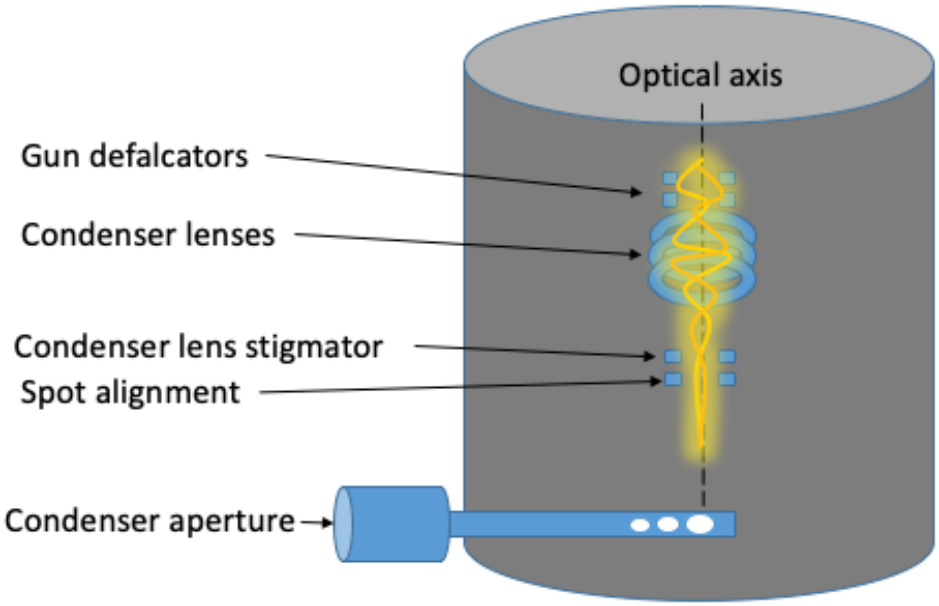

Figure 28: The condenser lenses. The beam comes from the anode (gun system) and passes through the gun deflectors. The beam will align to be with the optical axis. The beam will experience Lorentz force, and that will cause the beam to travel in a spiral trajectory shape (shown as yellow lines).

The third part of the TEM is the objective lens system, as can be seen in Figure 29a, which contains the beam deflector, specimen holder, and objective lens. The role of the beam holder is to align the beam within the optical axis. The sample will be on the specimen (also known as the TEM grid), and the specimen will be placed on a holder that can be controlled to move up, down, and tilt to the right or to the left. Under the specimen, there is the objective lens which is the lens that generates the image. Changing the focus on that lens will change the focus of the sample, as can be seen in Figure 29 b. The focus can be over (which means the focal point is close to the lens), or right focus (which means the focal point is the right distance from the lens) or can be under focus (which means the focal point is far away from the lens). Each focus can be beneficial to the image, depending on the morphology of the sample and the information required.[2]

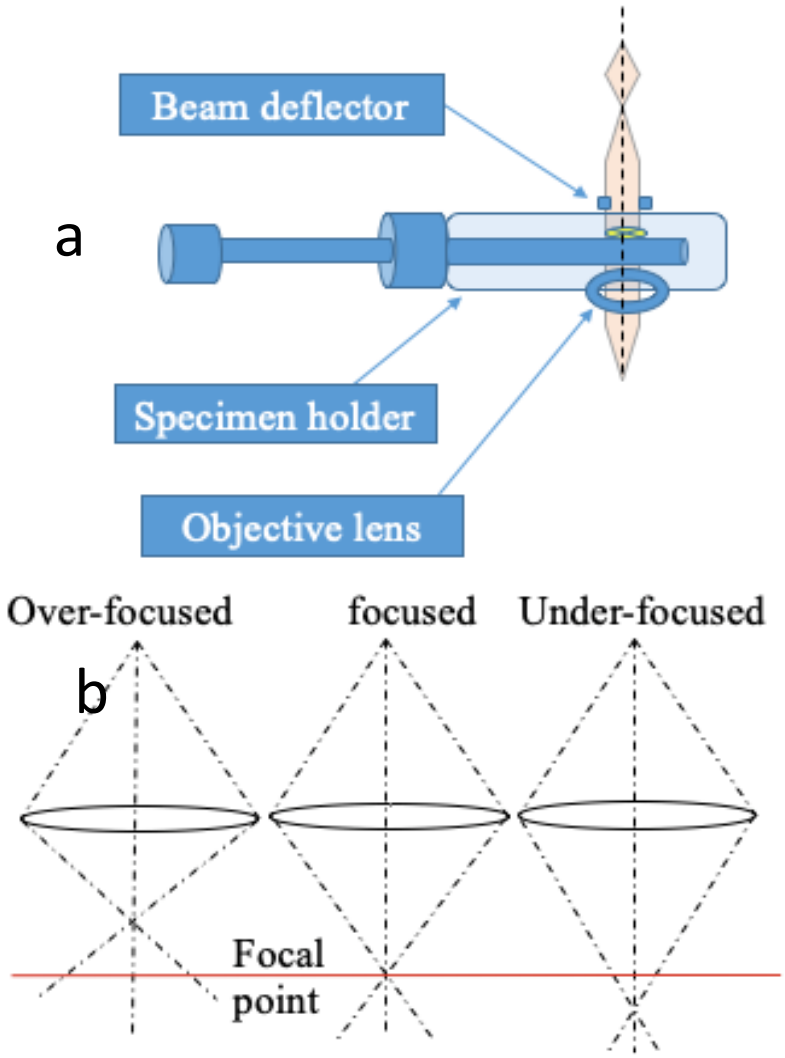

Figure 29: a) the objective lens system has a beam deflector, specimen holder, and objective lens. b) the focal points of the three focus options (over, right, or under-focused).

The fourth part is the projector lens system, which has image deflectors, an intermediate lens, projector lens deflectors, and the projector lens. In this part, the image created on the objective lens will be magnified by the intermediate lenses. There are three intermediate lenses. The reason for having intermediate lenses is that the focal point under the objective lens is within a few micrometres, which means the magnification will not be enough to see. Therefore, having intermediate lenses allows the image to be magnified

around a million times that of the original objective.[2] The projector lens system can be seen in Figure 30.

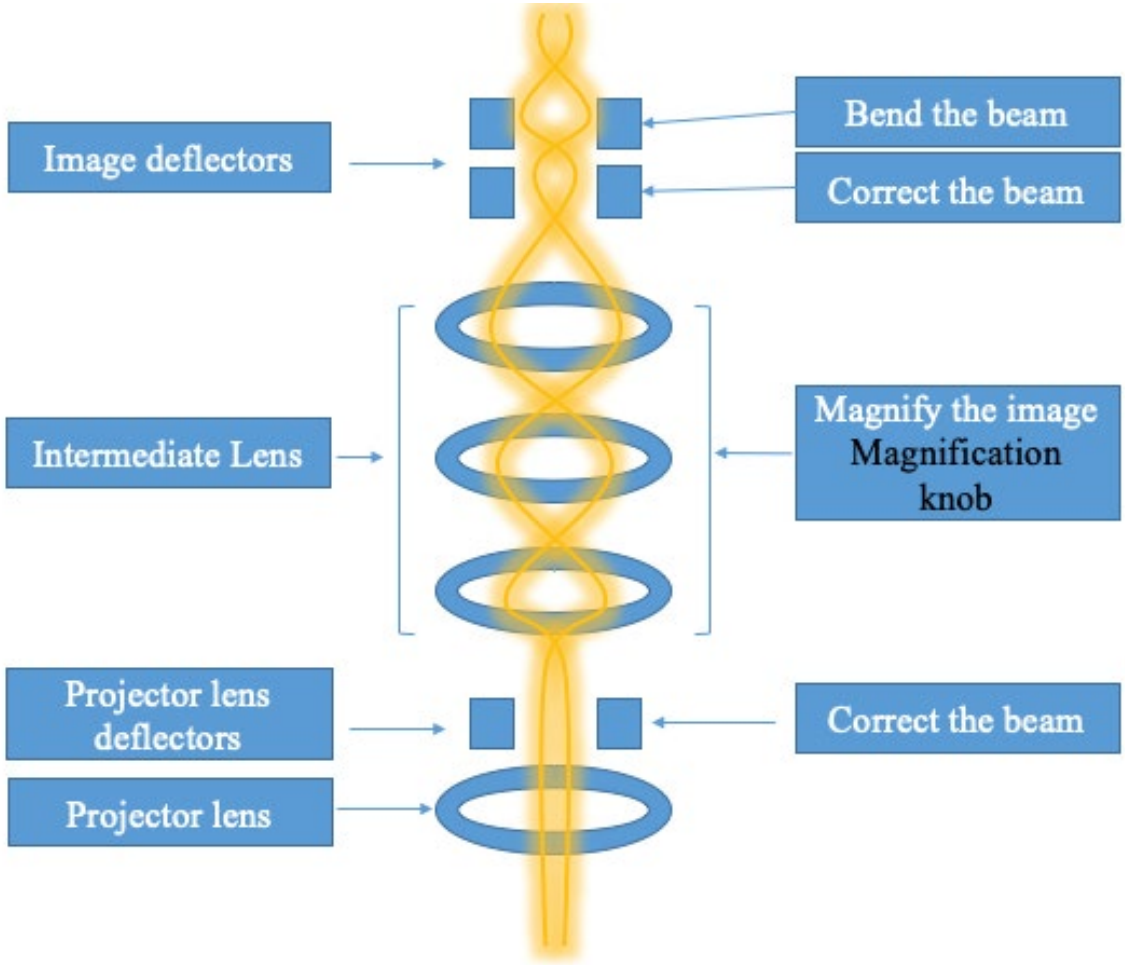

Figure 30: The projector lens system consists of image deflectors, an intermediate lens, a projector lens deflector, and a projector lens. The first intermediate lens is known as "low mag" on the Durham TEM, this lens can be operated alone, and that will be enough to see the surface of the grid. The second lens is known as mag 2 on the Durham TEM; this lens operates to magnify the image that can be seen from the first lens (low mag). The third lens is known as mag 1 on the Durham TEM. This lens operates to magnify the image that can be seen by the second lens (mag 2), which means all the lenses must be operated in that case.

The final part of the TEM is a CCD (charge-coupled device) camera. The original beam has high energy, which is hard to use directly by the detector. Therefore, before the beam

hits the CCD camera, the beam hits a scintillator, which basically is a phosphor. Once the electron beam hits the phosphor, a shower of photons will be generated. These photons will pass through the fibre optic coupling array to hit the CCD camera. On the CCD camera, the photons convert to electrons, and this transformation will be recorded as pixels, and an image can be formed.[2] The CCD camera can be seen in Figure 31.

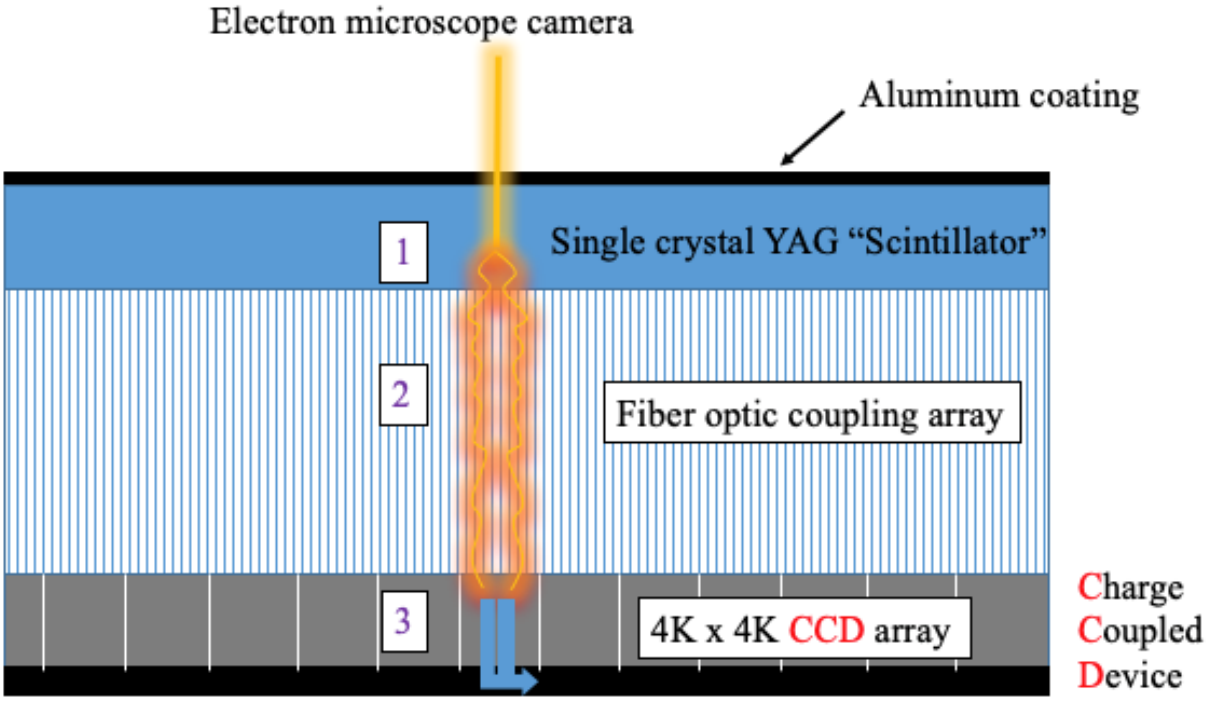

Figure 31: CCD camera on TEM. The mechanism of formation of an image is: 1- electron beam hits the phosphors (Scintillator), 2- convert the electrons to shower of photons and direct them through the fiber optical coupling array, finally, 3- on CCD camera, those photons will be converted back to electrons at specific pixels.

2.3 Ultraviolet-Visible (UV-Vis) spectroscopy

The basic principle behind the UV-Vis spectrometer is the interaction (absorbance or transmittance) between the photons (wavelength of light with energy in UV-Vis region from 200 to 800 nm) with orbitals molecules (or another sample) as a function of wavelength. This interaction promotes an electron from the bonding (σ, π, non-bonding) orbitals to the anti-bonding (σ^* or π^*) orbitals, as can be seen in Figure 32.

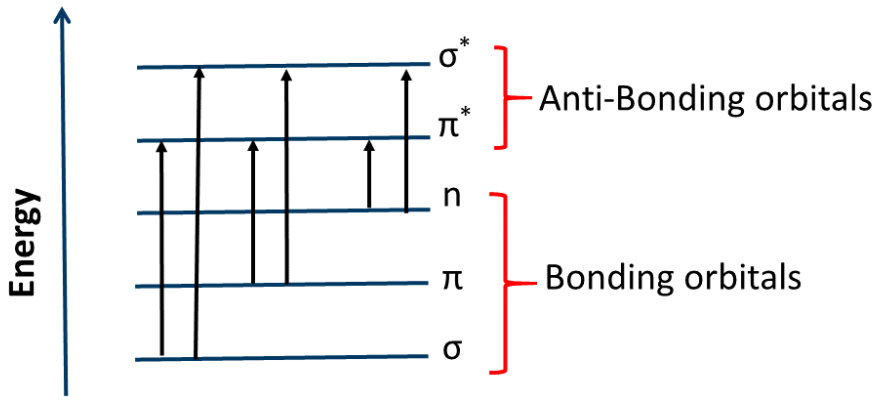

Figure 32: The positions for electrons to move after getting excited by the light. The electrons can be on the σ or π bonding orbitals. Lone pairs of electrons can be on n (none) bonding electrons. After the excitation, the electrons jump to the σ or π* anti-bonding orbitals.*

As each jump requires specific energy, this energy (just this specific amount of energy, not more, not less) can be obtained by absorbing the light (each wavelength of light has different energy). A larger jump will require higher energy which means higher frequency and lower wavelength of light, Equation 10 and Equation 11.

$$E = h\nu \tag{10}$$

$$\lambda = \frac{c}{\nu} \tag{11}$$

Where E is the energy, h is Planck's constant, λ wavelength, v is frequency, and c is the speed of light. The direct correlation between the frequency and the energy describes why the larger gap needs high energy. Moreover, the inverse relationship between the wavelength and the frequency shows that larger gaps will result in light absorption at a lower wavelength.

In 1947, the first commercial recording of UV-Vis was made available by Howard Cary. Seven years later, the cutting edge that was on the old UV-Vis instruments near to IR region was improved, and then the new generations were called UV-Vis-NIR. The essential parts of UV-Vis are the light source and the optics to direct the light beam to hit the sample and then, later on, the detector. Double beam instruments are designed to monitor the absorbance or the transmittance of the sample and blank sample simultaneously. This can be done by splitting the light beam into two beams, and then these beams hit the sample and the blank (reference sample) simultaneously.

The modern UV-Vis (like the one that was used in this work, a Cary 5000 UV-Vis-NIR spectrophotometer) has two light sources. A deuterium lamp produces wavelengths within the UV region (190-370 nm). The other lamp is a tungsten lamp, which can generate wavelength within the Vis region (320-1100 nm). The light is generated at the light source and then goes to the double monochromator through an entrance slit. The double monochromator separates the beam of light and generates different wavelengths. The selected wavelength range will pass through the exit slit and then will be directed by the optics to hit the sample and the sample reference (blank) at the same time. The intensity of the light that was absorbed or transmitted will be recorded after the beam passes through the sample (and the reference sample) and hits the detector, as is illustrated in Figure 33.

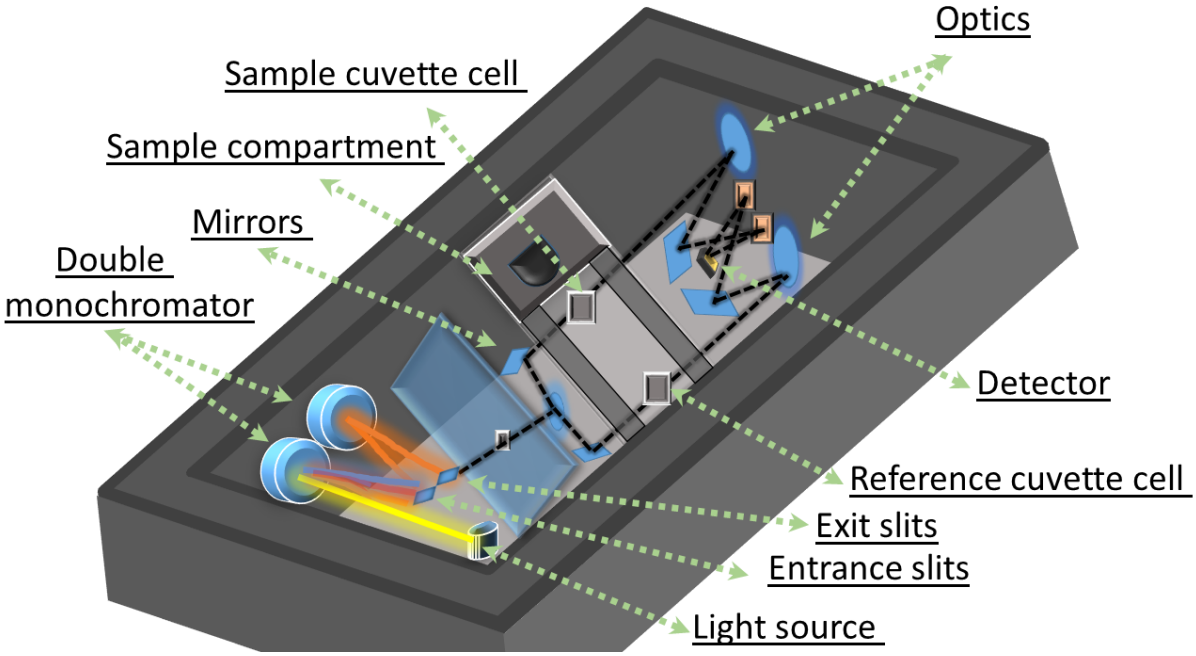

Figure 33: Cary UV-Vis instrument.

2.3.1 Colour Wheel

Once the light gets absorbed by a coloured substance, the only portion of the light wavelength will be absorbed, and the remaining light will pass without getting absorbed. This fact determines the colour seen, which can best be thought of in terms of a complementary wheel, where each complementary colour (the one seen) is opposite to another colour (the one absorbed), as can be seen in Figure 34. In the Ni experiments in this report, the blue-green solution absorbs the red-orange wavelength, and a peak in the vis region will appear around 800-580 nm.

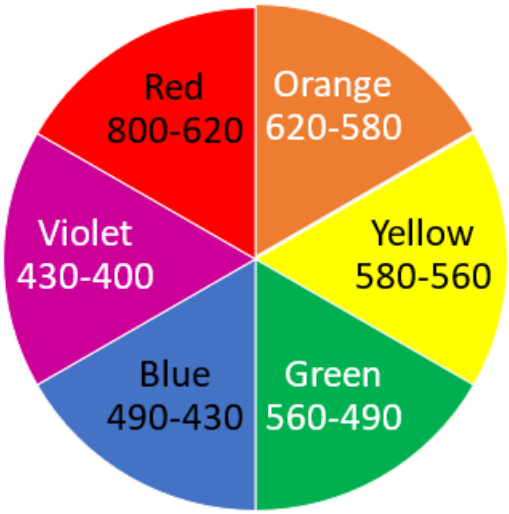

Figure 34: colour wheel with the corresponding wavelength in nm.

2.3.2 Selection rules and intensities

The intensity of the absorption bands is represented by the molar absorption coefficient ε_{max}, which is the constant in the Beer-Lambert law for transition, Equation 12

$$log\ T = -\varepsilon[X]L \tag{12}$$

Where $T=I_f/I_i$ is the final intensity of passing light over initial intensity, L is the solution length, and X is the molar concentration. Intense colours generally result from charge transfer, either:

1. by ligand-to-metal charge transfer (transfer of non-bonding electrons from a ligand orbital to a (usually) high oxidation state metal orbital), typically around 250-350 nm; For example, bands in the UV-vis spectra of d^4 metals with tetra-oxide change position based on the electrochemical series;

2. or, by metal-to-ligand charge transfer, which generally happens at lower energy (transfer of low oxidation state metal electron to a ligand with an available acceptor orbital), typically around 350-450 nm, for example, in the complex of diimine 2,2'-bipyridine with ruthenium to form tris(2,2'-bipyridyl)ruthenium(II). A summary of all charge transfer transitions is given in Figure 35.

The intensity of a transition is a consequence of the interaction between the electron and the magnetic field that will appear as either a strong coupling or weak coupling. The strength of the coupling could be measured by transition dipole moment, Equation 13

$$\mu_{fi} = \int \psi_f^* \mu \psi_i d\tau \tag{13}$$

Where μ is the dipole moment operator (odd function of r, displacement vector), ψ_i is the wavefunction of the state that has the electron before the transition (initial state), ψ_f is the wavefunction of the state that has the electron after the transition (final state). The outcome of the integral returns either a value of zero or non-zero. The integral of an odd function will generate a value of zero, which happens when the transition takes place from an orbital that is symmetric (also called even) to another symmetric orbital, such as s-s or p-p, d-d and f-f, resulting in forbidden transitions. In contrast, the integral of an even function will generate a non-zero value which happens when the transition takes place from an orbital that is symmetric (also called even) to an unsymmetrical orbital (also called odd), such as s-p, p-d and d-f, resulting in an allowed transition (gerade transition). This value describes the strength of the intensity.

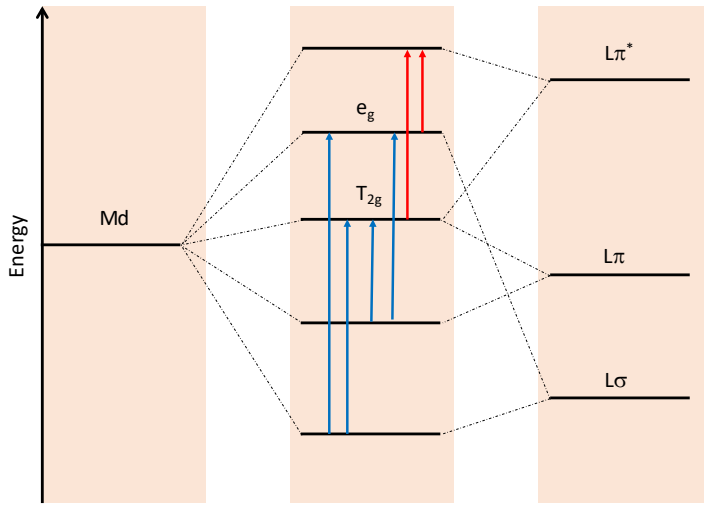

Figure 35: Using octahedral complex as an example to illustrate ligand-to-metal charge transfer transitions (blue lines) and metal-to-ligand charge transfer transitions (red lines).

Laporte selection rule, which can be explained by understanding the parity rule, which is about the changing in the quantum number of the orbital in centrosymmetric complexes (because the symmetry of the orbitals such as s-s, p-p, d-d or f-f, there is no change on parity and that will be described as forbidden transition whereas the other transitions are allowed). Starting from any point on the s or d orbital and inverting through the canter with giving the same wavefunction, and then this orbital will be classified as being symmetric orbital or grade, g, (gerade is a German word that means even in English). In contrast, p or f orbital will give different wavefunctions; therefore, the p orbital will be classified as asymmetric orbital ungerade, u (ungerade is a German word that means odd in English). Therefore, Laporte rule describes the transitions between s-d, and p-f by forbidden transitions (g-g or u-u) and s-p, p-d and d-f by allowed transitions (u-g or g-u).[8]

Allowed and forbidden transitions are also known as spectroscopic selection rules. The spin section rule indicates when the transition is going to be allowed (same multiplicity) or forbidden (different multiplicity) due to the electronic spin configuration. The interaction between the electron and the electromagnetic field of incident radiation cannot change the orientation of the electron spin. In other words, when $\Delta S=0$ a transition is spin allowed and

when $\Delta \neq 0$ a transition is spin forbidden. For example, Figure 36 shows the transition of an electron of d^3 complex (*e.g.* Cr^{+3}) that is going from t_{2g} to e_g. In Figure 36 (box A) the spin of the unpaired electron of the unexcited state is = 3/2, and for the excited state 3/2. The ΔS= 3/2-3/2=0, so it is spin allowed. In Figure 37 (box B), the s of the unpaired electron of the unexcited state is = 3/2 and for the excited state 1. The ΔS= 1-3/2=-1/2, so it is $\Delta \neq 0$, therefore, it is spin forbidden

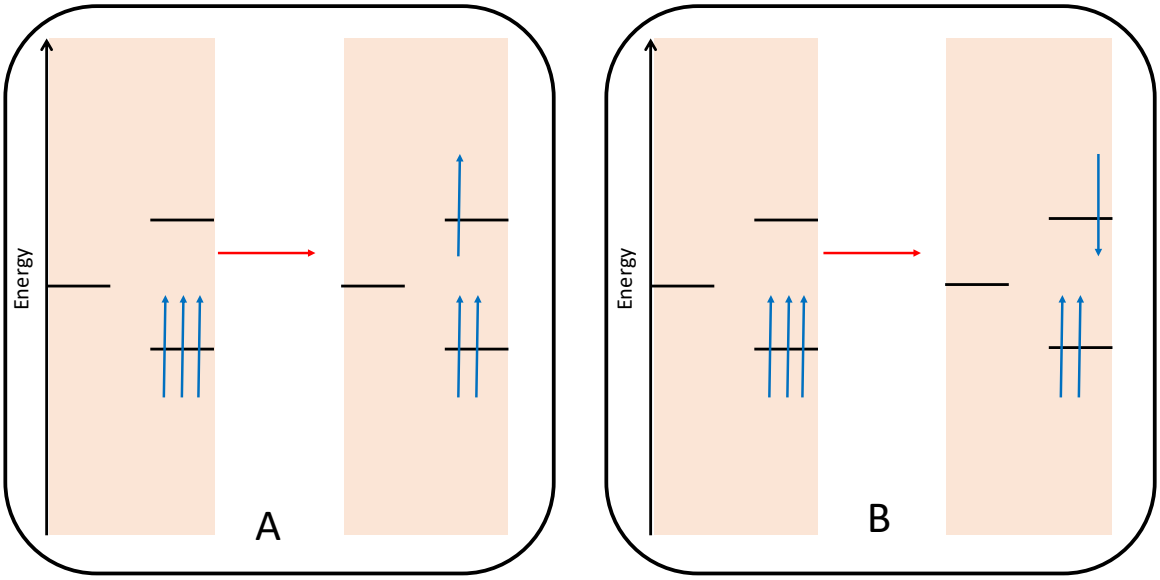

Figure 36: A shows a spin-allowed transition which does not change the multiplicity of the promoted electron. B shows a spin-forbidden transition which does change the multiplicity of the promoted electron.

2.4 Langmuir Blodgett (LB) Deposition method

Irving Langmuir and Katherine Blodgett, in the 20th century, invented the LB trough method for transferring Langmuir monolayers onto a substrate. An LB trough consists of a Teflon-coated trough, Teflon-coated barriers, Wilhelmy plate, and dipper, as illustrated in Figure 37. The trough is filled with high-purity water. The barriers move above the water's surface to the middle of the trough. Typically, a software program can control the movement of the barriers. The Wilhelmy plate carries out the surface pressure

measurements. The Wilhelmy plate attaches to an electronic microbalance which locates above it.[9]

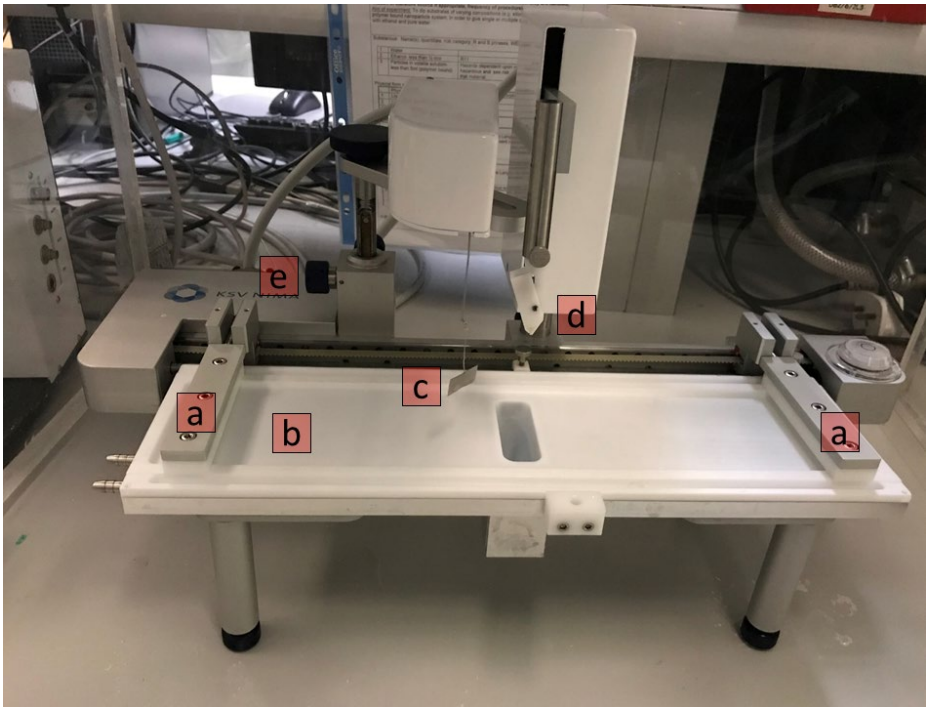

Figure 37: Picture of a LB trough showing the following parts: a) barriers, b) trough, c) Wilhelmy plate, d) dipper and e) Wilhelmy plate controller.

The LB deposition technique has also been found to be suitable for depositing monolayer films of nanoparticles, which is what it will be used for in the present work.[10] The LB deposition technique (Figure 37) works by moving floated nanoparticles on the surface of the liquid (*e.g.* UHP water) onto a solid substrate (*e.g.* glass microscope slide) to form a monolayer of nanoparticles and can be repeated to form multi-layers. Figure 38 illustrates the LB deposition method.

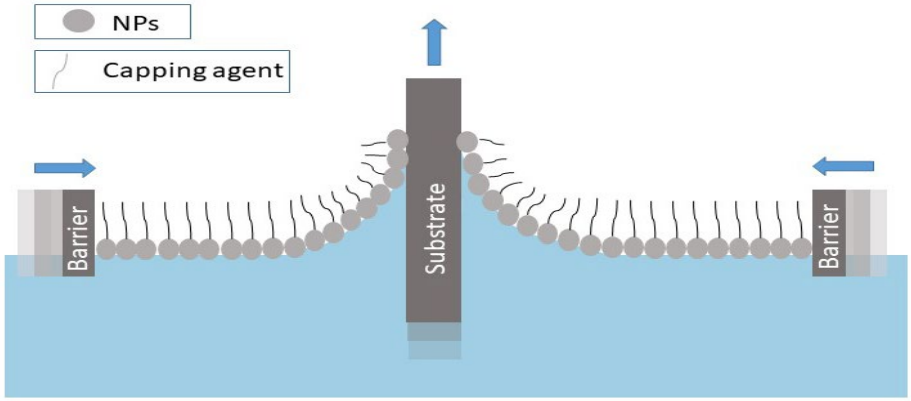

Figure 38: Schematic showing the LB deposition method.

Surface pressure measurement for nanoparticles is required to understand when a monolayer of nanoparticles is formed. The surface pressure testing for nanoparticles (*e.g.* copper nanoparticles) leads to the understanding that the nanoparticles at high surface pressure will be forming a double layer, as can be seen in the example of an isotherm in Figure 39 and Figure 40. When the trough area decreases (by moving the barriers), the surface pressure increases. This indicates the effect of steric in the organic layer around the nanoparticles (capping agents) as the nanoparticles get pushed closer together, which leads to an increase in surface pressure. The gradually increasing surface pressure means a monolayer of nanoparticles is forming, as in Figure 39, phase (a). Where the increase in surface pressure stops increasing or is lowered, this likely results from forming a double layer where some nanoparticles slide over the original layer and so allow relief of the surface pressure build-up, as in Figure 39, phase (b). Figure 40 schematically depicts the two processes.

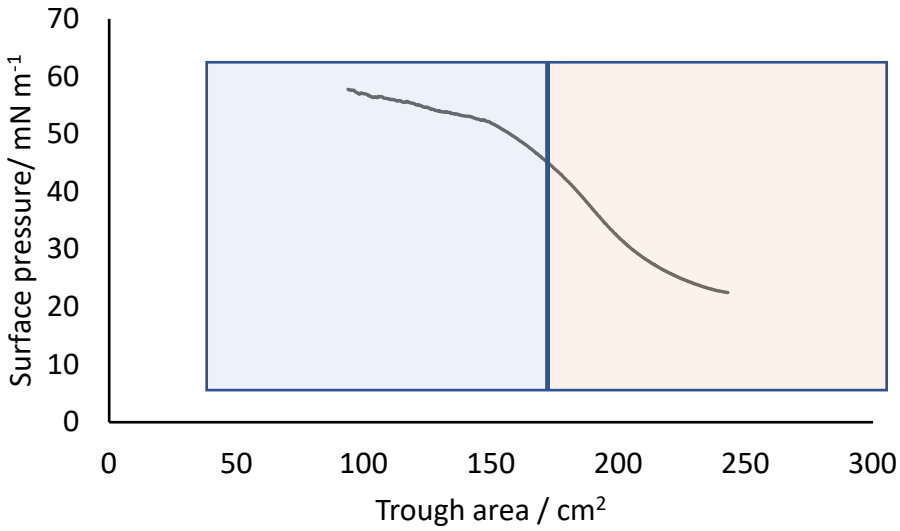

Figure 39: Example of a typical surface pressure measurement for Cu nanoparticles.

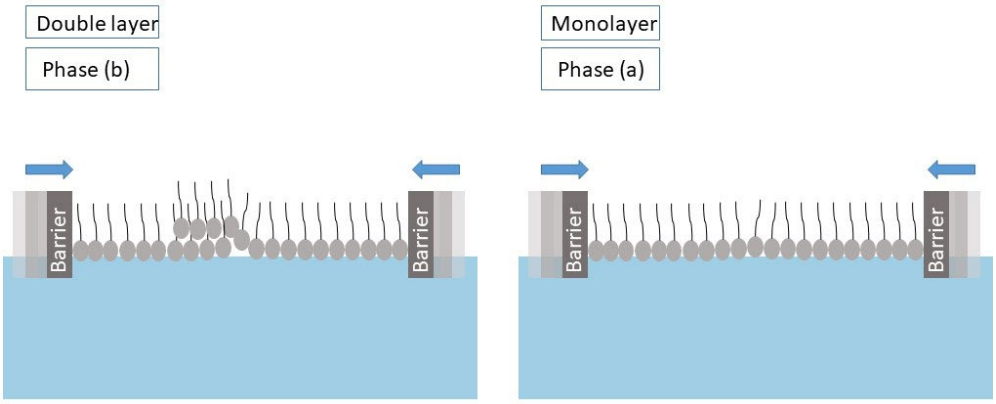

Figure 40: Two results of increasing the surface pressure of nanoparticles. Phase (a) NPs are forming a monolayer. Phase (b) NPs are forming a double layer.

Understanding surface pressure allows the determination of the surface pressure that can be used for the deposition of the most compressed possible monolayer of nanoparticles onto a substrate.

2.5 NMR

Nuclear Magnetic Resonance spectroscopy is an analytical technique that applies a large magnetic field (*e.g.* 400 MHz, 9.4 Tesla) to exploit the magnetic properties of atomic nuclei with non-zero spin in order to investigate the physical and chemical properties of the surrounding molecule. Bloch and Purcell developed the principle of NMR in 1946. Six years later, they earned Nobel Prize in Physics. A magnetic moment is generated from a spinning charge and is proportional to the spin; therefore, in the presence of an external magnetic field, the spin states become split – in the case of a nucleus with spin I=½, they split into two states, usually denoted. One will be parallel to the magnetic field, and the other will be antiparallel to the magnetic field (and so have different energies). Each specific group of nuclei can be excited by the exact amount of energy (radiation) due to the separation of the spin states. This irradiation will excite the nuclear spins from the lower to higher energy state. Once this absorption occurs, the nuclei will start to be in resonance mode. For example, ^{1}H can be excited at 100 MHz frequency and 2.34 T magnetic field strength.[11]

2.5.1 ^{11}B-NMR

^{11}Boron Nuclear Magnetic Resonance is a physical tool to investigate boron-containing compounds. The two natural isotopes are ^{11}B (3/2 spin) and ^{10}B (3 spin). The ^{11}B has higher naturally abundant (80%).

The investigation of boron-containing species by ^{11}B-NMR gives a peak area signal that is proportional to the number of boron atoms in the chemical formula. The location of the signals depends upon the number and type of the directly attached atoms. The adjacent atoms can shield the boron atom causing the signal to be shifted. For example, the common chemical shifting of BX_3 are $B(CH_3)_3$ has a signal at 86.2 ppm, $B(NR_2)_3$ has a signal at 27 ppm, and , $B(NHR)_3$ has a signal at 23 ppm.[11]

The ^{11}B-NMR has some limitations, especially with equilibria. For example, the equilibria between monomeric amino-boranes and dimeric amino-boranes. The reason for this is that the tri- and tetra-coordinate borane in the dimer BN chain leads to similar shifts in all species, as seen in Figure 41.[11]

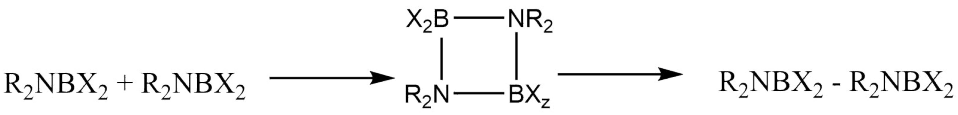

Figure 41: Two monomeric species form an intermediate and then a dimer with a BN chain.

2.6 ASAP mass spectrometry

Atmospheric Solids Analysis Probe (ASAP) mass spectrometry was developed by McEwan in 2005. It is a useful tool for analyzing volatile and semi-volatile solid and liquid samples by using electrospray ionization (ESI) or atmospheric pressure chemical ionization (APCI). This technique does not need further preparation for complex mixtures; it can be done directly from the source material, and it takes seconds to perform. The ASAP technique uses a heated N_2 stream flowing from ESI or APCI probe to volatilize the sample present as a solid or liquid on a disposable glass capillary tip. A corona discharge ionizes the thermally induced vapours under standard atmospheric pressure chemical ionization (APCI) conditions. This method provides a high degree of sensitivity towards low-polarity compounds that are not amenable to ESI. Figure 42 illustrates an ASAP instrument.[12]

ASAP can detect positive or negative ions. For positive ions, there are two methods for forming positive ions; these methods are protonation (for polar compounds) and charge transfer (for non-polar compounds). The protonation occurs when the corona discharge forms $N_2^{+\bullet}$; then, the nitrogen radical cation reacts with another N_2 to form $N_4^{+\bullet}$ that can react with water and form H_3O^+. The analyte will react with H_3O^+ and form protonated molecular ions. The second method is charge transfer which involves the reaction between the analyte and nitrogen radical ions ($N_2^{+\bullet}$/ $N_4^{+\bullet}$) to form radical molecular ions. Figure 43

summarizes both mechanisms. For the negative ion, O_2^- is used in a similar way as the reagent to produce [Analyte – H]$^-$.[12, 13]

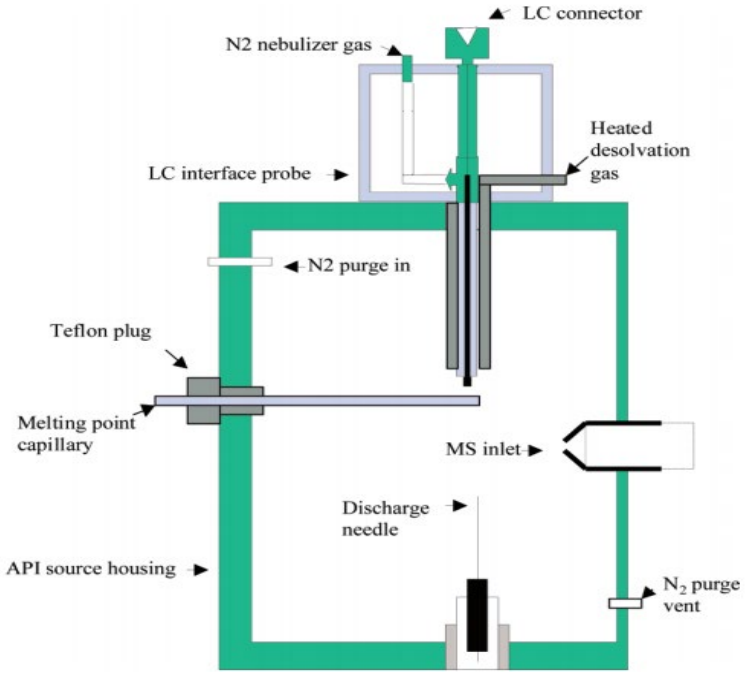

Figure 42: ASAP with LC/MS ion source instrument. Reproduced with permission from ref [14] (Copyright 2005 American Chemical Society)

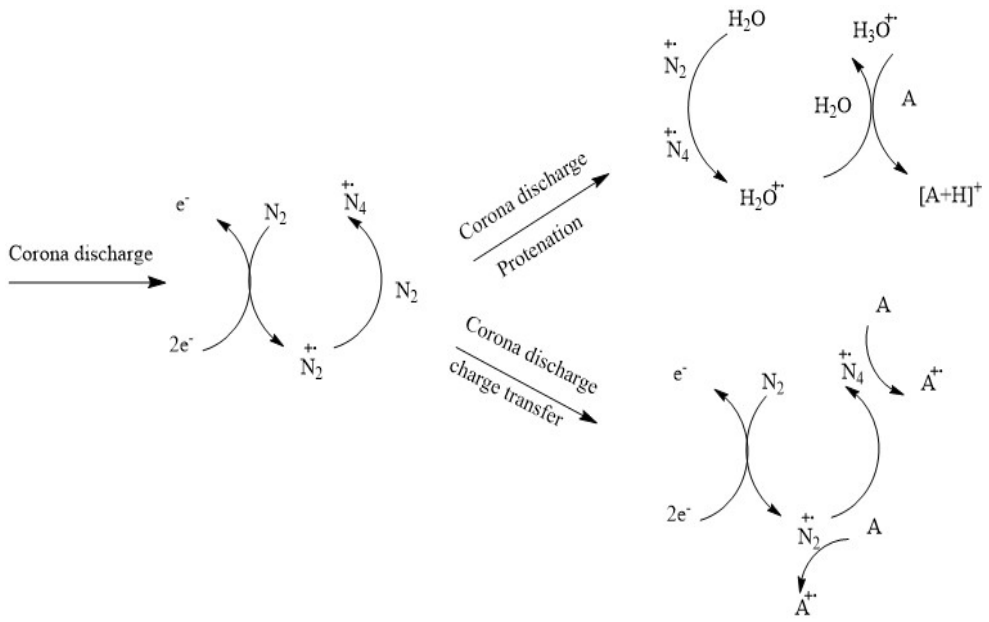

Figure 43: Positive ion mechanism in ASAP technique (A= analyte).[12, 13]

2.7 ICP-OES

Inductive Coupled Plasma-Optical Emission Spectrometry (ICP-OES) is an analytical method that is useful for inorganic analysis. It works by introducing plasma at high energy to a sample. The sample will be excited (going to a high electronic energy level) and emit electromagnetic radiation (returning to a lower energy level). The emitted rays that correspond to a specific photon wavelength are measured since these are atom specific, depending on the atomic structure of atoms of each element. The investigation of the element type can therefore be determined by the wavelength. The concentration of each element is obtained by the emitted rays' intensity.[15]

Plasma used for ICP-OES can be generated by using argon gas that has been ionized in the tip of a torch tube by high temperature (7000-10000 K) and an electromagnetic field that has been generated by a high-frequency electric current. The sample is introduced as a solution to the ICP. The sample then goes into the nebulizer to turn the solution sample into fine droplets. These droplets go to a coil to reach the plasma; then, the plasma will

atomize the molecule and excite the electronic states of the atoms. The OES process detects the photoemission by separation of the emitted rays by wavelength using prisms or gratings. Each wavelength will be detected, and the data can be recorded.[15]

1. Waseda, Y.; Matsubara, E.; Shinoda, K., *X-ray diffraction crystallography: introduction, examples and solved problems*. Springer Science & Business Media: 2011..
2. Williams, D. B.; Carter, C. B., The transmission electron microscope. In *Transmission electron microscopy*, Springer: 1996; pp 3-17.
3. De Broglie, L., The wave nature of the electron. *Nobel lecture* **1929,** *12*, 244-256.
4. Laub, H., Zustandsänderungen im permanent magnetischen Feld. *Archiv für Elektrotechnik* **1926,** *16* (6), 481-495.
5. Knoll, M.; Ruska, E., Das elektronenmikroskop. *Z. Phys.* **1932,** *78* (5-6), 318-339.
6. Ruska, E., The development of the electron microscope and of electron microscopy (Nobel Lecture). *Angew. Chem., Int. Ed. Engl.***1987,** *26* (7), 595-605.
7. McMullan, D., Scanning electron microscopy 1928–1965. *Scanning* **1995,** *17* (3), 175-185.
8. Weller, M. O. T. R. J. A. F. A., *Inorganic chemistry*. OUP, 2018.
9. Hussain, S. A.; Deb, S.; Bhattacharjee, D., *Langmuir-Blodgett technique a unique tool for fabrication of Ultrathin Organic Films*. 2005; Vol. 4, p 25-33.
10. Song, H.; Kim, F.; Connor, S.; Somorjai, G. A.; Yang, P., Pt Nanocrystals: Shape Control and Langmuir−Blodgett Monolayer Formation. *J. Phys. Chem. B* . **2005,** *109* (1), 188-193.
11. Hermanek, S., Boron-11 NMR spectra of boranes, main-group heteroboranes, and substituted derivatives. Factors influencing chemical shifts of skeletal atoms. *Chemical reviews* **1992,** *92* (2), 325-362.
11. Diehl, P.; Fluck, E.; Kosfeld, R., *NMR Basic Principles and Progress/NMR Grundlagen und Fortschritte*. Springer Sci. & Business Media: 2012; Vol. 7.
12. Petucci, C.; Diffendal, J., Atmospheric solids analysis probe: a rapid ionization technique for small molecule drugs. *J Mass Spectrom* **2008,** *43* (11), 1565-1568.
13. Dzidic, I.; Carroll, D. I.; Stillwell, R. N.; Horning, E. C., Comparison of positive ions formed in nickel-63 and corona discharge ion sources using nitrogen, argon, isobutane, ammonia and nitric oxide as reagents in atmospheric pressure ionization mass spectrometry. *Anal. Chem.* **1976,** *48* (12), 1763-1768.
14. McEwen, C. N.; McKay, R. G.; Larsen, B. S., Analysis of Solids, Liquids, and Biological Tissues Using Solids Probe Introduction at Atmospheric Pressure on Commercial LC/MS Instruments. *Anal. Chem.* **2005,** *77* (23), 7826-7831.
15. Thompson, M.; Walsh, J. N., Handbook of Inductively Coupled Plasma Spectrometry. **1989**.

Experimental

2.8 General methods and materials

Where reactions are indicated to have been conducted under nitrogen, this was accomplished by means of a standard Schlenk line equipped with Young's tap fittings, an oil bubbler and a vacuum supplied via an Edwards model RV3 rotary vane pump and monitored using a Kurt J. Lesker vacuum gauge. Glassware was oven-dried overnight at 120 °C. Glassware was evacuated and refilled three times with N_2 before use. The temperature was controlled using a PID-controlled isomantle with feedback from a K-type thermocouple immersed in the reaction solution, as can be seen in Figure 44.

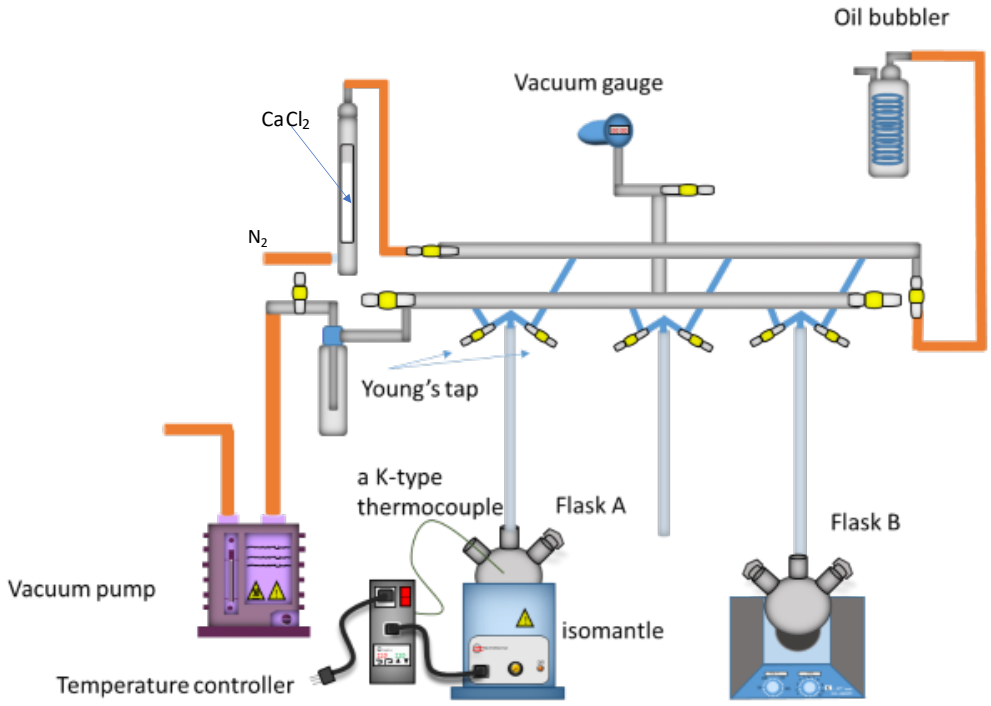

Figure 44: Schematic of a typical Schlenk line connected to round bottom flasks.

2.9 Chemicals, purities and sources

Borane complex (97%), $Pd(acac)_2$ (99%), morpholine borane trimethylamine (96%), $Ni(acac)_2$ (95%), were purchased from Alfa Aesar. Diphenyl ether (99%), pyridine (≥99%), methanol (≥99%), ethanol (≥99%), and boron tertbutylamine complex (97%) were purchased from Sigma-Aldrich. Octadecylmine (90%), $Cu(acac)_2$ (98%), oleylamine (80-90%), were purchased from Acros Organics. Calcium hydride (93%), HPLC grade hexane (95%), and oleic acid (extra pure), were purchased from Fischer-Scientific. High-purity water (18.2 Ω) was used as obtained from a Purite Neptune deionized water machine.

For copper experiments, all solvents were dried, degassed and stored under a nitrogen atmosphere in order to avoid oxygen contamination (unless otherwise stated). Pyridine was dried/degassed and stirred with calcium hydride (93%, Fischer-Scientific) overnight under nitrogen before being distilled and stored under nitrogen. Diphenyl ether was dried over molecular sieves and then degassed in three freeze/thaw cycles before being stored under a nitrogen atmosphere.

2.10 Synthesis of Cu NPs.

Under N_2, morpholine borane complex (0.024 g, $3.37x10^{-4}$ mol) was added to a round bottom flask (flask A) containing diphenyl ether (10.0 mL, $6.34x10^{-2}$ mol) and octadecylmine (0.29 g, $1.08x10^{-4}$ mol). This flask was heated at 80 °C overnight. Separately, flask B was stirred containing either:

a: $Cu(acac)_2$ (0.075 g, $2.84x10^{-4}$ mol) and pyridine (0.5 mL, $6.20x10^{-3}$ mol) under N_2 for 3 h.

b: $Cu(acac)_2$ (0.075 g, $2.84x10^{-4}$ mol) and pyridine (0.5 mL, $6.20x10^{-3}$ mol, ≥99%, Sigma-Aldrich) under N_2 overnight. or

c: $Cu(acac)_2$ (0.075 g, $2.84x10^{-4}$ mol) and pyridine (0.5 mL, $6.20x10^{-3}$ mol) and oleic acid (0.32 mL, 1.01x10-3 mol) under N_2 overnight.

Flask A was heated to 150-210 °C (as specified) before transferring by syringe the contents of flask B into flask A (as one portion), and the solution turned from colourless to dark brown. After 1 h, the reaction was cooled using an ice bath. The flask on the following step is under air (not under N_2). The nanoparticle product was then precipitated using the anti-solvent methanol (around 30 mL, 7.42×10^{-1} mol). The mixture was centrifuged at 8000 r.p.m. for 10 min, the supernatant decanted, and the precipitate redispersed in hexane (around 4 mL, 3.04 $\times 10^{-2}$ mol) and stored in 35 mL vial.

2.11 Synthesis of Pd NPs.

Synthesis of Pd NPs was done following the method that was reported by Parlett *et al*.[1] Under N_2, $Pd(acac)_2$ (0.073 g, 2.4×10^{-4} mol) and oleylamine (15 mL, 4.56×10^{-2} mol) were added to a round bottom flask and heated to 60 °C. On reaching 60 °C, borane trimethylamine (0.53 mL, 3.8×10^{-3} mol) was added to the flask by syringe (as one portion), and the solution turned from pale yellow to pale brown. The flask was heated to 90 °C for 15 min, and the solution turned from pale brown to black. After the black solution was noticed, the heating was continued at 90 °C for 90 min before cooling to room temperature.

The flask on the following step is under air (not under N_2). The nanoparticle product was then precipitated using the antisolvent ethanol (around 30 mL, 5.13×10^{-1} mol). The mixture was centrifuged at 8000 r.p.m. for 20 min, the supernatant decanted, and the precipitate redispersed in hexane (around 4 mL, 3.04 $\times 10^{-2}$ mol) and stored in 35 mL vial. The washing was done by evaporating hexane under flowing nitrogen until the volume was reduced to around 2 mL and adding 30 mL of ethanol, followed by separating NPs by centrifugation (6,000 r.p.m., 10 min). The washing was repeated three times to remove any excess of any unwanted residual synthetic agents.

2.12 Synthesis of Ni NPs.

Synthesis of Ni NPs was done following the method that was reported by Mazumder *et al.*[2] with some modifications. Under N_2, Ni $(acac)_2$ (257 mg, $8.17x10^{-4}$ mol, 95%, Alfa Aesar) was added to a round bottom flask (flask A) containing oleylamine (15 mL, $4.55x10^{-2}$ mol), and oleic acid (0.32 mL, 1.01x10-3 mol). This flask was heated while stirring to either:

a: 90 °C and held for 1 h. **b**: 110 °C and held for 1 h.; or **c**: 110 °C and held overnight.

Separately, borane tertbutylamine complex (264 mg, 3.03x10-3 mol) was stirred into oleylamine (2 mL, $6.07x10^{-3}$mol) for either **a**: 1 h under nitrogen (flask B) or **b**: heated to 90 °C for 10 min. After 1 h or 10 min, the temperature in flask A was decreased from desired temperature (a, b or c) to 90 °C before transferring by syringe (as one portion) the contents of flask B into flask A, and the solution turned black. After 1 h, the reaction was cooled using an ice bath. The flask on the following step is under air (not under N_2). The nanoparticle product was then precipitated using the antisolvent ethanol (around 30 mL). The mixture was centrifuged at 8000 r.p.m. for 10 min, the supernatant decanted, and the precipitate redispersed in hexane (around 4 mL) and stored in 35 mL vial.

2.13 TEM

TEM images were recorded on a JEOL 2100F Transmission Electron Microscope with a Schottky field emitter source. The accelerating voltage was 200 kV. High resolution (HR-TEM) images were recorded with a 2.3 Å point resolution and a 1.0 Å information limit. A GATAN model 792 Bioscan CCD camera was used for acquiring TEM images. Energy dispersive X-ray (EDX) spectroscopy was conducted using an Oxford INCAx-sight Si (Li) detector. All TEM samples were supported on carbon-film 300 mesh copper TEM grids (EMResolutions). ImageJ software was used for the manual measurement of the diameter of the particles. The reported particle size distribution was obtained from six different regions of the grid and at least 100 NPs. Measurements were conducted by taking all particles from the right half of each image in order to avoid biasing as a result of choosing

which particles to measure. Measurements were also taken horizontally for each particle to avoid the selection of longer or shorter axes that could bias the measurement. The TEM preparation was done by taking one droplet of sonicated sample (in hexane) and placing it on the grid before evaporating to dryness under a warm lamp.

2.14 UV-Vis-NIR samples preparation

The samples were analysed on the Cary UV-Vis-NIR using a 10 mm quartz cuvette. The sampling was done by taking 20 µL from the solution, then first diluting it with 1 mL of chloroform, and then 40 µL of the first diluted solution was further diluted into 4 mL of chloroform. The samples were submitted to the spectroscopy staff for analysis. The preparation protocols were different for each region as follows:

a: the samples scanned in the UV region (250-350nm); the sampling was prepared by taking 0.2 mL from the solution with 4 mL of chloroform. The samples were submitted to the spectroscopy staff for analysing them.

b: the samples scanned in the Vis region (400-700 nm); the sampling was prepared by taking 1 mL from the solution with 3 mL of chloroform. The samples were submitted to the spectroscopy staff for analysing them.

c: the samples scanned in the NIR region (700-800 nm); the sampling was prepared by taking 1 mL from the solution with 3 mL of chloroform. The samples were submitted to the spectroscopy staff for analysing them.

2.15 ICP-OES

Inductively coupled plasma-optical emission spectroscopy (ICP-OES) was performed on a Jobin Yvon Horiba Ultima-2 (ICP), thermoFisher iCAP 6500 (OES), sequential monochromator with a vertically oriented radial torch. ICP-OES standards Ni and Cu 1000 ppm were obtained from Fluka, and Pd 1000 ppm was obtained from Aldrich. Cu, Pd, and Ni measurements were based on the emission lines as follows: Cu lines at 224.700 nm and 324.754 nm; Pd lines at 324.270 nm and 340.458 nm; and Ni lines at 221.647 nm and

231.604 nm. The average of both lines were used to calculate the yields. The ICP-OES sample preparation was done as follows: the required measured amount (Appendix Chapter 3) of a solution of NPs was heated to 80 °C to evaporate all the hexane (the precipitated metal was seen on the tube wall), and after cooling, 3 mL of aqua regia (HNO_3:HCL, 1:3 v/v by volume) was added to the tube and heated up to 80 °C for 1 h, and after cooling the tube, the solution was transferred to a 25 mL volumetric flask and made to volume by using ultra-high purity water. A-C.3.1 shows the details of the ICP calculations.

2.16 ^{11}B NMR

^{11}B nuclear magnetic resonance (NMR) was performed on a Bruker Avance III-HD-400 spectrometer with an operating frequency of 128.32 MHz. The required amount of supernatant was placed in an NMR tube neat and submitted to the Durham NMR auto sampling service.

The spiked (sample EX0016 spiked with a known quantity of other boron compounds) samples were prepared by taking 5 mL from the supernatant and adding the required amount from the reference sample with 5 mL of methanol to a vial before transferring the mixture to an NMR tube neat and submitting it to the Durham NMR auto sampling service. The calculations can be seen in appendix chapter A-C.3.3.

Spectra were processed by MestreNova software:

1. Apodization 10Hz (typical of ^{11}B linewidths and reasonable in view of noisy spectra), then phase correction allowed to take place again. This was automatically applied as a processing template to all ^{11}B NMR spectra.
2. Manually rephrasing if one of the reference spectra does not match the tube-only spectrum.
3. Subtraction of the “Tube only spectrum” from each of the spectra to give background subtracted spectra.

2.17 ASAP-Q-TOF-MS

Atmospheric Solids Analysis Probe (ASAP) - quadrupole-time of flight-mass spectrometry was performed on a Xevo QToF mass spectrometer (Waters Ltd, UK). The required amount (2-3 mL) of NPs solution was placed in GCMS vials and submitted to the Durham MS Service for analysis.

2.18 Quantification of gas volume released during reactions of the amine-borane complex.

A 50 mL burette was filled up with water and flipped to be inside a 250 mL beaker that contained 150 mL water. The reaction takes place in another round bottom flask under an inert atmosphere as follows: first experiment (with), morpholine borane complex (0.024 g, 3.37×10^{-4} mol, 97%, Alfa Aesar) was added to a round bottom flask containing diphenyl ether (10.0 mL, 6.34×10^{-2} mol, 99%, Sigma-Aldrich) and octadecylmine (0.29 g, 1.08×10^{-4} mol, 90%, Acros Organics). Second experiment (without), round bottom flask contains only diphenyl ether (10.0 mL, 6.34×10^{-2} mol, 99%, Sigma-Aldrich) and octadecylmine (0.29 g, 1.08×10^{-4} mol, 90%, Acros Organics). The burette and the round bottom flask are connected by a rubber tube, as seen in Figure 45. The connection to the inert gas is sealed so that the released gas will move from the round bottom flask through the tube bubbling into the burette. The lowering volume of water from V1 (the starting point) to V2 (the new volume of water) is the volume of the hydrogen gas released from the solution. The reaction flask is set up under an inert atmosphere, and the tap adapter is used to purge some N_2 through the pipe before connecting to the burette. Also, the temperature was controlled using a PID-controlled isomantle with feedback from a K-type thermocouple immersed in the reaction solution. Figure 45 shows the setup for the hydrogen gas release experiment, and Figure 46 shows the sequence in which the temperature was ramped at 4 °C min^{-1} to 210 °C, held for 60 min, before cooling at 4 °C min^{-1} back to room temperature.

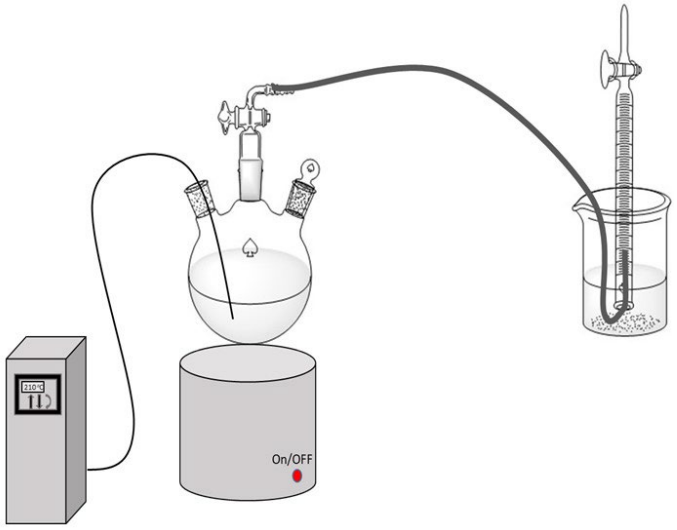

Figure 45: Setup of the gas volume experiment.

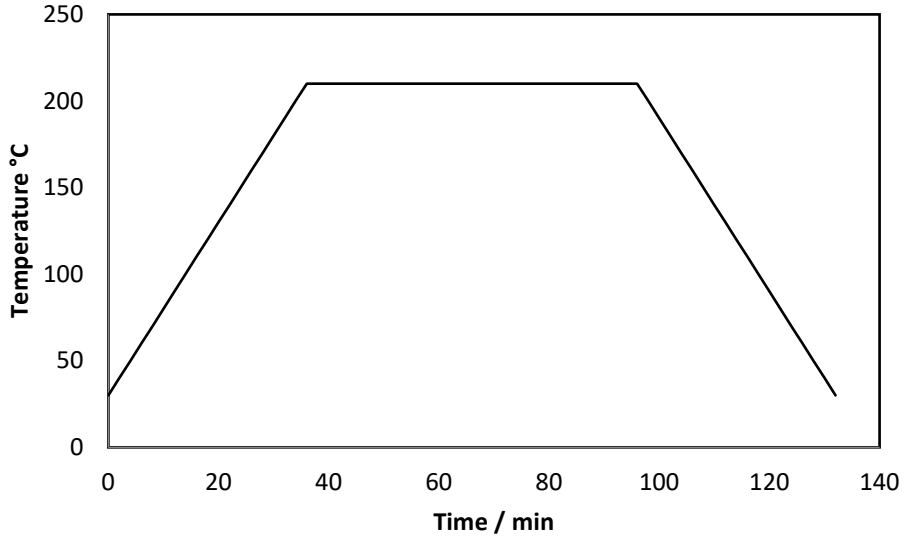

Figure 46: Temperature program used in gas release experiments. The temperature was ramped at 4 °C min^{-1} to 210 °C, and held for 60 min, before cooling at 4 °C min^{-1} back to room temperature

2.19 XRD

X-Ray Diffraction (XRD) was performed on a Bruker AXS D8 Advance with a Lynxeye Soller PSD Detector operated by by Mr. Oswald Gary. The source is a copper tube that produces a mixture of Kα (1 and 2) that have wavelengths of 1.5406 and 1.5444 Å, respectively. The diffractometer was run in Bragg-Brentano mode using variable slits, a nickel filter, and an automated sample changer. The slits were set at 6 mm. The collection range for 2θ was from 10 to 90 and the time was 17:17:50 (hh:mm:ss).

One-third of the nanoparticle dispersions produced in a typical reaction were placed on a sample holder (silicon wafer (100)-cut off orientation 9° towards (001), Sil'tronix Silicon Technologies, mounted in a plastic puck) by adding one drop and waiting for 15 min to ensure thoroughly dried before adding another drop. The sample was then submitted for analysis.

2.20 LB Trough

A Langmuir Blodgett trough (KSV NIMA) was used to measure the surface pressure isotherm of nanoparticle monolayers and for nanoparticle deposition. For the isotherm, 10 drops (of 30 mL of hexane that has NPs) of the nanoparticles were placed on top of UHP water (18.2 Ω) before using the KSV NIMA LB software to measure the isotherm. For deposition, a glass slide was used (Academy Microscope Slide), which was cleaned with tap water three times, soap (Decon 90, Lab Shop), ethanol, and UHP water (18.2 Ω)). The glass slide was inserted into the trough (around 2-4 mm protruding above the surface of the water), followed by placing the nanoparticles on the top of the surface. The software was used to move the barriers toward the glass slide. The surface pressure controller was used to stop the barriers at the appropriate pressure, and the sample was withdrawn at the required surface pressure (Pd = 20 mN m^{-1}, Ni = 30 mN $m^{-1,}$ and Cu = 40 mN m^{-1}). This method was used to form a monolayer; if multi-layers were required, the same processes were repeated.

Cleaning the LB trough parts was achieved by washing 15 times with tap water, soap (Decon 90 from Lab Shop), ethanol, and 15 times UHP water. The Wilhelmy plate was cleaned by soaking it in ethanol and flame annealing.

To test whether the LB trough was clean or not, the trough was filled with UHP water to the top of the trough; then, the Wilhelmy plate was placed on the surface, so the surface pressure was between 72.00 and 72.99 mN m^{-1}, as seen in Figure 47; finally, the barriers were set up to be closed at 30% speed. The final surface pressure was no more than 0.3 mN m^{-1} if the trough was sufficiently clean.

Nanoparticles in chloroform solution were placed using a pipette carefully onto the surface of the UHP water, always following sonication. They were spread evenly across the trough, as seen in Figure 47, and time (10 min.) allowed for all chloroform to evaporate before commencing any experiments.

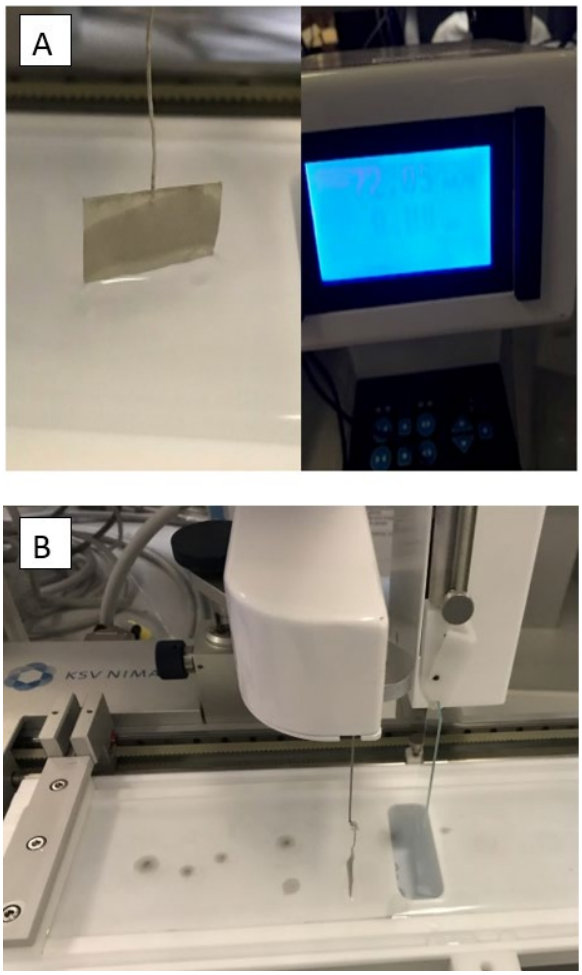

Figure 47: A: Wilhelmy on the surface of the water (left), the surface pressure monitor (right) 72.05 mN m^{-1}. B: Nanoparticles droplets on the surface of the water before the solvent evaporated and the NPs layer was formed on the top of the water surface.

2.21 Calculation of Nanoparticle Concentration (CNPs)

The calculation of nanoparticle concentration (C_{NPs}) was done following the method reported by Pikramenou *et al.*[3], assuming the model of a spherical nanoparticle. The *N* atoms in a spherical cluster have a relationship between cluster radius (R_c), Volume (V_c), surface area (S_c), atom radius (R_a), volume (V_a), and surface area (S_a), which can be described as follows.

First, the cluster volume can be known by multiplying the number of atoms in the atom's volume, Equation 1.

$$V_c = NV_a \tag{1}$$

The volume of the particle is that of a sphere, Equation 2.

$$volume\ (V_c)\ of\ a\ spherical\ shape = \frac{4}{3}\pi R^3 \tag{2}$$

Where *R* is the radius which is the distance from the centre to the edge.

Therefore, Equations 1 and 2 can be combined to give Equation 3.

$$\frac{4}{3}\pi R_c^3 = N\frac{4}{3}\pi R_a^3 \tag{3}$$

This can be rearranged further to give Equation 4.

$$R_c = N^{\frac{1}{3}}R_a \tag{4}$$

The surface area of the cluster can also be written as that of a sphere, Equation 5.

$$Surface\ area\ (S_c)\ of\ a\ spherical\ shape = 4\pi R^2 \tag{5}$$

The surface of the cluster in a similar way to the volume is given by Equation 6.

$$S_c = 4\pi {R_c}^2 = 4\pi\ (N^{\frac{1}{3}}R_a)^2 = 4\pi\ N^{\frac{2}{3}}\ R_a^2 \tag{6}$$

The number of surface atoms (N_s) in a cluster can be given by dividing the surface of the cluster by the cross-section of an atom, Equation 7.

$$N_s = \frac{4\pi N^{\frac{2}{3}} R_a^2}{\pi R_a^2} = 4N^{\frac{2}{3}} \tag{7}$$

To calculate *N*, R_c can be obtained from TEM, which is half the average diameter nm size, and R_a can be known from the literature value. Equation 4 can be rewritten as Equation 8.

$$N = (\frac{R_c}{R_a})^3 \tag{8}$$

After *N* becomes known, the number of surface atoms (N_s) of the cluster can be calculated from Equation 9.

$$N_s = 4N^{\frac{2}{3}} \tag{9}$$

Then, the number of atoms per cluster can be multiplied by the atomic mass (m_a) of a single atom to obtain the molecular weight of the cluster (M_w), Equation 10.

$$M_w = m_a \times N \tag{10}$$

The total number of atoms (N_t) can be divided by the number of atoms in the cluster (*N*) to obtain the number of clusters (N_c), Equation 11.

$$N_c = \frac{N_t}{N} \tag{11}$$

Where total number of atoms (N_t) is the number of moles in the whole sample multiplied by Avogadro's number, Equation 12.

$$N_t = No.mol \times Avogadro\ number \tag{12}$$

A-C.3.2 shows details of the calculation of Cu, Pd and Ni NPs.

2.22 Nanoparticle Coupling by EDC and/ or NHS and glass slide method.

NPs were deposited on the micro glass slide as reported earlier in the LB trough section and as can be seen in Figure 48. The coupling process was done by two different methods to find out which one can be used to best couple the Pd and Ni NPs. The Cu NPs were not used in the coupling section because of the interference on EDS (1-ethyl-3-(3-dimethylaminopropyl) carbodiimide hydrochloride) with TEM grids (also made of copper), making it harder to study the coupled particles.

The glass slide was soaked at room temperature for 30 min in an aqueous solution of 3-mercaptopropionic acid (3-MPA) (2-3 mg, 2.8 x 10^{-5} mol, >=99%, Sigma-Aldrich) to provide –COOH terminated surfaces, or in ethanol with 4-aminothiophenol (4-ATP) (2-3 mg, 2.4 x 10^{-5} mol 97%, Sigma-Aldrich) to provide -NH_2 terminated surfaces. Then, the glass slide was taken out of the solution and rinsed with ethanol to remove the excess of 3-MPA and 4-ATP. The ligand exchange was tested by using contact angle measurement, and Figure 49 shows a summary of the processes.

In the first method, the coupling of the amine with the acid was done by dissolving the NPs in an aqueous solution of EDC (7.6 mg, 4.0 x 10^{-2} mol, 98 + %, Alfa Aesar) and NHS

(N-hydroxysulfosuccinimide, 4.6 mg, 3.9 x 10^{-2} mol, 98 + %, Alfa Aesar) in water and stirring at room temperature for 6 h. Figure 50 illustrates the coupling processes.

In the second method, the coupling of the amine with the acid was done by dissolving the NPs with -COOH terminal in 10 mL pH 4 buffer (pH 4.01 Buffer Hannah instruments; deionized water, potassium hydrogen phthalate, amaranth red dye) with EDC (7.6 mg, 4.0 x 10^{-2} mol, 98 + %, Alfa Aesar) to make O-acylisourea, and adding an alkaline buffer to increase the pH to be between 7-8; about 20 mL (pH 10.01 Buffer Hannah instruments; deionized water, sodium carbonate, sodium bicarbonate, methylparaben, FD & C Blue) and then adding NHS (4.6 mg, 3.9 x 10^{-2} mol, 98 + %, Alfa Aesar) followed by the NPs with -NH_2 terminal groups and stirring at room temperature for 6 h. A summary of the second coupling method can be seen in Figure 51.

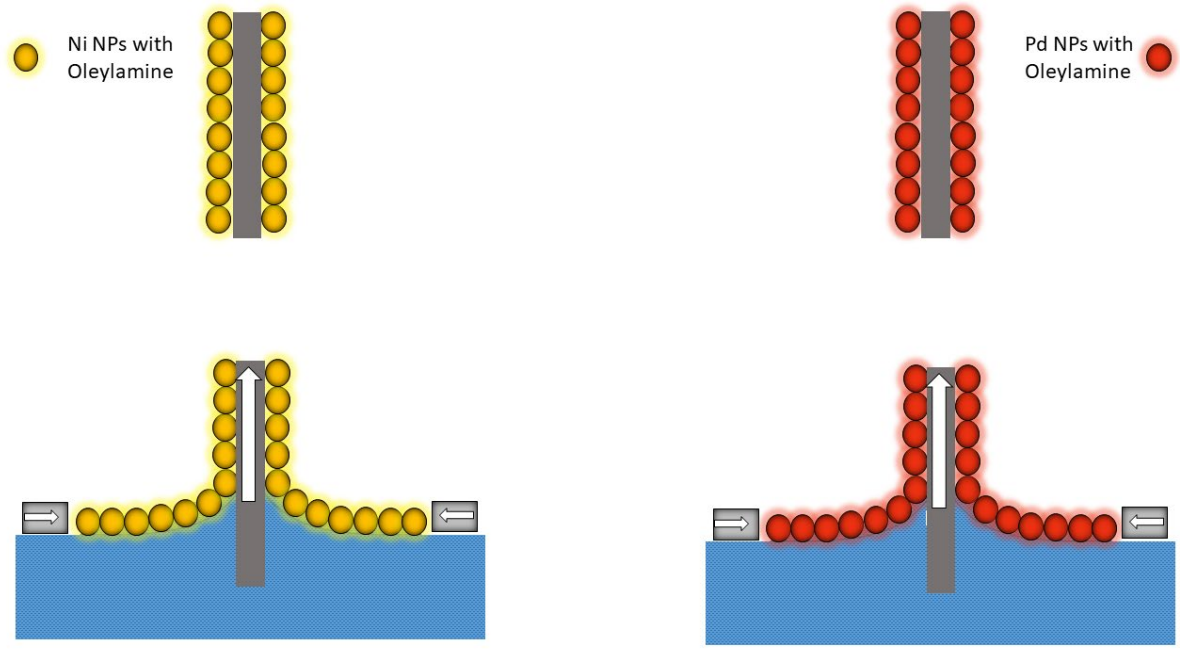

Figure 48: Deposition monolayer Ni (yellow–gold NPs on the left) and Pd (red NPs on the right) on a glass slide by using LB trough

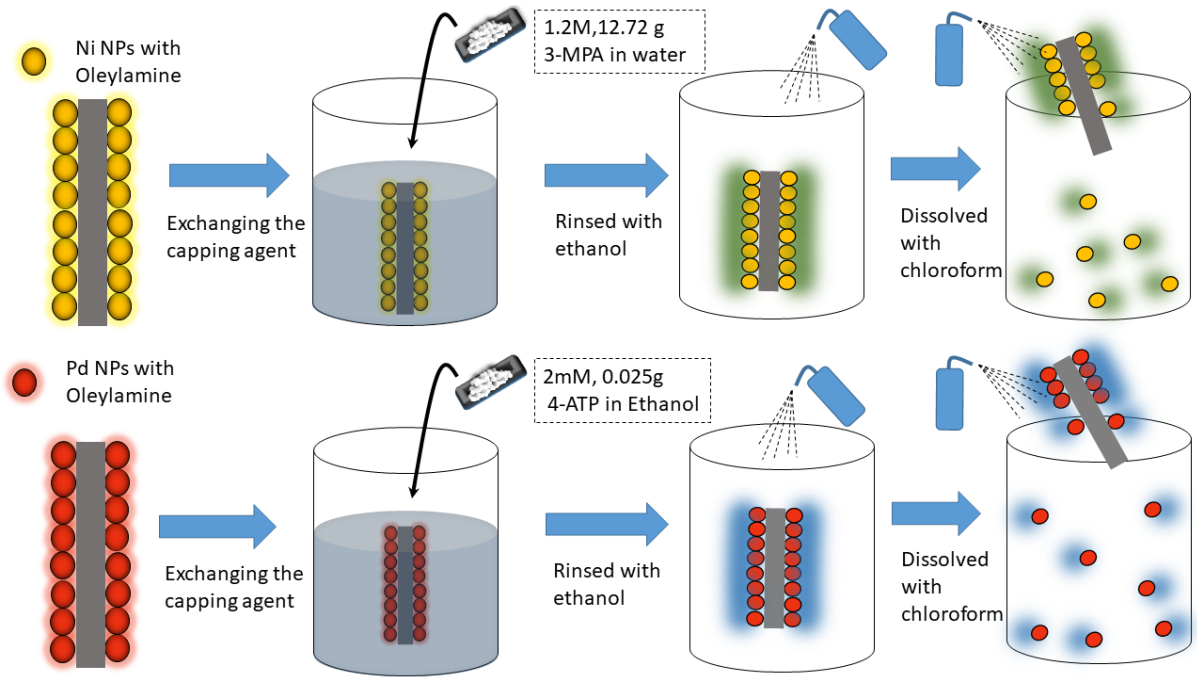

Figure 49: First method; The Ni glass slide was soaked in 3-MPA, and 100 ml water and then rinsed with ethanol before Ni NPs dissolved to another pecker by chloroform. The Pd glass slide was soaked in 4-ATP and 100 ml ethanol and then rinsed with ethanol before Pd NPs dissolved to another pecker by chloroform.

1st method

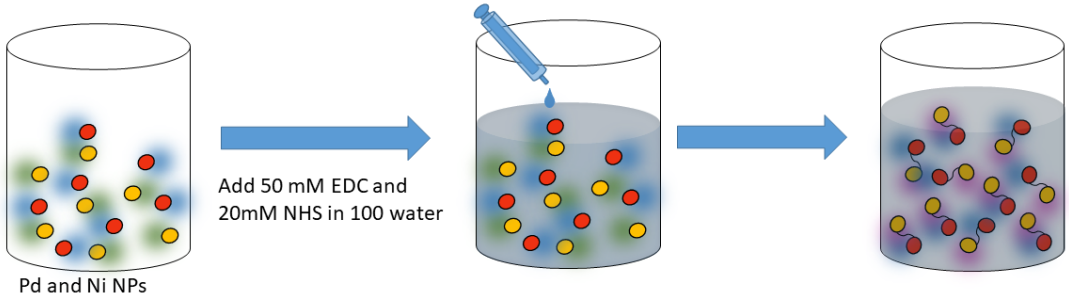

Figure 50. Pd NPs and Pd NPs coupled by adding 50mM EDC and 20nM NHS in H_2O.

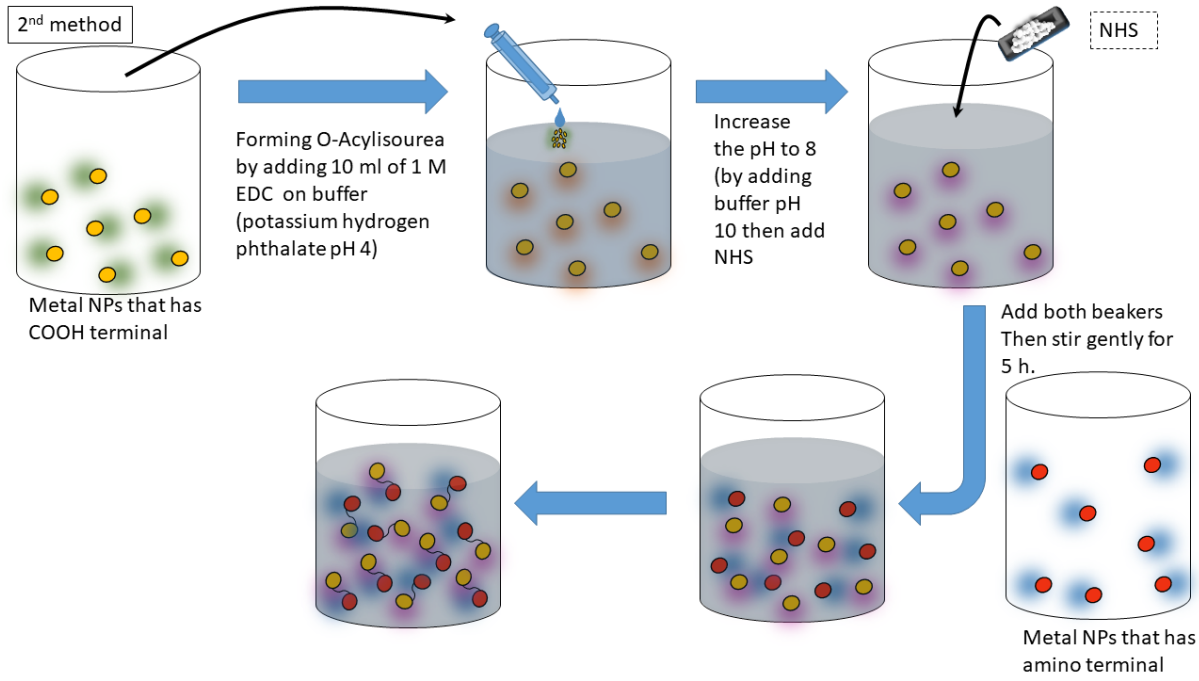

Figure 51: The Ni NPs treated with 3-MPA which makes the Ni NPs have -COOH terminal. The Ni NPs dissolved on 10 mL pH4 buffer, and then pH10 buffer was added to adjust the pH to 7-8 before adding the NHS and coupling to the Pd, which had been treated by 4-ATP to get -NH_2 terminal groups.

1. Mazumder, V.; Sun, S., Oleylamine-mediated synthesis of Pd nanoparticles for catalytic formic acid oxidation. *J. Am. Chem. Soc.* **2009,** *131* (13), 4588-4589.
2. Metin, O.; Mazumder, V.; Ozkar, S.; Sun, S. J. J. o. t. A. C. S., Monodisperse nickel nanoparticles and their catalysis in hydrolytic dehydrogenation of ammonia borane. **2010,** *132* (5), 1468-1469.
3. Lewis, D. J.; Day, T. M.; MacPherson, J. V.; Pikramenou, Z., Luminescent nanobeads: attachment of surface reactive Eu (III) complexes to gold nanoparticles. *Chem. commun.* **2006,** (13), 1433-1435.

Chapter 3 Synthesis of Ni Nanoparticles with average size 1.3 nm

3.1 Introduction

This chapter will focus on the synthesis of Ni NPs. The aim is to use a published method that uses the hot injection technique, long-chain amine hydrocarbon as a capping agent and amino boron complex as a reducing agent. Metin[1] synthesized 3.2 nm Ni NPs, and used this paper as a basis to study the synthesis of the size of Ni NPs and narrower particle size distribution.

3.2 The effect of changing the reducing agent on Ni NPs size

Synthesis of Ni nanoparticles was initially conducted following the method reported by Metin.[1] They reported that the size achieved was 3.2 nm, and the standard deviation was $1\sigma = 0.2$. Because the borane tributylamine complex is not commercially available, we used the borane tert-butylamine complex. The size distribution, where otherwise repeating Metin's method, was wider than what Metin achieved ($1\sigma = \pm 0.7$ vs 0.2 nm, as can be seen in Figure 52). The resultant Ni NPs had the same average size of 3.2 nm.

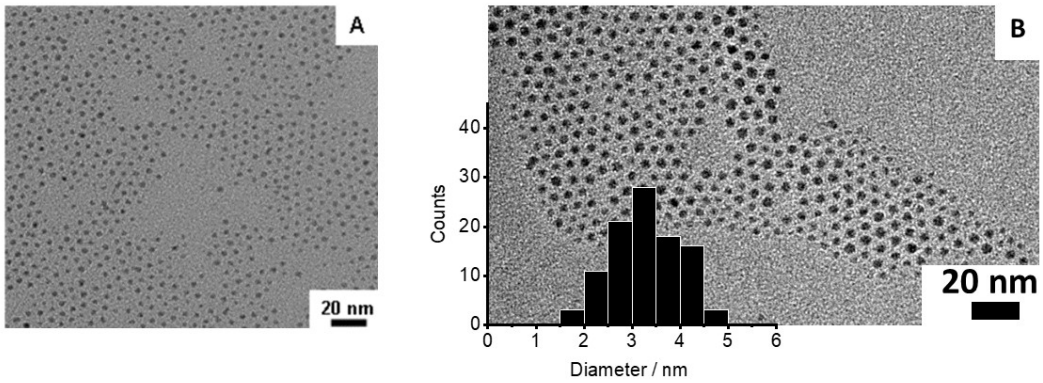

Figure 52: On the left (A), TEM images for 3.2 nm Ni NPs by Metin[1]. On the right (B), a TEM image and histograms for 3.2 nm Ni NPs synthesized following Metin [1], but with using tert-butylamine instead of tri-butylamine.

The size distribution was expected to be wider than the reported one by Metin[1,] and the reason for that is borane tert-butylamine complex decomposes around 125 °C, as can be seen in Figure 53. This did happen before and will be discussed in more detail in Chapter 5 with the synthesis of Cu NPs at 150 °C. For the copper synthesis, morpholine borane complex was the reducing agent, and the TGA shows the decomposition temperature is around 180 °C. The resulting Cu NPs from the reaction conducted below the decomposition temperature exhibited different sizes from those at temperatures above. Therefore, using borane tert-butylamine showed a similar result (compared to the resulted Cu NPs synthesized at 150°C) by having wider size distribution.

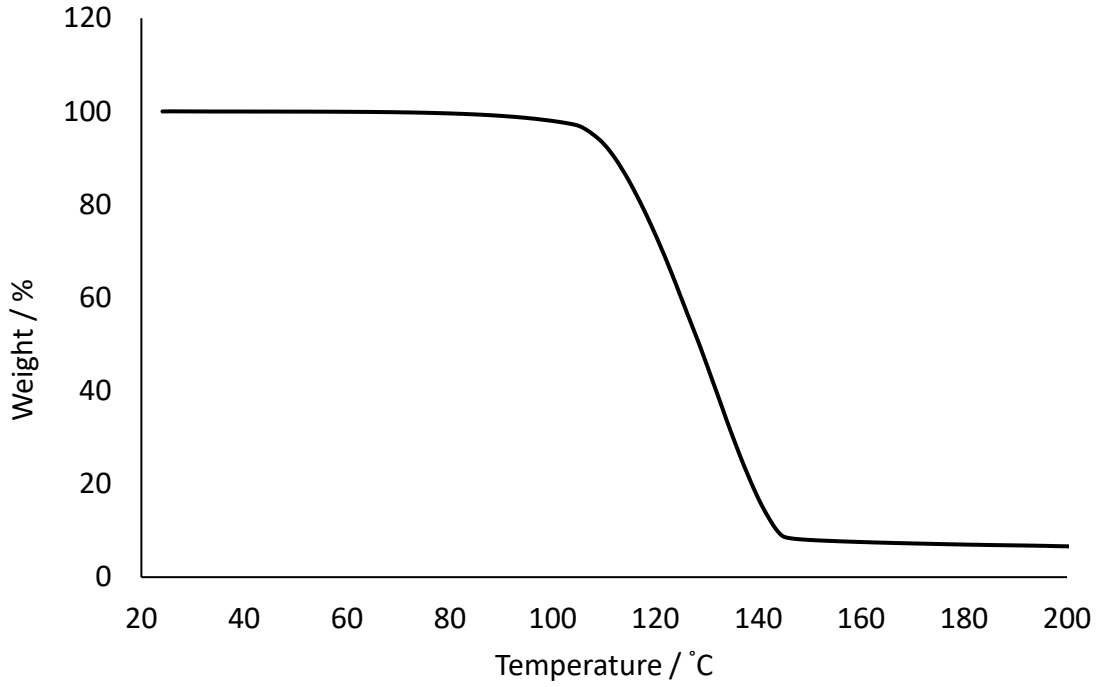

Figure 53: TGA of borane tert-butylamine complex in air and from room temperature to 200 °C. The ramp rate is 5 °C/min.

3.3 Studying the synthesis of Ni NPs at 110 °C

In the Metin report, they claimed the pre-heating of the oleylamine and precursor for 1 h at 110°C was for two reasons. Firstly, to form the Ni-oleate complex (they did not show any evidence for the formation, except noting the solution changed colour to "a nice green"). They also do not confirm the structure they envisage. The second reason given is "removing the humidity and oxygen from the solution," and for that reason, they claimed 1 h at 110 °C is needed. As will be shown, this 110 °C pre-treatment step plays a major role in the synthesis, and for that reason, this chapter will discuss how the size and the size distribution were decreased from 3.3 and $1\sigma = \pm 0.7$ to 1.3 and $1\sigma = \pm 0.4$ by variation of this step.

3.4 Investigation the 110 °C step.

As the literature report had indicated, 110 °C was needed to remove water and oxygen. This was investigated by observing the degassing during this reaction stage visually. During the reaction, it was noticeable that with increasing the temperature, the removal of the dissolved gases from the solution can be seen as forming of bubbles on the surface of the solution. Therefore, one hour at 110 °C worked to remove at least dissolved gases from the solution (as they claimed) because no more bubbles could be seen after 45-55 min at 110 °C. A summary of removing the dissolved gases from the solution can be seen in Figure 54. It is less likely that this removes all moisture from the solution as suggested initially because common primary amines form azeotropes with water (*e.g.* butylamine).[1]

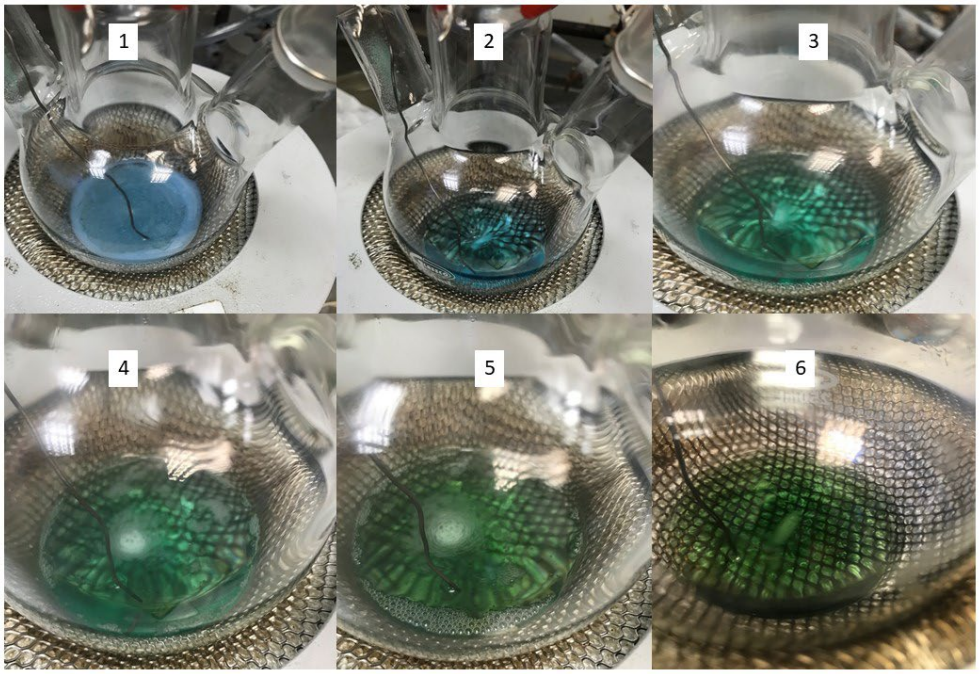

Figure 54: A solution of $Ni(acac)_2$, oleic acid and oleylamine stirred together at room temperature (image 1) and after the temperature was increased to 110°C before the injection of the reducing agent. The image 2 was taken at 50°C, image 3 at 90°C, image 4 at 110°C, image 5 at 110 °C after 30 min and image 6 at 110 °C after 45 min.

3.5 Comparison by TEM of nanoparticles resulting from different pre-equilibration protocols of nickel precursor, oleic acid and oleylamine before the reduction step

As described above, following Metin's method and using borane tert-butylamine complex led to particles with an average diameter of 3.2 nm and the size distribution of 1 σ = ± 0.7, as can be seen in Figure 55b. Different sizes of Ni NPs from the same sample (*e.g.* this method forms 1 nm Ni NPs and 4 nm Ni NPs) can affect the catalytic testing in future applications and would be desirable to avoid. Understanding the mechanism in general and the role of the pre-equilibration and inclusion of oleic acid was hoped to lead to improvements in the synthesis of Ni NPs. The TEM images were obtained from the same reaction mixture but following nanoparticle synthesis at 90 °C after three different equilibration procedures:

- reaction heated to 90 °C, then reducing agent added (protocol 1), NP yield by Ni% 40 ± 2.1%;.;
- reaction heated to 110 °C for 1 h, then cooled to 90 °C, then reducing agent added (protocol 2 – the one reported in the literature), NP yield by Ni% 41 ± 1.6%;.;
- reaction heated to 110 °C and kept overnight before cooled to 90 °C, then reducing agent added (protocol 3), NP yield by Ni% 47 ± 1.9%;.

The changing of solution colour of the Ni $(acac)_2$ also varied between these three procedures, as shown in Table 1.

Table 1: The three different equilibration procedures with the time that was needed to notice the change of the colour after the injection of the amine-borane complex.

Protocol	Speed of colour change on injection of amine-borane complex reducing agent
1. Heat to 90 °C, then reduce	~ 15 min
2. Heat to 110 °C for 1 h, then cool to 90 °C and reduce	5-6 s
3. Heat to 110 °C overnight, then cool to 90 °C and reduce	Immediate

The average particle size for the reduction at 90 °C (protocol 1) and after 1 h at 110 °C (protocol 2) is almost the same (3.5 and 3.3 nm; respectively), but the distribution of the resultant NPs after pre-equilibration at 110 °C was narrower than the distribution without (protocol 1), as can be seen in Figure 55 (a-b). Interestingly, the size and the size distribution

of the Ni NPs from the third reaction protocol (kept at 110°C overnight) both decreased to 1.3±0.4 nm, which can be seen in Figure 55 (c).

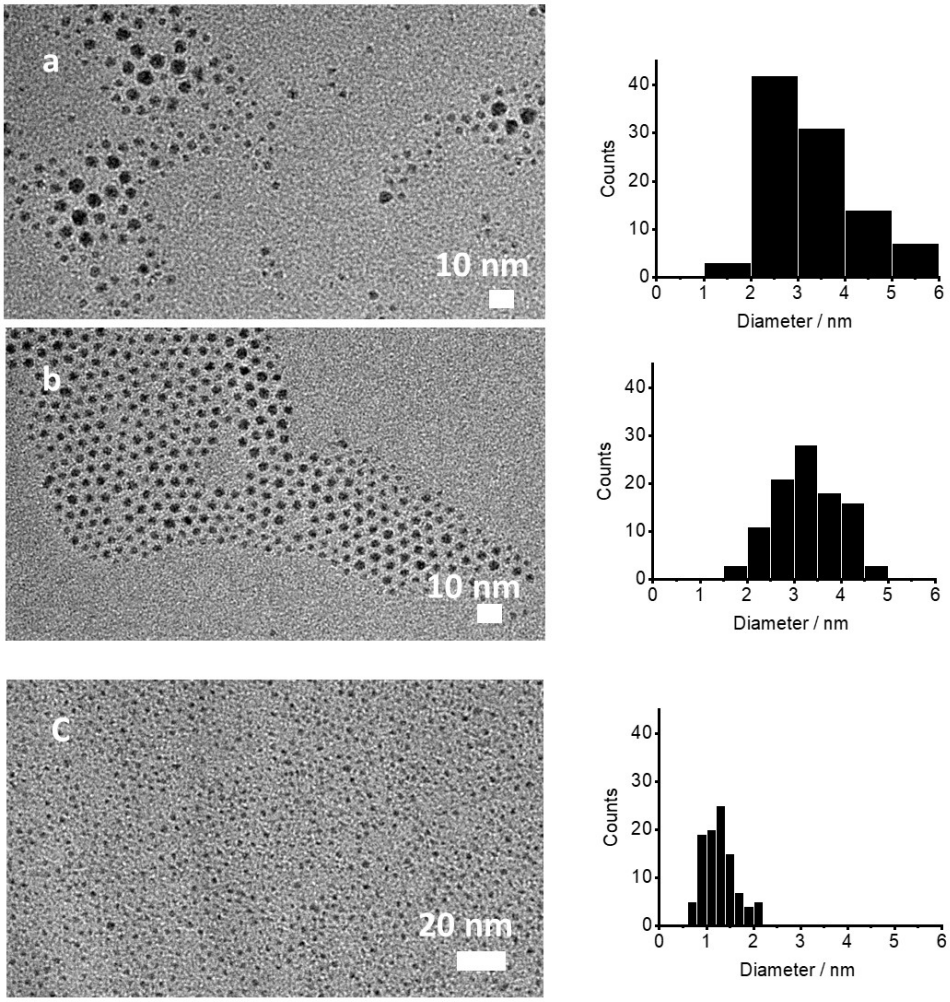

Figure 55:TEM images on the left side and histograms on the right side a) Typical TEM image and distribution quoted as ± 1σ of 3.5 ± 1.3 nm of Ni NPs. The injection of the reducing agent was at 90 °C, then the reaction was held at 90 °C for 1 h before being cooled to room temperature; b) TEM image and distribution quoted as ± 1σ of 3.3 ± 0.7 nm of Ni NPs. The solution was kept at 110 °C for 1 h before injection of the reducing agent at 90 °C; then the reaction was held at 90 °C for 1 h before being cooled to room temperature (based on prior literature method); c) TEM image and distribution quoted as ± 1σ of 1.3 ± 0.3 nm of Ni NPs. The solution was kept at 110 °C overnight before injection of the reducing agent at 90 °C; then the reaction was held at 90 °C for 1 h before being cooled to room temperature. Particle counts are of a minimum of 100 particles.

The preliminary hypothesis to explain this data was that at the point the reducing agent is injected in the first protocol, the precursor is still mostly $Ni(acac)_2$; the second protocol has a mix of $Ni(acac)_2$ and another species, “Ni-oleate” and the third protocol is conducted when the mixture has fully converted to a second species.

This would explain why the sample held at 110 °C overnight before the injection of the reducing agent produced a uniform size and smaller size distribution (c) if the reduction rate of the second species was fast enough to achieve “burst nucleation” as described in the LaMer model in the literature.[2]

In contrast, the broader distribution in the other samples could be because two (or more) Ni species are present, and their reduction rates differ, resulting in slower particle nucleation (as seen in Figure 56 the speed of the colour changes in . The Ni complex is blue, and the blue colour turns green with time and temperature increase. Ni oleate has a light green colour (as reported in literature[3]), which is perhaps what we are forming during the reaction. Metin’s report claimed that the conversion to a “nice green” resulted from oleate formation but included no evidence.[1] A summary of the colour changing of the solution during the reaction can be seen in Figure 56 a proposed reaction path for the different-sized nanoparticles resulting from different synthesis protocols.

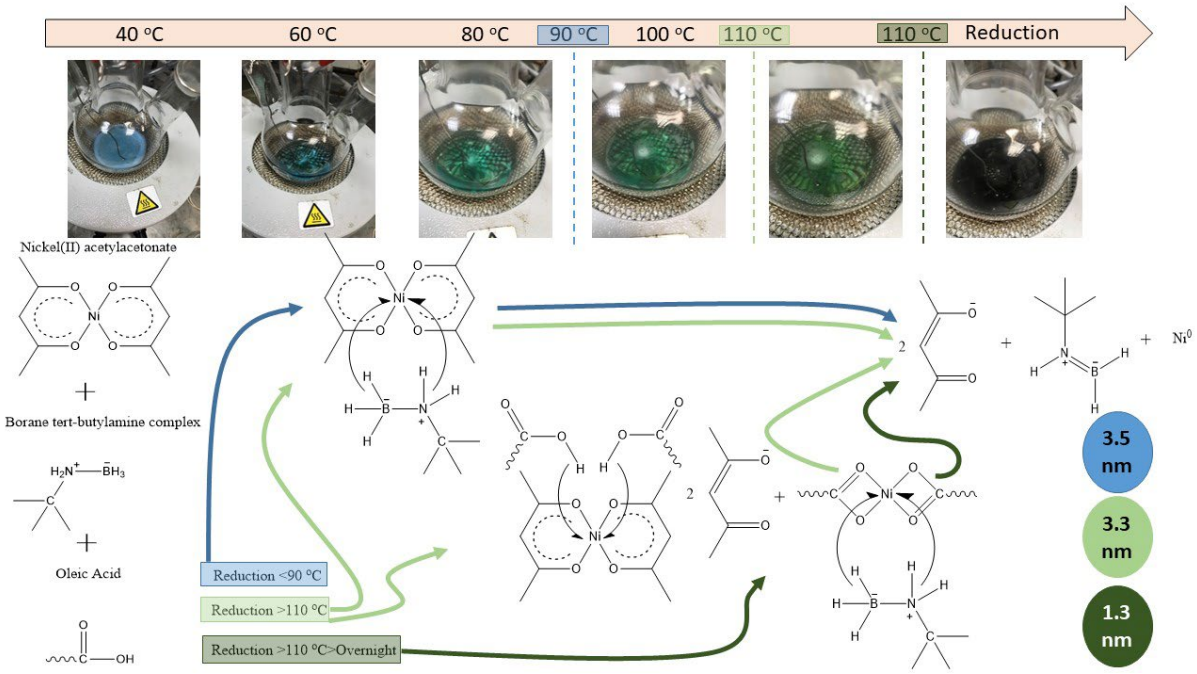

Figure 56: The change in the colour from the top-left flask to the top-right flask shows the increase in the temperature from 40 °C to 110 °C. The colour changes from blue to green. On the last flask on the top right, the solution turns to black after the injection of the BTB (reducing agent) and oleylamine into the solution. The blue arrow shows the pathway for the synthesis of 3.5 ± 1.3 nm Ni NPs. The light green arrow shows the pathway for the synthesis of 3.3 ± 0.7 nm Ni NPs. The dark green arrow shows the pathway for the synthesis of 1.3 ± 0.4 nm Ni NPs. (Distribution quoted as ± 1σ)

Therefore, based on the idea above that the different metal precursors will have different reduction rates, a proposed mechanism is shown in Figure 57.

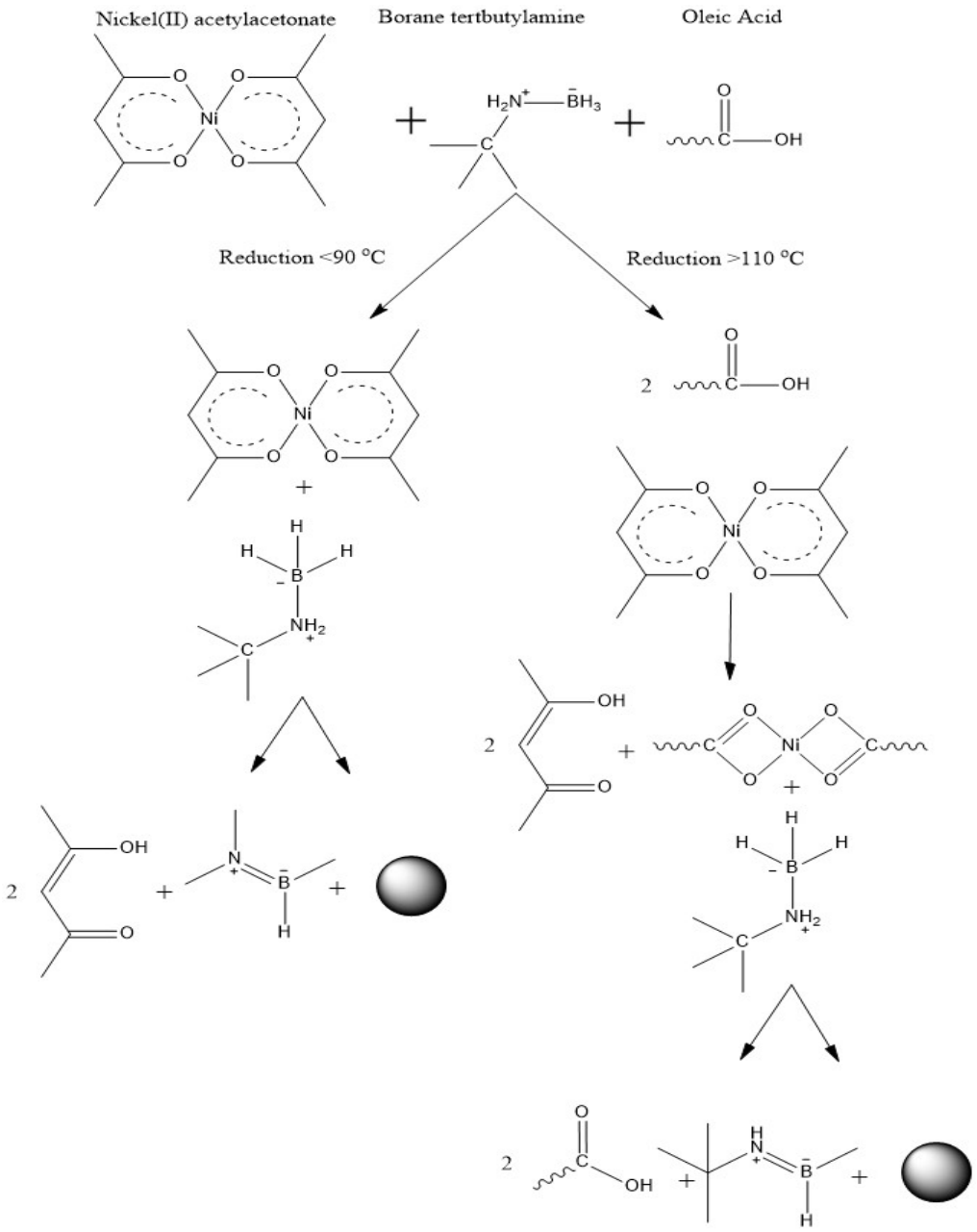

Figure 57: The proposed mechanism of Ni NPs synthesis.

It is helpful to consider the possible roles of oleylamine and oleic acid in this mechanism. The first point is the *in situ* formation of Ni-oleate or a second nickel precursor before reduction, which has been mentioned above. The synthesis in this chapter was adopted from Metin *et al*. who claimed the use of $Ni(acac)_2$, oleylamine and oleic acid[1]

enabled the transformation of the $Ni(acac)_2$ to $Ni(oleate)_2$ at 110 °C for 1h. However, no evidence for this assertion was given. A study by Yin *et al.* on the fate of $Pt(acac)_2$ in oleylamine and oleic acid used the analogy between butylamine and oleylamine to overcome the difficulty of analyses involving oleylamine. They found that the transformation of $Pt(acac)_2$ to $[Pt(amine)_4]^{2+}$ $2(acac^-)$ occurred when only amine was present, but $[Pt(amine)_4]^{2+}$ $2(carboxylate^-)$ was obtained in the presence of the acid.[4] This observation clearly poses the question of what happens in the case of nickel with oleylamine and oleic acid. This approach is not possible in the present case due to the higher synthesis temperature (well above the boiling point of short-chain acids and amines). At temperatures near the boiling point of butylamine and propionic acid, the expected colour changes seem at 110 °C are not seen.

Wenbo Bu *et al.* proposed that oleylamine enhances the formation of carboxylate anion, which coordinates strongly to the metal surface as a size/growth controlling agent (in their case, on selected facets).[5] To form the oleate, an oleylamine or any long-chain amine must be present to deprotonate the carboxylic acid.

3.6 Monitoring the transformation of the Ni precursor by UV-Vis

The sampling of the UV-vis samples was done while the pre-equilibrating mixture of $Ni(acac)_2$, and oleylamine, with or without oleic acid, was heated from 25 to 110 °C (without programming the temperature probe) then the reaction was kept at 110 °C overnight. The time, reaction mixture, and the temperature can be seen in Table 2 and Table 3.

Table 2: Sampling the UV-vis samples at different times and temperatures. The reaction mixture is oleic acid, oleylamine and $Ni(acac)_2$. (NA means the sampling was done before the timing start which starts after the solution reaches 100 °C)

Sample	Time (hh:mm)	Hours	Temperature/ °C
MYA-1	NA	NA	60
MYA-2	NA	NA	90
MYA-3	NA	NA	110
MYA-4	12:45	1	110
MYA-5	01:45	2	110
MYA-6	02:45	3	110
MYA-7	03:45	4	110
MYA-8	04:45	5	110
MYA-9	09:20	21	110
MYA-10	10:20	22	110
MYA-11	11:20	23	110
MYA-12	12:20	24	110
MYA-13	01:20	25	110
MYA-14	02:20	26	110
MYA-15	03:20	27	110
MYA-16	04:20	28	110
MYA-17	05:20	29	110

Table 3: Sampling the UV-vis samples at different time and temperature. The reaction mixture is oleylamine and $Ni(acac)_2$. (NA means the sampling was done before the timing start which starts after the solution reaches 100 °C)

Sample	Time hh:mm	Hours	Temperature/ °C
MYA-1-Ni-NoOA	NA	NA	60
MYA-2-Ni-NoOA	NA	NA	90
MYA-3-Ni-NoOA	NA	NA	110
MYA-4-Ni-NoOA	11:20	1	110
MYA-5-Ni-NoOA	12:20	2	110
MYA-6-Ni-NoOA	01:20	3	110
MYA-7-Ni-NoOA	02:20	4	110
MYA-8-Ni-NoOA	03:20	5	110
MYA-9-Ni-NoOA	04:20	6	110
MYA-10-Ni-NoOA	05:20	7	110
MYA-11-Ni-NoOA	11:20	24	110
MYA-12-Ni-NoOA	12:20	25	110
MYA-13-Ni-NoOA	01:20	26	110
MYA-14-Ni-NoOA	02:20	27	110
MYA-15-Ni-NoOA	03:20	28	110
MYA-16-Ni-NoOA	04:20	29	110
MYA-17-Ni-NoOA	05:20	30	110

3.7 Physical properties of the mixture that has oleic acid.

Oleylamine has a melting point of 15-22 °C (according to the manufacturer Acros Organic). The first three samples (MYA-1, MYA-2 and MYA-3) turned to a solid gel (at room temperature - RT) after they were taken from the solution. The rest of the samples (MYA-4 tell MYA-18) were liquid at RT, as can be seen in Figure 58-Figure 60. All samples were taken by syringe from the solution that is under N_2 and placed on 20 mL vials under air.

Also, the colour of the samples varied. The colour trend starts from light blue to light green. The first three samples have light blue colour (MYA-1 – MYA-3). Then, the second

five samples have a light blue-green colour (MYA-4 – MYA-8). The rest of the samples have a light green colour (MYA-9 -MYA-18), as can be seen in Figure 58 -Figure 62.

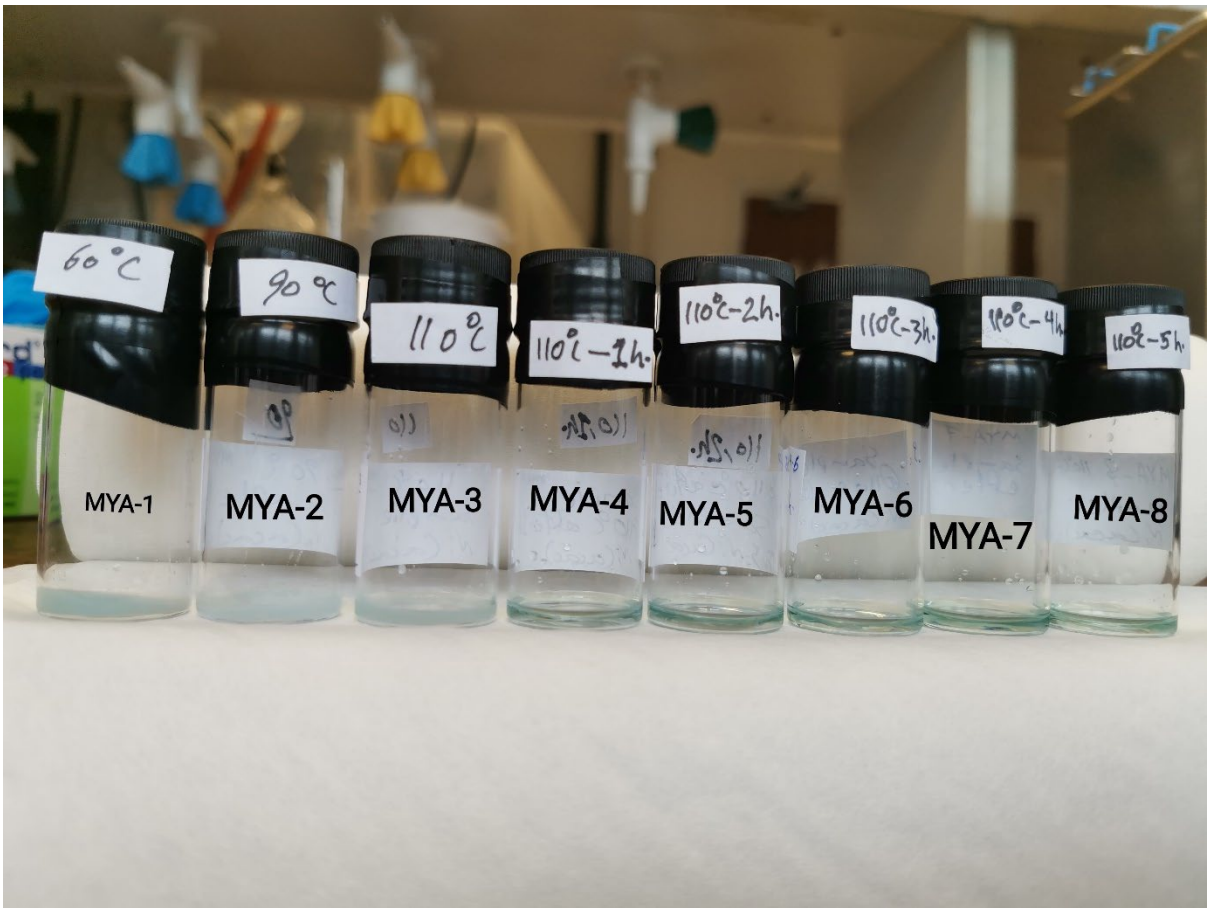

Figure 58: Photograph of samples taken from the solution (MYA-1 to MYA-8) at different temperatures and without dilution in chloroform, showing the trend in solidification of samples (MYA-1 – MYA-3).

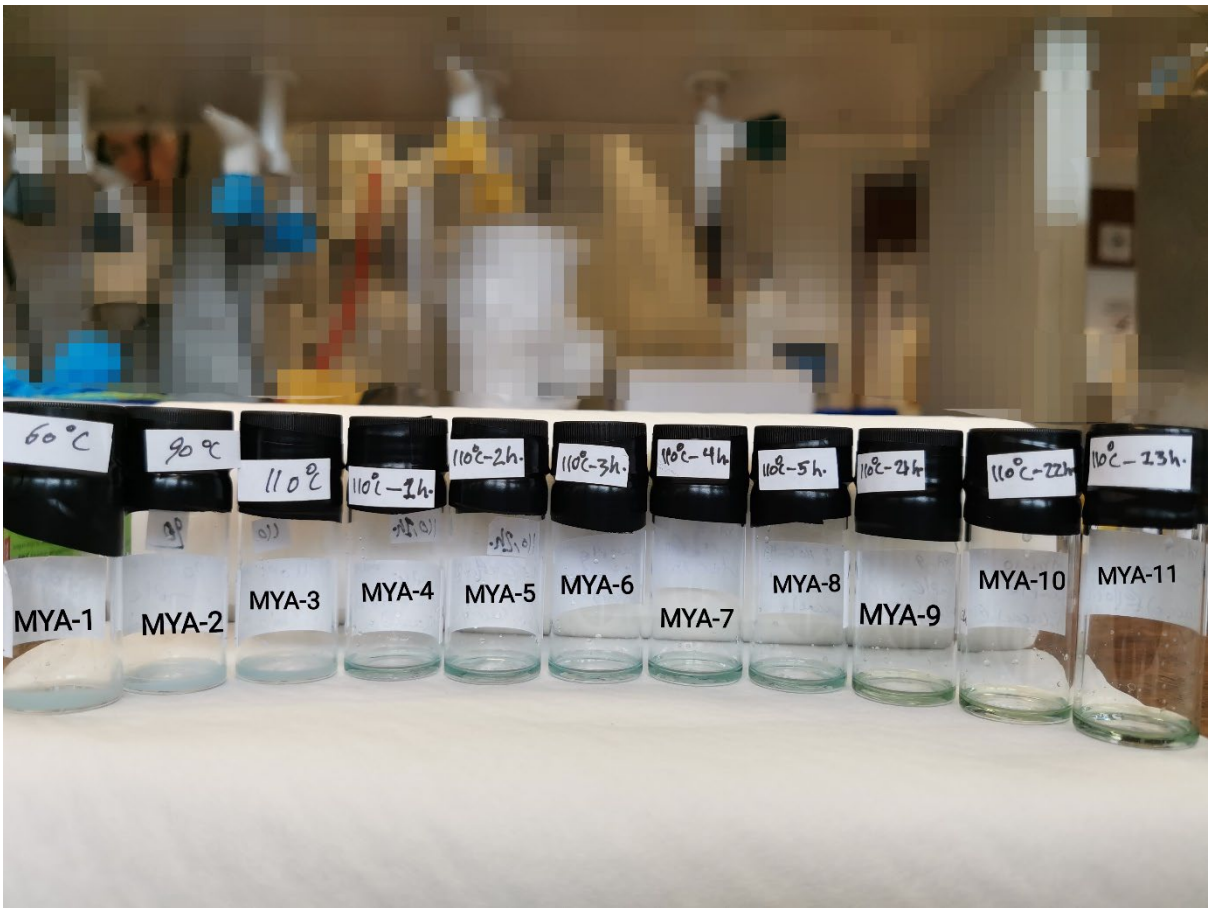

Figure 59: Photograph of samples taken from the solution (MYA-1 to MYA-11) at different temperatures and without dilution in chloroform, showing the trend in solidification of samples (MYA-1 – MYA-3). The change in the colour from the first sample MYA-1 to MYA-11. The time between them is 23 hours. The colour can be seen changing from light blue to light green. (Taken from the solution at a different temperature, without dilution in chloroform).

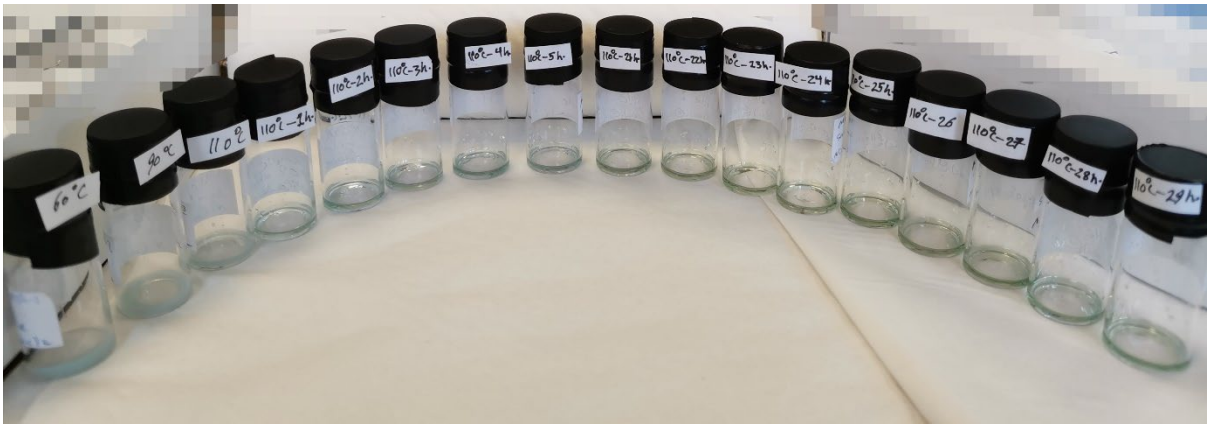

Figure 60: Photograph of samples taken from the solution (MYA-1 to MYA-17) at different temperatures and without dilution in chloroform. These samples were used for UV-vis.

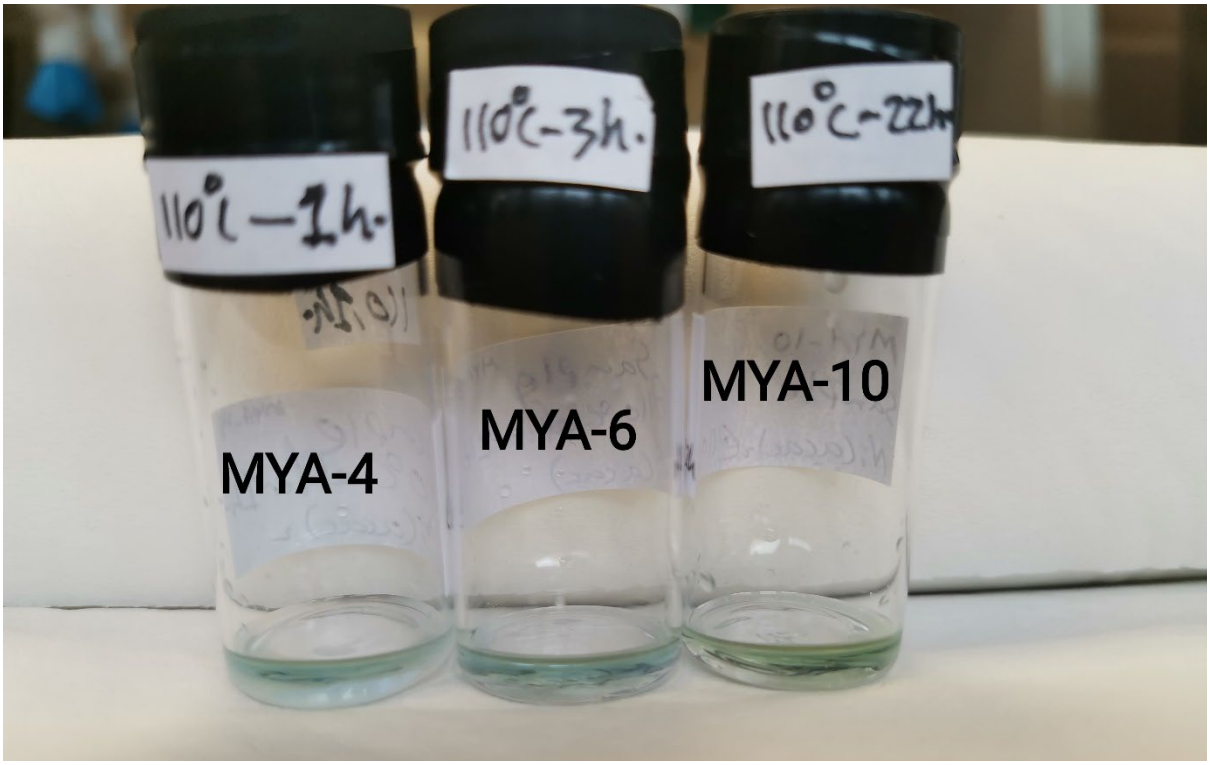

Figure 61: Photograph of samples taken from the solution (MYA-4, MYA-6 and MYA-10) at different temperatures and without dilution in chloroform. The change in the colour between samples was taken from the experiment after 1, 3 and 22 hours. (Taken from the solution at a different temperature, without dilution in chloroform).

Figure 62: Photograph of samples taken from the solution (MYA-4 to MYA-8 labelled the same day, and MYA-9 to MYA-13 labelled the next day). The trend of the colour in the samples that were taken on the same day that experiment was started and the samples on the next day. (Taken from the solution at a different temperature, without dilution in chloroform).

3.8 Physical properties of the mixture that does not have oleic acid.

The preparation of samples without using oleic acid was needed to understand the role of oleic acid when it is present in the reaction (the previous section). All the samples turned to a solid gel after they were taken from the reaction mixture, can be seen in Figure 63.

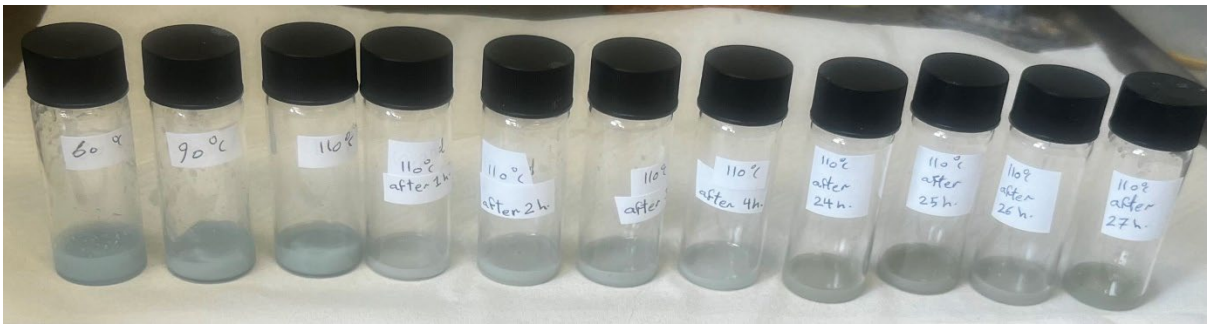

Figure 63: All the samples that were taken for UV-vis from the reaction mixture at different temperatures. (Taken from the solution at different temperatures, without dilution in chloroform).

The change in colour after the first three samples (with oleic acid Figure 58 and Figure 59) shows that even just heating to 110 °C does change the structure. Furthermore, the gel-like solid with oleylamine as solvent has a different interaction which changes the melting point.

3.8.1 Bound ligand vs free ligand

The Ni -containing solution has a number of different possibilities of ligand-Ni combinations, as several species could act as ligands and therefore be bound or free. The potential ligands are $acac^-$, oleylamine, oleic acid, oleylamine+acacH and oleylamine+acacH+oleic acid. To be clear about the differences between these ligands' transitions in the UV region, we will discuss them each in turn.

First, $acac^-$ being bound to the metal centre (*e.g.* $Ni(acac)_2$) has been reported to have different positions of the transitions depending on the solvent that was used due to the exchange between anhydrous trimer (in which there are bridging and non-bridging ligands) and solvent co-ordinated monomer.[6] Therefore, we will consider the position of transition that can happen in the presence of chloroform solvent used for the UV-vis analysis. Even though the presence of the oleylamine and oleic acid could alter the position, due to the lack of information on such a solvent system, we will just consider the

chloroform.[6] $Acac^-$ bound to Ni in $[Ni(acac)_2]_3$ in chloroform solvent appears as two peaks in the UV region.[6] One at ~260 nm and the other one (weaker) at 300 nm. This is attributable to the fact that the acac ligand is in both bridging and non-bridging co-ordination modes (the trimer structure is shown in Figure 64). In contrast, $Ni(acac)_2$ in methanol solvent (likely $Ni(acac)_2.2CH_3OH$) appears as a single peak at 300 nm (the structure of $Ni(acac)_2L_2$ is shown in Figure 64).[6] Hacac as a free species (protonated $acac^-$ ligand) has a single peak at 274 nm for the π -π^*.[7]

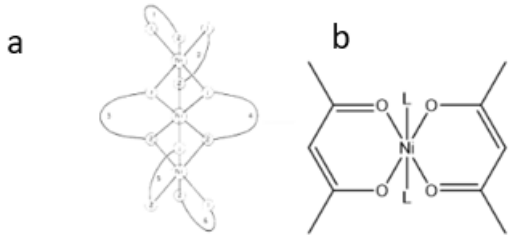

Figure 64: a) The trimer structure of the bis-(2,4-pentanediono)-nickel(II); Reproduced with permission from ref [6] (Copyright 1961 American Chemical Society); b) The structure of $Ni(acac)_2 L_2$.

Second, Oleylamine being bonded to a metal centre has been reported to the case of platinum rather than Ni (*e.g.* $Pt(acac)_2$ where the ligand has been displaced), has a single peak that appears at 274 nm.[7] Oleylamine as a free ligand appears as a single peak at 226 nm.[8] Oleylamine reacted with acacH has two peaks which appear at 274 and 312 nm.[7]

Finally, oleic acid being bound to a metal centre (*e.g.* again using example reported for displacement at $Pt(acac)_2$) has a single peak that appears at 312 nm.[7] Oleic acid as a free ligand has a peak that appears at 234 nm.[8] Oleic acid bound to oleylamine has a peak that appears at 237 nm.[8] Oleic acid bound to oleylamine and acacH has a peak that appears at 312nm.[7]

3.8.2 Using oleic (with) vs without using oleic acid (without)

UV-Vis-NIR were obtained both from the samples that come from the reaction mixture that has oleic acid and from the reaction mixture that does not have oleic acid for

comparison. The UV-Vis-NIR spectra in Figure 65-Figure 67 (each showing different wavelength regions) show the reaction between $Ni(acac)_2$ and oleylamine with/without oleic acid.

In the UV region, Figure 65 , for the sample without oleic acid there is a clear difference between 1 h and overnight. After 1 h, three peaks can be seen at 255, 263 and 270 nm. On the other hand, once left overnight four peaks which can be seen at 255, 263, 270 and 298 nm. The peak appearing at 298 nm is consistent with the peak reported[6] for $Ni(acac)_2$ in chloroform solvent as π -π^*C=C of the bond $acac^-$. The absence (or at least very weakened nature) of this peak (at 1 h) is surprising as both the dehydrated trimer and the axially ligated nickel monomers have a feature around 300 nm. This must mean the Ni complex is in a different structural form. Given the feature that is present more strongly in the 1 hour sample (~255 nm) is most similar to the bridging mode acac in the trimer, speculatively the species at 1 h could be oligomeric and therefore dominated by bridging acac. While such a structure is not reported, this could be a function of structural studies predominantly using X-ray crystallography as such species do not crystalize as readily as the individual molecular species. The sample held overnight then interacts with oleylamine or water to become the axially ligated nickel monomer with the dominant 298 nm band in the UV-vis. Time-dependent density functional theory (TD-DFT) modelling of the UV vis spectra would be required to investigate this point further. The absence of the peak at 312 nm indicates that oleylamine and $acac^-$ did not form acac-oleylamine.

When oleic acid is present, after 1 h, three peaks can be seen which are at 270, 278 and 311 nm. Overnight, three similar peaks can be seen at 271, 280 and 312 nm, albeit with slightly different intensity ratios. Compared to the “without OA samples” the spectra are quite different with loss of the features at 255, 263 and 298 nm and the presence of new peaks at 280 and 311 nm. These appear to shift slightly to higher wavelengths in the overnight sample. The peak at 311 nm agrees with the value reported in the literature[4] for free amino ketone π -π^* (acac-oleylamine) and also the value for bound oleate. The reaction of oleylamine and acac is sensible given the formation of this species is likely acid catalyzed

and thus promoted by the presence of oleic acid (as is later confirmed by ASAP MS). The peak at 280 nm is not that intense, and corresponds to none of the species in free solution, so likely is the result of a bound species such as the acac-oleylamine. The peak at 270 nm is consistent with metal bound oleylamine.

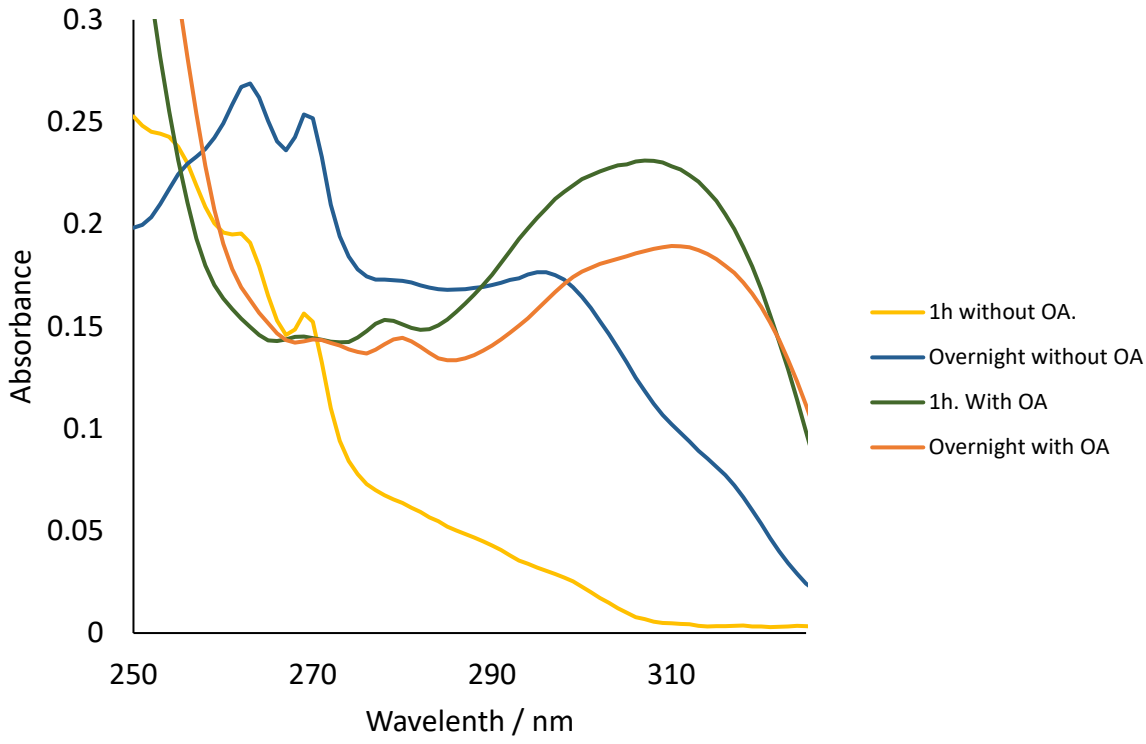

Figure 65: UV spectra for UV region of $Ni(acac)_2$ preheated solution (at 110 °C) with oleylamine and with/without oleic acid.

The visible region, Figure 66 , does not change significantly over time, but there is a distinct difference in the position of the most prominent feature from 587 nm without oleic acid to 618 nm with oleic acid. These are in the region typical of d-d transitions. The transition is notably weaker in intensity for the samples with oleic acid, possibly indicating a more centrosymmetric environment. For sample with and without oleic acid samples, there is an increase in intensity after overnight reaction at ~475 nm that is not present after

1 hour, a shoulder in the without OA case and a small peak in the with oleic acid case. This change is the same as the colour change seen visually upon aging overnight.

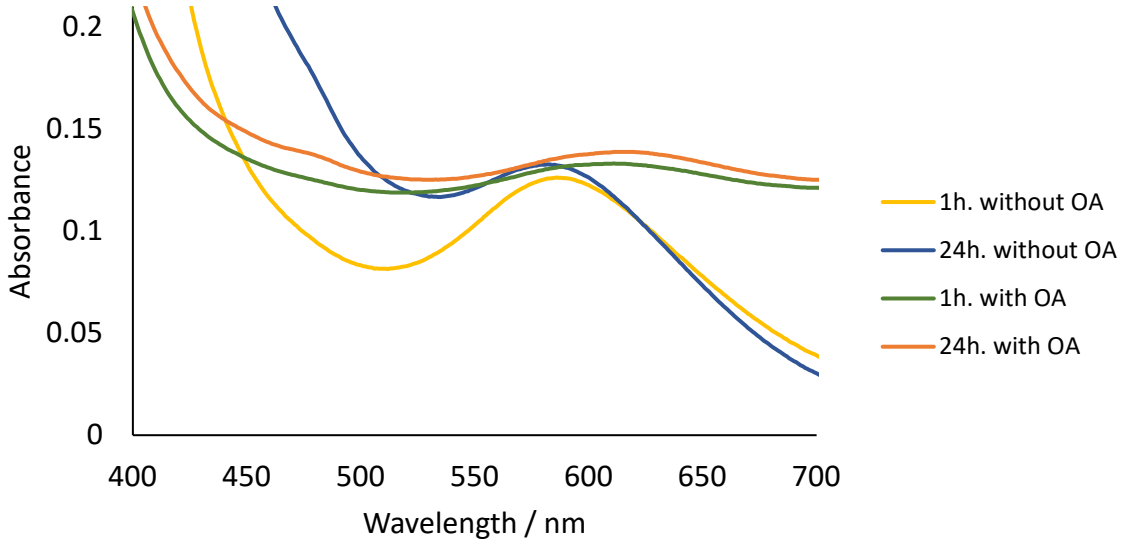

Figure 66: UV spectra for Vis region of $Ni(acac)_2$ preheated solution (at 110 °C) with oleylamine and with/without oleic acid.

The NIR region, Figure 67, shows that without oleic acid (at either time), there is a small peak at 722 nm, whereas with oleic acid (again at either time), there is a peak at 765 nm. Again these likely correspond to d-d transitions, although the 722 nm peak is quite sharp, suggesting it may be a ligand transition rather than a d-d transition. It is possible that the d-d transitions shift quite substantially – for an octahedral form (as most of the species here are expected to be based on the literature of Ni compounds of this type), the change from water to ethylenediamine for example changes the peaks from 400, 700 and 1100 nm to 350, 550 and 875 nm.[9] With the range of the spectrometer and the large intensity features at low wavenumber in the ligands it is hard to reliably index which transition is which without undertaking computational simulations.

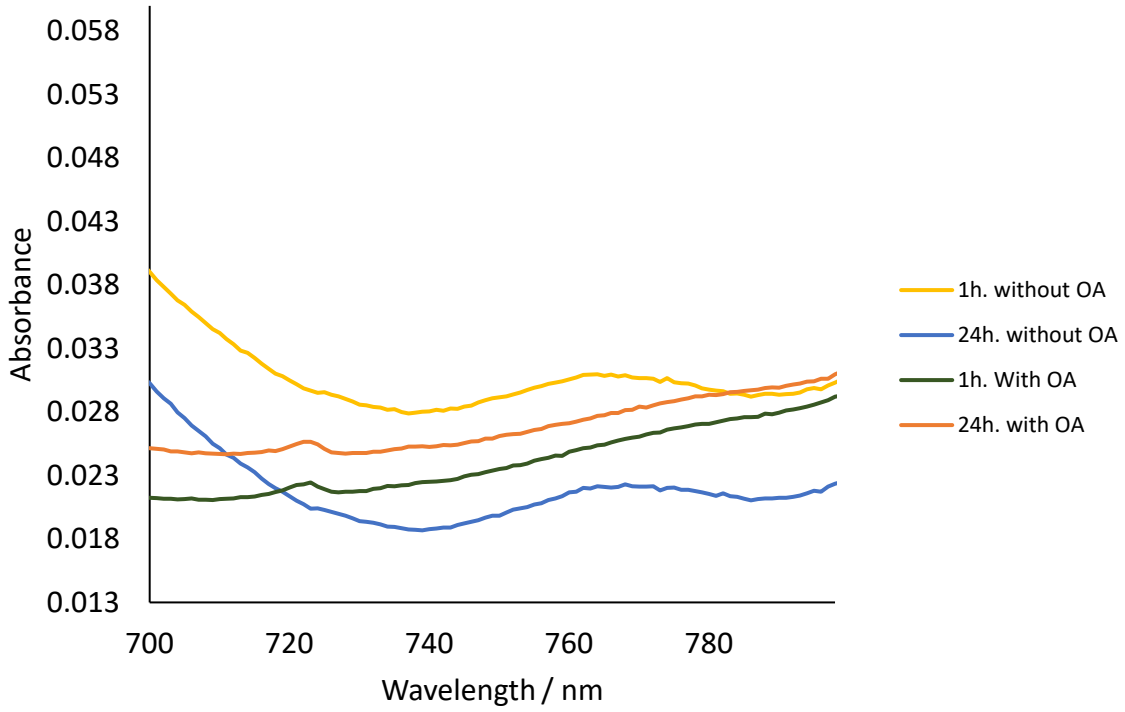

Figure 67: UV spectra for NIR region of $Ni(acac)_2$ preheated solution (at 110 °C) with oleylamine and with/without oleic acid.

The summary of UV-vis-NIR spectrum for the solution that does not have oleic acid vs solution that has oleic acid is; 1) the Ni complex is not the same during the heating up and overnight, and adding oleic acid changes the formation of the Ni complex. The best available hypothesis to explain the data is that without oleic acid present, the reaction starts off with an oligomeric form of $Ni(acac)_2$, and this changes after heating at 110 °C overnight to $Ni(acac)_2L_2$, where L is likely oleylamine. 2) adding oleic acid causes the $acac^-$ to react with oleylamine (confirmed by ASAP) for form acac-oleylamine and either this or oleate (oleylamine will deprotonate oleic acid to form oleate) binds to the Ni centre. 3) The visible region shows a change on the d-d transitions (618 vs 587 nm, with vs without), and that explains the change in colour during the heating up and overnight. 4) finally, the d-d transition in the NIR region shows a peak at 765 nm with oleic acid or 722 nm without. To understand the change of the structure of the Ni complex during the heating up (from RT

to 110 °C) and overnight (at 110 °C), further investigation needs to be done, but the best hypothesis that can be concluded from the UV-vis-NIR is:

1. The peak that was observed and assigned was the peak at 311 nm, which is the shift from 298 nm to 311 nm because of the reaction of oleylamine with $acac^-$ to form an amine-ketone moiety and the possible replacement of the $acac^-$ with oleic acid to form $Ni(oleate)_2$. Also, because of the use of excess of oleylamine, the final Ni complex will be [$Ni(oleate)_2$ $(oleylamine)_2$]. This observation suggests that the oleylamine connects to the Ni metal centre and forms an octahedral structure
2. The change in d-d transitions is not clear cut, but they key point is that on adding oleic acid there are clear changes. As the proposed chemistry on adding oleic acid involves a change from $acac^-$ ligands to oleate (a weaker field ligand) this would imply a smaller Δ_{oct}. Based on acac- being intermediate between water and ethylenediamine in ligand field strength it might be expected that this d-d transition would fall below 400 nm and be hidden under the tails of the much stronger π-π transitions.

The ASAP results (Figure 68 and Figure 69) show an agreement with the hypothesized mechanism discussed above (Figure 57). The oleic acid is replacing the $acac^-$ on $Ni(acac)_2$ and forms Ni-oleate. The $acac^-$ also reacts with the oleylamine to form a compound that appeared at 350 m/z, as can be seen in Figure 70. The second dominant signal around 516 m/z, which is suggested to be a structure such as that shown in Figure 71. In the hypothesized mechanism, the final products are Ni NPs and amino borane, which could undergo further interactions with the $acac^-$ and acac-oleylamine product to yield a species like this.

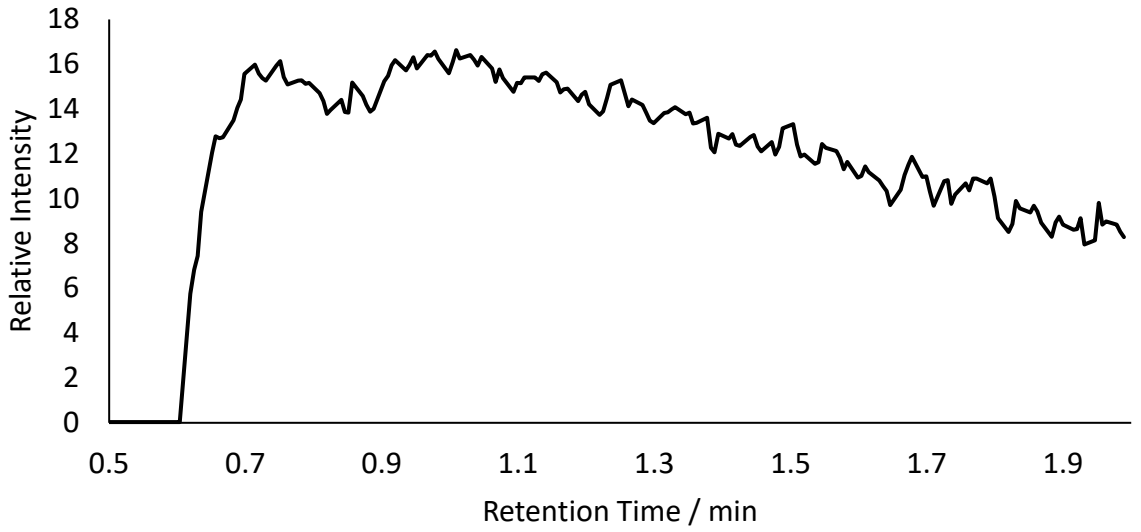

Figure 68: ASAP + ion trace for supernatant from nanoparticle synthesis experiment from the sample that was kept at 110 °C overnight in which oleylamine and oleic acid present. Y axes simplified by dividing by 100,000.

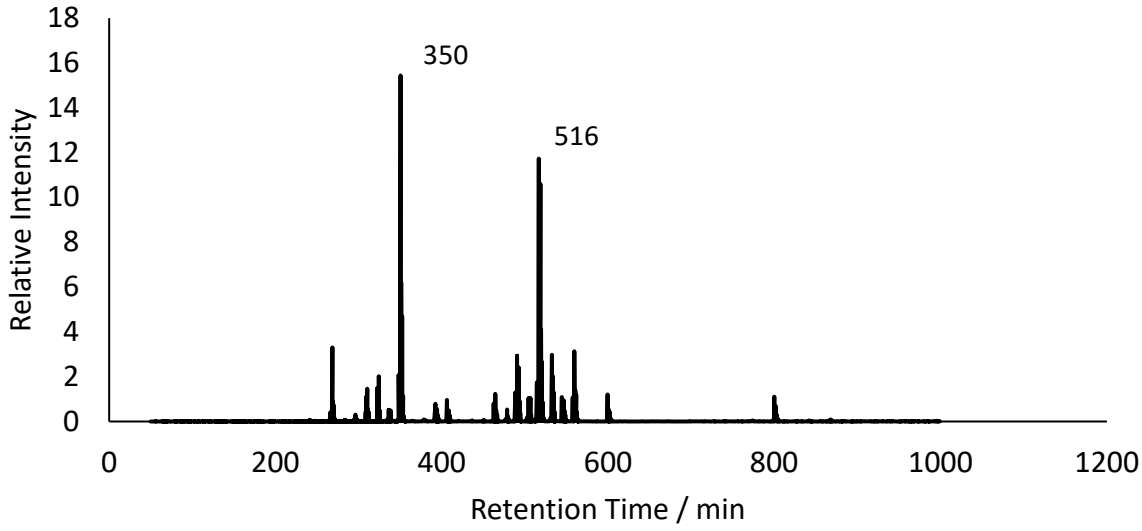

Figure 69: ASAP mass spectrum from nanoparticle synthesis experiment from the sample that was kept at 110 °C overnight in which oleylamine and oleic acid present. The Interesting peak is the peak on MS at 350 m/z, which proves the interaction between the oleylamine and acac-. Y axes simplified by dividing by 10,000.

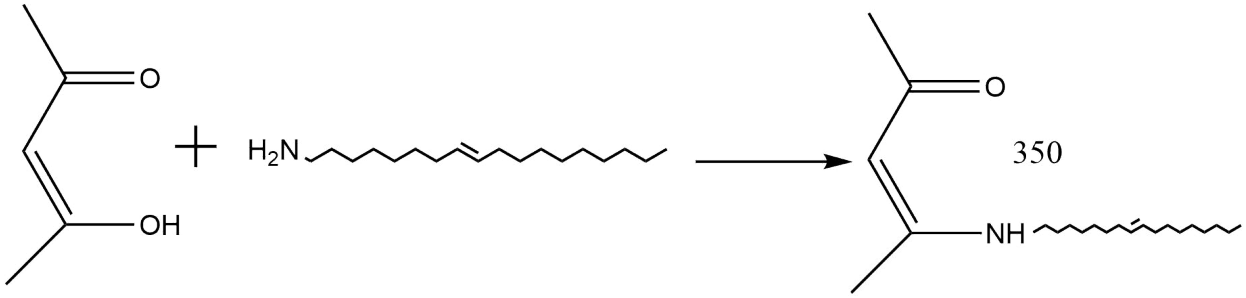

Figure 70: The reaction between the oleylamine and Hacac.

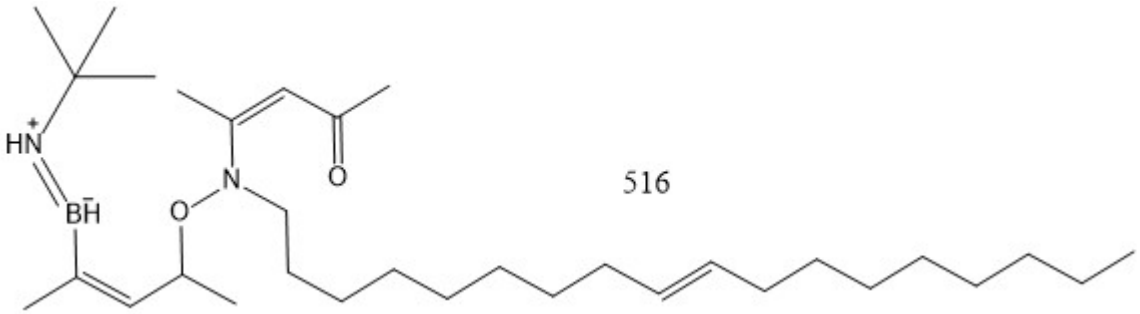

Figure 71: A suggested structure for the compound that appears at 516 m/z.

3.9 Conclusion

The synthesis of 3.2 nm Ni NPs was conducted following the 2010 report by Metin *et al*.. In his work, he showed that oleylamine (Oly) worked as a capping agent and BTB works as a reducing agent. Also, they suggested that oleic acid (OA) is replacing the $(acac)^-$ ligands and forming $Ni(oleate)_2$ at 110 °C for 1 h. This work was duplicated, and similar results were obtained. The mechanism was not clear, and there was no evidence to follow the proposed change from $Ni(acac)_2$ to $Ni(oleate)_2$, so the work in this chapter aimed to improve understanding of this process and in doing so a change in size from the 3.2 nm to 1.3 nm with very uniform size distribution was achieved.

- Firstly, 1 h at 110 °C showed the change between the ligands and the metal centre could affect the reduction time. Also, the change in the solution colour was evidence that Ni metal centre is going through some changes in the oxidation state or ligands electron density, and for that UV-vis-IR was important to study these changes.
- Secondly, the processes occurring were followed by UV-vis-NIR, which showed significant shifting in the UV region. The maximum shift was achieved by the overnight reaction, which indicates any change occurring was still incomplete after 1 h. The overnight reaction to change $Ni(acac)_2$ to $Ni\text{-}oleate_2$ or $[Ni(oleate)_2(oleylamine)_2]$ lead to the formation of Ni NPs of 1.3 nm size.

1. Metin, Ö.; Mazumder, V.; Özkar, S.; Sun, S., Monodisperse Nickel Nanoparticles and Their Catalysis in Hydrolytic Dehydrogenation of Ammonia Borane. *Journal of the American Chemical Society* **2010,** *132* (5), 1468-1469.

2. Wall, M. A.; Cossairt, B. M.; Liu, J. T., Reaction-Driven Nucleation Theory. *J. Phys. Chem C* **2018,** *122* (17), 9671-9679.

3. Li, J.; Wang, Y.; Tang, J.; Wang, Y.; Wang, T.; Zhang, L.; Zheng, G., Direct growth of mesoporous carbon-coated Ni nanoparticles on carbon fibers for flexible supercapacitors. *J. Mater. Chem. A* **2015,** *3* (6), 2876-2882.

4. Yin, X.; Shi, M.; Wu, J.; Pan, Y.-T.; Gray, D. L.; Bertke, J. A.; Yang, H., Quantitative Analysis of Different Formation Modes of Platinum Nanocrystals Controlled by Ligand Chemistry. *Nano Letters* **2017,** *17* (10), 6146-6150.

5. Bu, W.; Chen, Z.; Chen, F.; Shi, J., Oleic acid/oleylamine cooperative-controlled crystallization mechanism for monodisperse tetragonal bipyramid NaLa (MoO4) 2 nanocrystals. *J. Phys. Chem. C* . **2009,** *113* (28), 12176-12185.

6. Cotton, F.; Fackler Jr, J., Molecular Association and Electronic Structures of Nickel (II) Chelates. I. Complexes of Pentane-2, 4-dione and Some 1, 5-Di-substituted Derivatives. *J. Am. Chem. Soc.* **1961,** *83* (13), 2818-2825.

7. Yin, X., *Effects of metal ion-ligand interactions on the synthesis of metal nanostructures with controlled morphology*. University of Illinois at Urbana-Champaign: 2015.

8. Zhou, H.-P.; Zhang, Y.-W.; Mai, H.-X.; Sun, X.; Liu, Q.; Song, W.-G.; Yan, C.-H., Spontaneous Organization of Uniform CeO2 Nanoflowers by 3D Oriented Attachment in Hot Surfactant Solutions Monitored with an In Situ Electrical Conductance Technique. *Chem. Eur. J.* **2008,** *14* (11), 3380-3390.

9. Sone, K.; Fukuda, Y., Thermochromism of Nickel (II) Chelates in Solution. In *Inorganic Thermochromism*, Springer: 1987; pp 43-71.

Chapter 4 Synthesis of Cu Nanoparticles with average size 1.8 nm

4.1 Introduction

Cu nanoparticles have been synthesized following the method Bingham and Trussler developed in the Beaumont group, resulting in 4 nm Cu NPs. Previously this method was developed empirically, and the particle size was demonstrated, but little investigation had taken place into understanding the underlying mechanism or identifying key variables.

It had previously been shown that:[1]

1. Copper nanoparticles that were reasonably monodisperse could be prepared using long-chain amine capping agents, morpholine borane and the hot injection method of a copper acetylacetonate precursor to a diphenyl ether solution of the other reagents. The hot injection method of introducing the metal salt (solution) to the hot solution containing an amine-boron complex as a reducing agent provides a way to rapidly nucleate nanoparticles and yield smaller nanoparticles compared to those produced without a reducing agent.[2] The reaction is conducted under nitrogen using Schlenk techniques because copper reacts aggressively with oxygen.
2. The copper nanoparticles were thought to be metallic because of surface displacement reactions that were conducted successfully by galvanic displacement[3]: Cu(0) + Pd(II) → Cu(II) + Pd(0), evidenced by the presence of Pd in the resultant nanoparticles detected by ICP.

3. There appeared to be a discrepancy in the particle size produced above and below the decomposition temperature of the amine-borane complex – TGA shows that it decomposes with an onset temperature of ~150 °C in helium.
4. The fate of the amine-borane complex was unknown, but preliminary ^{11}B NMR experiments had shown some boron to be present in the supernatant recovered upon centrifugation of the reaction mixture.

This chapter will aim to improve the understanding of these preliminary findings on the Cu nanoparticle system by providing mechanistic insights and, in turn, showing the synthesis of smaller NPs size with uniform size distribution.

4.2 TGA of morpholine borane

The synthesis of Cu NPs at a range of temperatures from 150-210 °C was previously understood on the basis of the TGA of the morpholine borane reducing agent (Figure 72). It can be seen in Figure 72 that the decomposition started around 150 °C. Therefore, nanoparticle synthesis at temperatures 150, 185 and 210 °C was attempted in the current work to see the temperature's effect on the resultant NPs.

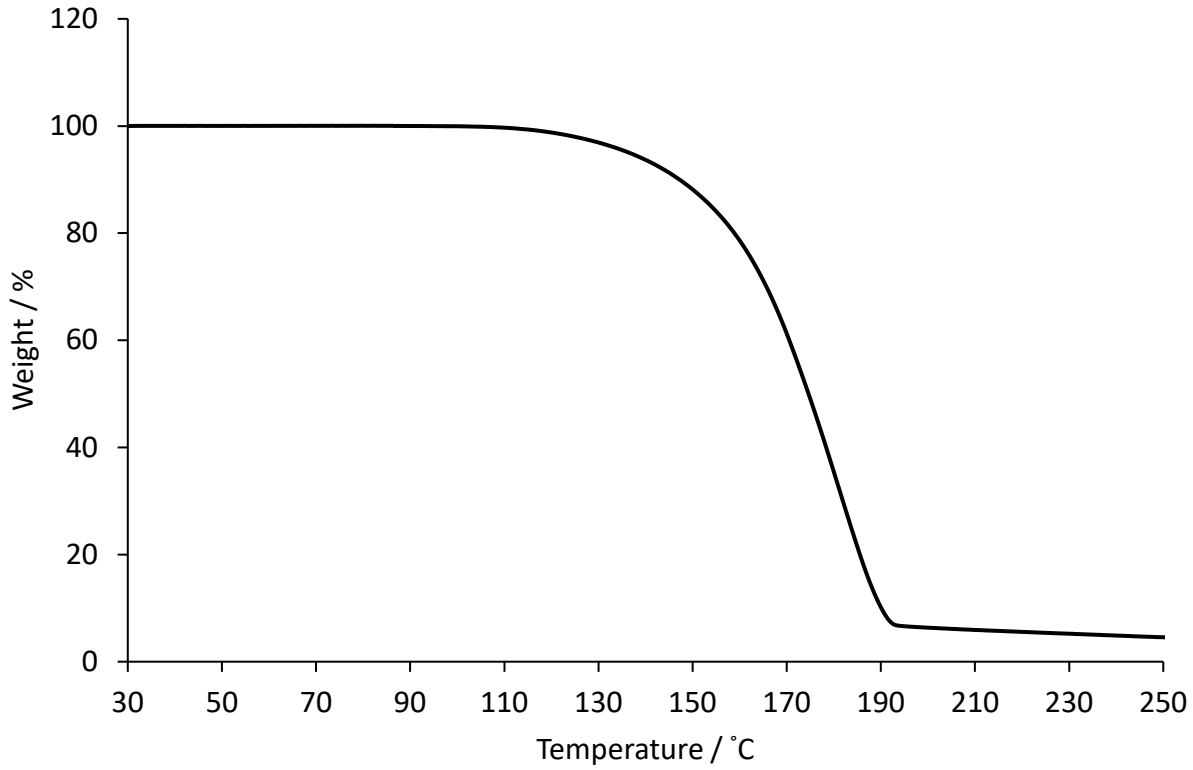

Figure 72: TGA for morpholine borane. The temperature range of decomposition is 110-190 °C.

4.3 TEM data and size distributions

4.3.1 Samples prepared following the procedure from previous work

Nanoparticles were prepared using the method previously reported by Bingham and Trussler, which is stirring $Cu(acac)_2$ with pyridine at room temperature and then injected to oleylamine, morphine borane and octadecylamine at a variety of temperatures from 150 to 210 °C. The solution turns black, indicating the formation of the Cu NPS. The time was different from sample to sample. For example, the samples that were synthesized at 150 and 185 °C took a longer time (around 5 s) to turn to black, which is longer than the sample that was synthesized at 210 °C (which turns black immediately after the injection). TEM has

been conducted to image the nanoparticles and to establish the size and size distribution of the Cu nanoparticles, which were synthesised at three different reaction temperatures, as can be seen in Figure 73.

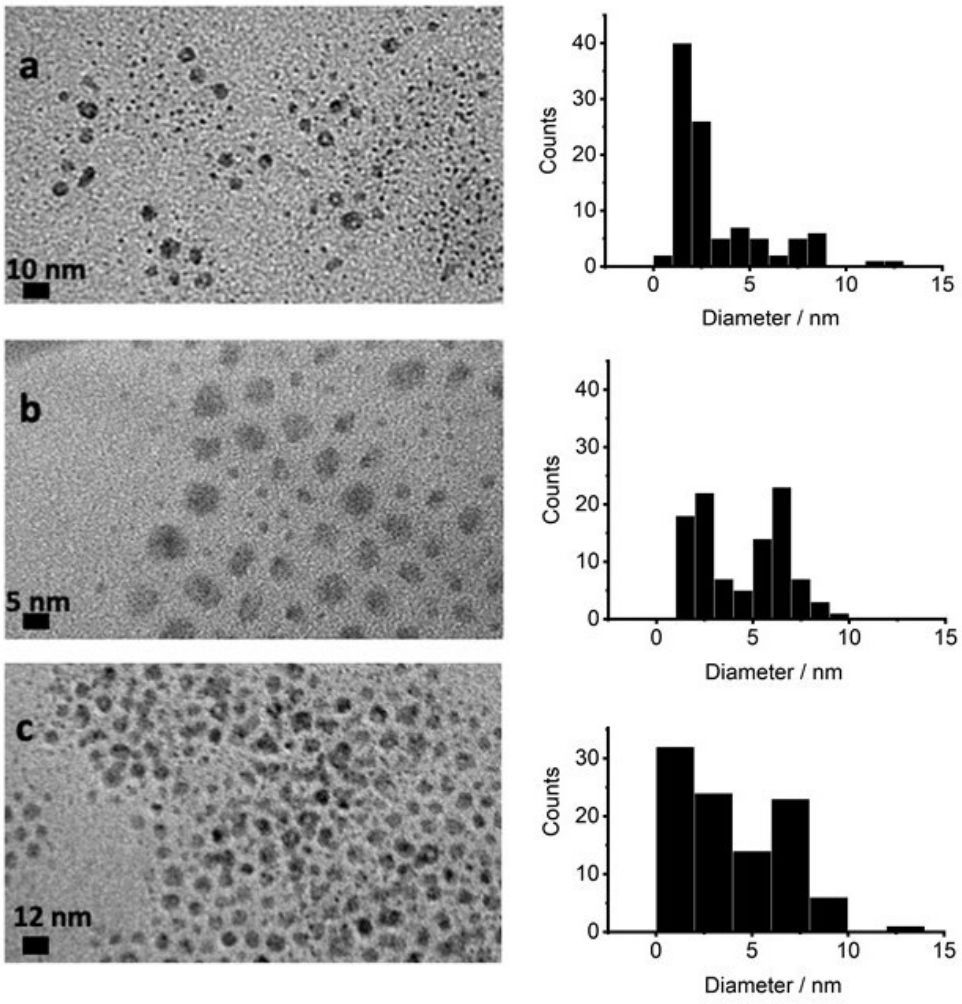

Figure 73: (left side shows the TEM images of the Cu NPs, and the right side shows a histogram of 100 particle sizes): a) Cu NPs synthesized at 150 °C; EX0003, b) Cu NPs synthesized at 185 °C; EX0011 and c) Cu NPs synthesized at 210 °C; EX0024.

The TEM images and histogram of the particle sizes were obtained for another two batches from each temperature reaction to check the reliability of using this method. Table 4 shows the summary of all the reactions conducted. The data indicate that small particles were produced at all temperatures, but all with broader than desirable size distributions.

The size range is similar to the 4 nm reported in the preliminary results by previous group members. There is slightly greater consistency in the resulting particles at 210 ˚C.

Table 4: A summary of all the samples done from each temperature with another two batches to show the producibility of each temperature synthesis.

Samples prepared at 150 °C	Nanoparticle size obtained and distribution return (1 σ) / nm	Samples prepared at 185 °C.	Nanoparticle size obtained and distribution (1 σ) / nm	Samples prepared at 210 °C	Nanoparticle size obtained and distribution (1 σ) / nm
EX0003	3.3 ±2.5	EX0011	2.1±0.6	EX0024	3.3 ± 2.2
EX0009	5.2 ±2.0	EX0016	4.4±2.2	EX0029	4.3 ± 1.7
EX0017	4.2 ±2.4	EX0018	5.5±1.1	EX0032	4.5 ± 00

Moreover, the histograms in Figure 73 show an almost bimodal appearance in each case, with particles distinctly under 4 and above 4 nm, which indicates that a better understanding of the processes that influence the reaction will help to improve the uniformity of the size and limit this broadening.

4.3.2 Summary of repeating the previous work at 150 185 and 210 °C

In general, the repetition of the previous work produced particles of broadly 4 nm as expected, but they were bimodal, and there was some variance in mean particle size on repeating the synthesis of samples at the same temperature. There was slightly greater consistency for the synthesis at 210 ˚C. These results, combined with the TGA of morpholine borane (the reducing agent), showed:

1. At low temperatures (lower than the full decomposition of the MB, which TGA shows is 190 °C), the reduction cannot generate the individual NPs

without generating agglomerates which means the full decomposition of the reducing agent assists in getting a uniform size of Cu NPs. On the other hand, at high temperatures (higher than the full decomposition of the MB, which TGA shows is 190 °C), the absence of agglomerates and uniform NPs with the same average size can be seen, such as done at 210 °C. This could mean the MB needs to be fully decomposed before introducing $Cu(acac)_2$ from the other flask.

2. The time of the reduction (the solution turns fully black) at 210 °C is faster than at 185 or 150 °C, which indicates either we have a different reducing agent or, for this reaction, a high temperature is needed in order to reduce the $Cu(acac)_2$ at the same time and generate the same number of Cu atoms.

4.3.3 Samples prepared to study the effect of reaction starting materials

Firstly, experiments were done in order to investigate the effect of drying or not drying the solvent diphenyl ether (DPE). This showed the same result without any effect on the resultant NPs. As can be seen in Figure 74.

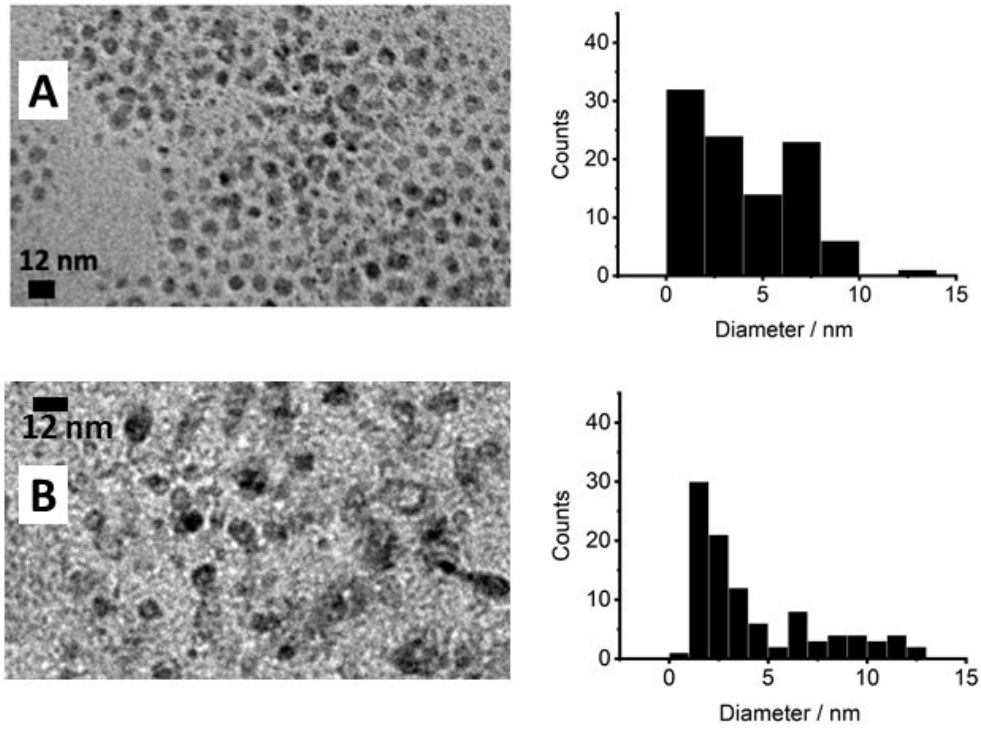

Figure 74: (left side shows the TEM images of the Cu NPs, and the right-side shows a histogram of 100 particle sizes): a) Cu NPs synthesized at 210 °C; EX0024, by using dried solvents b) Cu NPs synthesized at 210 °C by using undried solvents; EX0053.

The other parameter that was investigated is the mixing time (stirring) of $Cu(acac)_2$ with the solvent (pyridine), which is used, as it was found otherwise impossible to dissolve the $Cu(acac)_2$. Literature reports have shown the ability of pyridine to bind to metal atoms and work as a capping agent on NPs.[4] In the preparation of Cu NPs, pyridine is used as a solvent for the Cu precursor, $Cu(acac)_2$, which is dissolved over a period of time in a separate flask prior to injection into the hot reducing solution. It is possible that the time that is needed is due to the formation of $Cu(acac)_2$ pyridine adducts - the monoadduct is known but has smaller stability constant than similar compounds in the literature.[5] In the case of the TEM results discussed above and shown in Figure 73, the time for stirring of pyridine with $Cu(acac)_2$ before the addition was 3 h at room temperature, with the visual

interpretation that this allows the complete dissolution of the $Cu(acac)_2$. To investigate the effect of the mixing time with pyridine, the experiments described above were done by the $Cu(acac)_2$ stirred in pyridine overnight at room temperature. Figure 75 shows the TEM images and size distribution for Cu NPs following this overnight stirring protocol at different reaction temperatures, 150- 210 °C.

At low temperatures, sizes were somewhat variable – but at high temperatures a consistent size was obtained, although a few very large agglomerates were visible in most of these procedures. The only temperature able to produce a consistent size without large agglomerates was 210 °C.

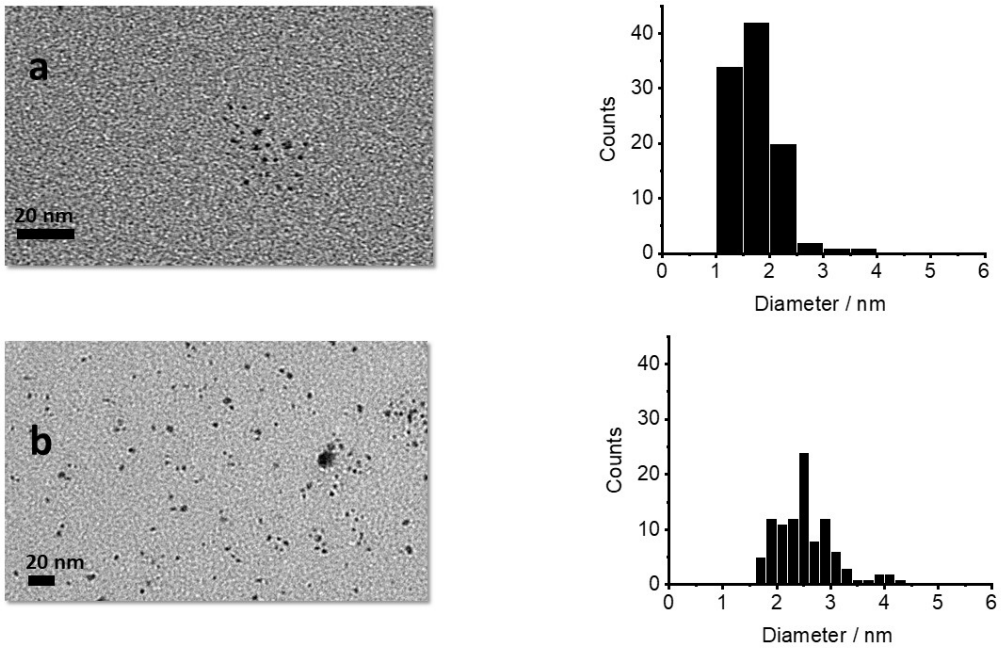

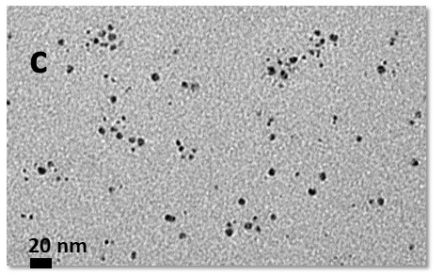
c
20 nm

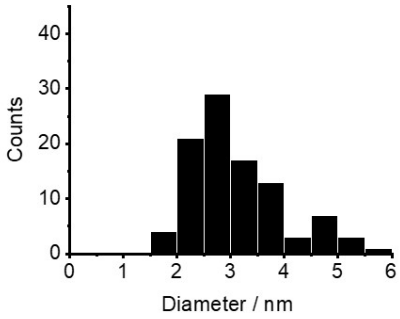
Counts
Diameter / nm

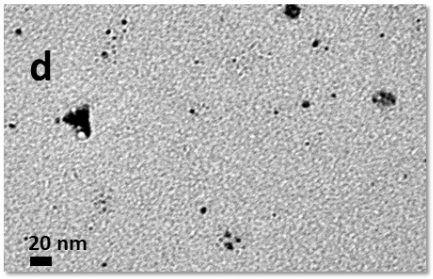
d
20 nm

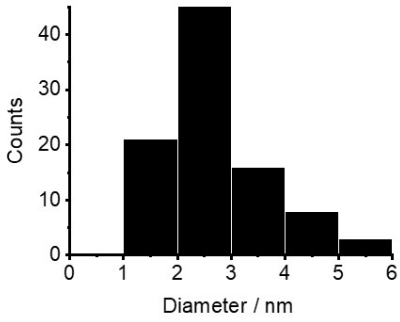
Counts
Diameter / nm

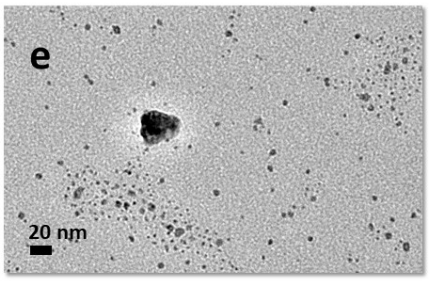
e
20 nm

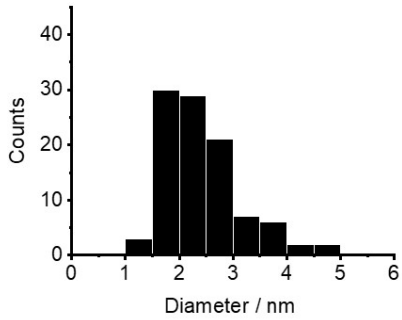
Counts
Diameter / nm

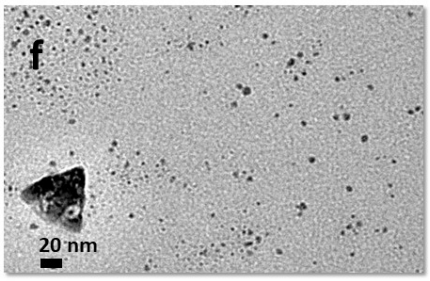
f
20 nm

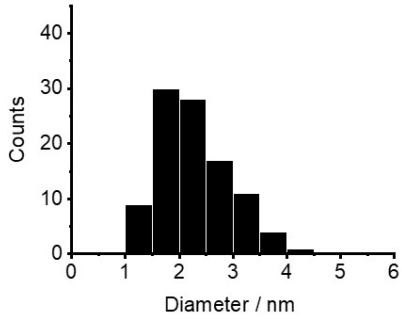
Counts
Diameter / nm

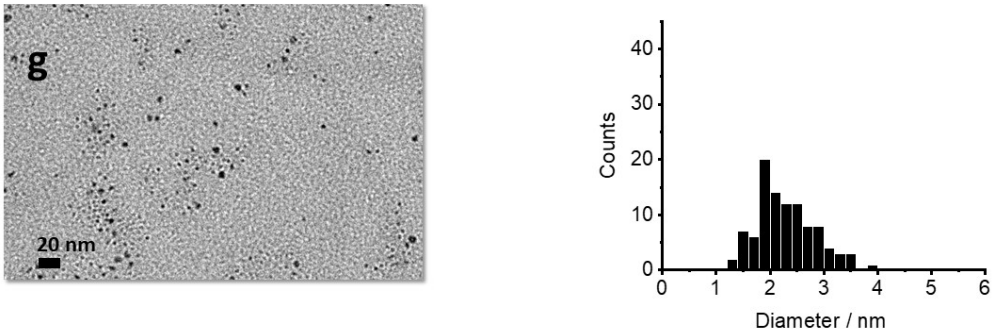

Figure 75: (left side shows the TEM images of the Cu NPs and the right side shows a histogram of 100 particle sizes): TEM images and size distributions of Cu NPs synthesized at different temperatures with the average size in nm and distribution quoted as ± 1σ: a) 150 °C, 1.7 ± 0.4 nm; (b) 160 °C, 2.5 ± 0.6 nm; (c) 170 °C, 3.2 ± 1.0nm; (d) 180 °C, 2.8 ± 1.0 nm; (e) 190 °C, 2.5 ± 0.7 nm; (f) 200 °C, 2.3 ± 0.7 nm; (g) 210 °C, 2.3 ± 0.5 nm. The pin width of the histograms was changed according to the nanoparticles size to give better description of the sizes.

The resultant NPs show smaller sizes and narrower size distributions. It is notable that although the average sizes appear smaller, the experiments done at 180-200 °C showed a small number of very large triangle NPs as well as the small NPs on the TEM grid. Also, in the 150 °C experiment, the number of NPs was small on the TEM grid, which (given the same procedure for grid preparation was used in each case) indicates loss of NPs or Cu during the separation by centrifugation, either due to small nanoparticles or more likely incomplete reduction of the metal precursor.

Interestingly, the NPs from the experiment that was done at 210 °C showed no triangle shape (large agglomerates), and the average size was 2.3 ± 0.5 nm, which is the smallest average size and narrowest size distribution among all the experiments. Figure 76 shows a comparison between the Cu NPs synthesized a) from 3 h, b) the overnight stirring of pyridine with $Cu(acac)_2$ before the injection. Stirring of the pyridine overnight shows an effect not only on the average size but also on the size distribution a) 2.3 ± 0.5, b) 4 ± 2.7 nm.

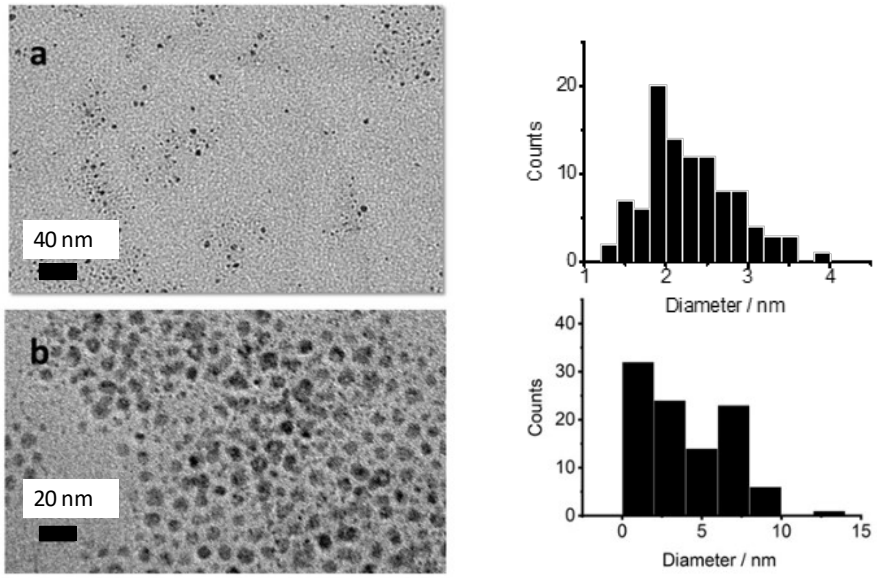

Figure 76: TEM images of Cu NPs synthesis at 210 °C and size distribution quoted as ± 1σ. a) 2.3 ± 0.5 nm of Cu NPs synthesized from $Cu(acac)_2$ that was stirred with pyridine overnight NP yield by Cu% 40 ±2.7%;, b) 4 ± 2.7 nm of Cu NPs synthesized from the $Cu(acac)_2$ that was stirred with pyridine for 3 h before the injection, NP yield by Cu% 43 ±3.3%; .

Using oleic acid during the reaction was found to be important to generate smaller NPs in the case of work in this thesis on nickel (discussed in more detail in Chapter 4). Therefore, the effect of oleic acid was also investigated during the synthesis of Cu NPs. Oleic acid was stirred overnight with pyridine and $Cu(acac)_2$, and the resulting NPs were found to be 1.8 ±0.5 nm, as can be seen in Figure 77, which compares the synthesis with and without using oleic acid. These are the smallest particles prepared via this route to date and also exhibit fewer large agglomerates present compared to the series of images in Figure 75.

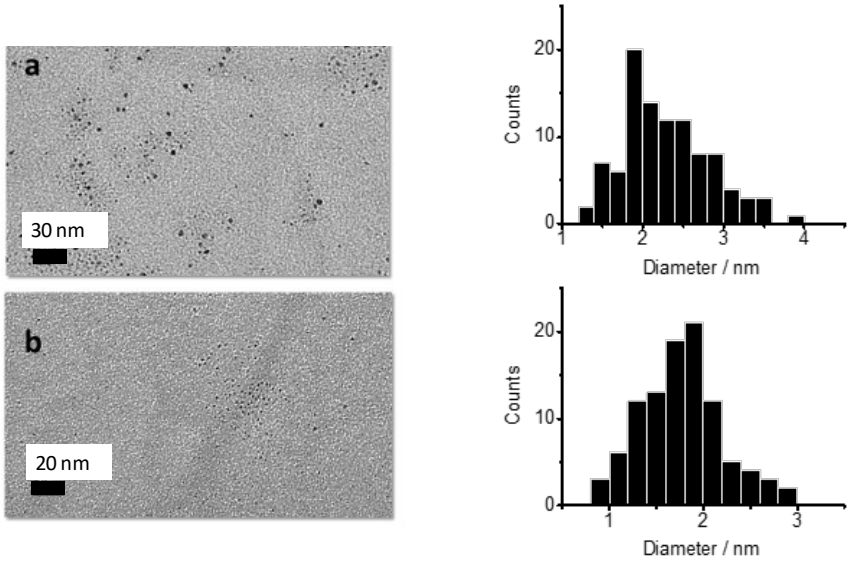

Figure 77: (left side shows the TEM images of the Cu NPs, and the right side shows a histogram of 100 particle sizes): TEM images of Cu NPs synthesis at 210 °C and the size distribution quoted as ± 1σ. a) 2.3 ± 0.5 nm of Cu NPs that synthesized from $Cu(acac)_2$ that was stirred with pyridine overnight, b) 1.8 ± 0.5 nm of Cu NPs that synthesized from the $Cu(acac)_2$ that was stirred with pyridine and oleic acid overnight, NP yield by Cu% 48 ±3.1%; . (Distribution quoted as ± 1σ)

Stirring the copper precursor with oleic acid prior to injection led to the best result among all the experiments that have been done to synthesize smaller Cu NPs (particle size 1.8 ± 0.5 nm). This could be the result of the formation of a different precursor before injection or due to the presence of the oleic acid in the reaction. In terms of the role of amino boron compounds as reducing agents, using acid solvents such as oleic acid can increase the rate of the process of releasing H_2.[13] However, it is envisaged that at a reaction temperature of 210 °C the morpholine borane has already decomposed to release hydrogen. Therefore, the oleic acid will not change the amount of H_2 that can be generated from MB at 210°C reaction temperature (because MB is already fully decomposed, TGA Figure 72), which means oleic acid is affecting the precursor either by working as another ligand or helping the pyridine to form two ligands around the $Cu(acac)_2$. Moreover, because the size of the resulting NPs was just slightly smaller compared to the ones without oleic acid and more consistent (1.8 ± 0.5 nm, with oleic acid and 2.3 ± 0.5 nm without oleic acid,

Figure 77). A possible rationalization is oleic acid promotes the formation of copper species with pyridine ligands.

4.4 XRD data analysis:

XRD was used to investigate the Cu NPs (crystal structure and size) and, in particular, to look for evidence of the formation of metallic copper rather than copper as oxides. The position of Cu (111) for metallic Cu is at 43.9 ° 2θ when using a Cu Kα source (ICSD: 78.25.196.216).[6]

XRD data is an essential result, as for applications requiring Cu metal, the attempted reduction of Cu_2O nanoparticles commonly produced[7] can cause sintering and loss of the small particle size desired. Broad background signals attributable to amorphous material are also present, likely due to the large quantity of carbonaceous stabilizer present. Similarity, this was also reported for different concentration of capping agent (mercaptoethnol) can affect the peaks at high 2 theta for ZnS nanoparticles.

Figure 78 shows the powder diffraction pattern obtained for the product of a typical synthesis of copper nanoparticles (EX0016, TEM particles size 4.4 ± 2.2 nm) and includes weakly the fcc Cu (111) reflection at 43.3° 2θ.

The Cu NP PXRD pattern clearly shows that the (111) reflection is very broad, as seen in the inset on the top right of Figure 78. Nanoparticles with a size of 1000 Å or less are expected to exhibit size broadening of their reflections in PXRD.[6] The Cu 111 fcc (Figure 79) can be affected by stacking effects in the NPs that result in line shifts and line broadening, which is the best explanation for line shifting (43.9° to 43.3°) and the line broadening (0.47 ± 0.07).[6] Strain effects can cause the broadening of a reflection, which can happen in the present case if there is CuO around the Cu nanoparticles (normal strain).[9]

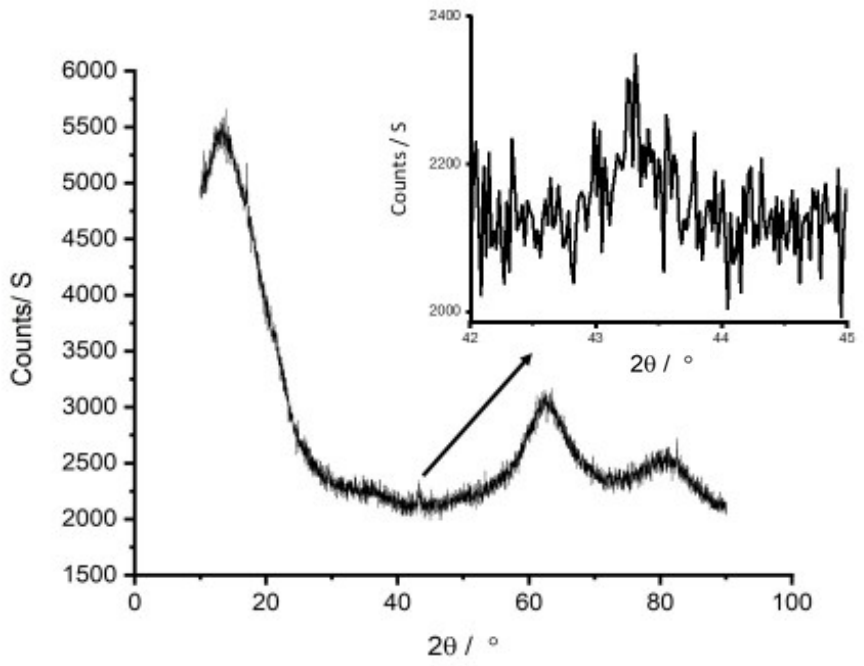

Figure 78: PXRD for the product of a standard synthesis Cu NPs at 210 °C from sample EX0016.

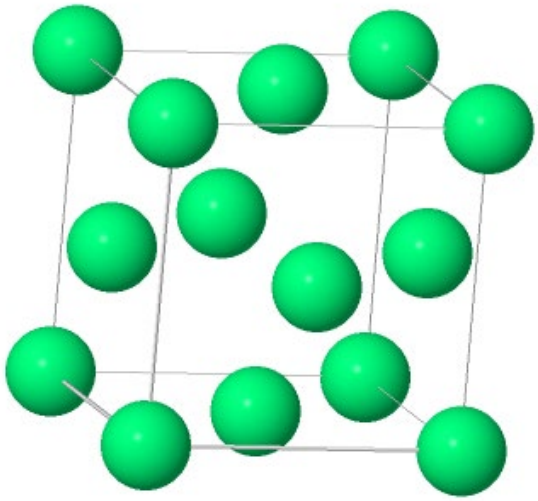

Figure 79: fcc-ccp copper metal. Reproduced from ICSD (78.25.196.216).[6]

The Scherrer equation was applied to provide a rough estimate of the Cu nanoparticle average size, assuming size broadening dominates. The FWHM, β, was

obtained using Origin software to carry out the best fit of the line-broadened reflection by using a Gaussian peak equation; summarized in Table 5

Table 5: Gaussian fitting equation applied to sample EX0016.

Model	Gaussian
Equation	y = y0 + A/(w*sqrt(pi/(4*ln(2)))) * exp(-4*ln(2)*(x-xc)^2/w^2)
Plot	B
y0	2120.4 ± 5.3
xc	43.31 ± 0.02
A	60.5 ± 9.1
w	0.47 ± 0.07
Reduced Chi-Sqr	2316
R-Square (COD)	0.38
Adj. R-Square	0.37

The fitted Gaussian is shown as a red curve in Figure 80**.** The size obtained was 18 nm by use of the Scherrer equation, shown in Equation 1. The discrepancy with TEM is discussed below.

$$D_{hkl} = \frac{K\lambda}{\beta\, Cos\, \theta_{hkl}} \quad (1)$$

Where; hkl = Miller indices of the plane (111; ICSD (78.25.196.216)), D= dimeter of the particles (perpendicular to the crystal plane; hkl), K= shape factor (most of the time is 0.9), θ =Bragg's angle, 2θ= 43.31384; θ/°= 43.31384/2= 21.65692; θ/ radians= 0.377985, (perpendicular to the crystal plane; hkl), β = full width at height of the reflection position; FWHM/°= 0.47523, FWHM/ radians= 0.008294

$$D = \frac{0.9 \times 1.5406}{0.008294 \times Cos 0.377985} = 179.9\ \text{Å}; 17.99\ nm$$

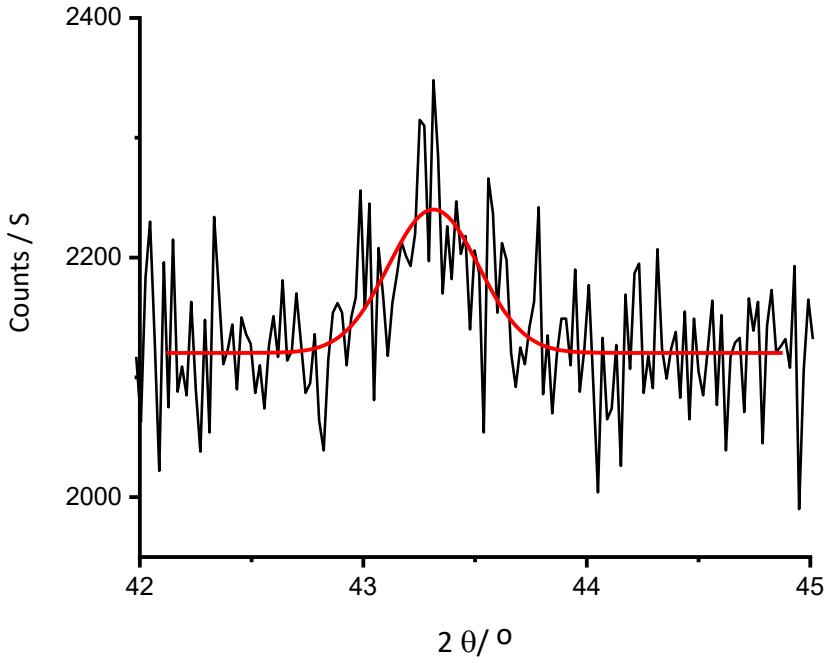

Figure 80: Gaussian profile fitting (red curve) by origin software.

To better understand the difference in size between XRD and TEM, several possible explanations need to be taken into consideration. The difference in techniques, TEM measures the NPs diameter distributions by the number of particles; in contrast, XRD measures the average size of crystallite domains by volume. XRD is, therefore, naturally prone to being dominated by larger particles, and the TEM distributions do suggest some larger particles present.[14] Also, the Gaussian fitting is rather crude due to the noisy data, as can be seen in Figure 80. The fitting of a Gaussian line with this reflection causes the width to be 0.47°, but it is possible that a number of other peaks could fit – the size obtained by TEM of 4.3 nm would require a β of 1.4° 2θ. It is, therefore, likely that the difference between TEM could be partly due to the noise around the reflection at 43.3°, making the peak difficult to fit and particularly due to the volume-sensitive nature of XRD to focus on larger particles. Furthermore, a high 2θ reflection would ideally be used to reduce errors in the trigonometric function in the Scherrer equation, but this is not possible due to only the strongest reflection for the copper metal being visible.

4.5 Identification of byproducts by Atmospheric Solids Analysis Probe (ASAP)

The fate of metal $acac^-$ with long-chain amines has been investigated by several groups.[10,12] Carenco mentioned that using an alkylamine such as hexadecylamine would be able to reduce $Ni(acac)_2$, claiming the reduction is by the amine moiety, not the alkene moiety as would be found in oleylamine. Then, they used GC-MS and ^1H NMR to identify the byproducts. One of the four products was keto-ene-amine which is colloquial $acac^-$ reacted with oleylamine. They identified the parent ion using GS-MS, a peak at 349 m/z and then used it to confirm the result. Yin *et al.* used UV-vis to identify the byproducts from the reactions of $Pd(acac)_2$ and $Ni(acac)_2$ with oleylamine in the presence/absence of oleic acid. They claimed the forming of keto-ene-amine needs to be in the presence of oleic acid (1:1:1, Oleylamine: oleic acid: $Pd(acac)_2$) and using 4 equivalents of oleic acid would increase the absorbance (the concentration/the formation) of keto-ene-amine.

In this thesis, similar results are reported based on using ASAP. The Hacac interacts with the products from the oxidation of the morpholine boron complex and octadecylamine (capping agent) and forms various byproducts. The investigation of byproducts was done by ASAP, which shows the supernatant contains $acac^-$ (m/z = 352) and morpholine borane (m/z =238) in significant quantities.

Figure 81 shows the products (obtained by ASAP) from the supernatant of the sample that was synthesized at 210°C, along with suggestions for how they could have been formed. The ASAP trace is shown in Figure 82. It is assumed the reaction starts with hydrogen reducing the $Cu(acac)_2$ to formally form Cu^0 and two Hacac molecules; however, it is possible $acac^-$ was liberated earlier as a result of pyridine copper interactions, as discussed earlier. The Hacac will further react with morpholine (appears at 171 m/z; and this will react with morpholine boron to form a compound that can be seen at 270 m/z, as seen in Figure 83). Also, another interesting ASAP peak is at 352 m/z (Figure 83), which comes from the interaction between $acac^-$ and octadecylamine. Figure 84 shows the

interaction between the compounds that appear at 270 and 352 m/z to form a compound that appears at 520 m/z.

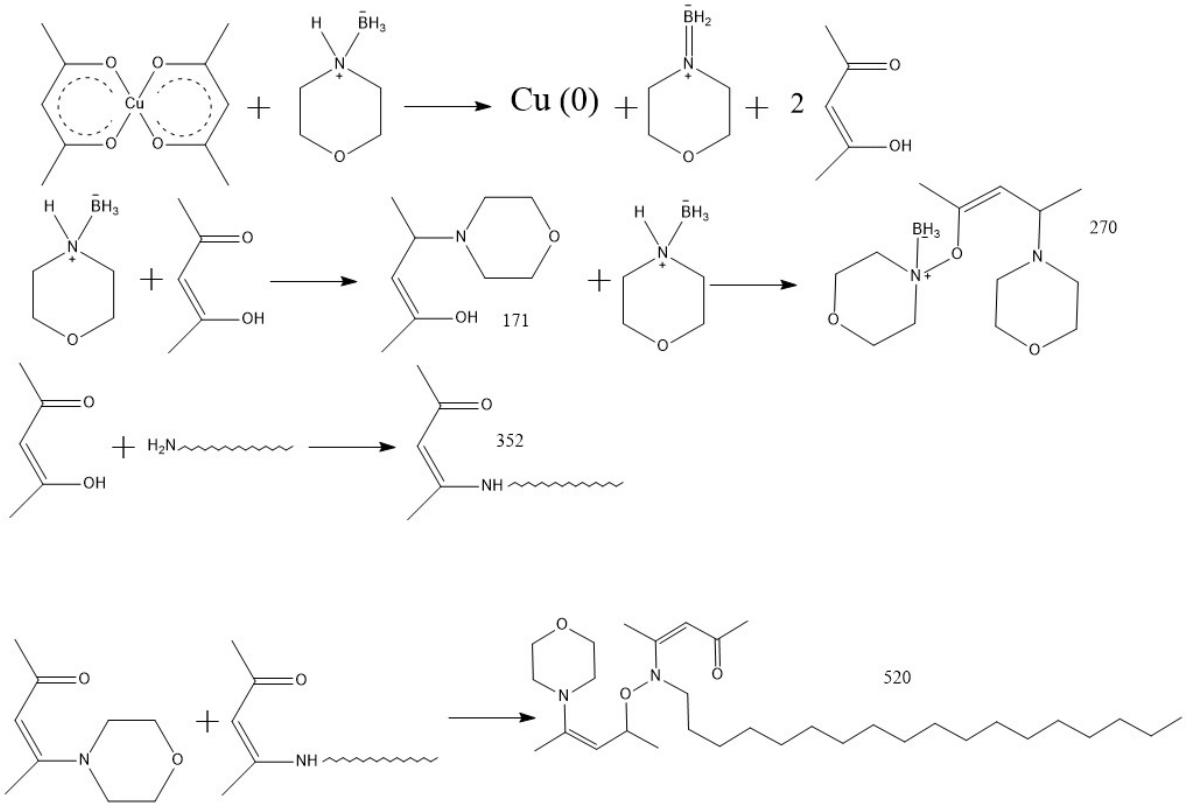

Figure 81: The possible side product formation routes from the Cu NPs synthesis, which starts with $Cu(acac)_2$ and (before the formation of Cu NPs).

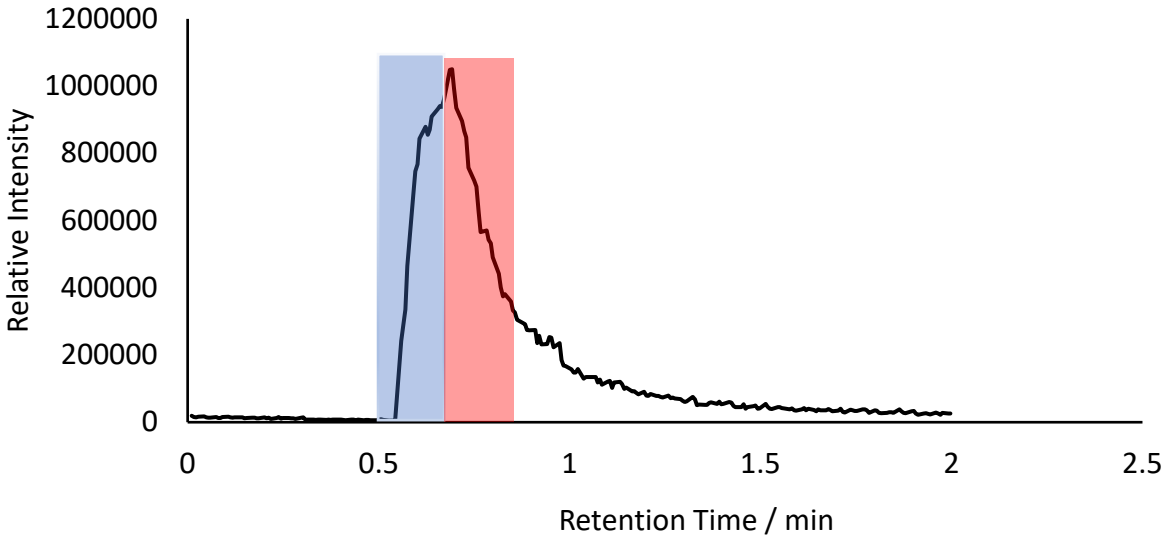

Figure 82: ASAP + ion supernatant experiment from sample EX0024 at 210 °C. The blue rectangle corresponds to a species with the most intense fragment at m/z = 352 amu (see Figure 83 below), and the red rectangle corresponds to a species with the most intense fragment at m/z = 520 amu (see Figure 84 below).

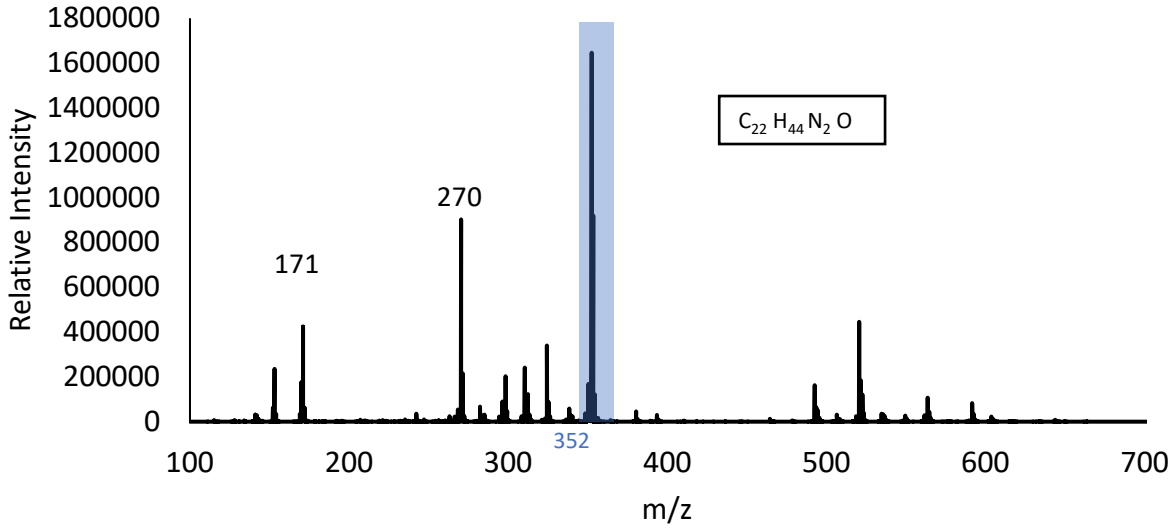

Figure 83: Mass spectrum from ASAP-MS supernatant experiment with peak 352 m/z (blue box on ASAP Figure 82).

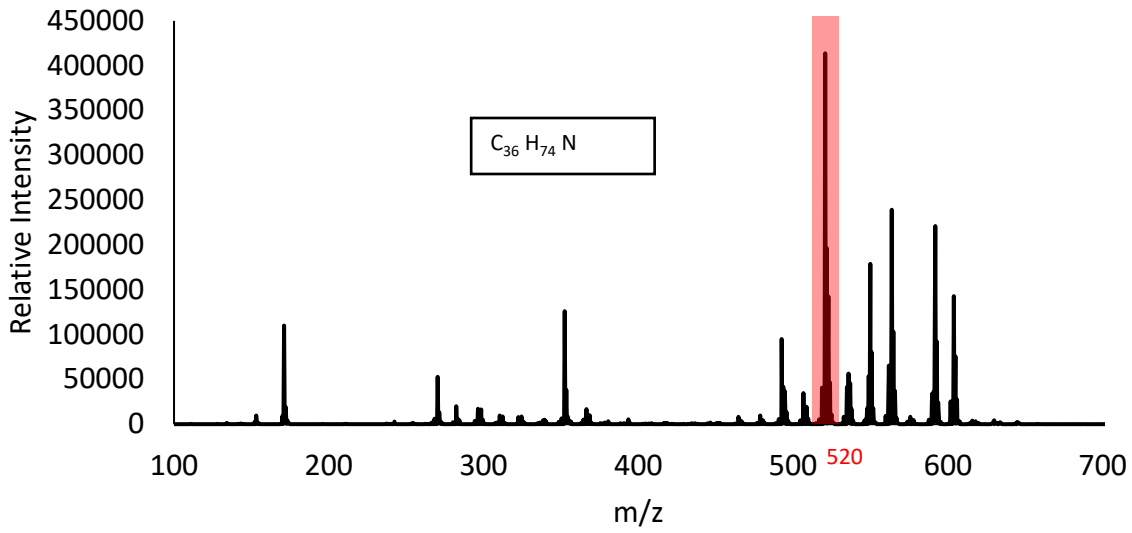

Figure 84: Mass spectrum from ASAP-MS supernatant experiment with peak 520 m/z (red box on ASAP Figure 82).

4.6 Conclusion

The synthesis of Cu NPs identified previously in the research group but not understood mechanistically was investigated. A method was established to synthesize Cu NPs with 1.8 nm size. Specifically:

- TEM showed that increasing the temperature affected the size and distribution of the resulting nanoparticles, and 210 °C produced the most consistent result and avoided large agglomerate formation.
- Drying of the diphenyl ether was not found to significantly affect the synthesis of Cu NPs.
- Stirring of pyridine with the precursor $Cu(acac)_2$ for a longer time before injection to the reducing agent solution was found to dramatically affect the size and distribution of resulting nanoparticles, likely due to the formation of pyridine adducts before injection.

- Stirring oleic acid with the precursor $Cu(acac)_2$ overnight before injection to the reducing agent solution was found to improve the size and distribution of resulting nanoparticles leading to 1.8 nm Cu NPs with a size distribution of 0.2 nm.
- The size of the NPs was determined by PXRD, but because of the small size of Cu NPs, the results were not accurate (18.2 nm), but it demonstrates the generation of Cu^0 metal, not CuO or Cu_2O.
- ASAP shows the byproducts produced in the reaction mechanism. For example, the hydrogen reduces the copper precursor, and the acac anion reacts with the capping agent. In particular, observation of boron-containing species in the supernatant suggests that the amine borane complex's decomposition products do not contribute strongly to capping the nanoparticle.

1. Bingham, Laura M. Development of nanoparticle catalysts and total internal reflection (TIR) Raman spectroscopy for improved understanding of heterogeneous catalysis. Durham University, Durham University e-Theses, 2018.
2. de Mello Donegá, C.; Liljeroth, P.; Vanmaekelbergh, D., Physicochemical Evaluation of the Hot-Injection Method, a Synthesis Route for Monodisperse Nanocrystals. *Small* **2005,** *1* (12), 1152-1162.
3. Lucci, F. R.; Liu, J.; Marcinkowski, M. D.; Yang, M.; Allard, L. F.; Flytzani-Stephanopoulos, M.; Sykes, E. C. H., Selective hydrogenation of 1, 3-butadiene on platinum–copper alloys at the single-atom limit. *Nature communications* **2015,** *6* (1), 1-8.
4. Pal, S., *Pyridine: A useful ligand in transition metal complexes*. IntechOpen: 2018.
5. Geraseva, N.; Shklyaev, A.; Anufrienko, V., Electron paramagnetic resonance of copper bis-(2-hydroxy-substituted camphorates) and their adducts with donor bases. *J. Struct. Chem.* **1976,** *16* (5), 719-723.
6. Otte, H. M. J. J. o. A. P., Lattice parameter determinations with an x-ray spectrogoniometer by the debye-scherrer method and the effect of specimen condition. **1961,** *32* (8), 1536-1546.

7. Patil, S. A.; Ryu, C.-H.; Kim, H.-S., Synthesis and Characterization of Copper Nanoparticles (Cu-Nps) using Rongalite as Reducing Agent and Photonic Sintering of Cu-Nps Ink for Printed Electronics. *ISSN International Centre* **2018,** *5* (2), 239-245.

8. Tamrakar, R.; Ramrakhiani, M.; Chandra, B., Effect of capping agent concentration on photophysical properties of zinc sulfide nanocrystals. *The Open Nanoscience Journal* **2008,** *2* (1)9. Young, W. C.; Budynas, R. G.; Sadegh, A. M., *Roark's formulas for stress and strain*. McGraw-Hill New York: 2002; Vol. 7.

10. Carenco, S.; Labouille, S.; Bouchonnet, S.; Boissière, C.; Le Goff, X.-F.; Sanchez, C.; Mézailles, N., Revisiting the Molecular Roots of a Ubiquitously Successful Synthesis: Nickel(0) Nanoparticles by Reduction of [Ni(acetylacetonate)2]. *Eur. J. Chem.* **2012,** *18* (44), 14165-14173.

11. Yin, X.; Shi, M.; Kwok, K.; Zhao, H.; Yang, H., (front cover) Dish-like higher-ordered palladium nanostructures through metal ion-ligand complexation. *Nano Res. h* **2018,** *11*, 3442-3452.

12. Yin, X.; Shi, M.; Wu, J.; Pan, Y.-T.; Gray, D. L.; Bertke, J. A.; Yang, H., Quantitative analysis of different formation modes of platinum nanocrystals controlled by ligand chemistry. *Nano lett.* **2017,** *17* (10), 6146-6150.

13. Leitao, E. M.; Manners, I., Catalysis in service of main group chemistry offers a versatile approach to p-block molecules and materials. *Nat. chem.y* **2013,** *5* (10), 817.

14. Hirschle, P.; Preiß, T.; Auras, F.; Pick, A.; Völkner, J.; Valdepérez, D.; Witte, G.; Parak, W. J.; Rädler, J. O.; Wuttke, S. J. C., Exploration of MOF nanoparticle sizes using various physical characterization methods–is what you measure what you get? **2016,** *18* (23), 4359-4368.

Chapter 5 Understanding the role of amine borane compounds as reducing agents in the synthesis of Cu and Ni nanoparticles

5.1 Introduction

In the last decade, amine borane (AB) compounds have been recognized in organic chemistry (releasing H_2 and as a reducing agent[1]) and inorganic chemistry for H_2 storage and as reducing agents (nanoparticles synthesis). AB compounds have a high dihydrogen percentage (19.6 wt. % for ammonia borane as an example[2]), and that makes them well known for hydrogen releasing and storage. Many published papers have shown the use of metals as catalysts (*e.g.* Ni NPs[3]) leads to the release of hydrogen from storage in the AB. The field has grown dramatically as a result of the wider applications of hydrogen as an energy vector, especially after the development of hydrogen fuel cell vehicles. This chapter aims to bridge the gap between the understanding of the AB compounds in organic chemistry (using AB compounds to release H_2) and inorganic chemistry (using AB compounds as reducing agents to synthesize NPs) – particularly trying to understand the role of the amine borane compounds in nanoparticle synthesis. The reasons for this work are:

1. Organic chemistry researchers have done many screens on different AB compounds to understand the releasing of the H_2 at room temperature or high temperature and with/without using metal NPs to catalyze the release process.
2. Inorganic researchers working on NPs synthesis are increasingly using AB compounds, but there is little attempt to draw on the research that has been done by the groups that have been using AB for releasing H_2.

Combining the approaches of these two groups, greater insight into the mechanism of metal precursor reduction by amine boranes, and especially understanding if the AB

compounds reduce the metals precursors by H_2 (after releasing the H_2) or by two hydrogen atoms directly from the AB compound acting as the reducing agent. This understanding can then be used to better design syntheses to control the size, shape and uniformity of metal NPs in the future.

5.2 Goals of this chapter

This chapter builds on prior work in which it was identified that copper nanoparticles could be prepared by the reduction of $Cu(acac)_2$ by morpholine borane, but the mechanism and choice of reaction conditions were not well understood.[4] The work reported in this thesis aimed for a better understanding of the processes that occur during the synthesis of NPs. Amine borane reducing agents were essential for the synthesis described in previous chapters to prepare both 1.9 ± 0.5 (mean ± 1σ) Cu NPs and 1.3 ± 0.4 (mean ± 1σ) Ni NPs, as can be seen in Figure 85.

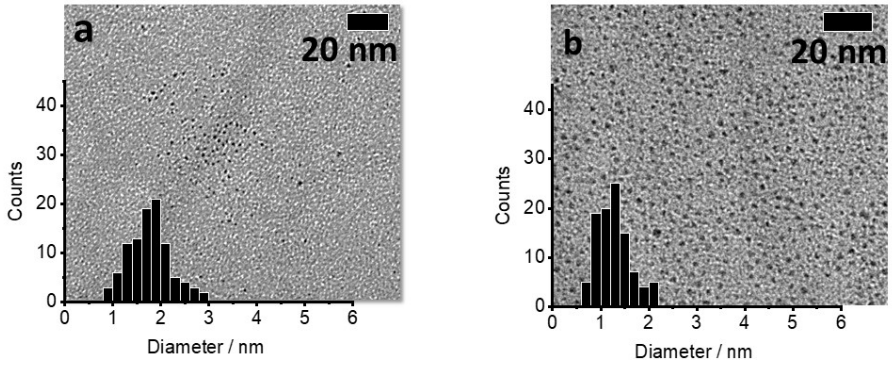

Figure 85: Representative TEM images and histograms and distribution quoted as ± 1σ of a) 1.9 ± 0.5 nm Cu NPs b) 1.3 ± 0.4 nm Ni NPs.

5.3 What are AB compounds?

In general, ammonium borane compounds are molecules that contain a nitrogen atom that is connected to a boron atom by a dative covalent bond. The nitrogen atom could have three hydrogens as the ammonium, or if there is a R group ($-CH_3$ or $-CH_2$), as each hydrogen is replaced, it becomes a primary, secondary and finally tertiary amine. On the

other hand, the boron atom will typically have three hydrogens and will be called borane (although substitution at boron is also known).

5.4 Dehydrogenation of AB compounds

Dehydrogenation of amine-borane compounds is well-studied, and it is known as dehydrocoupling. Dehydrocoupling is releasing H_2 and forming a bond between the two adjacent elements. The bond energies required to break the N-H and B-H bonds are almost the same at 386 and 389 kJ/mol, respectively. However, the difference in the electronegativity between the N and B with respect to H (B is 2.01 and N is 3.07 [5]) is the key to making the bond cleavage slightly exothermic, $+\Delta S$ (released H_2 gas) is positive and ΔH, is positive at temperature > 0 °C [6], as can be seen from the overall energy change accompanying Equation 1. This is the opposite of the bond cleavage and release of hydrogen in the case of ethane, as can be seen in Equation 2. The reason for the favorability of hydrogen release from an amine borane is that, unlike the C-C case of ethane, the polarity makes the N-H protic δ^+ and B-H hydridic δ^- and this permits the H_2 release at mild temperatures.[7, 8]

$$\mathrm{H_3N-BH_3} \rightarrow \mathrm{H_2N=BH_2} + H_2\ \Delta G\ (298) = -5.1\ KJ\ mol^{-1} \quad (1)$$

$$\mathrm{H_3C-CH_3} \rightarrow \mathrm{H_2C=CH_2} + H_2\ \Delta G\ (298) = 32.6\ KJ\ mol^{-1} \quad (2)$$

5.5 Results and discussion

In this chapter, Cu NP synthesis will be used as an example to explain in more depth the role of the releasing of the H_2 from the morpholine boron complex (MB; the chemical structure can be seen in Figure 86) and the influence of this process on NP formation. Morpholine borane (MB) acts as the overall reducing agent when synthesising nanoparticles by this route.

This work was conducted after the work on nickel nanoparticles and leaves further possibilities for optimisation of that route as the nickel nanoparticle synthesis temperature appears to be very similar to the decomposition temperature (see Chapter 4, so hydrogen may not be released into the solution until some of the nickel metal has formed that can catalyse further hydrogen release). More work is required to understand the role of amine borane in the nickel system.

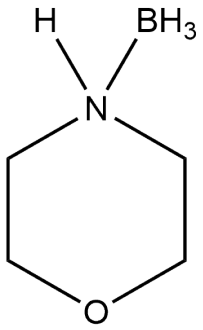

Figure 86: The chemical structure of morphine borane complex.

5.5.1 TGA of morpholine-borane to identify the temperature at which hydrogen release and decomposition occur.

TGA shows that the morpholine boron complex decomposes temperature around 110 °C in helium, as seen in Figure 87. It should be noted that the complete loss of all mass at this temperature may be due to the exothermicity of the hydrogen release volatilising the remaining sample from the sample pan but has been seen with all amine boranes subjected to TGA.

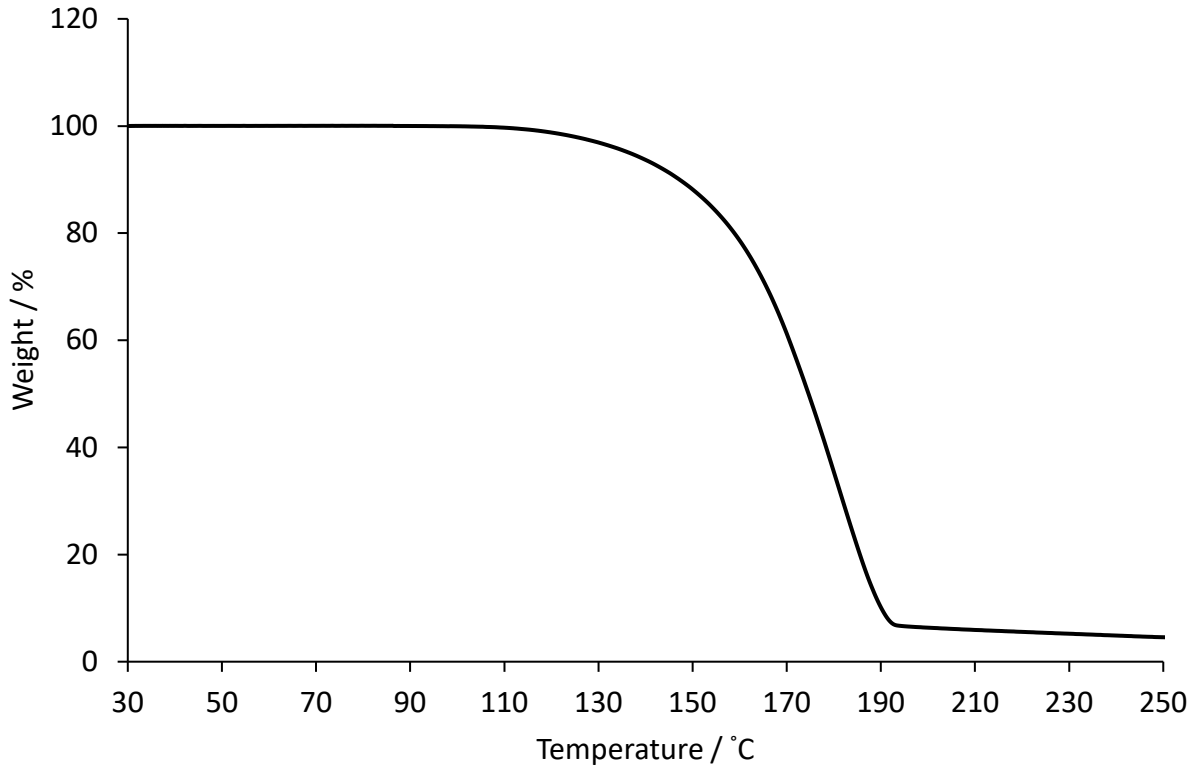

Figure 87: TGA of morphine borane shows the decomposition range from 110-190 °C.

5.5.2 Investigation of gas volume released from solution following amine borane decomposition.

In order to understand more about the availability of H_2 released during synthesis, the volume of hydrogen gas released from a solution similar to the synthesis mixture was measured as a function of temperature. The idea is that this method provides an indication of what temperature at the hydrogen gas (from morpholine borane) is likely to be released.

Measurement of the released H_2 (in solution) will be compared to the calculated theoretically possible volume that can be released and, in conjunction with TGA results (in helium) that show H_2 will be released from the amine borane at ~ 170 ˚C, used to understand the solubility of H_2. The three possibilities are:

1. The measured H_2 volume is equal to the theoretically calculated volume. This would mean the solubility is almost zero because all the generated gas can be released from the solution.
2. The measured H_2 volume is less than the calculated volume. This would mean some of the H_2 is soluble in the solution or all of the H_2 are soluble and did not leave the solution. If the volume of hydrogen released would not normally be soluble in the solution, this would make the solution supersaturated.
3. The measured H_2 volume is greater than the theoretically calculated volume, which means the MB is releasing more hydrogen than expected – this could be due to the wrong stoichiometry being assumed in the theoretical calculation (*i.e.* more than one H_2 molecule per morpholine borane molecule).

The experiment is complicated by the fact that the gas in the apparatus will expand, and other species, such as dissolved gases, are possibly released at elevated temperatures. To overcome this, a comparison with and without MB present was performed.

In Figure 88, the results of experiments “with” and “without” MB can be seen. In both cases with, octadecylamine (OCA) is present, and the process is carried out in diphenyl ether (DPE) solvent.

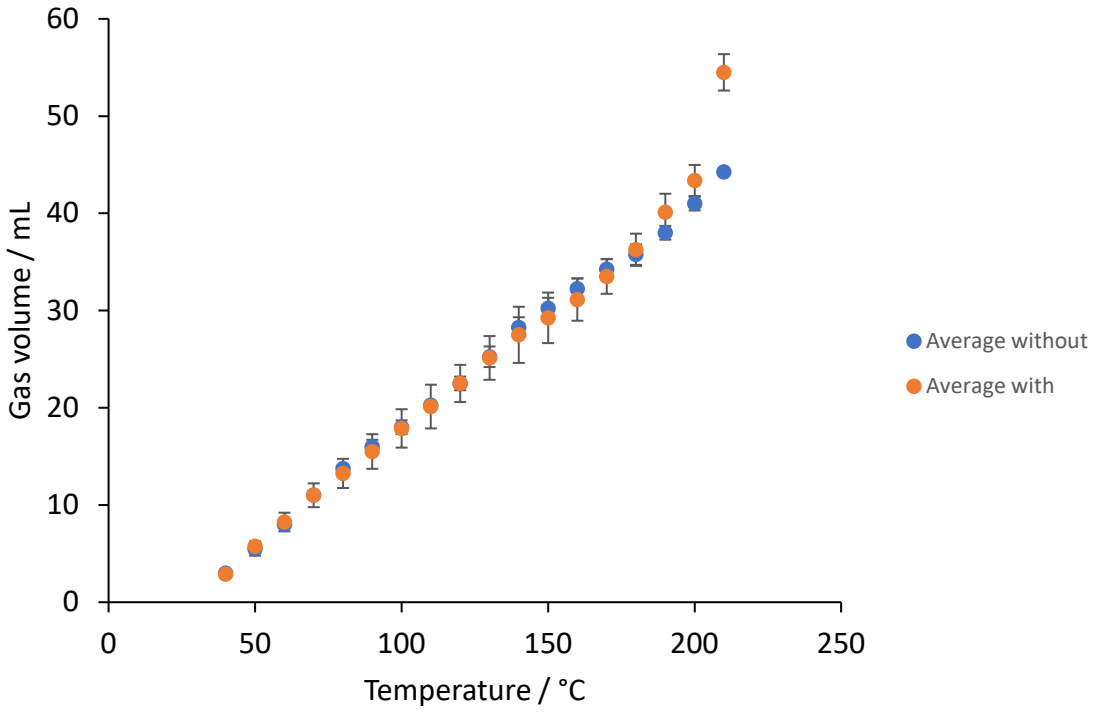

Figure 88: Graph showing the volume of gas released when heating ODA in DPE with or without MB (0.024 g, 3.37x10^{-4} mol) at 4 ˚C min^{-1} to 210 ˚C. The standard deviations of multiple runs (4 morpholine borane complex (MB), octadecylamine (OCA), and diphenyl ether (DPE) (with) and 2 experiments octadecylamine (ODA), and diphenyl ether (DPE) (without)) are shown as error bars on the graph.

Since the volume of hydrogen released experimentally is very close to the theoretical amount (can be seen in A-C.3.3) for a 1:1 stoichiometric release of hydrogen, this is good evidence that stoichiometric hydrogen is released into the solution. Importantly, given TGA shows hydrogen is released from the molecule at 170 °C, but this gas release experiment shows it is only released from the solution at 210 °C, it is very likely the solution (total volume 10 cm^3) contains all of the hydrogens in this temperature window, equating to a dissolved concentration of around 5 mmol mol^{-1}. For comparison, hypothetical linear extrapolation of atmospheric pressure hydrogen solubility data between 25 and 100 °C for common solvents including toluene, THF and acetonitrile [9] (broadly representative of DPE solvent and amine in the reaction mixture) to this temperature window (170-210 °C, solubility increase slightly with temperature) gives a range from 0.3 to

1.6 mmol mol^{-1}. This is several times lower than the amount of hydrogen apparently in solution between 170-210 ˚C, suggesting the solution must become supersaturated with molecular hydrogen. A number of nanoparticle synthesis reactions have been reported using Fisher-Porter glassware at ~ 3 bar H_2 that do not occur with atmospheric pressure hydrogen.[10-12] This raises the possibility of the reduction occurring as a result of increased local hydrogen concentration.

5.5.3 TEM results from a typical procedure for Cu NP synthesis using morpholine borane reducing agent

Although Figure 85 showed examples of the very small copper nanoparticles reported in Chapter 5, the initial experiments in this project were done as follows (setup in Figure 89), producing the NPs that can be seen in Figure 90. In a typical synthesis, $Cu(acac)_2$ was stirred with pyridine (in flask B) and then introduced to flask A, which already contained diphenyl ether, octadecylamine and morpholine borane heated to 210 °C (allowing the morpholine borane to possibly release hydrogen into solution and possibly the gas phase, based on the TGA and gas release experiments above). In the synthesis $Cu(acac)_2$ is added shortly after reaching 210 °C, and dissolved H_2 may not have been released, allowing H_2 to act as the reducing agent.

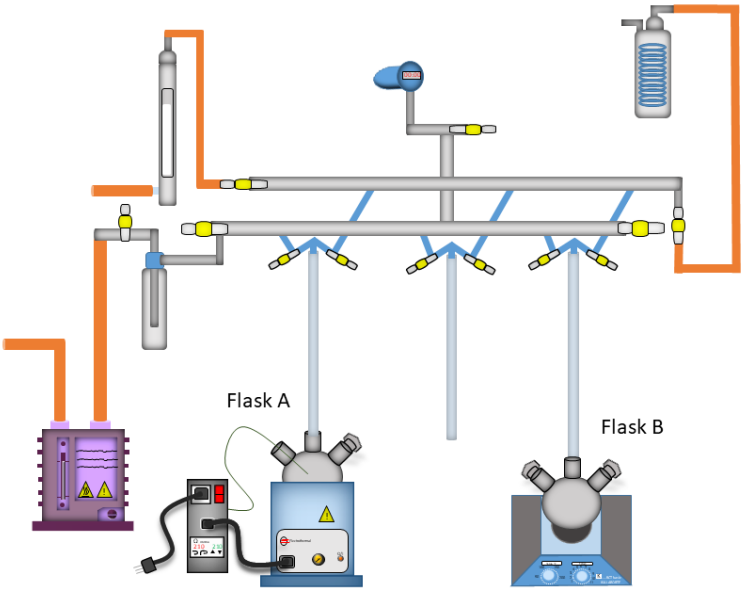

Figure 89: The setup used for synthesizing Cu NPs under N_2 gas.

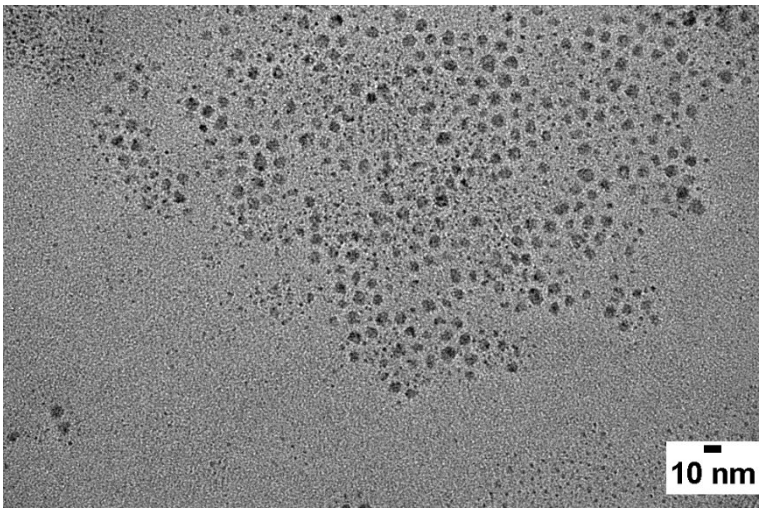

Figure 90: Cu NPs synthesized by injecting $Cu(acac)_2$ and pyridine to diphenyl ether, octadecylamine and morpholine borane at 210 °C. The average size and distribution quoted as ± 1σ is 5.1 ± 1.2 nm.

5.5.4 ^{11}B NMR spectroscopy of the reaction mixture as a function of temperature before the addition of metal precursor.

^{11}B NMR is a valuable tool for studying morpholine borane and its reaction products (because of the presence of boron atoms as a handle). Ramachandran *et al.* reported ^{11}B NMR data of morpholine borane at -15 ppm (for the boron atom), which will be compared in this section to shifting of the B signal of morpholine borane during heating .[13] A series of ^{11}B NMR spectra for the reactant mixture in flask A above (before injection of the copper precursor, containing MB, Octadecylamine and DPE) at different temperatures from 150 °C (which is below the decomposition of MB as shown by TGA) to 210 °C (which is higher than the gas came out of solution in the gas volume experiment) were recorded (Figure 91) in order to establish the change in ^{11}B NMR signal.

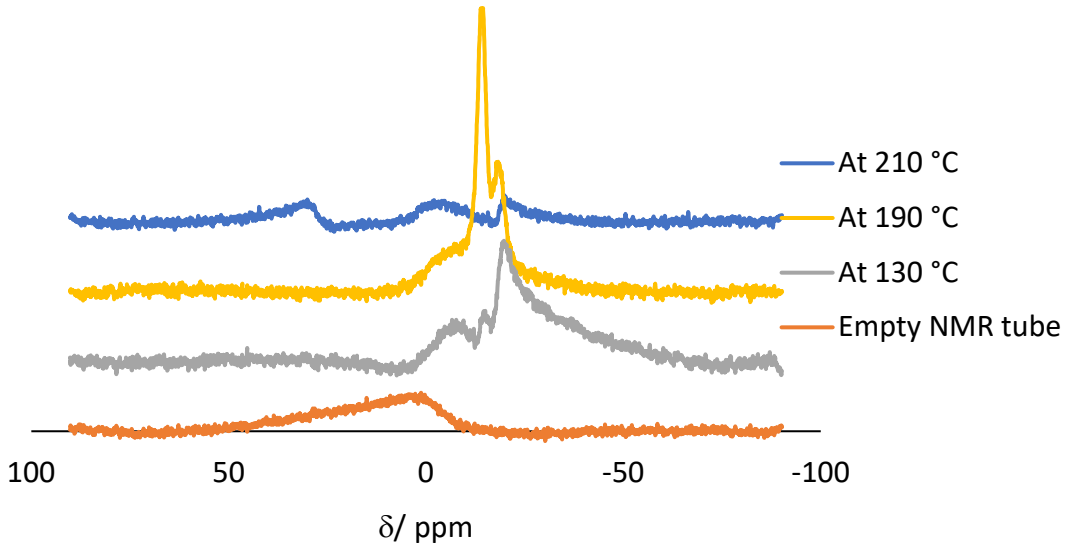

Figure 91: ^{11}B NMR for the mixture of starting materials (MB, DPE, Oct) before injection of the Cu precursor at different temperatures and the ^{11}B NMR tube alone that was to obtain all spectra and was used for background correction of the other spectra.

It can be seen clearly at low temperature (130 °C); there are two peaks at -15 and -18 ppm. But with increasing the temperature to 190 °C, the peak at -18 decreased in intensity and the peak at -15 increased. By 210 °C a small broad feature appears at 30 ppm, while the peaks that were at -15 and -18 ppm almost disappear. Morpholine borane itself (without the addition of octadecylamine) is reported at -15 ppm, while a calculated value for the aminoborane $H_2B{=}NMe_2$ (which actually exists as a dimer) is reported at +39 ppm (which may be indicative of the morpholine borane decomposition product $H_2B{=}NC_4H_8O$.[14] The process seen by ^{11}B NMR, therefore, appears to broadly mirror that expected from the TGA and gas release experiments, but possibly without the release of the hydrogen in the solution until slightly higher temperatures than predicted by TGA for the solid (*i.e.* above 190 °C). The reason for these being only a weak signal in the 210 °C sample is unclear, but as boron is still present in the sample, it indicates the loss of the morpholine borane, which was seen clearly.

5.5.5 ^{11}B NMR spectroscopy of boron containing product in the supernatant following nanoparticle synthesis.

^{11}B NMR was also carried out to investigate the supernatant product from the Cu NPs synthesis on the basis that the boron-containing products may be detected and indicate something about what had taken place. ^{11}B NMR for the supernatants from Cu NP synthesis at 150, 185, and 210 °C were recorded in the same NMR tube to have the same background (the ^{11}B NMR from the NMR tube contains a broad feature due to boron in borosilicate glass), as seen in Figure 92. Also, Table 6 shows the ^{11}B NMR performed on supernatants from many different experiments at different temperatures to confirm the reproducibility of the additional sharp peak around 5 ppm appearing in only the supernatant from the 210 °C synthesis.

Table 6: ^{11}B NMR for different supernatant at different temperatures.

^{11}B NMR # and MYA-EX00	Temp. / °C	Boron Peak at 5 ppm
24140138 EX0009	150	No
24140506 EX0012	185	No
24140603 EX0013	185	No
24140635 EX0016	210	Yes
08155957 Empty NMR tube		No
08160300 EX0017	150	No
08160342 EX0018	210	Yes
11162930 EX0016	210	Yes
15150651 EX0015	185	No
15152533 EX0011	185	No
15155522 EX0018	210	Yes
15160425 EX0017	150	No
07154446 EX0023	210	Yes
21153132 EX0024	210	Yes

Typical ^{11}B NMR is shown in Figure 92 for supernatants from reactions at 150, 185 and 210 °C, and another repeated sample to confirm the reproducibility of the additional sharp peak around 5 ppm. The first thing to note is that they all contain some more evidence for boron than the empty tube – as a broad peak in all three, with an additional sharp peak in the 210 °C samples. The spectra shown are typical of the repeat experiments listed in Table 6.

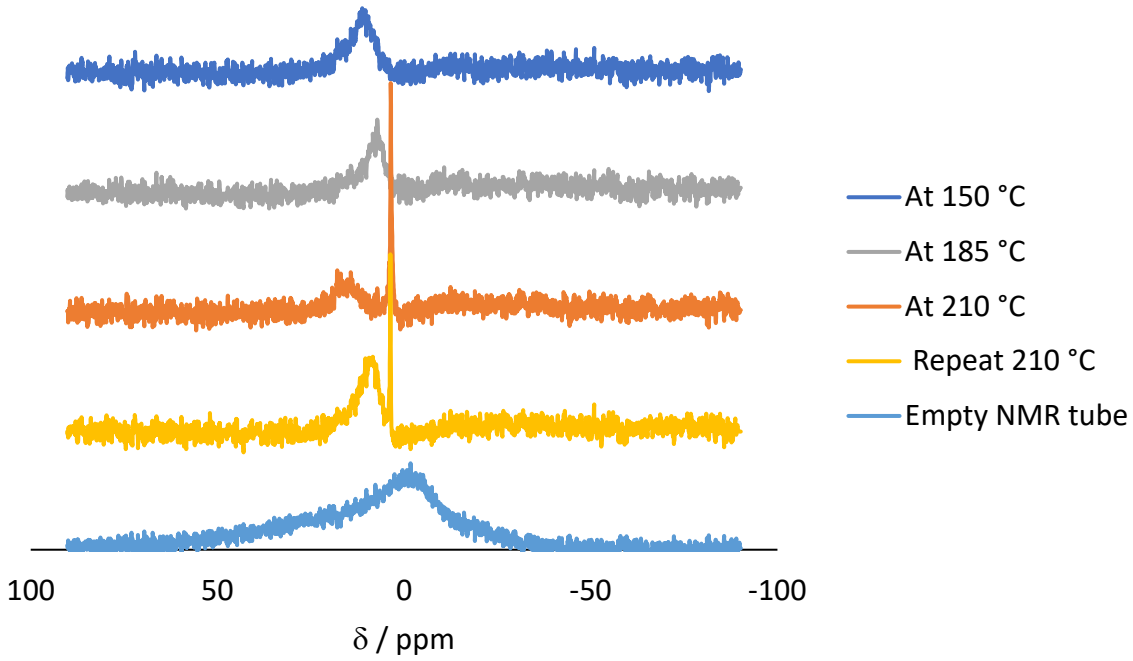

Figure 92: ^{11}B NMR for supernatants from the standard synthesis of Cu NPs at temperatures shown. The ^{11}B NMR of the same tube was used with all spectra to give background subtracted spectra.

The $B(acac)_2^+$ product cation proposed by Lidor-Shalev *et al*.[15] is expected to have one boron atom that is surrounded by four oxygen atoms, which they claimed results in a sharp single peak ~ 18.5 ppm. Our results showed a sharp peak at ~ 5ppm, which is similar to literature $B(OH)_4$ ~ 5 ppm.[16] This could be the sharp peak seen in the 210 °C sample, although the formation mechanism is not currently clear. Also, a large fraction of the area is seen in all spectra at 8-10 ppm and a broad peak indicative of equilibria broadening of the signal as discussed in 2.5.1**.** The NMR experiments do not therefore offer useful insight into the fate of the reducing agent due to the peak broadening.

5.5.6 ^{11}B NMR data analysis for supernatant spikes with other boron compounds

To get an idea of whether the total boron content is a significant fraction of the boron put into the synthesis in the form of morphine borane, an experiment was done to spike EX0016 with a known quantity of other boron compounds that would hopefully appear separately from all the other peaks in the NMR Figure 93.

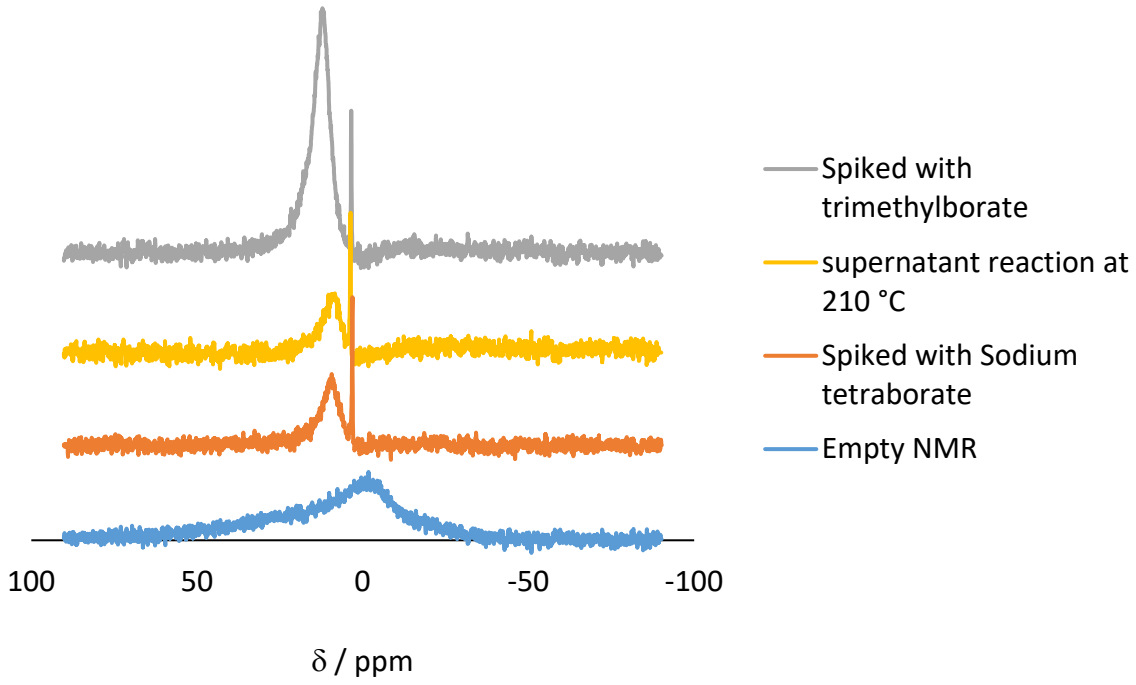

Figure 93: A summary of ^{11}B NMR data from the supernatant of EX0016 Cu NPs synthesis that was spiked with trimethylborate (top) and sodium tetraborate(middle). Also, the ^{11}B NMR for the empty NMR tube was recorded.

It can be worked out that the boron seen in these supernatant samples corresponds very roughly to around 35% of the total boron used in the experiment. It must be remembered that some may be in further washings or entrained in the nanoparticle capping, but the point is that this is a non-negligible percentage – *i.e.* the signals observed relate to a significant fraction of the boron present in the reactions.

5.6 Conclusion

This chapter aims to understand the role of using amino-borane compounds as reducing agent for NPs synthesis. The synthesis that was chosen for the study is the synthesis of Cu NPs (Chapter 5). The synthesis uses MB as a reducing agent to reduce $Cu(acac)_2$ at different temperatures starting from 150 to 210°C.

It was not clear (to the best of my knowledge) how amino-borane compounds is reducing the $M(acac)_2$ in order to understand the mechanism that can describe how the reduction happens. The following conclusions show a better understating of how amino-borane compounds such as MB reduces $Cu(acac)_2$ and produces Cu NPs.

- TGA shows the MB decomposes with an onset temperature of 150 °C in helium. Therefore, the reduction temperature was chosen to be from 150 to 210 °C.
- Gas volume experiment shows that the volume of H_2 released is very close to the theoretical amount for a 1:1 stoichiometric release of hydrogen. This H_2 volume was released at 210 °C, which is higher than what TGA shows. This indicates it is very likely that the solution contains the H_2 at the temperature window.
- ^{11}B NMR showed:

1. At low temperature (150 °C), two peaks could be seen at -15 and -18 ppm for boron species (derived from MB). At 190 °C, the -18 ppm peak decreased, and the -15 ppm peak increased. At 210°C, both -15 and -18 ppm peaks decreased, and a new peak appeared at 30 ppm. This shifting at 210 °C could be the result of a change in structure on releasing H_2.
2. After reduction has happened, for the samples of the reaction supernatant for samples from 3 temperatures, 150, 185 and 210 °C, a sharp peak appears around ~

5 ppm just in the samples from the synthesis at 210 °C not from 130 and 185 °C supernatant samples.

3. Although boron containing species were being seen in the supernatant, it was a concern to identify whether this was actually the fate of the majority of the boron, or whether the boron was actually not being washed off the nanoparticles. The ^{11}B NMR from the supernatant of the sample that was synthesised at 210 °C was spiked with another boron compound (trimethylborate). That shows that at least 35 % of the boron is seen in the supernatant, which given the washing and handling processes means it is likely the fate of the boron is in a solution phase species.

1. Faverio, C.; Boselli, M. F.; Medici, F.; Benaglia, M., Ammonia borane as a reducing agent in organic synthesis. *Org. Biomol. Chem. ORG* **2020,** *18* (39), 7789-7813.

2. Neiner, D.; Karkamkar, A.; Linehan, J. C.; Arey, B.; Autrey, T.; Kauzlarich, S. M., Promotion of hydrogen release from ammonia borane with mechanically activated hexagonal boron nitride. *J. Phys. Chem. C* . **2009,** *113* (3), 1098-1103.

3. Metin, O.; Mazumder, V.; Ozkar, S.; Sun, S. J. J. o. t. A. C. S., Monodisperse nickel nanoparticles and their catalysis in hydrolytic dehydrogenation of ammonia borane. **2010,** *132* (5), 1468-1469.

4. Bingham, Laura M. Development of nanoparticle catalysts and total internal reflection (TIR) Raman spectroscopy for improved understanding of heterogeneous catalysis. Durham University, Durham University e-Theses, 2018.

5. Little Jr, E. J.; Jones, M. M., A complete table of electronegativities. J. Chem. Educ. **1960,** *37* (5), 231.

6. Hamilton, C. W.; Baker, R. T.; Staubitz, A.; Manners, I., B–N compounds for chemical hydrogen storage. *Chem. Soc. Rev.* **2009,** *38* (1), 279-293.

7. Leitao, E. M.; Manners, I., Catalysis in service of main group chemistry offers a versatile approach to p-block molecules and materials. *Nature chemistry* **2013,** *5* (10), 817.

8. Melen, R. L., Dehydrocoupling routes to element–element bonds catalysed by main group compounds. *Chem. Soc. Rev.* **2016,** *45* (4), 775-788.

9. Brunner, E., Solubility of hydrogen in 10 organic solvents at 298.15, 323.15, and 373.15 K. *J. Chem. Eng. Data* . **1985,** *30* (3), 269-273.

10. Ibrahim, M.; Wei, M.; Deydier, E.; Manoury, E.; Poli, R.; Lecante, P.; Philippot, K., Rhodium nanoparticles stabilized by ferrocenyl-phosphine ligands: synthesis and catalytic styrene hydrogenation. Dalton trans. **2019,** *48* (20), 6777-6786.

11. Uznanski, P.; Bryszewska, E., Synthesis of silver nanoparticles from carboxylate precursors under hydrogen pressure. J. Mater. Sci. **2010,** *45* (6), 1547-1552.

12. Debouttière, P. J.; Coppel, Y.; Denicourt-Nowicki, A.; Roucoux, A.; Chaudret, B.; Philippot, K., PTA-Stabilized Ruthenium and Platinum Nanoparticles: Characterization and Investigation in Aqueous Biphasic Hydrogenation Catalysis. Wiley Online Library: 2012.

13. Ramachandran, P. V.; Kulkarni, A. S., Nucleophilic displacement of ammonia from ammonia borane for the preparation of alkylamine-, pyridine-and phosphine-boranes. *RSC advances* **2014,** *4* (50), 26207-26210.

14. Wrackmeyer, B., The B–N Bond in some aminoboranes and an iminoborane, studied by 11B and 15N NMR spectroscopy and DFT methods. *ZAAC* **2015,** *641* (14), 2525-2529.

15. Lidor-Shalev, O.; Zitoun, D., Reaction mechanism of “amine–borane route” towards Sn, Ni, Pd, Pt nanoparticles. *RSC Advances* **2014,** *4* (109), 63603-63610.

16. Takao, K.; Tsushima, S., The oxidation of borohydrides by photoexcited [UO2(CO3)3]4− Dalton trans. **2018,** *47* (15), 5149-5152.

Chapter 6 Coupling two metals nanoparticles with covalent tethers.

6.1 Introduction

In heterogeneous catalysis, using separated bicomponent catalysts is often associated with spillover, especially for hydrogenations. The hydrogen spillover phenomenon was reported by Khoobiar in 1964. Khoobaiar's work showed the H_2 could be dissociated by Pt/Al_2O_3 (0.5 w. % Pt), and then, in a second step, H adatoms migrated to neighbouring particles (yellow WO_3) and reduced it to blue W_4O_{11} and then to brown WO_2.[1] Khoobiar did not use the word spillover for this phenomenon, but four years later, Boudart *et al.*'s paper described this migration by spillover, and it has been known as spillover since 1968.[2] In general, spillover can be defined as forming or absorbing a species on a specific surface then moving this species to another surface which does not adsorb or form under the same condition.[3, 4]

Hydrogen is the most studied spillover. These studies compared different metals and metal oxides on different supports to achieve better reduction. Our study was inspired by the work that was done by Karim *et al.*[5], showing the reduction of iron oxide NPs at different distances from platinum nanoparticles on titanium oxide and aluminium oxide supports. The outcomes were not just showing how the aluminium support slows the hydrogen spillover compared to the titanium oxide, but also, interestingly, the distance between the two NPs affects the reduction degree. The reduction degree of the iron oxide by the hydrogen atoms spilled from platinum NPs at the furthest distance showed no reduction, and the closest distance showed the highest reduction degree.[5]

Karim's report inspired us to try linking two metals in a way that they could be deposited on any support (Karim's lithographic method only allowed 2D systems with quite large particles). Developing a method that can be used to couple two metals without support will involve the following:

1. Using a crosslinking technique that will involve using a linker that has different lengths to allow us in future to study the effect of the distance between the metals;

2. Using a technique that allows us to use the ~ 1 nm NPs that we have synthesized using the hot injection method (in previous chapters);
3. Using a technique that can control the directionality of the coupling allows us to just couple one metal NP with another metal NP.

This chapter starts with introducing the crosslinking reagents chosen to link the NPs, and in order to use this agent, modification to the NPs capping agents is needed. This will be achieved by exchanging the existing capping agent with a different capping agent that can be used later with this linker chemistry during the coupling process. The technique that I have employed to make the nanoparticles unsymmetrical is Langmuir–Blodgett trough deposition, which allows us to have a film of metal NPs one NP deep on a glass slide. This is used to control which side of each nanoparticle the capping agents can be exchanged from in the solution. Finally, the TEM images presented will show the results of successive attempts to improve this coupling strategy, which show it is a promising route for preparing the type of coupled nanoparticles that meet the above criteria for studies of hydrogen spillover. Successive steps are more synthetically complex, as we sought to identify the minimum number of additional regents and steps that could alter nanoparticle size or impact their eventual use as catalysts.

6.2 Coupling two metals nanoparticles by using EDC, and NHS Ester using a glass slide and (Langmuir Blodgett trough).

The coupling approach using EDC (1-ethyl-3-(3-dimethylaminopropyl) carbodiimide hydrochloride) and/or NHS (N-hydroxysulfosuccinimide) has been studied for bimolecular (peptides or proteins) crosslinking, but it was anticipated here that the same approach could be used to couple the nanoparticles. EDC is a water-soluble carbodiimide which has been used to promote the formation of an amide bond between a carboxylic acid and an amine. The carbodiimide is sufficiently reactive to form an O-urea intermediate. The amine group (nucleophile) then attacks the O-urea derivative resulting in the overall formation of

the amide.[6, 7] The disadvantage of using EDC is that the O-urea (active ester intermediate) is slow to react with the amine and because the reaction is taking place in aqueous solution, the chance of hydrolyzing the intermediate is high.[8, 9] Adding NHS to the EDC crosslinking process instead forms sulfo-NHS esters which are hydrophilic reactive groups that can react rapidly with the amine in water. Staros *et al*. reported that the use of NHS enhanced the yields by forming an active aster which increased the solubility and the stability of the active ester intermediate.[10] The mechanisms for these reactions are given in Figure 94 and Figure 95.

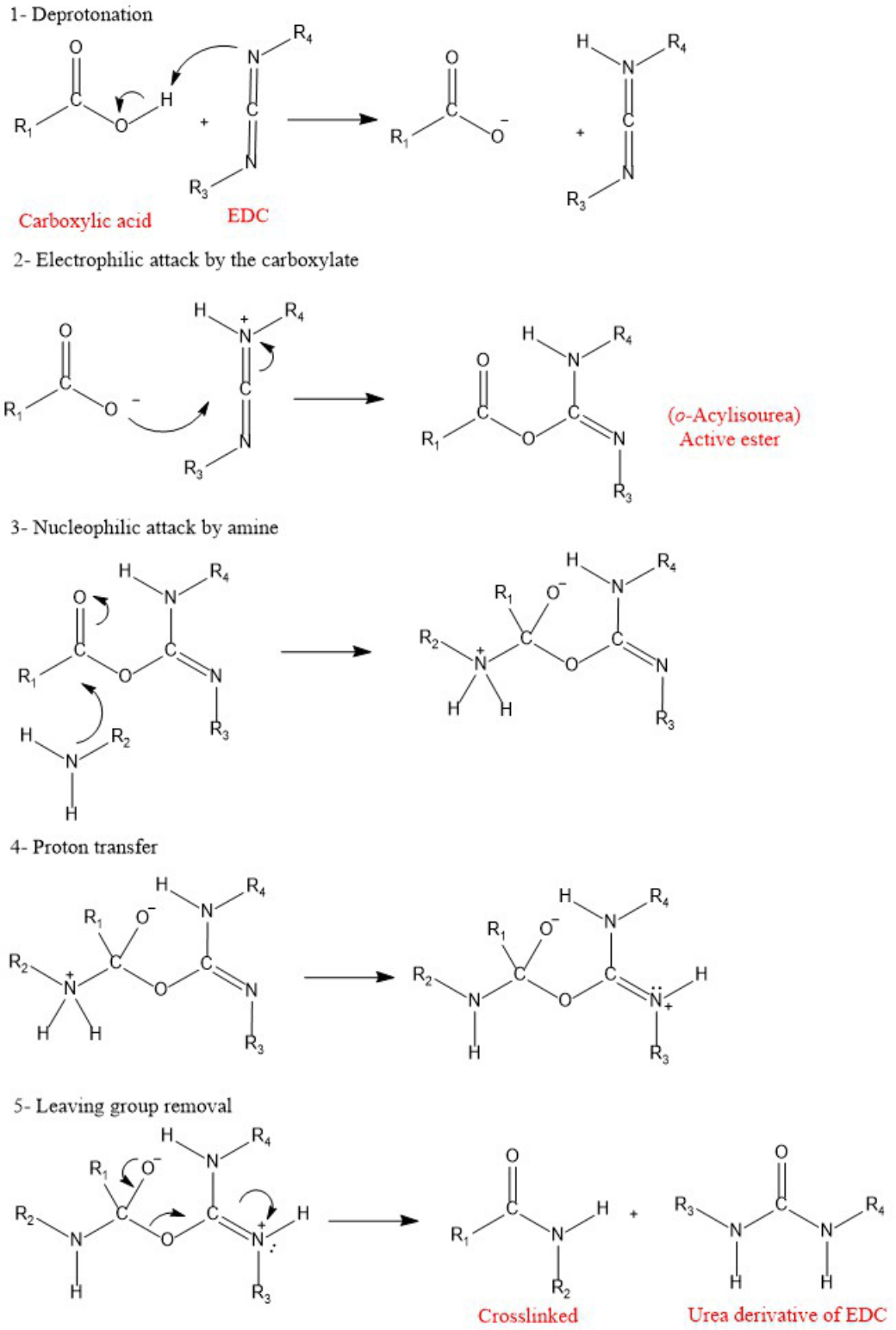

Figure 94: Mechanism for coupling R and R_2 using carboxyl-amine with EDC as a coupling agent.

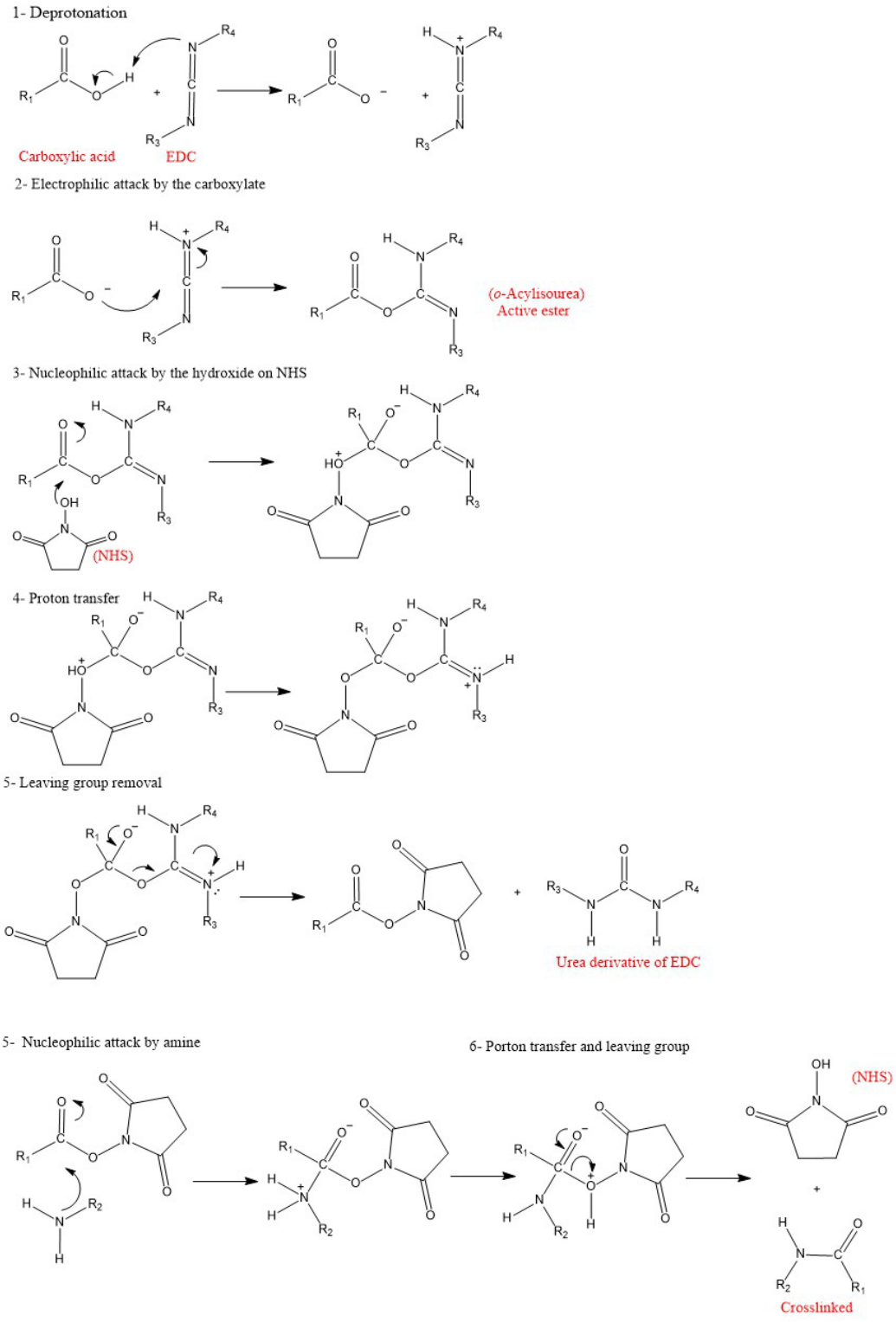

Figure 95: Mechanism for coupling R and R_2 using carboxyl-amine with EDC and NHS as coupling agents.

To enable the use of this as a coupling method to pair different types of nanoparticles controllably (*e.g.* one copper and one palladium), the nanoparticles need to be made unsymmetrical. To achieve this, the nanoparticles can be coated on one side by depositing them as a monolayer on a glass slide using Langmuir Blodgett (LB) deposition. This makes only the side facing away from the glass slide available for reaction, allowing the directionality to be introduced. Figure 96 illustrates the use of an LB Trough to form a film of NPs on the water surface and then deposit them on a glass slide.

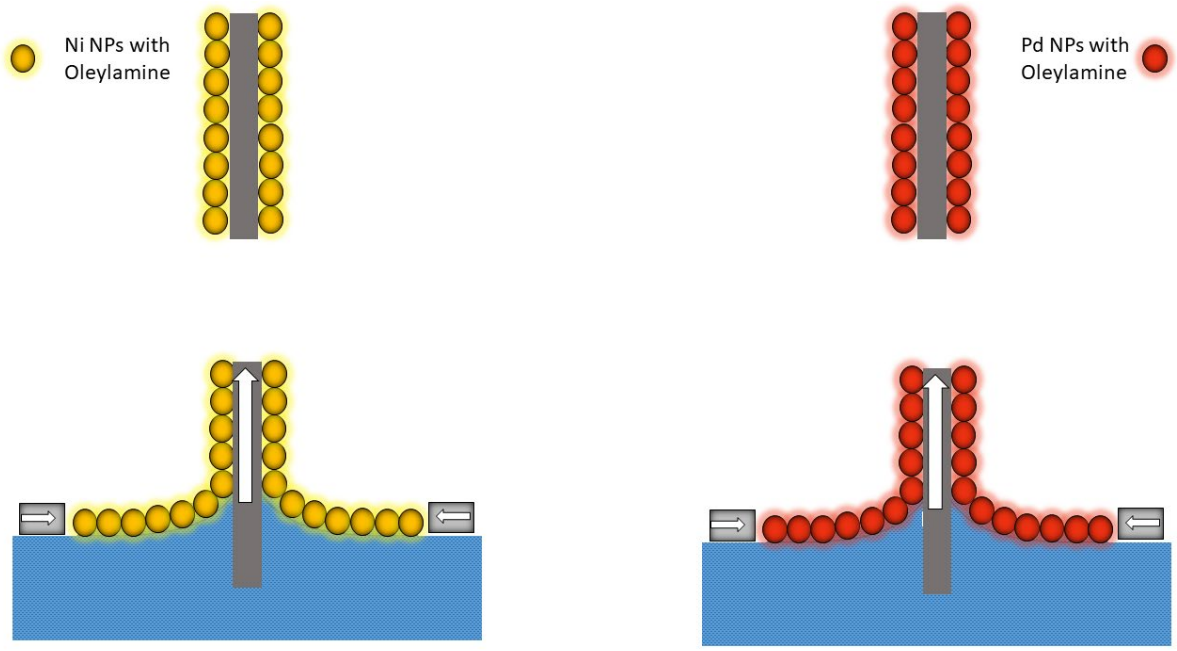

Figure 96: Deposition of a monolayer of Ni (yellow–gold on the left) and Pd (red on the right) NPs on a glass slide by using LB trough.

The synthesis of the nanoparticles outlined in previous chapters uses long-chain amine capping agents around the nanoparticles (NPs-NH2-$(CH2)_n$–CH_3). Ligand exchange reactions, whereby a more strongly binding ligand displaces the long-chain amine, provide a way to introduce the linking molecules to the surface that can couple as above. For instance, 3-mercaptopropionic acid and 4-aminothiophenol both contain sulphur atoms

expected to bind more tightly to the metal surface than the amine, which will provide the intended coupling functional group on the outward-facing surface of the NPs.[11]

6.3 Deposition of nanoparticles into a tightly packed film on a glass slide.

To enable LB deposition of nanoparticle samples in the tightest packed films possible (maximizing number of nanoparticles in film), for each of the three nanoparticle species synthesized (Pd 4.3 nm, Cu 1.8 nm, and Ni 1.3 nm), the surface pressure isotherm was measured using an LB trough. Surface isotherms of the NPs were used to identify the surface pressure at which a monolayer of nanoparticles was formed.

The LB isotherms for the samples of Cu NPs (monolayer at 40 mN m^{-1}), Pd NPs (monolayer at 20 mN m^{-1}), and Ni NPs (monolayer at 35 mN m^{-1}) used in the coupling reaction are shown in Figure 97, Figure 98, and Figure 99, respectively.

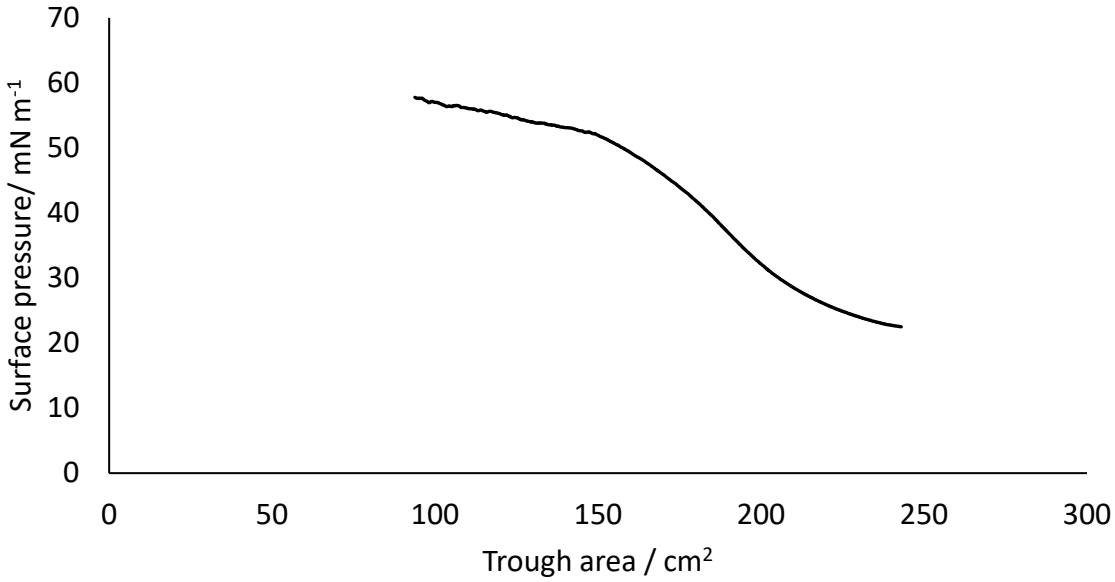

Figure 97: Surface isotherm of Cu NPs; the curve between 30 to 40 mN m^{-1} indicates the formation of the first layer of the NPs.

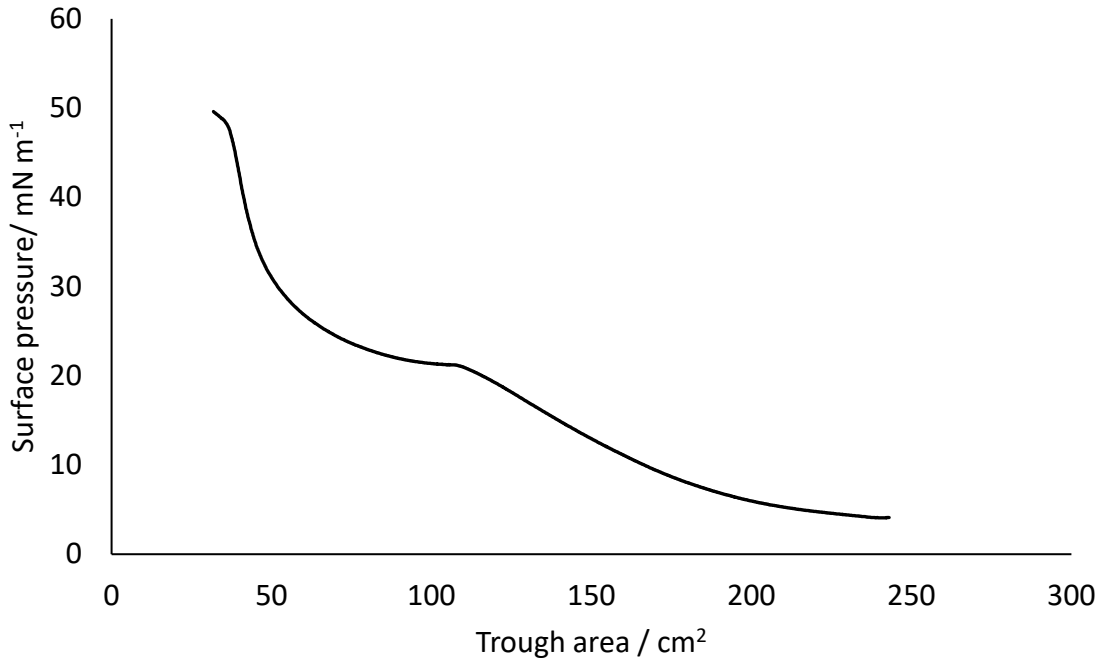

Figure 98: Surface isotherm of Pd NPs; the curve between 10 to 20 mN m^{-1} indicates the formation of the first layer of the NPs.

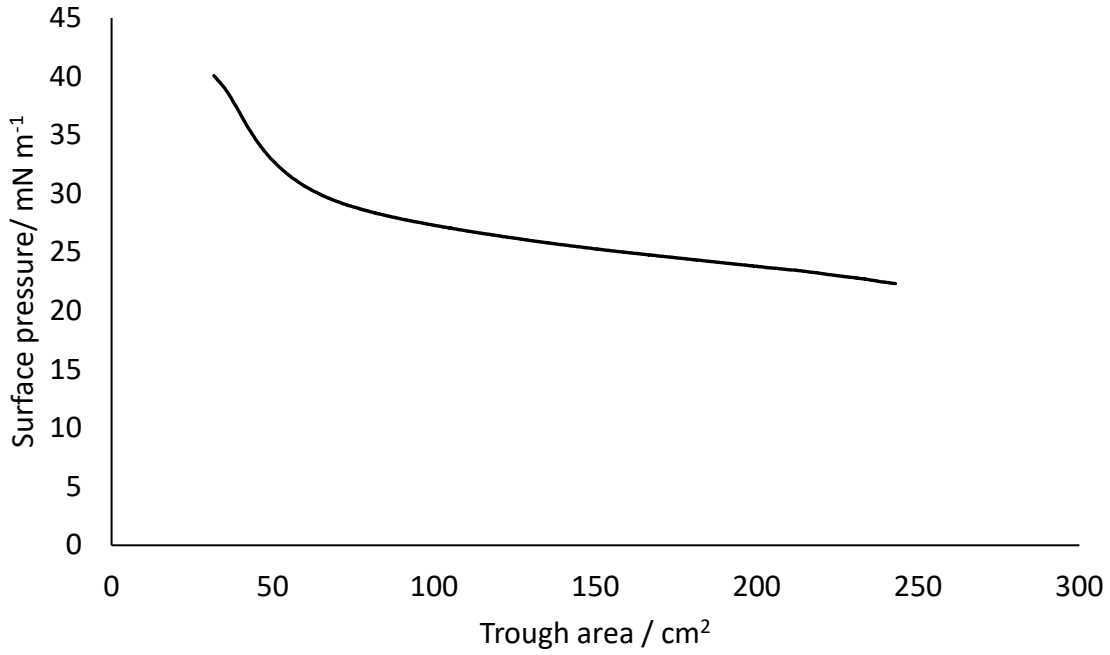

Figure 99: Surface isotherm of Ni NPs; the curve between 30 to 40 mN m^{-1} indicates the formation of the first layer of the NPs.

6.4 Ligand exchange by 3-MPA and 4-ATP

Surface functionalization by using 3-MPA or 4-ATP has been reported in many publications.[12-14] Moreover, 3-mercaptopropionic acid (3-MPA) consists of a thiol group which is needed to bond to the nanoparticle; also, it has a carboxylic group at the other end, which is needed to form the intermediate with (EDC). The choice of a thiol group is expected to displace the amine from the nanoparticle surface as thiols bind well to metal surfaces.[11] The 4-aminothiophenol (4-ATP) similarly consists of a thiol group, which is needed to bond the other nanoparticle, but also contains an amine group which reacts with the activated intermediate in the coupling reactions and forms the link between the two nanoparticles. Figure 100 shows the mechanism of the ligand exchange method and targeted coupling mechanism.

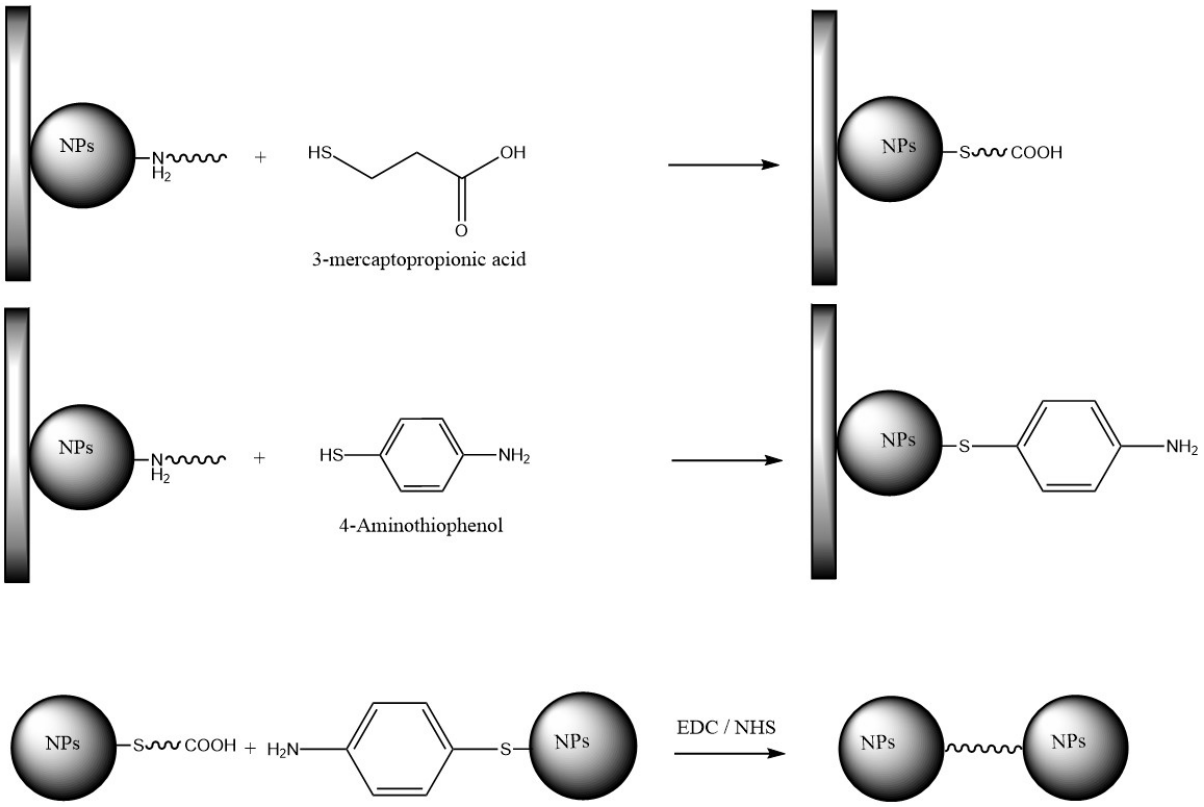

Figure 100: Proposed ligand exchange and nanoparticle coupling mechanism. Top: the NPs attached to the glass slide before ligand exchange reaction with 3-MPA (6 h at RT or 60 °C). Middle: the NPs attached to the glass slide before ligand exchange reaction with 4-ATP (6 h at RT or 60 °C). Bottom: the coupling mechanism between the NPs after getting rinsed by ethanol and detaching from the glass slide by washing in chloroform and coupling by using EDC (RT or 60 °C for 6 h).

Figure 101 and Figure 102 show the contact angle experiments to show the ligand exchange at room temperature (red, Figure 101) and at 60 °C (blue, Figure 102). On the left side of the picture, the water droplet was on the hydrophobic end of the capping agent. On the right side of the picture, the water droplet was on the hydrophilic end of the new ligands. Therefore, after the ligand exchange experiment was done, the contact angle of the water droplet was decreased substantially, indicating the successful exchange of the long-chain amine for 3-MPA. Similar observations were seen in the case of the 4-ATP exchange. 3-MPA and 4-ATP ligands were exchanged with capping agents at room temperature and at 60 °C to examine the effect of the temperature. From the contact angle experiments, no effect of the temperature could be reported. In this case, the lower temperature is always

preferred as it avoids the risk of particle sintering, detachment, or other changes from thermally driven processes.

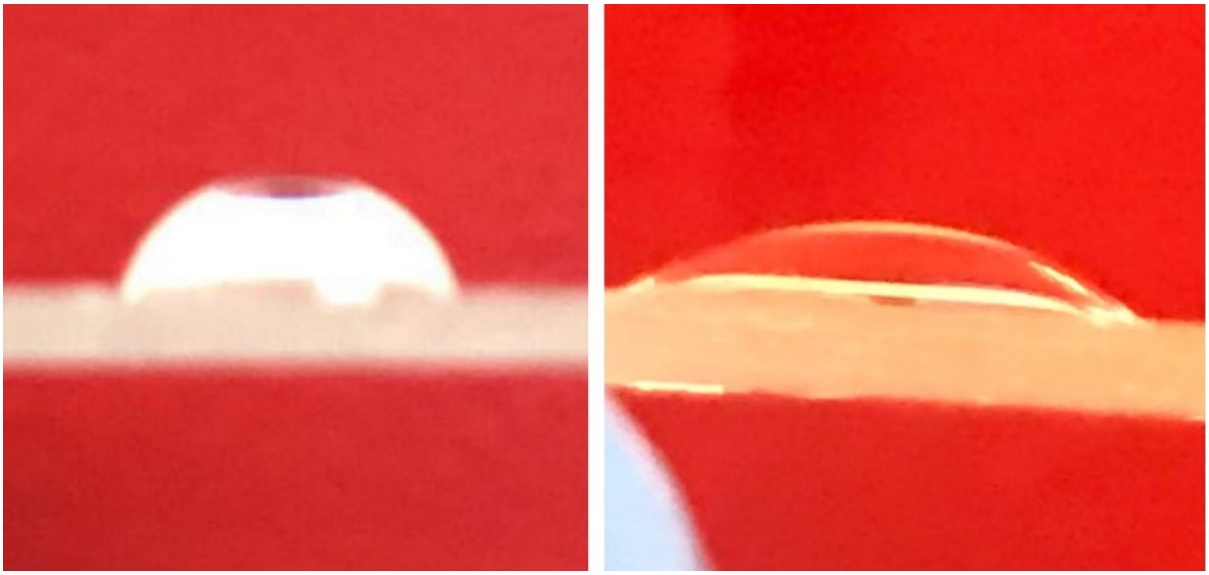

Figure 101: Contact angle experiment before (left) and after (right) 3-MPA was exchanged with Cu NPs at 60 °C.

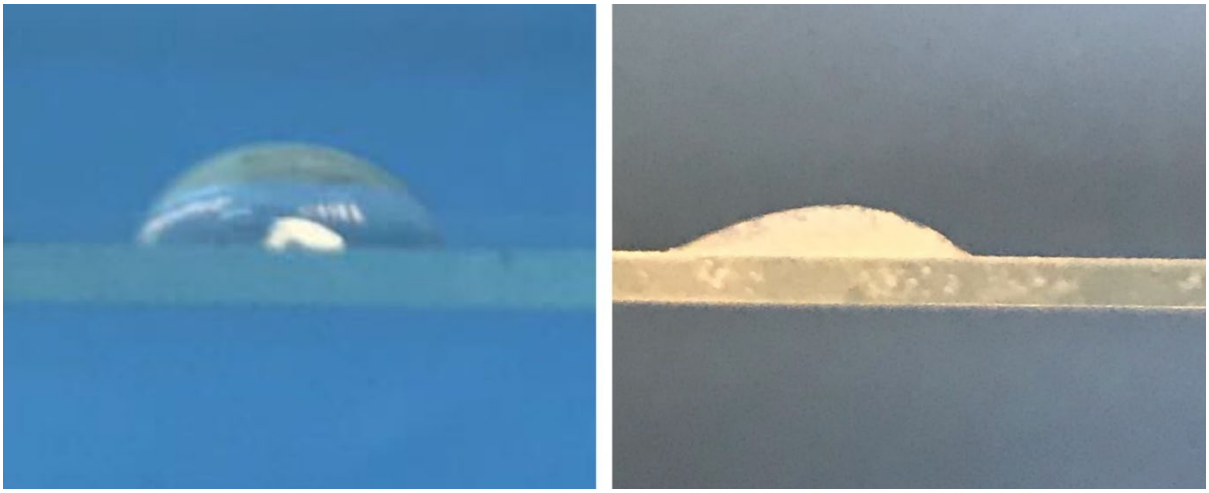

Figure 102: Contact angle experiment before (left) and after (right) 3-MPA was exchanged with Cu NPs at room temperature.

6.5 Coupling of the two unsymmetrically functionalized nanoparticles using the EDC method

The EDC coupling described above will form two nanoparticles that connect via an amide (-CONH-) linker, as can be seen in Figure 103. Again, these experiments were done at room temperature, as reported in previous studies,[9, 10] and 60 °C to examine the effect of the temperature. Preliminary attempts to couple Cu-Pd and Ni-Pd at 60 °C showed possible instances of coupling by TEM, as seen by the particles located next to each other in Figure 104 and Figure 105. Obtaining TEM evidence for the coupling, however, was very challenging because of the need to work under very dilute conditions (*i.e.* very few nanoparticles on the grid) to ensure pairs could be distinguished from co-incidentally co-located nanoparticles. Furthermore, the solvent for the coupling reactions was chloroform which was used to avoid using water (aqueous solution hydrolyzes the active aster[9]), and it was reported that using chloroform enhanced the formation of the ester.[15]

As mentioned above, the stability of the O-urea intermediate is weak, and the ability to hydrolyze this reactive complex (by oxygen atom from the water solution) before the coupling could happen and cause inactivating EDC itself and cleavage of the reactive complex (the activated ester intermediate).[9] This means the target amine does not have enough chance to react with the active carboxylate and finish the coupling reaction before it hydrolyzes. To overcome the hydrolyzation problem, chloroform solvent was chosen to be used for this coupling reaction. Unfortunately, this was found to contaminate or damage the TEM grids resulting in poor images that were difficult to obtain.

These two problems could be solved by using NHS as an additive and doing the reaction in water, as can be seen in the next section 7.6.

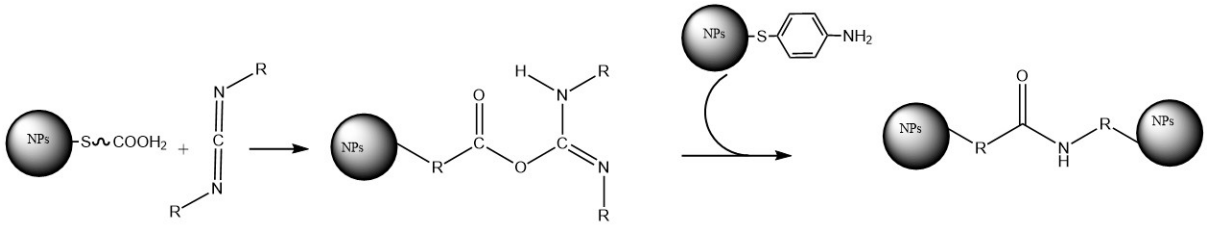

Figure 103: Schematic of coupling two metal NPs by using EDC crosslinking method.

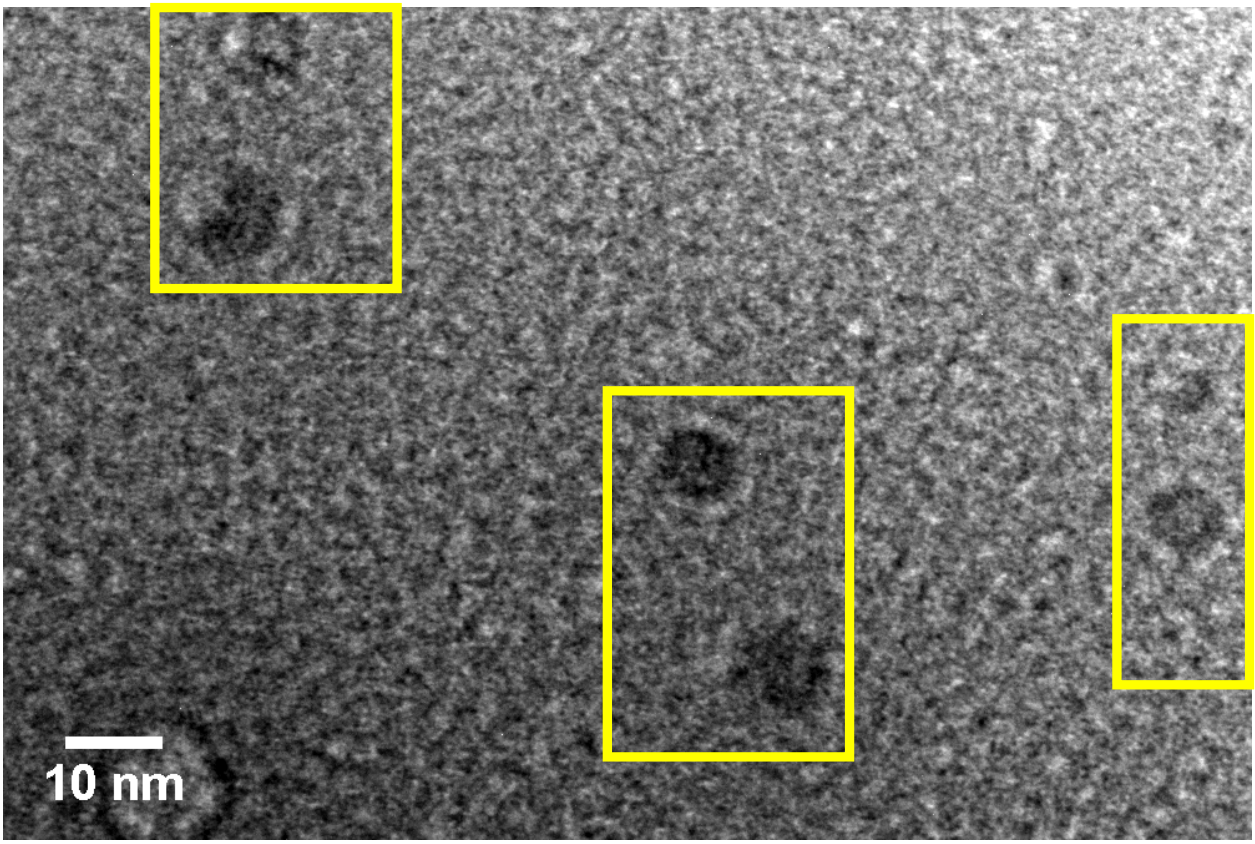

solution to avoid using chloroform solvent. Similarly to the EDC coupling experiment above, these experiments were done at room temperature, as reported in previous studies,[10] and 60 °C to examine the effect of the temperature on the coupling reaction after adding NHS to the reaction. Preliminary attempts to couple Cu-Pd at 60 °C showed an increase in the number of coupling NPs by TEM, as seen by the particles located next to each other in Figure 107. Note again that nanoparticles were placed on the grid at low dilution to enable

distinction between coupled nanoparticles and coincidentally located pairs. Using water instead of chloroform solvent additional helps to overcome the difficulty with TEM imaging that was encountered when using chloroform. Also, the coupling was planned to just use Pd (4 nm) with either Cu (1.8 nm) or Ni (1.3) to understand the coupling visually by the difference on sizes. Moreover, the chance to couple the same metal NPs is hardly to be happen because the capping agents (3-MPA and 4 ATP) have be known to bind tightly to the surface.

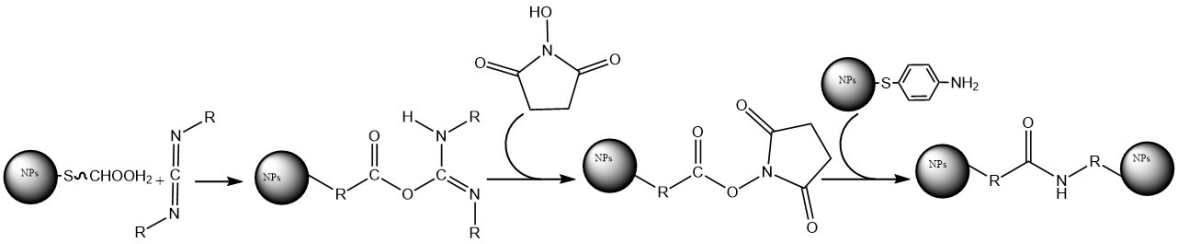

Figure 106: Schematic of coupling two metals NPs by using NHS and EDC crosslinking method.

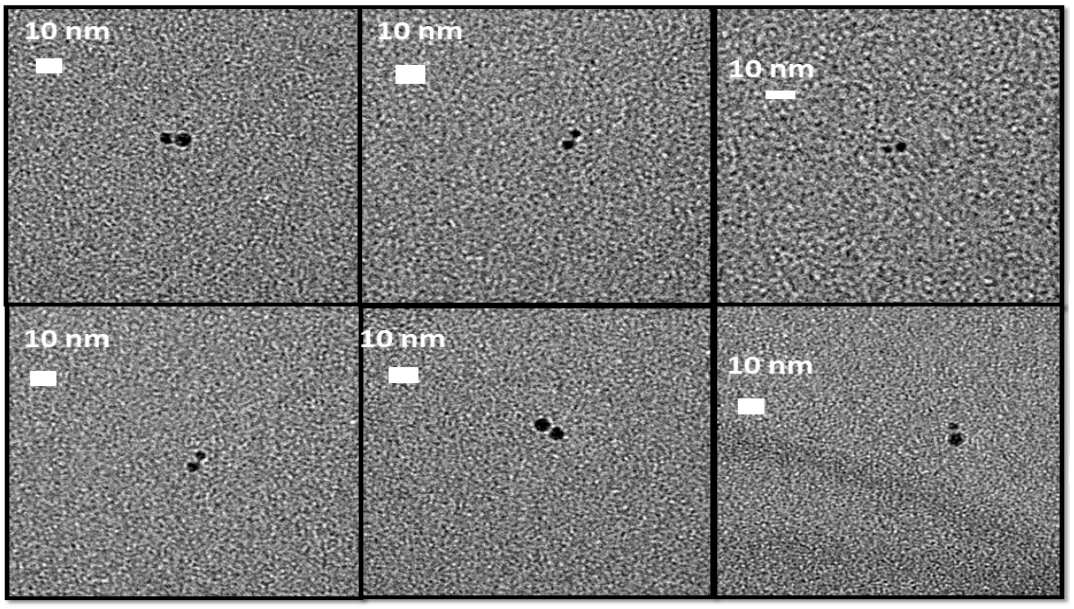

Figure 107: Representative TEM images of coupled NPs (Cu-Pd). The reaction was done in water and at 60 °C.

The reaction was done at two different temperatures to study the effect of the ability to couple NPs at room temperature and at 60 °C. The reason for not going higher than 60 °C is to avoid agglomerating the NPs. The attempt to couple the NPs at room temperature did not happen, as was judged by not finding any paired NPs on the TEM grid. On the other hand, attempting the coupling at 60 °C showed paired NPs but not all NPs were coupled or paired. Based on the full dataset of images from which those in Figure 107 are taken, the number ratio of paired: isolated NPs on the TEM grid was found to be around 1:100. Therefore, the next section will discuss another attempt to improve the coupling process.

6.7 Improvements to the coupling of the two metals NPs with using buffers.

Some researchers also show using buffers can enhance the coupling process when used with proteins. Therefore, I attempted to adapt these coupling methods by using buffers when coupling the metals NPs. For example, a study showed the need of using a two-step protocol with the buffer system.[17] The first step is to react the acid (in our case 3-MBA) with the EDC. They found pH 4.5-7.5 was needed in order to have the EDC link to the COOH. The second step, after reacting with EDC, requires the pH to be increased to 8.0 before adding the amine (in our case, the other metal NPs which had been treated with 4-ATP). This two-step process has been published by a number of groups.[9, 18]

The result of using this method to couple the unsymmetrically ligand-exchanged NPs is promising. The number of coupled NPs was substantially more than the number of coupled NPs that could be seen without using the buffer. For example, in Figure 107, just these 6 paired NPs could be imaged by TEM from one TEM grid, and the ratio of paired: isolated was around 1:100, whereas in Figure 108 the number of paired NPs in just that image is 37 paired NPs. This indicates that the use of a buffer system significantly increases the number of paired NPs. Unfortunately, not all the NPs are paired and not all the paired NPs are just two NPs some are isolated, and some appear to have grouped more than two

NPs. The ratio of unpaired NPs (isolated): to paired NPs (just two NPs): to more than two NPs that can be seen in Figure 108 is summarized in Table 7.

Table 7: The ratio of unpaired NPs (isolated): to paired NPs (just two NPs): to more than two NPs

Isolated nanoparticles	Paired NPs (just two NPs)	More than two NPs
13	37	14

It must be noted that although these results used Pt-Ni and the experiment without buffer used Pd-Cu the ligand exchange was thought to be efficient in all cases, so this should not have a large effect on the subsequent coupling reactions. As the goal of this work was to demonstrate the successful preparation of paired NPs, samples available at the time were used, and further work could confirm the applicability to all NP types.

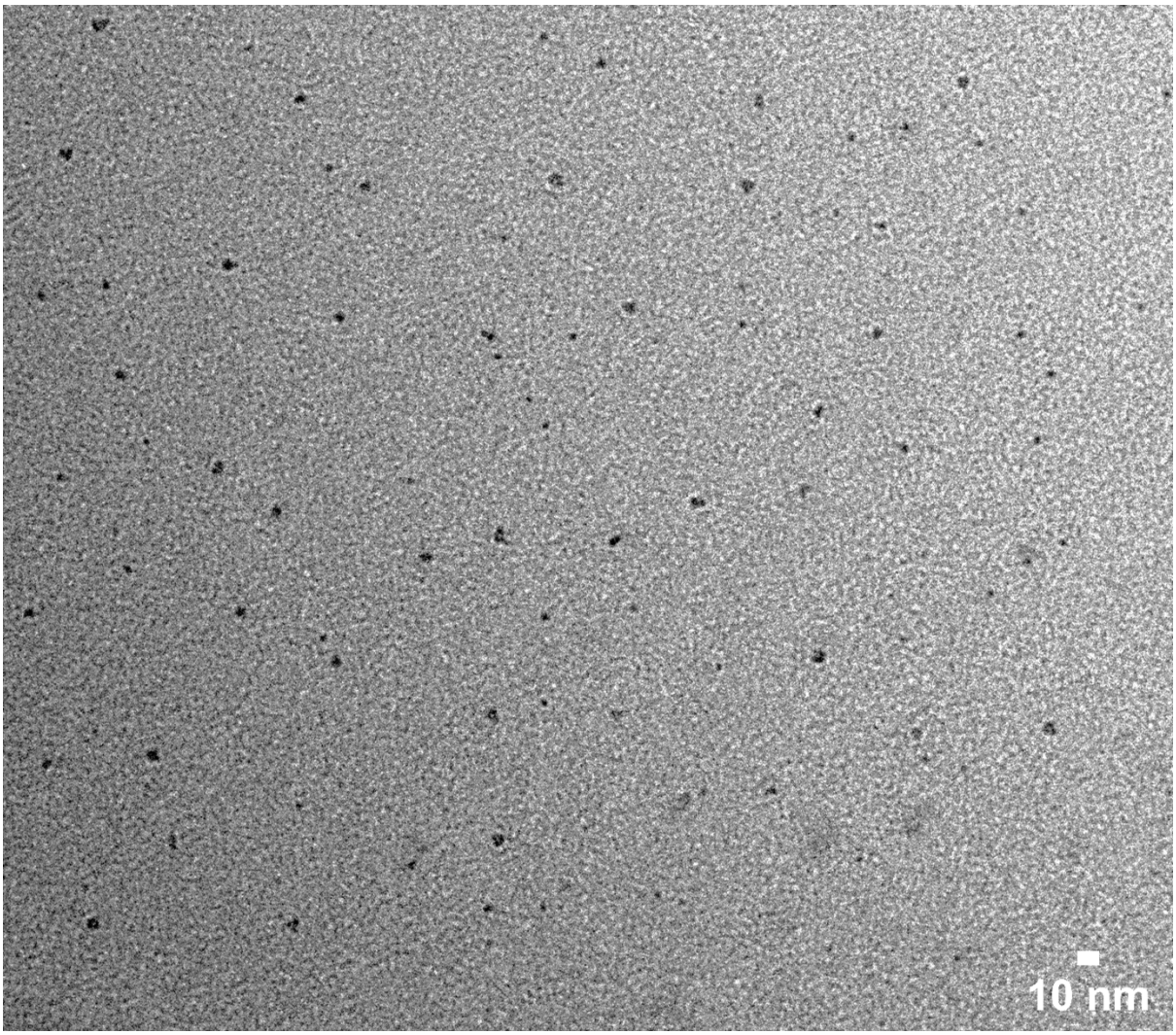

Figure 108: TEM image of Pd-Ni coupled NPs by using buffer method. The ratio of isolated NPs to pried NPs to more than two paired NPs is 13:37:14.

6.8 Conclusion

This chapter investigated the use of synthesized Pd, Ni and Cu NPs for preparing coupled NPs. The method that was used in this chapter was adapted from different works. For example, the method involving EDC as crosslinking agent is well-known and is one of the most frequently used crosslinking chemistries.[9] Although the EDC method has some

limits, such as the reversal of the reactions, NHS can be used to overcome these problems and increase the yields of the desired product.[19]

- The LB Trough method allowed us to deposit a monolayer film of NPs to a glass slide – as identified from the corresponding surface pressure isotherms.
- Contact angle measurements confirmed it was possible to ligand exchange the NPs with capping agents suitable for the coupling reaction while nanoparticles were still deposited on a glass slide (and so only one face of each nanoparticle was exchanged).
- After the nanoparticles were removed from the glass slide, using the EDC coupling method at room temperature and 60 °C showed some limited evidence by TEM of nanoparticle pairs. The effect of the temperature was not noticeable because both samples showed similar results by TEM. To avoid using water as solvent in the reaction, chloroform was used, which made the TEM grid damaged, and only poor TEM images could be collected.
- Adding NHS to create a more active ester intermediate and to overcome the stability issue by just using an EDC agent improves the coupling results based on TEM and allows the reaction in an aqueous solution to facilitate TEM grid preparation. Unfortunately, the number of paired NPs was low compared to isolated NPs on the TEM grid, with the estimated ratio of paired: too isolated particles around 1:100.
- Using a 2-step process using buffers enhanced the coupling reaction substantially and increased the number of paired NPs on the TEM grid with the estimated ratio of isolated: paired: more than two NPs clustered to be 13:37:14 – *i.e.* 58% of nanoparticles form the desired paired product.

1. Khoobiar, S., Particle to particle migration of hydrogen atoms on platinum—alumina catalysts from particle to neighboring particles. *J. Phys. Chem. A* **1964,** *68* (2), 411-412.

2. Boudart, M.; Vannice, M.; Benson, J. E., Adlineation, portholes and spillover. *ZPC* **1969,** *64* (1_4), 171-177.

3. Conner, W., Jr.; Falconer, JL Spillover in Heterogeneous Catalysis. *Chem. Rev* **1995,** *95*, 759-788.

4. Falconer, J.; Conner Jr, W., Second international conference on spillover: Leipzig, GDR, June 13–15, 1989. *Appl. Catal.* **1989,** *56* (2), N28-N29.

5. Karim, W.; Spreafico, C.; Kleibert, A.; Gobrecht, J.; VandeVondele, J.; Ekinci, Y.; van Bokhoven, J. A., Catalyst support effects on hydrogen spillover. *Nature* **2017,** *541* (7635), 68-71.

6. Khorana, H., The Chemistry of Carbodiimides. *Chem. Rev* **1953,** *53* (2), 145-166.

7. Zhou, H.-P.; Zhang, Y.-W.; Mai, H.-X.; Sun, X.; Liu, Q.; Song, W.-G.; Yan, C.-H., Spontaneous Organization of Uniform CeO2 Nanoflowers by 3D Oriented Attachment in Hot Surfactant Solutions Monitored with an In Situ Electrical Conductance Technique. *Eur. J. Chem.* **2008,** *14* (11), 3380-3390.

8. Hoare, D. t.; Koshland, D., A method for the quantitative modification and estimation of carboxylic acid groups in proteins. *Biol. Chem.* **1967,** *242* (10), 2447-2453.

9. Hermanson, G. T., *Bioconjugate techniques*. Academic press: 2013.

10. Staros, J. V.; Wright, R. W.; Swingle, D. M., Enhancement by N-hydroxysulfosuccinimide of water-soluble carbodiimide-mediated coupling reactions. *Anal. Biochem.* **1986,** *156* (1), 220-222.

11. Yang, Y.; Serrano, L. A.; Guldin, S., A versatile AuNP synthetic platform for decoupled control of size and surface composition. *Langmuir* **2018,** *34* (23), 6820-6826.

12. Dewi, M. R.; Laufersky, G.; Nann, T., A highly efficient ligand exchange reaction on gold nanoparticles: preserving their size, shape and colloidal stability. *RSC Advances* **2014,** *4* (64), 34217-34220.

13. Bagaria, H. G.; Ada, E. T.; Shamsuzzoha, M.; Nikles, D. E.; Johnson, D. T., Understanding mercapto ligand exchange on the surface of FePt nanoparticles. *Langmuir* **2006,** *22* (18), 7732-7737.

14. Pong, B.-K.; Trout, B. L.; Lee, J.-Y., Modified ligand-exchange for efficient solubilization of CdSe/ZnS quantum dots in water: A procedure guided by computational studies. *Langmuir* **2008,** *24* (10), 5270-5276.

15. Kubyshkin, V.; Budisa, N., Hydrolysis, polarity, and conformational impact of C-terminal partially fluorinated ethyl esters in peptide models. *Beilstein J. Org. Chem.* **2017,** *13* (1), 2442-2457.

16. Scientific, T., Thermo scientific crosslinking technical handbook. *Waltham (USA): Thermo Scientific* **2012**.

17. Wickramathilaka, M. P.; Tao, B. Y., Characterization of covalent crosslinking strategies for synthesizing DNA-based bioconjugates. *J. Biol. Eng.* **2019,** *13* (1), 1-10.

18. Grabarek, Z.; Gergely, J., Zero-length crosslinking procedure with the use of active esters. *Anal. Biochem.* **1990,** *185* (1), 131-135.

19. Wickramathilaka, M. P.; Tao, B. Y., Characterization of covalent crosslinking strategies for synthesizing DNA-based bioconjugates. *J. Biol. Eng.* **2019,** *13* (1), 63.

Chapter 7 Conclusion

Producing well-defined models of transition metal nanoparticles (NPs) for heterogeneous catalysis is the main purpose of the work in this thesis. Moreover, understanding the mechanism of the synthesis of NPs should give a clear understanding of controlling the size of the NPs, which is an important factor in terms of catalytic activity and selectivity, and essential for using NPs in studies to establish structure-performance relationships.

Chapter 4, the synthesis of Ni NPs was initially started by following the method reported by Metin. The mechanism of the synthesis was not clear and their claim of producing Ni-oleate after 1 hour at 110 °C was not supported by any data. Therefore, chapter 4 aims to achieve a better understanding of all the steps of the reaction. Starting from the Ni complex and the colour changes during the heating up (at 110 °C), and the effect of the time on the precursor Ni complex. UV-Vis-NIR was used to study the changing colour, and the data shows the formation of different Ni complexes as time progresses (overnight). ASAP was used to study the supernatant (after the formation of Ni NPs) and identify biproducts, such as the formation of a compound of oleylamine and $acac^-$ that appears at 350 m/z. Modification in the synthesis based on these experiments led to the ability to synthesize 1.3 nm Ni NPs.

Chapter 5, the synthesis of Cu NPs previously developed in our group was examined. The same processes that were done with the Ni synthesis were done here to understand the steps of the reduction reaction. Here, pyridine is the solvent that can change the size of the Cu NPs when stirred for a long time (overnight) before the reduction – again highlighting the importance of the speciation of the metal species in solution. Also, the temperature was having a huge effect on the formation of the produced Cu NPs, so a series of reactions at different temperatures were done, which indicated the temperature that can generate monodispersed Cu NPs most effectively was 210 °C. The reducing agent is morpholine boron (MB), the role of which was not clear. Therefore, Chapter 6 investigated the reduction of

$M(acac)_2$ by MB. Amine borane (*e.g.* morpholine borane, MB) reduces the $Cu(acac)_2$ to form Cu NPs. TGA showed the decomposition temperature of MB at ~150°C; therefore, the reduction temperatures started from 150 – 210 °C. The supernatant (after separation of the Cu NPs from the rest of the reaction materials) was used to study the fate of the B by ^{11}B NMR, which only showed a signal from the sample synthesised at 210 °C. Releasing of H_2 is investigated too to help understand at which temperature the H_2 is released altogether from the solution, and the experiment showed a higher releasing of H_2 at 210 °C. Therefore, we concluded that for the syntheses at 210 °C (injection of metal shortly after this temperature is reached) the supersaturation of the solution with H_2 occurs, and this acts as the reducing agent.

In Chapter 7, coupling two metal NPs by using linkers was attempted. Modifying the surface of the NPs by exchanging the capping agent with another capping agent followed by LB trough deposition was used, followed by a coupling reaction. The first time this coupling reaction was done by coupling EDC at room temperature and 60 °C, and the results were not sufficient(using TEM imaging to see the coupled NPs). The second method is by adding NHS to the same coupling reaction, and the results show a few coupled NPs, but not as a majority species. Finally, the last method was done by adding EDC and NHS in a buffer solution, and the TEM images showed that over 50 % were in a pair structure.

Chapter 8 Future work

Key ideas for future work from this thesis which could be topics for further research for each Chapter, are provided below.

- For chapter 4, The addition of the stirring time for $Ni(acac)_2$ with oleylamine oleic acid from 1h to overnight before the injection (*i.e.* before starting the reduction) led to a completely different size of Ni NPs. Without stirring overnight (just 1 h) the size of the Ni NPs is 3.2 nm, but with adding extra time for the stirring (overnight) the size was 1.3 nm. Therefore, understanding the role of the time in terms of how the interaction between the $Ni(acac)_2$ and the solvent system (oleylamine and oleic acid) could change the size and uniformity of the Ni NPs is important. Therefore, a topic for further research is to understand how the solvent system interacts with $M(acac)_2$ (*e.g.* $Ni(acac)_2$). Testing different solvent systems (with the same combination of long chain amine with acid) could also be another topic for further research.

  Having achieved small Ni nanoparticle, growing larger nickel nanoparticles remains challenging in the absence of phosphorous reagents that lead to incorporation.[1] These small nickel nanoparticles could potentially lead to seeds to carry out a seeded growth type approach[2] either with the same or a different metal to make larger or bimetallic particles for use in catalytic studies of size and composition effects.
- For chapter 5, the additional time for mixing pyridine with the $Cu(acac)_2$ from 3 h to overnight led to remarkable monodisperse Cu NPs going from 4.3 to 2.8 nm. However, the way pyridine interacts with $Cu(acac)_2$ is not clear. Therefore, understanding the interaction between pyridine and $M(acac)_2$

(*e.g.* $Cu(acac)_2$) will be a topic for further research. Also, pyridine is classified as a psuedo-tertiary amine, so another topic for further research could be testing the different classes of amine at different times to understand which amine class could be used to synthesise smaller and uniform NPs and why a class is better than the other ones. Oleic acid was also added to pyridine for the overnight reaction, and that led to 1.8 ± 0.5 nm particles. However, how the effect happened was not clear and testing different acids (*e.g.* benzoic acid) could be a topic for further research.

- For chapter 6, releasing H_2 by increasing the reaction temperature could open to a new area of understanding of how amine borane reducing agents work. Different reaction temperatures were tested and the temperature that was above the releasing of H_2 somewhat surprisingly led to optimal results. Therefore, a topic for further research could be doing ^1H NMR for the solution that has released H_2 (to find where the H_2 peak appears) and then doing another ^1H NMR from the same solvent system (oleylamine) but without heating the solvent and with just bubbling H_2 through the solution. Hydrogen has previously been seen in a study of monitoring of dissolved H_2 via flow NMR. This idea could also be taken one step further by doing *in situ* ^1H NMR and understanding when and how much H_2 gas can be generated, although this may require special high temperature equipment. Testing different amine borane reducing agents could also be a topic for further research to be used to test the synthesis of NPs from different amounts of released H_2. Indeed, the finding in this chapter suggest the nickel synthesis might be revisited if a amine borane decomposing below the synthesis temperature could be identified.
- For chapter 7, The current results showed 60% coupled NPs by the current technique. Therefore, the coupling could be improved by doing further research on the coupling conditions, which was not possible due to time

constraints. One example of improving the coupling is by testing different buffer systems. Also, testing the same coupling technique with bigger NPs size because the ligand exchange could be more effective / directional when using bigger NPs size (more surface to use to link the 3-MPA and 4-ATP) and compare the result to the small NPs in this thesis to give better understanding if the size of the NPs could affect the coupling process. Finally, a topic for further research is using polyethylene glycol (PEG) as the surface for the ligand exchange. This method was studied by Li *et al*.[3] By using the same principles as I have tried to use with glass slides but using polyethylene glycol (PEG) single crystals. PEG can be bi-functionalised to be COOH-PEG-SH or BOC-NH-PEG-SH (SH covalently binds to NPs and COOH and NH_2 to be used with EDC/NHS coupling). Figure 109 shows the NPs coupling route they reported (although only a few images of individual pairs are shown, so it is likely to need considerable work to render this route to be high yielding for nanoparticle pairs). The NPs are deposited on the surface of the PEG single crystal to interact with the thiol. When thiol is terminated PEG crystallises the PEG is known to separate to the surfaces. The thiol on the PEG surface attaches to the NP. The unattached NPs surfaces were capped with a layer of dodecanethiol (DDT). Two types of M-NPs@PEG were synthesised, namely COOH-PEG-M-NPs-DDT and BOC-NH-PEG-M-NPs-DDT. The BOC protecting group can be removed to produce NH_s-PEG-M-NPs-DDT. Carbodiimide chemistry between the carboxylic acid and amine group was targeted by using N-(3-Dimethylaminopropyl)-N'-ethylcarbodiimide hydrochloride (EDC) and 4-aminothiophenol (NHS). Figure 109 illustrates the coupling processes by using PEG single crystal. This would be advantageous to apply as the surface area of PEG crystals would be much greater than that of the glass slide enabling a higher yield, and it would remove the time consuming LB deposition step from the process.

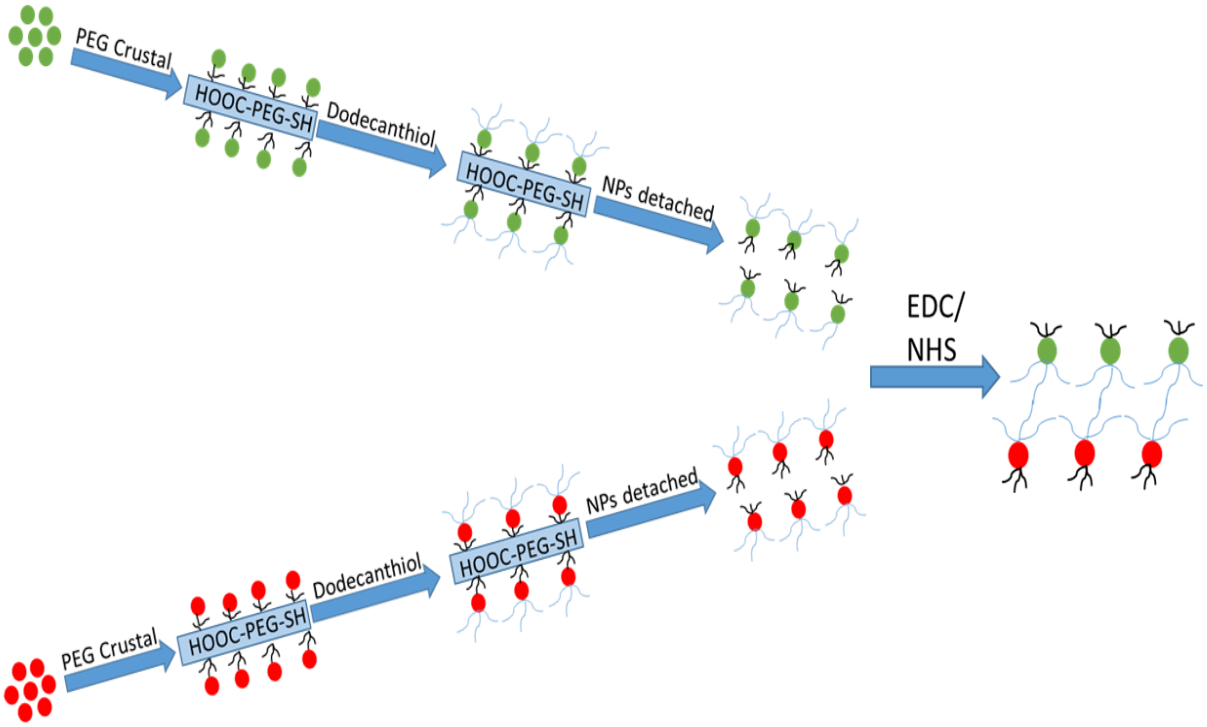

Figure 109: NPs coupling by using PEG and EDC/NHS. Reproduced from literature.[3]

1. Moreau, L. M.; Ha, D.-H.; Bealing, C. R.; Zhang, H.; Hennig, R. G.; Robinson, R. D., Unintended phosphorus doping of nickel nanoparticles during synthesis with TOP: a discovery through structural analysis. *Nano Lett.s* **2012,** *12* (9), 4530-4539.

2. Zettsu, N.; McLellan, J. M.; Wiley, B.; Yin, Y.; Li, Z. Y.; Xia, Y., Synthesis, Stability, and Surface Plasmonic Properties of Rhodium Multipods, and Their Use as Substrates for Surface-Enhanced Raman Scattering. *Angew Chem.* **2006,** *118* (8), 1310-1314.

3. Dong, B.; Li, B.; Li, C. Y., Janus nanoparticle dimers and chains via polymer single crystals. *J. Mater. Chem.* **2011,** *21* (35), 13155-13158.

Chapter 9 Appendix

A-C.3.1 ICP digestion of unsupported nanoparticles

The mass of samples needed and an appropriate volume in which to dilute the sample had been calculated to achieve measurable concentrations, as seen in tables 1-3. For each sample, a duplicate sample has been made to confirm the results. A similar calculation had been carried out for a known inorganic compound (reference), as seen in Tables 4-6. All the samples were submitted after digestion to the metal analysis service in DU Chemistry Department to carry out the experiments.

Table 1: ICP calculations for copper nanoparticles sample.

	Amount needed	Units
Mass $Cu(acac)_2$ In preparation	0.075	g
Fraction Cu by Mw	0.242	Uniteless
Mass Cu in centrifuge tube	0.018	g
Volume in the centrifuge tube	19	mL
Concentration in the centrifuge tube	0.00095	g mL-1
Desired concentration	0.01 to 1; 80% = 0.8 mg/l	mg L-1
Desired concentration	0.0008	mg mL-1
Desired volume of dilute sample	25	mL
Mass needed in the dilute sample	0.02	mg
The volume of Metal NPs concentrate from centrifuge tube needed	0.020	mL
	20.87	µL

Table 2: ICP calculations for Pd nanoparticles sample.

	Amount needed	Units
Mass $Pd(acac)_2$ In preparation	0.073	g
Fraction Pd by Mw	0.349	
Mass Pd in Centrifuge tube	0.025	g
Volume in centrifuge tube	19	mL
Concentration in centrifuge tube	0.001	gmL-1
Desired concentration	0.1 to 1; 80% = 0.8 mg/l	mg L-1
Desired concentration	0.0008	mg mL-1
Desired volume of dilute sample	25	mL
Mass needed in dilute sample	0.02	mg
Volume of Metal NPs concentrate from centrifuge tube needed	0.014	mL
	14.90	µL

Table 3: ICP calculation for Ni nanoparticles sample.

	Amount needed	Units
Mass $Ni(acac)_2$ In preparation	0.257	g
Fraction Ni by Mw	0.228	
Mass Ni in Centrifuge tube	0.058	g
Volume in centrifuge tube	19	mL
Concentration in centrifuge tube	0.002	gmL-1
Desired concentration	8	mg L-1
Desired concentration	0.008	mg mL-1
Desired volume of dilute sample	25	mL
Mass needed in dilute sample	0.2	g
Volume of Metal NPs concentrate from centrifuge tube needed	0.091	mL
	91.97	µL

Table 4: ICP calculation of Cu standard.

Standard	Amount needed	Units
mw Cu(acac)2	261.76	mol g-1
mw Cu	63.546	mol g-1
Ratio by mw Cu in Cu(acac)2	0.2427	Unitless
Desired Conc. (80%)	0.8	mg L-1
Desired Conc. (80%)	0.0008	mg mL-1
Desired volume	25	mL
Concentration of Cu	0.02	mg
Required amount of Cu	2.0596	mg mL-1
Desired volume (first dilution)	25	mL
Concentration of Cu in 1st dil.	0.5	mg mL-1
Required amount of Cu	1	mL
Desired volume (second dilution)	25	mL
Concentration of Cu in Sec. dil.	0.02	mg mL-1

Table 5: ICP calculation of Pd standard.

Standard	Amount needed	Units
mw $Pd(acac)_2$	304.64	mol g-1
mw Pd	106.42	mol g-1
Ratio by mw Pd in $Pd(acac)_2$	0.3493	Unitless
Desired Conc. (80%)	0.8000	mg L-1
Desired Conc. (80%)	0.0008	mg mL-1
Desired volume	25.000	mL
Concentration of Pd	0.0200	mg mL-1
Required amount of Pd	1.4313	mg mL-1
Desired volume (1^{st}. dilution)	25.000	mL
Concentration of Pd in 1^{st} dil.	0.5000	mg mL-1
Required amount of Pd	1.0000	mL
Desired volume (2^{nd}. dilution)	25.000	mL
Concentration of Pd in 2^{nd}. dil.	0.0200	mg mL-1

Table 6: ICP calculation of Ni standard.

Standard	Amount needed	Units
Mw $Ni(acac)_2$	256.91	mol g-1
mw Ni	58.693	mol g-1
Ratio by mw Ni in $Ni(acac)_2$	0.2284	Unitless
Desired Conc. (80%)	8.0000	mg L-1
Desired Conc. (80%)	0.0080	mg mL-1
Desired volume	25.000	mL
Concentration of Ni	0.2000	mg mL-1
Required amount of Ni	21.885	mg mL-1
Desired volume (1^{st}. dilution)	25.000	mL
Concentration of Ni in 1^{st} dil.	5.0000	mg mL-1
Required amount of Ni	1.0000	mL
Desired volume (2^{nd}. dilution)	25.000	mL
Concentration of Ni in 2^{nd}. dil.	0.2000	mg mL-1

A-C.3.2 Calculation of nanoparticle concentrations

A-C.3.2.1 Calculation of Cu NPs Concentration (C_{NP});

From TEM, Cu NPs distribution average size = 1.8 nm

$$Rc = 1.8/2 = 0.9\ \text{nm} \quad (1)$$

The copper atomic radius is 0.128 nm.[1]

$$Ra = 0.128/2 = 0.064\text{nm} \quad (2)$$

First, the number of copper atoms per cluster is;

$$N = (\frac{R_c}{R_a})^3 = (\frac{0.9 \times 10^{-9}}{0.064 \times 10^{-9}})^3 = 2781\ Cu\ atoms/cluster \quad (3)$$

Second, the number of copper atoms on the surface of a cluster;

$$N_s = 4N^{2/3} = (4 \times 2781)^{\frac{2}{3}} = 498\ Cu\ atoms\ on\ surface/cluster \quad (4)$$

Third, the molecular weight of the Cu cluster;

$$M_w = m_a \times N = 63.546 \times 2781 = 176\ kDa \quad (5)$$

Forth, estimating the number of copper clusters that have formed;

1st, calculation of the total number of atoms that can be formed from the copper(acac)$_2$,

3.37×10^{-4} mol (Cu (acac)$_2$ used) X 6.022×10^{23} mol^{-1} = 20.29414×10^{19} (6)

Then;

$$N_{NP_s} = \frac{N_t}{N} = \frac{20.294 \times 10^{19}}{2781} = 7.3 \times 10^{16} \quad (7)$$

A-C.3.2.2 Calculation of Pd NPs Concentration (C_{NP});

From TEM, Pd NPs distribution average size = 4.3 nm

$$Rc \ = \ 4.3/2 = \ 2.15 \text{ nm} \quad (8)$$

The palladium atomic radius is 0.137 nm.[2]

$$Ra \ = \ 0.137/2 = \ 0.0685\text{nm} \quad (9)$$

First, number of palladium atoms per cluster is;

$$N = (\frac{R_c}{R_a})^3 = (\frac{2.15 \times 10^{-9}}{0.0685 \times 10^{-9}})^3 = \ 30920 \ Pd \ atoms/cluster \quad (10)$$

Second, number of palladium atoms on surface of a cluster;

$$N_s = 4N^{2/3} = (4 \times 30920)^{\frac{2}{3}} = 2482 \ Pd \ atoms \ on \ surface/cluster \quad (11)$$

Third, the molecular weight of Pd cluster;

$$M_w = m_a \times N = 106.42 \times\ 30920\ = 3290kDa \quad (12)$$

Forth, estimating amount of Pd clusters that have formed;

1st, calculation of the total number of atoms that can be formed from the palladium(acac)$_2$,

$$2.4x10^{-4}\ \text{mol (Pd (acac)}_2\ \text{used) X}\ 6.022 \times 10^{23}\ \text{mol}^{-1} = 1.445 \times 10^{20} \quad (13)$$

Then;

$$N_{NP_s} = \frac{N_t}{N} = \frac{1.445 \times 10^{20}}{30920} = 4.673 \times 10^{15} \quad (14)$$

A-C.3.2.3 Calculation of Ni NPs Concentration (C_{NP});

From TEM, Ni NPs distribution average size = 1.3 nm

$$Rc\ =\ 1.3/2 =\ 0.65\ \text{nm} \quad (15)$$

The nickel atomic radius is 0.124 nm.[3]

$$Ra\ =\ 0.124/2 =\ 0.062\ \text{nm} \quad (16)$$

First, number of nickel atoms per cluster is;

$$N = (\frac{R_c}{R_a})^3 = (\frac{0.65 \times 10^{-9}}{0.062 \times 10^{-9}})^3 = 1152\ Ni\ atoms/cluster \quad (17)$$

Second, number of nickel atoms on surface of a cluster;

$$N_s = 4N^{2/3} = (4 \times 1152)^{\frac{2}{3}} = 277\ Ni\ atoms\ on\ surface/cluster \quad (18)$$

Third, the molecular weight of Ni cluster;

$$M_w = m_a \times N = 58.693 \times 1152 = 67kDa \quad (19)$$

Forth, estimating amount of Ni clusters that have formed;

1st, calculation the total number of atoms that can be formed from the nickel $(acac)_2$,

$$8.17x10^{-4}\ \text{mol (Ni (acac)}_2\text{ used) X } 6.022 \times 10^{23}\ \text{mol}^{-1} = 4.92 \times 10^{20} \quad (20)$$

Then;

$$N_{NP_s} = \frac{N_t}{N} = \frac{4.92 \times 10^{20}}{1152} = 4.3 \times 10^{17} \quad (21)$$

A-C.3.3 Calculation of spiked samples

The expected volume of H_2 to be released from morpholine borane was calculated by using the ideal gas law, Equation 1, and the calculation can be seen in Equation 2:

$$PV = nRT \quad (1)$$

Where: P= pressure / atm = 1, V= volume / L, n= number of moles / g mol^{-1} = $3.37x10^{-4}$, based on the number of moles of amine borane in the reaction mixture, R Molar gas constant/ [(atm.L)/mol.K)]= 0.0821 and T= temperature / K = 25+273= 298

$$V = \frac{0.000337 \times 0.0821 \times 298}{1} L = 8.2 \times 10^{-3} L = 8.2\, mL \quad (2)$$

for one molecule of hydrogen being produced for each amine borane molecule in the reaction mixture

1. Murali, S.; Srikanth, N.; Vath, C. J., An analysis of intermetallics formation of gold and copper ball bonding on thermal aging. *Mater. Res. Bull.* **2003,** *38* (4), 637-646.
2. Keuler, J. N.; Lorenzen, L.; Sanderson, R. D.; Prozesky, V.; Przybylowicz, W. J., Characterization of electroless plated palladium–silver alloy membranes. *Thin Solid Films* **1999,** *347* (1), 91-98.
3. Inoue, A.; Zhang, T.; Masumoto, T., Zr–Al–Ni amorphous alloys with high glass transition temperature and significant supercooled liquid region. *Mater. Trans., JIM* **1990,** *31* (3), 177-183.